Editorial

With this issue, the *Journal of Astrophysics and Astronomy* enters its sixth year of publication. In the course of the last five years, we have brought out four regular volumes and also a special volume commemorating the Golden Jubilee of the Indian Academy of Sciences. The process of typesetting, printing and distribution has been streamlined. 156 articles by 194 authors have been published in 18 issues totalling about 2000 pages. (The General Index is in press, and will be released shortly).

The Editorial Board is grateful to the entire astrophysical community which has made this possible, whether by contributing research papers, or by improving the quality of research through refereeing, or by reading the articles and citing them.We are hoping for increased support in future since the *Journal has* a tremendous potential to grow, particularly in terms of a larger number of pages per issue and more frequent publication. Further, as in the past, it will keep an open mind towards divergent scientific opinions and views as long as they can be formulated objectively and substantiated by arguments.

We have had a very good response from the referees. Generally, each paper has been refereed by two among the best workers in the field. They have expended considerable time and effort to improve the papers and have rarely been prejudiced, overcritical or indifferent. It is unfortunate that we did not receive revised versions of many articles for which the referees suggested substantial improvement. I would request our authors to always consider the referee's comments seriously and in good faith, and to keep in mind that the referees have spared a good deal of their time with the sole purpose of improving the quality of the papers. We are listing below the names of most of our referees. Not included in the list are a few who have desired to be totally anonymous, the referees of very recent papers, and the members of the editorial board who sometimes took the responsibility on themselves. We are deeply grateful to all of them.

The success of a journal depends largely on its readers. We are happy to note that the *Journal of Astrophysics and Astronomy* has acquired a considerable readership and that the articles published in it have been cited well. However, the astrophysical community cannot artificially be divided into authors, referees, and readers. We hope for a greater degree of overlap in their activities and also for increased involvement with the *Journal*. We would particularly like to solicit more research papers, as we can easily handle a larger influx without augmenting the processing time.

V. Radhakrishnan
Chairman, Editorial Board

J. Astrophys. Astr. (1985) **6,** 5–19

Tidal Interactions in Binary Stellar Systems

S. M. Alladin, N.Ramamani & T. Meinya Singh *Centre of Advanced study in Astronomy, Osmania University, Hyderabad 500007*

(*Invited article*)

Abstract. The tidal interactions in binary stellar systems are studied under the assumption that the orbital motion of the binary is negligible in comparison with the stellar motion. By integrating over time the tidal forces acting on the stars, the energy changes are derived. These are used to obtain simple analytical expressions for the rates of disruption and merging. This method gives appropriate value for the Roche density ρ_R and it is found that the disruption rate of a satellite of density ρ changes drastically at $\rho \simeq \rho_R$ A comparison is made with earlier results obtained under the simplifying assumption that stellar motion is negligible in comparison with the orbital motion of the binary and its implications are discussed.

Key words: stellar dynamics—Roche density—interacting galaxies

1. Introduction

It is well known that tidal disruption of a satellite system occurs if its density ρ is less than a critical density, the Roche density ρ_R If $\rho < \rho_R$ the satellite disrupts whereas for $\rho > \rho_R$ the disruption is considered negligible. In this case the tidal effects of the satellite. on the outer parts of the primary generally turn out to be quite important and lead to the decay of the orbit of the satellite.Numerical studies of mergers of binary systems have been made by several workers (see Tremaine 1981; Alladin & Narasimhan 1982; White 1983a for reviews). Tidal disruption and merging are two important processes that govern the dynamical evolution of a binary stellar system.

The dynamical friction formula of Chandrasekhar (1942) is of much utility in the study of tidal effects in interpenetrating binaries, as confirmed by the numerical study of Lin & Tremaine (1983). However, the limitations of the formula in describing completely the underlying physics, despite its usefulness to predict decay rates rather correctly, has been indicated by the simulations of sinking satellites by White (1983b). Non-interpenetrating binaries also spiral into each other as a result of tidal effects, where the above formula cannot be used.

Alladin & Parthasarathy (1978) (hereinafter referred as Paper I) studied the energy transfer in binary, spherical stellar systems under the *impulsive approximation* (IA) wherein it is assumed that the stellar motions may be neglected in comparison with the orbital motion of the binary. They derived analytical expressions for the times of disruption and merging for non-interpenetrating pairs.

The use of IA for estimating the changes in energy in hyperbolic encounters has much justification. Even in the case of slow hyperbolic encounters, this approximation is quite good (Toomre 1977); but when used for slower bound orbits of binary galaxies this

approximation generally overestimates tidal effects. Spitzer's (1958) numerical work with simple harmonic motion for the stars in the test system and uniform rectilinear motion for the perturber shows that IA is probably better than 20 per cent on the average if $\beta = 2p\omega/V < 2$ where $2\pi/\omega$ is the oscillation period of the star in the test system and p and V are the distance and velocity of the perturber attheClosestapproach. For $\beta > 4$ IA overestimates the tidal effects by more than an order of magnitude. The criterion $\beta < 2$ implies $\omega < \omega'$ where ω' is the angular velocity of the perturber at the Closest approach. Even at Roche density ρ_R for the circular orbit of the binary, the assumption of stationary star has been employed by King to obtain a very useful formula for the tidal radius (Equation 21). However, for a component of the binary whose density is much higher than the Roche density, IA will overestimate the disruptive effects for the circular orbit of the binary.

In the case of bound orbits, the other extreme approximation, the *adiabatic approximation* (AA) wherein it is assumed that the orbital motion of the pair may be neglected in comparison with the motion of the stars in the system, is much better. This approximation has been used earlier by Avner & King (1967) to study the secular change in the angular momentum of stars in the Galaxy due to the tidal influence of Magellanic Clouds. They did not expect any secular change in energy. As pointed out by Richstone (1975), in a slow bound orbit of the binary, no change is expected in the energy of a star in circular orbit about its parent due to adiabatic invariance. But an adiabatic invariant is not constant over infinite time. Since the total energy of the entire binary system is conserved, the existence of dynamical friction implies that there is ecular increase in internal energy.

In this paper we study the tidal interactions in binary stellar systems under AA. We consider the stars to be moving in circular orbits. As in Paper I, the changes in energies of the stars in the test (parent) system are derived by integrating over the time the tidal forces acting on them. These are used to make estimates for the rates, of disruption and merging.

If the potential due to the perturber is time independent, there cannot be any secular energy change in the test system.Hence the neglect of the motion of the perturber in our treatment (AA) is incompatible with secular energy transfer from orbital motion of the binary to the internal motions. Nevertheless we shall use this approximation as an assumption. A similar situation is encountered in the widely used IA where it is generally assumed that the perturber moves in a straight line with uniform velocity. This assumption is also incompatible with energy transfer. But it has been successfully used to calculate the energy transfer.

An interesting feature of the present work is that it highlights the drastic change that occurs in the rate of disruption near the Roche density. The theory also gives reasonable estimates for the rates of merging of binary galaxies, and of globular clusters, with the parent galaxy.

2. Energy changes

2.1 *Velocity Perturbation in the Adiabatic Approximation*

We consider the stellar systems to be spherically symmetric and non-interpenetrating and the stars to be moving with circular velocities and having circularly symmetric distribution of velocity vectors.

Consider a stellar system of mass M_1 (the perturber) at a distance D (assumed constant) from another system of mass M (the test system). We denote the quantities pertaining to the perturber by the subscript 1. We define a Cartesian coordinate system (X, Y, Z) with origin at O, the centre of M. As in Fig. 1, we take the X-Y plane to be the orbital plane of the star under consideration and let the X-axis be in the direction of the projection of the radius vector of O_1, the centre of M_1, on the X-Y plane and the Y-axis 90° away in the direction of revolution of the representative star S. The Z-axis is taken in the right-handed sense.

Since the problem involves the motion of S with respect to O, the relevant force is the differential force exerted by M_1 at S, relative to the force at O exerted by M_1. This is the tidal force on S due to M_1 per unit mass and is given by

$$\mathbf{f} = \mathbf{f}_* - \mathbf{f}_0 = GM_1[\mathbf{r}'/r'^3 - \mathbf{D}/D^3] \tag{1}$$

where $\mathbf{f}_*$ and $\mathbf{f}_0$ are the accelerations due to M_1 at S and O respectively, and $\mathbf{r}'$ and $\mathbf{D}$ are the radius vectors of S from O_1 and O_1 from O respectively. Let the position vector of S be $\mathbf{r}$ with components ($r\cos\theta$, $r\sin\theta$, 0), where θ is the angle measured from the X axis. Since

$$\mathbf{r}' = \mathbf{D} - \mathbf{r},$$

the components of Equation (1) can be written as

$$f_x = \frac{GM_1}{D^2}\left[\left(\frac{D^3}{r'^3} - 1\right)\cos b - \frac{rD^3}{Dr'^3}\cos\theta\right] \tag{2a}$$

$$f_y = -\frac{GM_1}{D^2}\left[\frac{rD^3}{Dr'^3}\sin\theta\right] \tag{2b}$$

$$f_z = \frac{GM_1}{D^2}\left[\left(\frac{D^3}{r'^3} - 1\right)\sin b\right] \tag{2c}$$

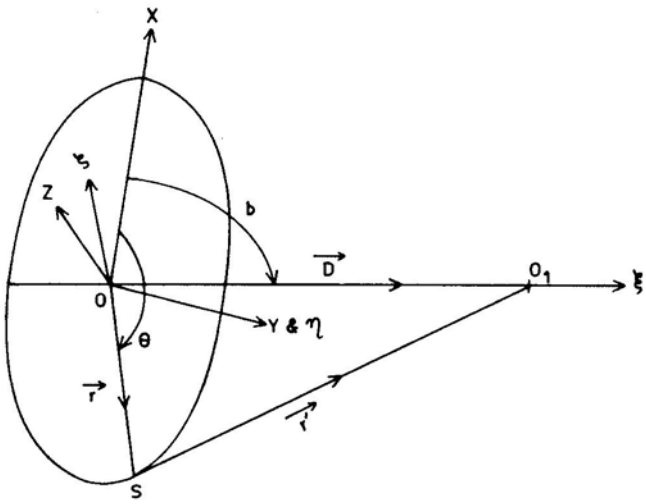

Figure 1. The Coordinate Systems

where b is the angle which **D** makes with the X-axis. These equations are the same as Equations 4, 5 and 6 in Avner &King (1967). The change in velocity of a star in time t is obtained from

$$\Delta \mathbf{V}(t) = \int_0^t \mathbf{f}\,\mathrm{d}t. \tag{3}$$

Since we assume that the perturber's motion may be neglected, we set $\mathrm{d}b / \mathrm{d}t = 0$. Hence the above equation takes the form

$$\Delta \mathbf{V} = \int_{\theta_0}^{\theta_1} \mathbf{f} \frac{\mathrm{d}t}{\mathrm{d}\theta}\,\mathrm{d}\theta \tag{4}$$

where θ_0 is the value of θ at $t = 0$ and θ_1 its value at time t.

In the approximation in which the perturber remains stationary, ΔV depends on time both through θ and $\mathbf{r}'$. The distance r´ is given by

$$r'^2 = D^2 + r^2 - 2Dr\cos b\cos\theta \tag{5}$$

so that

$$D^3/r'^3 = [1 + (r/D)^2 - 2(r/D)\cos b\cos\theta]^{-3/2}. \tag{6}$$

Writing $a = r/D$ and expanding the right-hand side of Equation (2) binomially, and neglecting terms of powers of a beyond 8 since a is small, we get

$$\begin{aligned}\Delta V_x = \frac{GM_1a^2}{VD}\int_{\theta_0}^{\theta_1} &[(3\cos^2 b - 1)\cos\theta + \tfrac{3}{2}a\cos b\\ &\times \{\cos^2\theta(5\cos^2 b - 2) - 1\} + \tfrac{1}{2}a^2\{5\cos^3\theta\\ &\times (7\cos^4 b - 3\cos^2 b) - 3\cos\theta(5\cos^2 b - 1)\}\\ &+ \tfrac{5}{8}a^3\{7\cos^4\theta(9\cos^5 b - 4\cos^3 b)\\ &- 3\cos^2\theta(14\cos^3 b - 4\cos b) + 3\cos b\}\\ &+ \tfrac{3}{8}a^4\{7\cos^5\theta(33\cos^6 b - 15\cos^4 b)\\ &- 70\cos^3\theta(3\cos^4 b - \cos^2 b) + 5\cos\theta\\ &\times (7\cos^2 b - 1)\} + 7a^5\{33\cos^6\theta(13\cos^7 b\\ &- 6\cos^5 b) + 45\cos^4\theta(11\cos^5 b - 4\cos^3 b)\\ &+ 15\cos^2\theta(9\cos^3 b - 2\cos b) - 5\cos b\}]\,\mathrm{d}\theta,\end{aligned} \tag{7a}$$

$$\begin{aligned}\Delta V_y = -\frac{GM_1a^2}{VD}\int_{\theta_0}^{\theta_1} &[\sin\theta\{1 + 3a\cos b\cos\theta + \tfrac{3}{2}a^2\\ &\times (5\cos^2 b\cos^2\theta - 1) + \tfrac{5}{2}a^3\cos b\cos\theta\\ &\times (7\cos^2 b\cos^2\theta - 3) + \tfrac{15}{8}a^4\\ &\times (21\cos^4 b\cos^4\theta - 14\cos^2 b\cos^2\theta + 1)\\ &+ \tfrac{21}{8}a^5\cos b\cos\theta(33\cos^4 b\cos^4\theta\\ &- 30\cos^2 b\cos^2\theta + 5)\}]\,\mathrm{d}\theta,\end{aligned} \tag{7b}$$

$$\begin{aligned}\Delta V_z = \frac{GM_1a^2}{VD}\int_{\theta_0}^{\theta_1} &[3\sin b\cos b\cos\theta + \tfrac{3}{2}a\sin b\\ &\times (5\cos^2 b\cos^2\theta - 1) + \tfrac{5}{2}a^2\sin b\cos b\cos\theta\\ &\times (7\cos^2 b\cos^3\theta - 3) + \tfrac{15}{8}a^3\sin b\end{aligned}$$

$$\times (21\cos^4 b\cos^4\theta - 14\cos^2 b\cos^2\theta + 1)$$
$$+ \tfrac{21}{8}a^4 \sin b\cos b\cos\theta(33\cos^4 b$$
$$\times \cos^4\theta - 30\cos^2 b\cos^2\theta + 5) + \tfrac{7}{16}a^5$$
$$\times \sin b(429\cos^6 b\cos^6\theta - 495\cos^4 b$$
$$\times \cos^4\theta - 135\cos^2 b\cos^2\theta - 5)]\,\mathrm{d}\theta. \tag{7c}$$

The velocity perturbations in a fixed frame (ξ, η, ζ) with the same centre O in which the ξ-axis is taken in the direction of O_1, the η-axis in the direction of the Y-axis and the ζ-axis perpendicular to both ξ and η axis in the right-handed sense as shown in Fig. 1, can be obtained by using the transformation equations

$$\Delta V_\xi = \Delta V_x \cos b + \Delta V_z \sin b, \tag{8a}$$
$$\Delta V_\eta = \Delta V_y, \tag{8b}$$
$$\Delta V_\zeta = -\Delta V_x \sin b + \Delta V_z \cos b. \tag{8c}$$

2.2 *Short-Term Energy Changes*

In this section we derive the changes in the energies of stars on a timescale equal to half its period. We shall refer to this time as short term. If the density of the system is less than the Roche density, the evolution of the system will be dominated by the short-term tidal forces.

Equation (7) gives on integrating over half the period (*i.e.*, integrating over θ from θ_0 to θ_1, where $\theta_1 = \theta_0 + \pi$),

$$\Delta V_x(P/2) = \frac{GM_1a^2}{VD}[2(3\cos^2 b - 1)(-\sin\theta_0) + \tfrac{3}{2}\pi a(\tfrac{5}{2}\cos^3 b$$
$$- 2\cos b) + \tfrac{5}{2}a^2\{(\tfrac{7}{6}\cos^4 b - \tfrac{1}{2}\cos^2 b)(-\sin 3\theta_0)$$
$$+ (\tfrac{21}{2}\cos^4 b - \tfrac{21}{2}\cos^2 b + \tfrac{6}{5})(-\sin\theta_0)\} + \ldots], \tag{9a}$$

$$\Delta V_y(P/2) = -\frac{GM_1a^2}{VD}[2\cos\theta_0 + 3a^2\cos\theta_0(5\cos^2 b\cos^2\theta_0 - 1)$$
$$+ \tfrac{15}{4}a^4\cos\theta_0(\tfrac{21}{2}\cos^4 b\cos^4\theta_0$$
$$- \tfrac{14}{3}\cos^2 b\cos^2\theta_0 + 1) + \ldots], \tag{9b}$$

$$\Delta V_z(P/2) = \frac{GM_1a^2}{VD}[6\sin b\cos b(-\sin\theta_0) + \tfrac{3}{2}\pi a\sin b$$
$$\times (\tfrac{5}{2}\cos^2 b - 1) + \tfrac{5}{2}a^2\sin b\cos b$$
$$\times \{\tfrac{7}{6}\cos^2 b(-\sin 3\theta_0) + (\tfrac{21}{2}\cos^2 b - 6)$$
$$\times (-\sin\theta_0)\} + \ldots]. \tag{9c}$$

From Equation (9) we obtain

$$[\Delta \mathbf{V}(P/2, r)]^2 = [\Delta V_x(P/2)]^2 + [\Delta V_y(P/2)]^2 + [\Delta V_z(P/2)]^2. \tag{10}$$

The stars undergo different changes in energies depending on the values of θ_0. On an

average; a star with a given value of b would acquire in a half period $(\Delta \mathbf{V})^2$ given by

$$[\Delta \mathbf{V}(P/2, r)]^2 = 1/2\pi \int_0^{2\pi} [\Delta \mathbf{V}(P/2, r)]^2 \, d\theta_0. \tag{11}$$

Because of the assumption of unperturbed circular orbits for the stars there is no change in the potential energy of the stellar system. Hence, $\Delta U = \Delta T$, where ΔU is the change in the internal energy and ΔT, the change in its kinetic energy. This is similar to the case of IA where the potential energy does not change due to the assumption of stationary stars. The change in the energy per unit mass of a star at a distance r from the centre of M over half the period of its orbital motion, is given by

$$\Delta U(P/2, r) = \tfrac{1}{2}[\mathbf{V}^2(P/2, r) - \mathbf{V}^2(0, r)], \tag{12}$$

where $\mathbf{V}$ (P / 2, r) and $\mathbf{V}$(0, r) are the velocities of the star at r at times t = P/2 and 0 respectively. Now,

$$\mathbf{V}(P/2, r) = \mathbf{V}(0, r) + \Delta \mathbf{V}(P/2, r). \tag{13}$$

Hence Equation (12) becomes

$$\Delta U(P/2, r) = \mathbf{V}(0, r) \cdot \mathbf{V}(P/2, r) + [\Delta \mathbf{V}(P/2, r)]^2/2. \tag{14}$$

The first term on the right-hand side is a fluctuating term which can be positive or negative for a star. Since we assume that the stars have a circularly symmetric distribution of velocities, to every star which moves in a certain direction, there is another star moving in the opposite direction. Hence the first term gives zero for any shell of radius r. We therefore get for a shell of radius r

$$\Delta U(P/2, r) = \frac{1}{2\pi} \int_{-\pi/2}^{\pi/2} [\Delta V^2(P/2, r)] \, db = \frac{3.5 G^2 M_1^2 r^4}{V^2 D^6} [1 - 2(r/D)^2]. \tag{15}$$

As pointed out by Spitzer & Chevalier (1973) it is meaningful to estimate the change in the internal energy at median radius, R_h. Keeping only the dominant first term in Equation (15), we get for n = 4 polytropic model

$$\Delta U(P/2, R_h)/|U(R_h)| = 12 M_1^2 R_h^6 / M^2 D^6 \tag{16}$$

where U (R_h) is the energy per unit mass at R_h. The numerical constant depends weakly on the model chosen: for n = 1 to 4, the constant varies from 10 to 12. Let $\rho_h = M/2(4\pi R_h^3/3)$ and $\rho_1 = M_1/(4\pi D^3/3)$.In terms of these densities,

$$\Delta U(P/2, R_h)/|U(R_h)| \simeq (2\rho_1/\rho_h)^2. \tag{17}$$

This ratio provides a good order-of-magnitude estimate for the intensity of the tidal force at R_h. The stellar system may be regarded as stable so long as this ratio is less than unity. Hence for stability we require, $\rho_h > 2\rho_1$. If disruption at the periphery of the system ($r = R$) is considered, ρ_h should be replaced by $\rho = M/(4\pi R^3/3)$.

Equation (17) is in good agreement with the criterion of stability given by Kurth (1957) and von Hoerner (1957). von Hoerneralso neglected the motion of the perturber as in our case.

Chandrasekhar (1942) obtained for the stability of a homogeneous, ellipsoidal star cluster moving in a circular orbit of radius D under the gravitational potential of the Galaxy

$$\rho > \rho_R \tag{18}$$

where the critical or Roche density ρ_R is, in our notation

$$\rho_R = \frac{1}{\pi G b'}\left(\frac{d^2 \mathcal{V}}{dD^2} - \frac{1}{D}\frac{d\mathcal{V}}{dD}\right) \tag{19}$$

where b' depends on the ratio of the axes of the ellipsoid, b' is 1.33 for a homogeneous sphere. For spherically symmetric systems, the above equation yields

$$\rho > 3\rho_1. \tag{20}$$

The same result can also be deduced from King's (1962) formula for stability which states that the test system is stable if its radius is smaller than the tidal radius which is given by

$$R_t^3 = R_p^3\left[\frac{M}{M_1(3+e)}\right] \tag{21}$$

where e is the eccentricity of the cluster orbit and R_p the distance of closest approach.

The result of the present analysis is therefore in good agreement with earlier results. The present treatment also shows that

$$\Delta U(P/2, R_h)/|U(R_h)| = (\rho_R/\rho_h)^2 \tag{22}$$

where the Roche density

$$\rho_R = 2\rho_1. \tag{23}$$

2.3 *LongTerm Energy Changes*

In his analysis, Chandrasekhar neglected the higher order terms in r/D in the expansion of the galactic potential $\mathcal{V}$. These give rise to small but interesting long-term effects which we shall presently discuss. To obtain these, we integrate the tidal force over a period of the star, *i*.e., Equation (7) over θ from 0 to 2π. Irrespective of the value of θ_0, all stars at a distance r would have the same value of $\Delta\mathbf{V}$ when the integration is performed from θ_0 to $\theta_0 + 2\pi$. Hence there is no need to average over θ as was done for short-term effects. The changes in velocities are

$$\Delta V_x = \frac{GM_1\pi a^3}{VD}\left[\tfrac{3}{2}\cos b(5\cos^2 b - 4) + \tfrac{15}{32}a^2\cos b(63\cos^4 b - 64\cos^2 b + 24) + \tfrac{35}{128}a^4\cos b(429\cos^6 b - 729\cos^4 b + 432\cos^2 b - 64) + \ldots\right] \tag{24a}$$

$$\Delta V_y = 0 \tag{24b}$$

$$\Delta V_z = \frac{GM_1\pi a^3}{VD}\left[\tfrac{3}{2}\sin b(5\cos^2 b - 2) + \tfrac{15}{32}a^2\sin b(63\cos^4 b - 56\cos^2 b + 8) + \tfrac{35}{128}a^4\sin b(429\cos^6 b - 594\cos^4 b + 216\cos^2 b - 16) + \ldots\right]. \tag{24c}$$

From these we get

$$\Delta\mathbf{V}^2 = \frac{22.2G^2M_1^2r^6}{V^2D^8}\left[(5\cos^4 b - 8\cos^2 b + 4) + \frac{5r^2}{8D^2}\right.$$

$$\times (49\cos^6 b - 102\cos^4 b + 72\cos^2 b - 16)$$
$$+ \frac{5r^4}{256D^4}\left(7749\cos^8 b - 19936\cos^6 b + 18704\cos^4 b - 7296\cos^2 b + \frac{2752}{3}\right)\Bigg]. \tag{25}$$

From the above equation, we get for a shell of radius r

$$\Delta U(P, r) = \frac{1}{2\pi}\int_{-\pi/2}^{\pi/2} [\Delta V^2(P, r)]\,db \tag{26a}$$

$$= \frac{20.8G^2M_1^2r^6}{V^2D^8}[1 - (0.989r/D)^2 + (1.157r/D)^4]. \tag{26b}$$

The change in energy at the median radius R_h is given by

$$\frac{\Delta U(P, R_h)}{|U(R_h)|} = \frac{64M_1^2R_h^8}{M^2D^8} = 16(\rho_1/\rho_h)^2(R_h/D)^2. \tag{27}$$

In Equation (27) we have retained only the dominant

Assuming that the secular energy change for a star varies linearly with time and that the relative orbit of the binary is circular, the change in its internal energy over T, the orbital period of the binary, is given by

$$\Delta U(T, r) = T[\Delta U(P, r)]/P \tag{28}$$

$$= \frac{20.8G^{0.5}M_1^2r^{5.5}}{[M(r)]^{0.5}(M_1 + M)^{0.5}D^{6.5}}. \tag{29}$$

The changes in the internal energy of M due to all the stars is given by

$$\Delta U(T) = \int_M \Delta U(T, r)\,dM$$

$$= \frac{20.8G^{0.5}M_1^2}{(M_1 + M)^{0.5}D^{6.5}}\int_0^R \frac{r^{5.5}(dM/dr)\,dr}{[M(r)]^{0.5}}. \tag{30}$$

Most of the contribution to this integral comes from the outer parts of the system in spite of the fact that there is very little mass there. If the stellar system is represented by a polytropic model, this reduces to

$$\Delta U(T) = \frac{20.8G^{0.5}M_1^2K_nR_h^{5.5}}{D^{6.5}(1 + M_1/M)^{0.5}} \tag{31}$$

where K_n = 4.2, 9.1 and 56.3 for polytropic indices n = 2, 3 and 4 respectively.

From the energy conservation law, the change in the external energy is

$$\Delta E(T) = -[\Delta U(T) + \Delta U_1(T)]. \tag{32}$$

Normalizing this with $E = -GMM_1/2D$, the energy of the binary orbit, we get,

$$\frac{\Delta E(T)}{E} = \frac{38.5}{(M + M_1)^{0.5}D^{5.5}}[M_1K_nR_h^{5.5}/M^{0.5} + M(K_n)_1(R_h)_1^{5.5}/M_1^{0.5}]. \tag{33}$$

2.4 Reversal Phenomenon in Tidal Effects

It follows from Equations (26) and (16) that $\Delta U\,(R_h) / |U\,(R_h)|$ obtained for half a stellar period is greater than that obtained for the full period. This implies that the tidal effects during the second half of the stellar period work in the opposite direction to a great extent. This can be seen mathematically by noting that when Equation (7) is integrated from 0 to 2π, the alternate terms give zero. The terms which are dominant in the case of half period do not contribute anything over a full period. This phenomenon of the reversal of tidal effects was earlier noted by Ahmed & Alladin (1981) in their study of changes in sizes and shapes of initially spherical galaxies in fast head-on collisions. They found from their numerical work that the galaxies became more and more prolate until their Closest approach. But as they receded from each other after their Closest approach, the prolate structure was destroyed. This happens because the tidal acceleration in the direction of motion of the galaxies gets reversed after their closest approach. On the other hand, the transverse acceleration works in the same direction throughout. This can also be inferred from the analytical derivation given by Toomre (1977) for a head-on collision of Plummer model galaxies under the impulsive approximation.

3. Rates of disruption and merging

As in Paper I, we assume that as the two systems spiral into each other, the changes in energy vary linearly with time. We define the rate of disruption at median radius by

$$t_{dh}^{-1} = [\Delta U(R_h)/|U(R_h)|]P^{-1}. \tag{34}$$

Using Equation (27) we get

$$t_{dh}^{-1} = \frac{7.3G^{0.5}M_1^2R_h^{6.5}}{M^{1.5}D^8}. \tag{35}$$

We define the rate of merging as

$$t_m^{-1} = \langle dE/dt \rangle/E = (\Delta E/E)T^{-1}. \tag{36}$$

Using Equation (33) we get,

$$t_m^{-1} = \frac{6.6G^{0.5}}{D^7}[M_1M^{-0.5}K_nR_h^{5.5} + MM_1^{-0.5}(K_n)_1(R_h)_1^{5.5}]. \tag{37a}$$

Miller (1984) has discussed that the translational energy lost by a satellite due to dynamical friction is partly used in increasing the velocity dispersion of the background and partly in deforming the satellite and increasing its binding energy. These two parts are represented by the second and first terms respectively in Equation (37a).

If we assume that M is ä mass point moving in a circular orbit with velocity V_{orb}, in Equation (37a) the first term may be neglected and it can be written in the form

$$t_D = A_nV_{orb}^3/(G^2M\rho_1) \tag{37b}$$

where $A_n = 0.036(D/R_{hl})^{5.5}/(K_n)_1$ This may be compared with the dynamical friction time given by Larson (1976), *i.e.,* the time required for dynamical friction to decelerate significantly a massive object moving with typical velocity V,

$$t_D \sim 4 \times 10^8 V^3/(M\rho_{local})\ \text{yr}, \tag{37c}$$

where M is in $M_\odot$, V in km s^{-1} and ρ_{local} in $M_\odot pc^{-3}$. In Larson's formula, the local density of M_1 is to be used while in Equation (37b), the density interior to D is used. For spherically symmetric models

$$\frac{\rho_1}{\rho_{local}} = \frac{3M_1/D}{dM_1/dD}.$$

In Fig. 2, we plot t_m^{-1} against the separation D/R_h taking $M = M_1 = 10^{12} M_\odot$ and $R_h = 10$ kpc for two mass distributions of polytropic indices $n = 2$ and $n = 4$. It can be seen from Fig. 2 that merging is always much faster than disruption for non-interpenetrating identical galaxies and that two typical elliptical galaxies ($n = 4$) will merge within a Hubble time if the separation of their centres is less than 70 kpc. t_{dh}^{-1} is also shown m Fig. 2. It is nearly the same for $n = 2$ and $n = 4$.

4. Transfer of angular momentum

On account of the simplifying assumptions we have made, the stellar systems cannot acquire a net change in angular momentum. However, the changes in the angular momentum of individual stars can be studied under AA as was done by Avner & King (1967). A rough estimate for the changes in the angular momentum in the stellar systems can however be made from the change in the orbital energy by making use of the results of several workers (*e.g.,* Tremaine, Ostriker & Spitzer 1975; White 1978; Lin & Tremaine 1983; Villumsen 1982) that dynamical friction tends to circularize the relative orbit of the binary. We shall therefore assume that the initially circular orbit remains circular throughout. It then follows from Goldstein's (1950) Equation (3-48) that

$$J^2 = -G^2(MM_1)^3/2E(M + M_1) \tag{38}$$

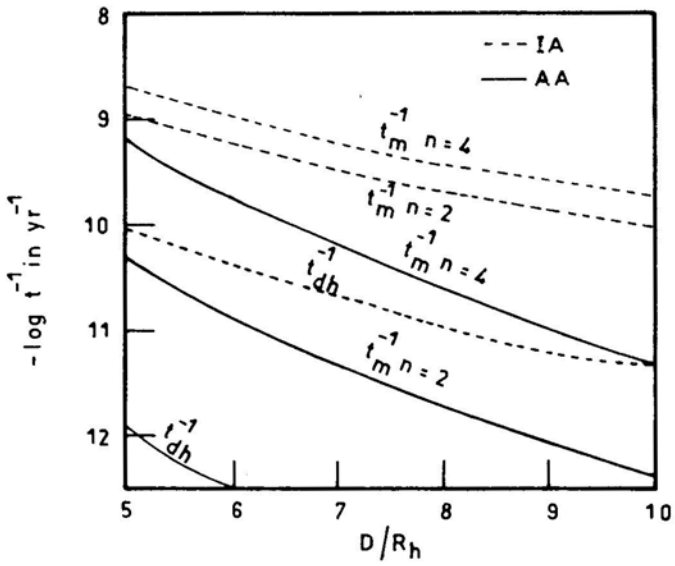

Figure 2. Rates of merging and disruption under *adiabatic approximation* (AA) and *impulsive approcimation* (IA) in an equal component binary with $M = M_1 = 10^{12}\ M_\odot$ and $R_h = (R_h)_1 = 10$kpc.

and

$$\frac{1}{J}\frac{\mathrm{d}J}{\mathrm{d}t} = \frac{1}{2E}\frac{\mathrm{d}E}{\mathrm{d}t}. \tag{39}$$

The fractional change in angular momentum of the orbital motion of the binary is therefore half the change in energy. The stars in the two stellar systems will gain angular momentum at the rate dJ/dt.

The merger process imparts rotation to the stellar system in the same sense as the orbital motion. Tidal interaction is enhanced if a system rotates in the direction of revolution of the binary (White 1979; Innanen 1979). Since the rates of disruption and merging have been derived without taking this factor into account, the actual rates would be greater than our values.

5. Discussion

AA predicts smaller tidal effects in comparison with IA. This is because the tidal effects in AA depend on higher powers of r/D than in IA. The merging rate of close equal-component binary galaxies obtained from Equation (37) does not differ so much from that given by Equation (2.23) in Paper I, as the disruption rate obtained from Equation (35) differs from that given by Equation (2.18) in Paper I. This is elucidated in Fig. 2, which compares the rates predicted by IA and AA. This is because the merging is largely determined by the energy changes occurring in the outer parts of the stellar systems where the motion of the stars is slower and hence IA is better, whereas the disruption occurs due to the energy changes in the relatively interior parts where the stars move faster. The neglect of the motion of the stars in the interior parts in IA in determining the disruption rate is quite serious for $\rho > \rho_{\mathrm{R}}$.

In Fig. 3 we compare the disruption rates of a satellite predicted by AA, IA and by

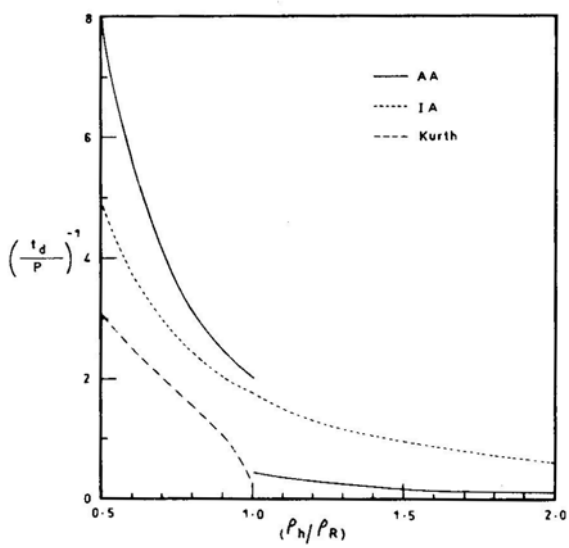

Figure 3. Rate of disruption under *adiabatic approximation* (AA), *impulsive approximation* (IA) and Kurth's (1957) formula. In plotting the results for AA, we have used Equations (17) and (23) for $\rho_{\mathrm{h}} < \rho_{\mathrm{R}}$ and Equations (23) and (27) with $D/R_h = 3$ for $\rho_{\mathrm{h}} > \rho_{\mathrm{R}}$.

Kurth's (1957) formula over the range $0.5\rho_R < \rho_h < 2\rho_R$. For $\rho_h > \rho_R$ we have assumed $D/R_h = 3$ in AA. It can be seen from Fig. 3 that AA predicts a drastic change in the disruption rate near ρ_R. We have modified Kurth's formula to obtain disruption at the median radius instead of disruption at the periphery by writing ρ_h instead of ρ. IA estimates are obtained from Paper I using $U(R_h) = 3U$. Over the range $0.6\ \rho_R < \rho_h < 0.9\rho_R$, the three formulae give the same order of magnitude estimate for the disruption rate. IA overestimates for $\rho_h > \rho_R$.

Considering the Galaxy and a globular cluster as a binary stellar system, the merging and disruption times of the globular cluster were calculated in Paper I under IA using Schmidt's (1965) model for the Galaxy. The globular cluster was modelled as a polytropic distribution of index $n = 4$, mass $= 10^5\ M_\odot$ and $R_h = 7$pc. We give in Table 1 t_m^{-1} and t_{dh}^{-1} derived from the present treatment for the same model of the globular cluster using the more recent Ostriker & Caldwell (1979) model for the Galaxy. Values of t_D^{-1} (Larson 1976) are also given. A comparison of the results also shows that the disruption rates are considerably reduced in AA. The merging is always faster than disruption for a globular cluster until it reaches near the Roche limit and not slower as predicted by IA. This is also consistent with the scenario given by Tremaine, Ostriker & Spitzer (1975) according to which globular clusters spiral inward until they are tidally disrupted at the Roche limit. For $D < 500$ pc the disruption is rapid. Application of the theory discussed here to the Galaxy–LMC pair has been made by Ramamani, Meinya Singh & Alladin (1984).

In Paper I it was mentioned that under IA $\Delta U/|U|$ in a parabolic orbit is 8 times smaller than that in a circular orbit of radius equal to the distance of Closest approach in the parabolic case. This statement needs to be modified. It is more appropriate to infer $\Delta U/|U|$ for the parabolic case from IA and for the circular case from AA. When this is done, it follows that the transition from parabolic to circular orbit increases the tidal effects by not more than a factor of 3 if $\rho = \rho_R$. But if $\rho > \rho_R$, $\Delta U/|U|$ for a circular orbit would be considerably reduced below the parabolic value because the rapid motion of the stars tend to reduce the tidal effects. Thus as one goes from hyperbolic encounter to a circular orbit, the tidal effects at first increase until the parabolic limit is

Table 1. Rates of disruption and merging fora globular cluster in the Galaxy.

D kpc	$M(D)$ $M_\odot$	t_{dh}^{-1} yr^{-1}	t_m^{-1} yr^{-1}	t_D^{-1}† yr^{-1}
0.5	8.8(+9)	1.3(−10)	9.5(−12)	4.5(−11)
1.0	1.5(+10)	1.6(−12)	1.6(−12)	1.3(−11)
2.0	2.6(+10)	1.4(−14)	3.8(−13)	5.3(−12)
3.0	3.7(+10)	8.6(−16)	1.8(−13)	2.5(−12)
4.0	5.0(+10)	1.3(−16)	1.1(−13)	1.2(−12)
5.0	6.1(+10)	4.7(−17)	6.7(−14)	6.8(−13)
6.0	7.3(+10)	2.0(−17)	4.4(−14)	4.3(−13)
7.0	8.4(+10)	9.3(−18)	3.5(−14)	2.8(−13)
8.0	9.4(+10)	5.1(−18)	2.6(−14)	1.9(−13)
9.0	1.0(+11)	2.9(−18)	2.1(−14)	1.2(−13)
10.0	1.1(+11)	1.6(−18)	1.8(−14)	1.0(−13)

(n) indicates 10^n
† Larson (1976)

reached and later they decrease. The tidal effects are generally at their maximum near the parabolic case.

A comparison between the nature of tidal effects in fast encounters and in slow bound orbits can be made by comparing the predictions of IA and AA. In AA the energy of the orbital motion of the binary is chiefly transferred to the internal motion in the outer parts of the stellar systems in spite of the fact that these parts contain little mass. But in IA more energy (not energy per unit mass) is transferred to the inner region ($r \sim R_h$) and the outer parts are relatively deprived. Thus if the inner region of a stellar system shows signs of being much perturbed by the companion, it is likely that a fast encounter may have occurred. Observations indicate that in some galaxies with companions the tidal haloes do begin in the deep interior (Kormendy 1982).

The empirical mass-radius relation of elliptical galaxies, $M \propto R^n$ where $1 < n < 2$, indicates that on an average the more massive elliptical galaxies are less dense. In a fast collision, the mass ratio is more important than the density ratio in determining the effects of mutual disruption, and hence the smaller galaxy suffers greater disruption in spite of its higher density (Narasimhan & Alladin 1983). On the other hand AA indicates that in bound orbits the density ratio plays a more important role and change in the structure of the bigger galaxy would be equal or greater. Since the relative velocities of galaxies are large in rich clusters and small in groups, it follows that bigger galaxies experience greater disruption in groups than in clusters.

There is a striking analogy between an analytical expression (Equation 35) obtained here and that obtained by Zahn (1977) in the study of energy transfer in binary stars due to tidal effects. In close binary stars each star experiences a force arising from the tidally distorted non-spherical part of the mass distribution of the companion. The work done by this force causes secular change in the energy of the orbital motion of the binary. Zahn derived the circularization time or the time required by the elliptic orbit to become circular on account of this energy transfer as

$$1/t_{\mathrm{circ}} = 63kq(1+q)R^8/4t_f a^8 \tag{40}$$

where k depends on the structure of the star, $q = M_1/M$ in our notation, t_f is the timescale of fractional dissipation and a is the semi-major axis of the orbit. From Equations (27) or (35) it can be seen that for binary stellar systems

$$1/t_{\mathrm{dh}} = (b_n/P)(M_1/M)^2(R_h/D)^8. \tag{41}$$

A comparison of Equations (40) and (41)shows that the rate of energy transfer depends on the eighth power of the dimension of the object of interest and the separation of the components in both cases. b_n depends weakly on the model of the system.

6. Concluding remarks

Just as IA provides simple analytical expressions for estimating the tidal effects in fast encounters, AA provides similar expressions for binary systems in bound orbits. It leads to the value of the Roche density which is in agreement with the earlier works and it shows that the disruption rate falls steeply as the density becomes higher than the Roche density. The long term effects lead to reasonable values for the merging time. Concepts of Roche density and dynamical friction are important in stellar dynamics. The present analysis gives a unified treatment in which both emerge from an analysis of energy

transfer. However, the simplifying assumptions made are quite drastic and a more rigorous treatment of the problem is certainly desirable. It would be also helpful if *n*-body simulations throw light on the utility and limitations of the analytical formulae derived here.

The tidal evolution of a binary stellar system is governed by the complementary processes of disruption and merging. In the case of equal component binaries, the merging process dominates while in the case of a satellite of density less than or not much greater than the Roche density, the disruption is more important. The relative importance of the two processes for any given binary can be estimated by using the analytical expressions derived here for the merging and disruption times.

Acknowledgements

We thank J. P. Ostriker, R. K. Kochhar, K. S. V. S. Narasimhan, G. Somsunder and R. K. Bhatia for helpful discussions and the referee for valuable comments S. M. A. benefited by visiting the Indian Institute of Astrophysics, Bangalore and thanks J. C. Bhattacharyya for hospitality. We also thank the University Grants Commission, New Delhi for awarding us fellowships during the tenure of this work.

References

Ahmed, F., Alladin, S. M. 1981, *J. Astrophys. Astr*., **2, 349**.
Alladin, S. M., Narasimhan, K. S. V. S. 1982, *Phys. Rep*., **92,** 339.
Alladin, S. M., Parthasarathy, M. 1978, *Mon. Not. R. astr. Soc*, **184,** 871 (Paper I).
Avner, E. S., King, I. R. 1967, *Astr. J.,* **72,** 650
Chandrasekhar, S.1942, *Principles of Stellar Dynamics,* Dover, New York, pp. 222, 252.
Goldstein, H.1950,*Classical Mechanics,* Addison-Wesley,Massachusetts, p. 78.
Innanen, K. A. 1979, *Astr. J*., **84,** 960.
King, I. R. 1962, *Astr. J.,* **67**, 471.
Kormendy, J. 1982, in *Morphology and Dynamics of Galaxies,* EdsL. Martinet &M.Mayor, Geneva Observatory, p. 113.
Kurth, R. 1957, *Introduction to the Mechanics of Stellar Systems,* Pergamon Press, NewYork, p. 88.
Larson, R. B. 1976, in *Galaxies,* Eds L. Martinet & M. Mayor, Geneva Observatory, p. 69**.**
Lin, D. N. C., Tremaine, S. 1983, *Astrophys. J*., **264,** 364.
Miller, R. H. 1984, ESO Preprint No. 343.
Narasimhan, K.S.V.S.,Alladin, S.M.1983, *Bull. astr. Soc. India,* **10,** 244.
Ostriker, J. P.,Caldwell, J. A. R.1979, in*IAU Symp.*84;*The Largescale Characteristics of the Galaxy,* Ed. W. B. Burton, D. Reidel, Dordrecht, p. 441.
Ramamarti, N.,Meinya Singh, T.,Alladin, S.M. 1984,in *IAU Symp.* 106:*The Milky Way Galaxy*, (submitted).
Richstone, D. O. 1975, *Astrophys. J.,* **200,** 535.
Schmidt, M. 1965, in *Galactic Structure,* EdsA.Blaauw& M.Schmidt, p.513.
Spitzer, L. 1958, *Astrophys.J.,* **127**, 17.
Spitzer, L.,Chevalier, R.A.1973, *Astrophys. J*., **183,** 565.
Toomre, A. 1977, in *The Evolution of Galaxies and Stellar Populations,* EdsB. M.Tinsley& R. B. Larson,YaleUniversity Observatory, p.401.
Tremaine, S.D.1981,*The Structure and Evolution of Normal Galaxies,* Eds S. M. Fall & D. Lynden-Bell, Cambridge University Press, p. 67.
Tremaine, S.D.,Ostriker, J. P., Spitzer, L.1975, *Astrophys. J*., **196,** 407.
Villumsen, J. V. 1982, *Mon. Not. R. astr. Soc,* **199,** 493.

von Hoerner, S. 1957, *Astrophys. J.*, **125,** 451.
White, S. D. M. 1978, *Mon. Not. R. astr. Soc*, **184,** 185.
White, S. D. M. 1979, *Mon. Not. R. astr. Soc,* **189,** 831.
White, S. D. M. 1983a, in *IAU Symp.* 100; *Internal Kinematics and Dynamics of Galaxies,* Ed. E. Athanassoula, D. Reidel, Dordrecht, p. 337.
White, S. D. M. 1983b, *Astrophys. J.*, **274**, 53.
Zahn, J. P. 1977, *Astr. Astrophys*., **57,** 383.

J. Astrophys. Astr. (1985) **6,** 21–34

Nonlinear Development of Convective Instability within Slender Flux Tubes. II. The Effect of Radiative Heat Transport

P. Venkatakrishnan *Indian Institute of Astrophysics, Bangalore 560 034*

Received 1984 March 5; accepted 1984 November 23

Abstract. Inclusion of radiative heat transport in the energy equation for a slender flux tube leads to oscillations of the tube. The amplitude of the oscillations depends on the radius of the tube when lateral heat exchange alone is considered. Longitudinal heat transport has a greater influence on the evolution of the instability than lateral heat exchange for the particular value of tube radius considered in the calculation. Heat transport is seen to reduce the efficiency of concentration of magnetic fields by convective collapse in the case of polytropic tubes.

Key words: Sun, magnetic field—Sun, convection—fluid dynamics, unsteady flow—heat transport

1. Introduction

The general behaviour of convectively unstable fluids in the presence of magnetic field and heat diffusion has been well studied in the past on the basis of linear theory. For a Boussinesq fluid Chandrasekhar (1961) showed that whenever the electrical resistivity η was greater than the heat diffusivity χ, convective instability sets in as a monotonically growing instability at a critical value of the Rayleigh number $R^{(e)}$. This value increases with magnetic field, thereby demonstrating the stabilizing influence of the field. In stellar interiors, the radiative heat diffusivity is generally much larger than the electrical resistivity of the fluid. In such a situation, Chandrasekhar (1961) proved that overstability could set in at a Rayleigh number $R^{(o)}$ which is less than $R^{(e)}$, the critical Rayleigh number for onset of overturning convection.

The effect of compressibility on the instability for an ideally conducting fluid was studied by Kato (1966). In the case of an inviscid Boussinesq fluid, Kato (1966) showed that any arbitrary adverse temperature gradient led to overstability, irrespective of the value of the magnetic field. When compressibility is included, a regime of damped oscillations exists whenever the magnetic field is greater than a critical value. Thus, for weak magnetic fields in non-resistive inviscid fluids, convective instability always sets in as an overstability. Katos analysis, being a local analysis, could not take boundary conditions into account. The classification and behaviour of the linear modes of a polytropic fluid with vertical magnetic field and imposed boundary conditions have been explored in detail by Antia & Chitre (1979). They found that convective-slow modes would be overstable for weak magnetic fields, while at moderate values of the magnetic field, overstable fast modes would dominate the spectrum. Moreover, the growth rate of both series showed a maximum with respect to the horizontal wave number, thereby indicating the suppression of instability on small length-scales. For

horizontally structured magnetic fields, Roberts (1976) has demonstrated the existence of overstable modes.

All the above results lead us to expect similar oscillatory convection for slender magnetic flux tubes as well. The linear stability of slender radiating flux tubes has not been explicitly studied although Webb & Roberts (1980a,b) have considered the spatial and temporal damping of optically thin disturbances in slender flux tubes. In this paper we first derive the energy equation for a slender optically thick flux tube (Section 2). We then investigate, albeit in a restricted sense, the linear stability of such a tube in Section 3. The initial and boundary conditions are spelt out in Section 4. We then describe the results of a few nonlinear calculations in Section 5 and discuss these results in Section 6.

2. The Basic Equations

The equations of continuity and motion for a slender magnetic flux tube are (Roberts & Webb 1978):

$$\frac{\partial}{\partial t}(\rho/B)+\frac{\partial}{\partial z}(\rho v/B)=0, \tag{1}$$

$$\frac{\partial}{\partial t}v+v\frac{\partial v}{\partial z}+\frac{1}{\rho}\frac{\partial p}{\partial z}+g=0, \tag{2}$$

$$B^2=8\pi(p_e-p). \tag{3}$$

The complete energy equation in the presence of nonadiabatic terms is given by

$$\left(\frac{\partial}{\partial t}+\mathbf{v}\cdot\nabla\right)p-\left(\frac{\gamma p}{\rho}\right)\left(\frac{\partial}{\partial t}+\mathbf{v}\cdot\nabla\right)\rho + (\gamma-1)\nabla\cdot\mathbf{F}=0, \tag{4}$$

where

$$\mathbf{F}=-K\nabla T \tag{5}$$

with

$$K=\rho C_v\chi \tag{6}$$

and

$$\chi=16\sigma T^3/3\kappa\rho, \tag{7}$$

where ρ, ρ, v, B, T are the pressure, density, velocity, magnetic field and temperature inside the tube, p_e is the pressure outside the tube, **F** is the radiative heat flux, K is the radiative heat conductivity, χ is the heat diffusivity, k is the Rosseland mean opacity and σ is the Stefan-Boltzmann constant. Equations (5) through (7) are valid for an optically thick tube in the 'diffusion' approximation.

For thin tubes the lateral exchange of heat is important as can be seen from the magnetostatic models of Spruit (1977). When such a lateral exchange of heat is considered, one can no longer neglect the radial dependence of the dynamical variables as was done previously for the adiabatic flow (Venkatakrishnan 1983; hereinafter referred to as Paper I). We shall now follow Roberts & Webb (1978) to further simplify Equation (4). If Λ is the scale length of variation of the tube radius along its axis, then we shall consider terms of zero order in (r/Λ) in Equation (4). The first two terms reduce to

$$\left(\frac{\partial}{\partial t}+v\frac{\partial}{\partial z}\right)p-\left(\frac{\gamma p}{\rho}\right)\left(\frac{\partial}{\partial t}+v\frac{\partial}{\partial z}\right)\rho+O(r/\Lambda), \tag{4a}$$

vide equation (Al0) of Roberts & Webb (1978).

The evaluation of the zeroth order of the third term in (4a) needs some consideration. For this, let us assume the following profile for the radial dependence of temperature, *viz*

$$T = T_0(z) + T_1(z)(r/\Lambda) + T_2(z)(r/\Lambda)^2 + \ldots \tag{8}$$

After substituting Equation (8) in Equations (3) and (5), and multiplying the resulting equation by r/Λ, we have upto first order in r/ Λ,

$$(\gamma-1)\nabla\cdot\mathbf{F} = -\left(\frac{\gamma-1}{\Lambda^2}\right)\left[\frac{KT_1}{(r/\Lambda)} + \left(\frac{\partial K}{\partial T} + \frac{\partial K}{\partial p}\frac{\partial p}{\partial T}\right)\left\{T_1^2 + \Lambda^2\left(\frac{\partial T_0}{\partial z}\right)^2\right\}\right.$$

$$\left. + K\left(4T_2 + \Lambda^2\frac{\partial^2 T_0}{\partial z^2}\right)\right] + O(r/\Lambda). \tag{9}$$

From Equations (4), (4a) and (9) we have

$$-\left(\frac{\gamma-1}{\Lambda^2}\right)\frac{KT_1}{r/\Lambda} + \left(\frac{\partial}{\partial t} + v\frac{\partial}{\partial z}\right)p - \left(\frac{\gamma p}{\rho}\right)\left(\frac{\partial}{\partial t} + v\frac{\partial}{\partial z}\right)\rho$$

$$-\left(\frac{\gamma-1}{\Lambda^2}\right)\left[\left(\frac{\partial K}{\partial T} + \frac{\partial K}{\partial p}\frac{\partial p}{\partial T}\right)\left\{T_1^2 + \Lambda^2\left(\frac{\partial T_0}{\partial z}\right)^2\right\}\right.$$

$$\left. + K\left(4T_2 + \Lambda^2\frac{\partial^2 T_0}{\partial z^2}\right)\right] + O(r/\Lambda) = 0. \tag{10}$$

Equating the coefficients of each power of r/Λ to zero, we have

$$(\gamma-1)KT_1/\Lambda^2 = 0, \tag{11}$$

and

$$\left(\frac{\partial}{\partial t} + v\frac{\partial}{\partial z}\right)p - \left(\frac{\gamma p}{\rho}\right)\left(\frac{\partial}{\partial t} + v\frac{\partial}{\partial z}\right)\rho - \left(\frac{\gamma-1}{\Lambda^2}\right)\left[K\left(4T_2 + \Lambda^2\frac{\partial^2 T_0}{\partial z^2}\right)\right.$$

$$\left. + \left(\frac{\partial K}{\partial T} + \frac{\partial K}{\partial p}\frac{\partial p}{\partial T}\right)\left\{T_1^2 + \Lambda^2\left(\frac{\partial T_0}{\partial z}\right)^2\right\}\right] = 0. \tag{12}$$

Finally, by setting $T = T_i$ at $r = 0$ we have

$$T_0 = T_i \tag{13}$$

and by setting $T = T_e$ at $r = r_0$, we have

$$T_2 = (T_e - T_i)(\Lambda/r_0)^2,$$

where r_0 is the radius of the tube and T_e and T_i are the temperatures outside and inside the tube respectively. Substituting Equations (13) and (14) in Equation (12) we have finally,

$$\left(\frac{\partial}{\partial t} + v\frac{\partial}{\partial z}\right)p - \left(\frac{\gamma p}{\rho}\right)\left(\frac{\partial}{\partial t} + v\frac{\partial}{\partial z}\right)\rho = (\gamma-1)\left[K\left\{4\left(\frac{T_e - T_i}{r_0^2}\right) + \frac{\partial^2 T_i}{\partial z^2}\right\}\right.$$

$$\left. + \left(\frac{\partial K}{\partial T} + \frac{\partial K}{\partial p}\frac{\partial p}{\partial T}\right)\left(\frac{\partial T_i}{\partial z}\right)^2\right]. \tag{15}$$

The first term on the right hand side of Equation (15) represents the lateral influx of heat from the surroundings. The second term represents the longitudinal diffusion of heat while the last term arises because of variations of the heat conductivity with temperature and pressure. In what follows we will present a restricted linear stability analysis of a slender flux tube in the presence of lateral heat exchange alone and with constant diffusivity χ. We shall then numerically study the effect of lateral heat exchange, with constant conductivity K, on the nonlinear evolution of convective instability. We will next include longitudinal heat transport with constant K and finally consider a case of variable heat conductivity as well.

3. Linear stability of slender radiating flux tubes

The linearized version of Equations (1), (2), (3) and (15) are

$$\frac{1}{B_0}\left(\frac{\partial}{\partial t}\delta\rho + \frac{\mathrm{d}\rho_0}{\mathrm{d}z}\delta v\right) - \frac{\rho_0}{B_0^2}\left(\frac{\partial}{\partial t}\delta B + \delta v_1 \frac{\partial B_0}{\partial z}\right) = 0, \tag{16}$$

$$\rho_0 \frac{\partial}{\partial t}\delta v + \frac{\partial}{\partial z}\delta p + \delta\rho g = 0 \tag{17}$$

and

$$\left(\frac{\partial}{\partial t}\delta p - \frac{\gamma p_0}{\rho_0}\frac{\partial}{\partial t}\delta\rho\right) + \delta v\left(\frac{\mathrm{d}p_0}{\mathrm{d}z} - \frac{\gamma p_0}{\rho_0}\frac{\mathrm{d}\rho_0}{\mathrm{d}z}\right)$$

$$= (\gamma - 1)\left\{K\left(\frac{\partial^2}{\partial z^2}\delta T - 4\frac{\delta T}{r_0^2}\right) + \left(\frac{\mathrm{d}T_0}{\mathrm{d}z}\right)\left(\frac{\partial K}{\partial p}\frac{\partial}{\partial z}\delta p\right.\right.$$

$$\left.\left. + \frac{\partial K}{\partial T}\frac{\partial}{\partial z}\delta T\right) + \frac{\partial K}{\partial z}\frac{\partial}{\partial z}\delta T\right\}, \tag{18}$$

where

$$\delta T = T_0(\delta p/p_0 - \delta\rho/\rho_0), \quad \delta B = -4\pi\delta p/B_0$$

and δ represents a perturbation of a variable whose zero order is represented by asubscript '0'. In the presence of lateral heat transport alone, Equation (18) becomes

$$\left(\frac{\partial}{\partial t}\delta p - \frac{\gamma p_0}{\rho_0}\frac{\partial}{\partial t}\delta\rho\right) + \delta v\left(\frac{\mathrm{d}}{\mathrm{d}z}p_0 - \frac{\gamma p_0}{\rho_0}\frac{\mathrm{d}\rho_0}{\mathrm{d}z}\right)$$

$$= -4(\gamma - 1)K\delta T/r_0^2. \tag{19}$$

We further write $K = \rho_0 C_v \chi$ where χ is the radiative diffusivity and assume that χ is constant. Then the final energy equation is

$$\left(\frac{\partial}{\partial t} + \frac{1}{\tau}\right)\delta p - \left(\frac{\gamma p_0}{\rho_0}\right)\left(\frac{\partial}{\partial t} + \frac{1}{\gamma\tau}\right)\delta\rho + \delta v\left(\frac{\mathrm{d}p_0}{\mathrm{d}z} - \frac{\gamma p_0}{\rho_0}\frac{\mathrm{d}}{\mathrm{d}z}\rho_0\right) = 0, \tag{20}$$

where

$$\tau = r_0^2/4\chi.$$

We impose the following boundary conditions,

$$\delta v = 0 \qquad \text{at } z = 0 \quad \text{and} \quad z = d. \tag{21}$$

Furthermore we choose perturbations of the form

$$q(z, t) = \hat{q}(z) \exp(\sigma t).$$

Substituting this form of the perturbation in Equations (16), (17) and (20), and eliminating $\delta\rho$, $\delta\rho$ and δB, we obtain

$$\frac{d^2}{dz^2}(\rho_0 \delta v) + a_1 \frac{d}{dz}(\rho_0 \delta v) + a_0(\rho_0 \delta v) = 0, \tag{22}$$

where

$$a_1 = \frac{1}{\Lambda}\left(\frac{\Gamma - 1}{\Gamma} + \frac{1}{2} - \frac{\delta_0 \sigma}{\sigma + 1/\gamma\tau}\right)$$

$$a_0 = \frac{1}{\Lambda^2}\left[\left(\frac{1}{2} - \frac{\delta_0\sigma}{\sigma + 1/\gamma\tau}\right)\left(\frac{\sigma + 1/\tau}{\gamma\sigma + 1/\tau}\right) - \frac{\sigma}{\gamma g}\left(\frac{\gamma\beta}{2} + \frac{\sigma + 1/\tau}{\sigma + 1/\gamma\tau}\right)\right.$$

$$\left. \times \left(\sigma\Lambda - \frac{g\delta_0}{\sigma + 1/\gamma\tau}\right)\right]$$

where

$$\delta_0 = \left(\frac{\Gamma - \gamma}{\Gamma\gamma}\right) \quad \text{and} \quad \Lambda = \mathscr{R}T_0/g.$$

Let us assume isothermal stratification, in which case the coefficients in Equation (22) would become independent of z, admitting solutions of the form $A_1 \exp(k_1 z) + A_2 \exp(k_2 z)$. Substituting this form into the boundary conditions yields the dispersion relation

$$b_4\sigma^4 + b_3\sigma^3 + b_2\sigma^2 + b_1\sigma + b_0 = 0, \tag{23}$$

where

$$b_4 = \beta_0 + 2(1 + \delta_0); \quad b_3 = 2\varepsilon(1 + \delta_0)(\beta_0 + \delta_0 + 2);$$

$$b_2 = -\left[1 + \delta_0(1 + \beta_0) - \left\{\frac{2\pi^2 n^2}{d^2} + \frac{7}{4} + \varepsilon^2(1 + \delta_0)^2(2 + \beta_0)\right\}\right];$$

$$b_1 = -\varepsilon(1 + \delta_0)\left[\delta_0(1 + \beta_0) + \frac{7}{4} - \frac{2\pi^2 n^2}{d^2}\right];$$

$$b_0 = -\varepsilon^2(1 + \delta_0)^2\left(\frac{1}{16} + \frac{2\pi^2 n^2}{d^2}\right);$$

where η is the order of the harmonic, $\varepsilon = (\Lambda / g\tau^2)^{1/2}$, β_0 is the ratio of gas to magnetic pressure, $\delta_0 = (\Gamma - \gamma)/\Gamma\gamma$ is the superadiabaticity and d is the length of the tube. We see that Equation (23) is of fourth degree in σ. It must be mentioned that Webb & Roberts (1980a) obtained a third degree polynomial for an unstratified tube and fourth degree polynomial for a stratified tube (Webb & Roberts 1980b). They have not commented on

Table 1. Frequencies and growth rates of slender radiating flux tube.
$\beta = 6.0 \quad \delta = 0.3$

d	ε	Re(σ)	Im(σ)
1	0.05	0.0017	1.4454
	0.10	0.0018	1.4545
	0.15	−0.0009	1.4685
	0.20	−0.0069	1.4862
	0.25	−0.0162	1.5063
	0.30	−0.0287	1.5281
	0.35	−0.0438	1.5508
	0.40	−0.0614	1.5741
3.65	0.05	−0.0592	0.1120
	0.10	−0.0945	0.1970
	0.15	−0.1268	0.2509
	0.20	−0.1584	0.2926
	0.25	−0.1899	0.3264
	0.30	−0.2214	0.3543
	0.35	−0.2527	0.3777
	0.40	−0.2841	0.3973

the extra mode. An inspection of Equations (16) through (20) shows that the fourth mode arises out of stratification and nonadiabaticity. Following the nomenclature of Defouw (1970) we shall call this mode as the thermal-convective mode. In the limit $\varepsilon \ll 1$ the roots of Equation (23) separate clearly into thermal and dynamical modes. It can also be shown that in such an eventuality overstability is possible only if the equilibrium state is adiabatically stable and that for adiabatically unstable states the thermal effects only modify the growth rates.

For finite values of ε, such a demarcation of the modes is not obvious. Table 1 shows the complex roots determined numerically in the case of finite ε for two values of d corresponding to an adiabatically stable and unstable state respectively. Overstability is seen only for the adiabatically stable state. The growth rate increases with increasing ε and then decreases for large value of ε. The frequencies of the overstability are not sensitive to the value of ε. However, the frequencies in the nonadiabatic case must decrease as the equilibrium approaches a neutrally stable state in the adiabatic limit and thus the period of oscillation must be dependent on the magnetic field of the tube.

However, this limited study does not include the case of unequal zero-order temperatures inside and outside the tube. It is quite possible that unequal temperatures might lead to overstability even when the equilibrium is adiabatically unstable, by the excitation of new modes which are suppressed in the case of equal temperatures.

4. Initial and boundary conditions for the nonlinear Calculations

Equations (1), (2) and (15) form a system of hyperbolic partial differential equations provided we treat the derivatives of temperature as source terms. Thus the problem is

an initial value problem requiring specification of the initial conditions. We chose the initial conditions, in the case of constant conductivity K, as a polytropic stratification with

$$T_e = T_e(z=0) - \left(\frac{\Gamma-1}{\Gamma}\right) z,$$

$$T = T_e,$$

$$p \propto T^{\Gamma/(\Gamma-1)},$$

and

$$B = (8\pi p/\beta_0)^{1/2}.$$

Practical computational considerations require the imposing of boundary conditions at finite values of z. We chose the following boundary conditions:

$$p = p(t=0) \quad \text{at} \quad z = 0$$

and

$$p = p(t-\Delta t) - \frac{\Delta t}{\Delta z} v(t-\Delta t,\, z=d)\{p(t-\Delta t,\, z=d) - p(t-\Delta t,\, z=d-\Delta z)\} \quad \text{at} \quad z = d.$$

The lower (z = 0) boundary condition implies that the radius of the tube does not change in time while the upper boundary condition implies that there is no lateral leak of matter at the top. This has been explained in Paper I. Sometimes more boundary conditions become necessary whenever some characteristic emanating from the boundary fails to communicate with the interior. The additional boundary conditions used in such cases were

$$\rho(t, 0) = \rho(t-\Delta t, 0)$$

and

$$\rho(t, d) = 2\rho(t, d-\Delta z) - \rho(t, d-2\Delta z).$$

It must be remarked here that the density boundary condition at z = d is different from that used in Paper I where it was

$$\rho(t, d) = \rho(t-\Delta t, d).$$

The introduction of the new density boundary condition saved the calculations from the numerical breakdown of zero pressure encountered in Paper I.

The calculations were performed in terms of dimensionless units which are described in Paper I and which essentially use the base pressure as the unit for gas and magnetic pressure, the base density and temperature as the units for the corresponding variables, the sound speed at the base as velocity unit, the pressure scale-height at the base as unit of length and the freefall time over this length as the unit of time.

5. Results

The convective instability will be a maximum in a region few hundred kilometres below the photosphere where the superadiabaticity is large. In this region the radiative diffusivity ranges from 2.33×10^{10} cm ^{2}s $^{-1}$ at a temperature of 1.003×10^4 K to 3.504×10^{12} cm^2 s^{-1} at the photosphere (Spruit 1977). We have, however, first

considered a constant radiative conductivity representing a 'mean' value, in order to understand the physical effects produced by heat diffusion. We shall also briefly describe results of a single calculation involving a variable diffusivity at the end of this section.

5.1 *Effect of Lateral Heat Exchange*

The results were all obtained in dimensionless units with the reference units that were defined in Paper I. In those dimensionless units, the radiative conductivity was 0.001 which is representative of a layer $\simeq$ 200 km below the photosphere. Since the term representing lateral heat exchange in Equation (15) depends inversely on the area of cross-section of the tube, we shall first look at the effect of tube radius on the development of the instability.

Fig. 1 shows the time variation of longitudinal velocity at z = 0.48 for β_0 = 6.0, for 4 values of r_0, the tube radius. We see an oscillatory behaviour for the velocity. The oscillations have nearly the same period of $\simeq$ 12 units for all values of r_0. The amplitude seems to be large for r_0 = 0.5. For smaller values of r_0 we find that after some time the gas pressure inside the tube exceeds the external gas pressure making the magnetic field vanish in the slender flux tube approximation. Thus, the calculations could not be extended for these cases. Fig. 2 shows the behaviour of β, the ratio of gas pressure to magnetic pressure inside the tube, at z= 0.48 as a function of time for different values of r_0. The behaviour of β is essentially similar to that of velocity except

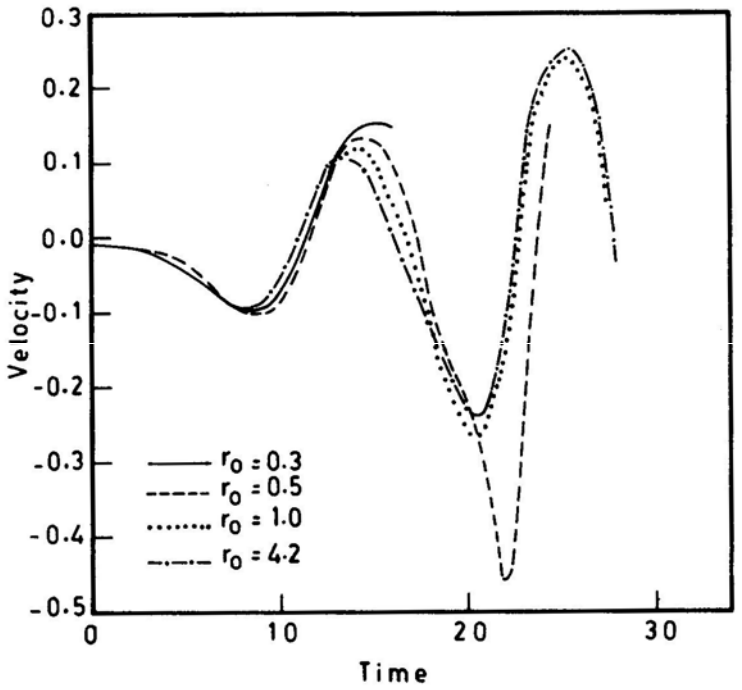

Figure 1. Time dependence of velocity at z = 0.48 in an 'open' tube, for β_0 = 6.0 and different values of radius r_0, laterally exchanging heat with its surroundings.

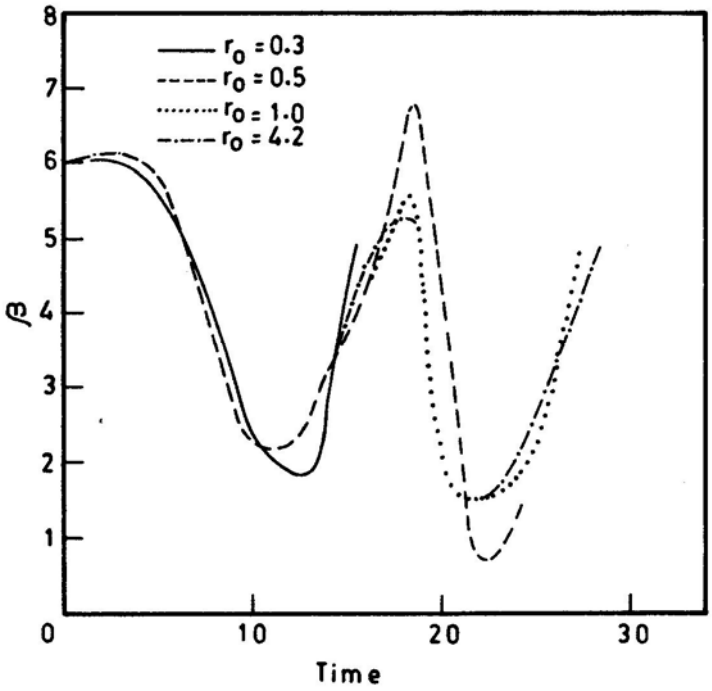

Figure 2. Variation of β with time in the tube considered for Fig. 1.

for the phase. We notice transient intensification of the field to values of β as low as 1.0.

The stabilizing influence of the initial magnetic field can be seen in Fig. 3. Here the velocity at z = 0.48 in a tube of radius r_0 = 0.5 is plotted as a function of time for different values of β_0. There is no discernible change in the period of oscillations but the amplitudes are considerably affected as can be seen from the low values for β_0 = 4.0 compared to those for larger β_0.

5.2 *Effect of Longitudinal Heat Transport*

Let us now consider the effect of longitudinal heat transfer with constant heat conductivity on convective instability. We, therefore, retain only the first two terms on the right-hand side of Equation (15). In a rigorous sense, the character of the system of differential equations changes here from hyperbolic to parabolic due to the appearance of the second derivative of temperature. We shall, however, continue to regard the system as hyperbolic and treat the derivatives of temperature as 'source' terms. These source terms were calculated on the previous time-line using a standard IBM subroutine for numerical differentiation. Such a procedure does not cause serious problems as long as the thermal conductivity is small. Figs 4 and 5 show the temporal behaviour of velocity and plasma-β in a tube with β_0 = 6.0 and 4.0 respectively, with r_0 = 0.5. One notices three facts, *viz.* the presence of overstability, the smaller period of oscillation and the greatly diminished amplitude of oscillation as compared to the case with lateral heat exchange alone. Compared to this, the differences between the case of lateral heat exchange alone and the adiabatic case are rather small. This indicates that

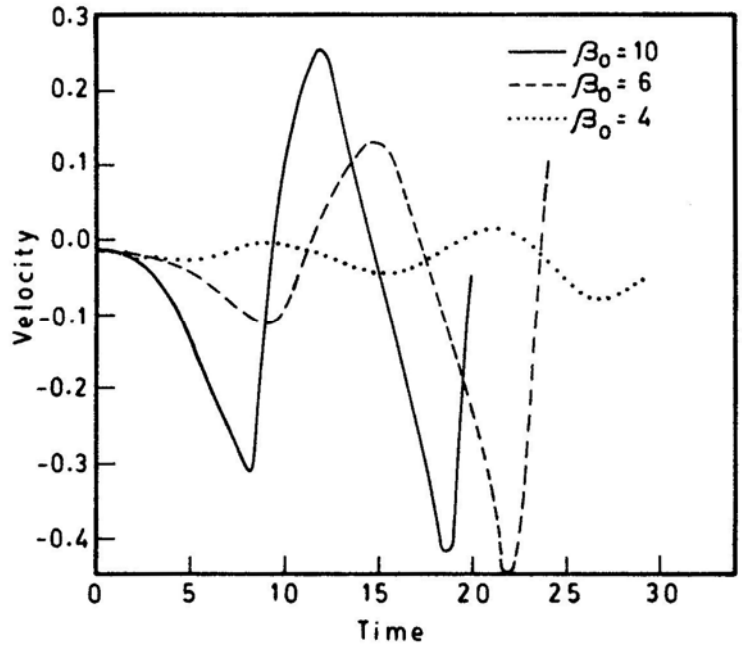

Figure 3 Dependence on *β0* of the time development of velocity in a tube of radius $r_0 = 0.5$.

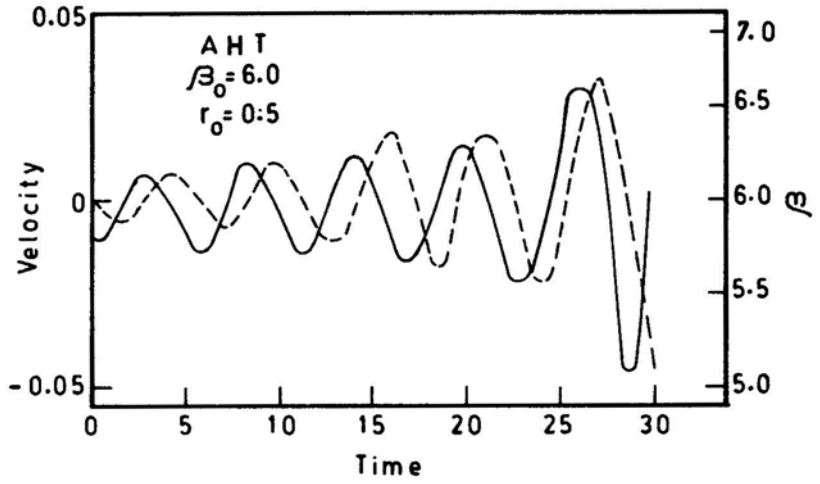

Figure4. Time dependence of velocity (dashed curve)and β (solid curve)at $z = 0.48$ in an open tube with heat transport and with $\beta_0 = 6.0$.

longitudinal heat transport has a greater effect on the convective instability of a flux tube with $r_0 = 0.5$. However, one cannot predict the relative importance of longitudinal heat transport on thinner tubes. In the context of solar photospheric magnetic fields, it is also interesting to see that intensification of such tubes by convective instability with heat transport would most probably be transient and would be accompanied by only

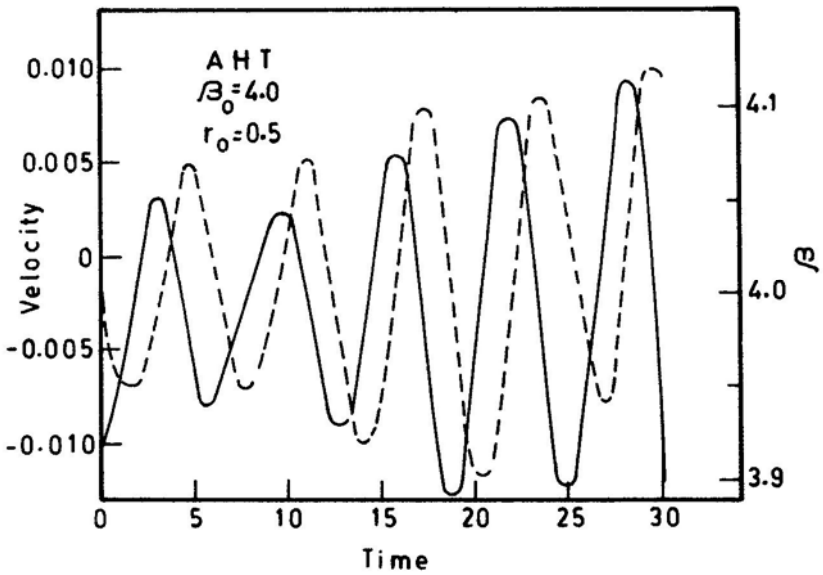

Figure 5. Time dependence of velocity (dashed curve) and β (solid curve) at z = 0.48 in an open tube with heat transport and with $\beta_0 = 4.0$.

small and oscillatory flows. Here the calculations were not continued beyond $t \simeq 30$ and, therefore, we do not know the saturation amplitudes of the overstability. However, $t \simeq 30$ corresponds to $\simeq 1000$ s for tubes with base temperature $T_b = 10^4$ K. Therefore, other processes such as granulation might interfere with the development of the overstability within this time.

5.3 *Effect of α Variable Heat Conductivity*

Below the solar photosphere the heat conductivity is not constant but varies by a few orders of magnitude as mentioned earlier. In order to study such a situation we need to first calculate a static equilibrium model for the environment of the flux tube with such a variable conductivity. For this we first calculated the opacity by obtaining a least-squares fit for the relation

$$\kappa = \kappa_0 (p/p_0)^{\mu} (T/T_0)^{\nu}, \tag{24}$$

using Spruit's (1977) values for k , ρ and T. Here, $p_0 = 3.126 \times 10^5$ dyn cm $^{-2}$ and $T_0 = 1.003 \times 10^4$ K corresponding to a depth of 1.779×10^2 km in the model. We obtained

$$\nu = 12 \quad \text{and} \quad \mu = -0.65.$$

From Equations (6), (7) and (24) one can write K as a function of p and T. Further, we simultaneously solve the static energy equation

$$K \frac{dT}{dz} = K_0 \left(\frac{dT}{dz} \right)_0 \tag{25}$$

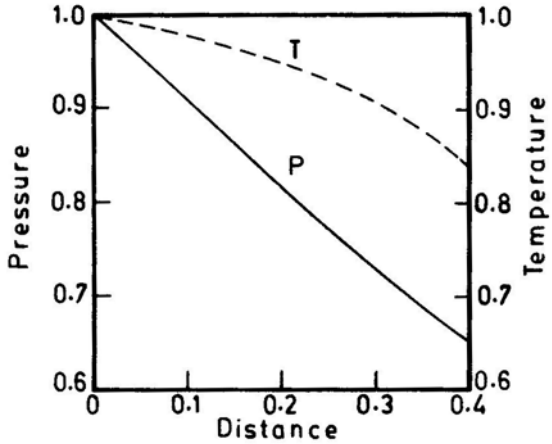

Figure 6 Initial hydrostatic state for a tube's environment (p_o, T_o) where heat transport is solely by radiation with opacity varying as $k = k_o(T/T_o)^{12}(p/p_o)^{-0\,65}$.

and the equation of hydrostatic pressure balance,

$$\frac{dp}{dz} = -\frac{pg}{\mathscr{R}T}, \tag{26}$$

using an Adam's predictorcor-rector algorithm to obtain the equilibrium state which is given in Fig. 6. One should notice that the thickness of the layer between temperatures 10^4 K and 0.6×10^4 K in Fig. 6 is smaller than the corresponding thickness in Spruit's model because we have entirely ignored the convective transport of heat.

We can now calculate the initial state of the tube from the equilibrium state of its environment using the condition of horizontal pressure balance and by assuming $T_e = T_i$ (see Roberts & Webb 1979). In this particular case we chose $\beta_o = 6.0$.This initial state was perturbed with a small initial velocity perturbation and the evolution of the flow was studied using the complete energy Equation (15). The development of the flow at two spatial points is shown in Fig. 7. There is once again oscillatory behaviour with a larger frequency and smaller amplitude as compared to the cases of constant conductivity. This calculation does not have direct relevance to the solar convection zone because of the neglect of convective transport in the environment of the tube. However, the general trend of oscillatory behaviour is seen even for this case. Another interesting feature of this calculation is the systematic flattening of the spatial profile of temperature gradient with time as seen from Fig. 8. However, one does not know from a single calculation whether the general tendency of heat transport is to smoothen out the variations in the temperature gradient.

6. Discussion

All these results, though not exhaustive, indicate that the general behaviour of convectively unstable flux tubes, in the presence of heat transport, is oscillatory. The change of period of oscillation on introducing longitudinal heat transport could be due to the excitation of a new mode or a new harmonic. The further decrease in period for

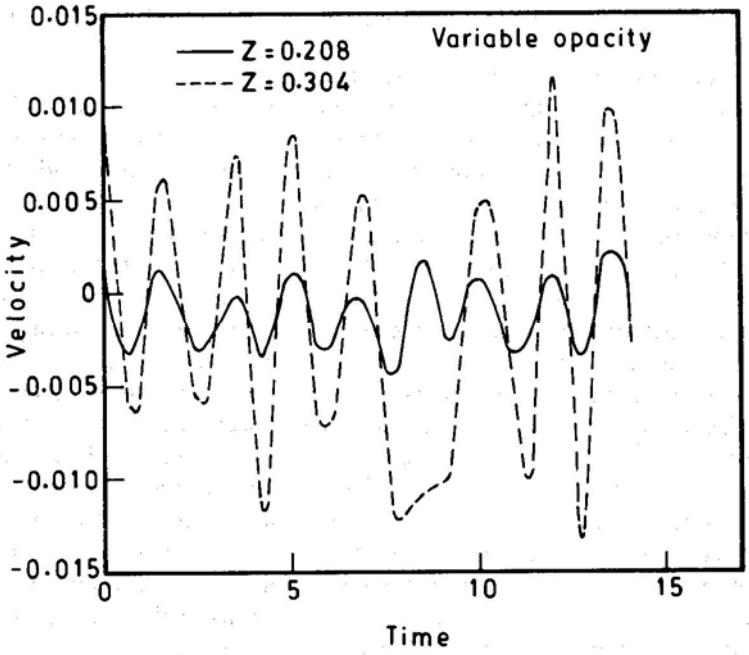

Figure 7. Variation of velocity in a tube embedded in an atmosphere given by Fig. 6 and with βo =6.0.

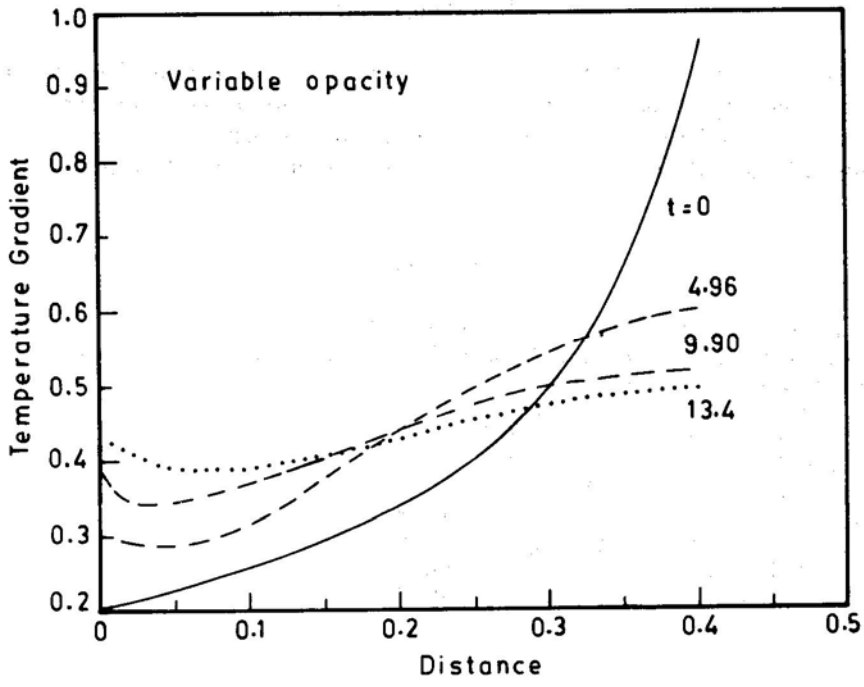

Figure 8. Evolution of the spatial profile of temperature gradient within the tube considered for Fig. 7.

the case of variable conductivity could perhaps be due to the shorter length of the tube considered.

Linear theory predicts both overstable fast modes and monotonically growing convective modes for sufficiently weak and laterally unstructured magnetic fields. The main result of the present work is to demonstrate that when nonlinear effects are considered, the interaction of convection and overstable modes leads to a net oscillatory behaviour within slender flux tubes.

Furthermore, the intensification of the field is also transient and much reduced as for example in the case of $\beta_0 = 4.0$ with longitudinal heat transport. On the other hand, it was seen that in the adiabatic case (Paper I) an 'open' flux tube with $\beta_0 = 4.0$ and a smaller initial superadiabatic gradient attained an intense steady state with $\beta_{\text{final}} \simeq 1.0$ and downflow velocity $\simeq 0.8$ at $z = 0.5$. Thus, the heat transport has a stabilizing influence apart from imparting an oscillatory behaviour. Furthermore, tubes with $\beta_0 = 6.0$,which corresponds to the 'equipartition'field concentrated by convective eddies, are also not seen to collapse to very intense states in the present calculation.

Thus the mechanism of concentration of flux tubes by convective collapse seems to become somewhat inefficient when heat transport is also included. Obviously it will be necessary to consider a realistic stratification for the initial state of the tube before one can confirm this fact and before one starts a search for alternative mechanisms of tube concentration. The use of realistic initial states would also help in the prediction of exact periods and amplitudes of the radiatively driven oscillations,* which will have important observational implications.

Acknowledgement

The author thanks Dr. M. H. Gokhale for numerous discussions. The use of an interpolation programme developed by Mr.A. V. Raveendran and of a programme to solve ordinary differential equations using Adam's predictor-corrector algorithm developed by Mr. P. M. S. Namboodiri is also gratefully acknowledged.

References

Antia, H. M., Chitre, S. M. 1979 *Solar Phys*., **63**, 67.
Chandrasekhar, S.1961,*Hydrodynamic and Hydromagnetic Stability,* Clarendon Press, Oxford
Defouw, R. J. 1970, *Solar Phys*., **14**, 42.
Hasan, S. S. 1984, *Astr*, *Astrophys*., (in press).
Kato, S. 1966, *Publ. astr. Soc. Japan,* **18,** 201.
Roberts, B. 1976, *Astrophys. J*., **204,** 268.
Roberts, B., Webb, A. R. 1978, *Solar Phy*., **56,** 5.
Spruit, H. C. 1977, *PhD Thesis,* University of Utrecht.
Venkatakrishnan, P. 1983, *J. Astrophys. Astr*., **4,** 135 (Paper I).
Webb, A. R., Roberts, B. 1980a, *Solar Phys*., **68,** 71.
Webb, A. R., Roberts, B. 1980b, *Solar Phys*., **68,** 87.

* Recent results for solar flux tubes laterally exchanging heat with their surroundings (Hasan 1984) do show overstability similar to the polytropic tubes, but vertical transport of heat is yet to be considered there.

J. Astrophys. Astr. (1985) **6,** 35–47

Interstellar Scintillation Measurements of Pulsars at 326.5 MHz

V. Balasubramanian *Radio Astronomy Centre, Tata Institute of Fundamental Research, P.O.Box* 8, *Ootacamund 643001*
S. Krishnamohan *Radio Astronomy Centre, Tata Institute of Fundamental Research, P.O. Box 1234, Bangalore 560012*

Received 1984 May 30; accepted 1984 November 27

Abstract. We have measured the decorrelation frequency (f_v) and decorrelation time (t_v) for 15 pulsars. We show by combining our data with those of others that $f_v \propto \mathrm{DM}^{-1\cdot79\pm0\cdot14}$ and $t_v \propto \mathrm{DM}^{-0\cdot80\pm0\cdot15}$ up to a dispersion measure (DM) of about 60 cm^{-3} pc. The combined data set does not form a complete sample, but the relations obtained from our measurements on 14 pulsars, which form almost a complete sample up to 41 cm^{-3} pc, are consistent with the above relations, suggesting that these relations are not seriously affected by selection effects. The relations are broadly in agreement with those expected from a homogeneous interstellar medium and are in disagreement with earlier conclusions by others that these relations steepen even for low-DM pulsars. The agreement suggests that the local interstellar medium is homogeneous at least up to a distance of about 2 kpc.

Key words: pulsars, interstellar scintillations–interstellar medium

1. Introduction

Pulsars have been used as probes of the interstellar medium (ISM) to study the distribution and the turbulence of thermal electrons (see, *e.g.* Armstrong, Cordes & Rickett 1981; Vivekanand & Narayan 1982). The electrons cause different radio frequencies to travel at different speeds and the fluctuations in the electron density scatter the radio waves. At metre wavelengths the scattering is strong, *i.e.*, the modulation index of the intensity fluctuations due to scattering is close to unity and the decorrelation frequency of these fluctuations is much smaller than the frequency of observation. The relative motion between the observer, the ISM, and the pulsar causes the observed intensities to be decorrelated over a finite length of time. These effects, called interstellar scintillations (ISS) have been so far detected only in the case of pulsars. As the scattered waves take more time to reach the observer, pulses emitted by pulsars appear to be broadened. Scattering also leads to angular broadening of radio sources. This effect leads to paucity of small-angular-diameter sources at low galactic latitudes when observed at metre wavelengths. The angular broadening has been studied by several workers using IPS and VLBI techniques (Mutel *et al.* 1974; Duffett–Smith & Readhead 1976; A. Pramesh Rao & S. Ananthakrishnan 1984). ISS parameters measured by using pulsars help in interpreting such

angular size measurements. ISS measurements are also important in judging the significance of the absence of ISS of extragalactic radio sources showing low-frequency variability (Cordes 1982; Dennison 1982). Lyne & Smith (1982) have shown that the velocities of pulsars derived from ISS measurements are consistent within a factor ~ 3 with their proper motions obtained by using radio interferometry. Velocity is an important parameter of pulsars as values of velocities are needed in deriving ages and hence birthrates of pulsars. Apart from the above, ISS measurements are evidently needed for modelling the ISM.

Measuring the decorrelation time and frequency is a difficult task due to the presence of broadband intensity variations and due to the long observing time needed on each pulsar (see, *e.g.* Roberts & Abies 1982). The origin of broadband intensity variations, though not yet established, is unlikely to be the conventional ISS. Sutton (1971) and Krishnamohan & Balasubramanian (1984) presented methods to take into account the broadband variations in the measurement of decorrelation frequency and decorrelation time respectively. We used these methods in arriving at the results presented in this paper.

The dependence of decorrelation frequency (or a related quantity—the pulse scattering broadening) and decorrelations time on the dispersion measure (DM) has been used to study the interstellar medium. The two competing models for the power spectrum of the electron density irregularities, the Gaussian and the power-law spectrum, predict slightly different dependences (see Rickett 1977 for a review). Among the power-law spectra, one with an index of 11/3—called the Kolmogorov spectrum—received much attention as it is supposed to naturally arise whenever disturbances that are smaller in scale size are fed by larger ones. Several authors, beginning with Sutton (1971), had inferred that the observed dependences on DM are much steeper than those expected from the theory. Inhomogeneity of the interstellar medium is one of the often used explanations for the observed discrepency. The analysis presented in this paper shows that there is no disagreement atleast upto a DM of 60 cm^{-3} pc. This implies that the local interstellar medium is homogeneous at least up to a distance of about 2 kpc.

2. Observations

The observations were done with the Ooty Radio Telescope mostly during 1976 to 1978. The telescope operates at 326.5 MHz. The observations were done with a 12-channel system with filters whose bandwidth can be set to either 300 kHz or 50 kHz. The separation between the centre frequencies of the adjacent channels was also either 300 kHz or 50 kHz, with the exception that the frequency separation between the last three channels for the 50 kHz filters was 500 kHz. The 50 kHz filters were used mainly for observing pulsars with dispersion measure(DM) larger than about 35 cm^{-3} pc. The RC time constant was 3 ms and each channel was sampled every 2 ms. From the data acquired using a general purpose programme, two data arrays per channel are formed. The first array contains averaged ONPULSE values for a given channel. The averaging is done, after subtracting base levels, over 2 to 32 consecutive pulses to reduce the fluctuations due to pulse-to-pulse intensity variations. The base levels are determined by averaging samples over a duration comparable to ONPULSE duration midway between adjacent pulses. The second array contains the averaged OFFPULSE values which are formed in a similar manner from the samples on either side of the pulse.

2.1 *The Sample*

At the time of observation, 157 pulsars were known. We selected, for ISS studies, the pulsars that satisfied the following criteria: (i) the declination (δ) of the pulsar is within the range of the telescope, *i.e.* $-32° \leqslant \delta \leqslant 32°$,and(ii) the listed average flux density of the pulsar gives at least a signal-to-noise ratio of 5 when 1000 pulses are averaged using the 12-channel system. Out of the 40 pulsars that satisfied the criteria, 6 could not be observed as they were too weak to observe at that time. In addition, PSR 0950 + 08 was also dropped out from the observations as the available total bandwidth of ~ 3.6 MHz is not sufficient to measure its decorrelation bandwidth. Rest of the 33 pulsars were observed for durations ranging from an hour to 18 hours.

16 out of the 33 pulsars have DM less than or equal to 41 cm $^{-3}$ pc and the rest more than 41 cm^{-3} pc. Even the 50 kHz filters proved to be too wide to observe the ISS of pulsars with DM greater than 41cm^{-3}pc except for PSR 1749 – 28.Two of the pulsars with DM less than 41 cm^{-3} pc did not show measurable ISS effects when observed with the 300 kHz filters (PSR 1822 – 09) and 50 kHz filters (PSR 1857 – 26). Thus we could estimate the ISS parameters for only 15 out of the 33 pulsars observed. In the later analysis of the measurements on this sample, we exclude PSR 1749 – 28 for the reason given at the end of Section 5.1. Thus out of the flux-and dispersion-measure-limited sample of 16 pulsars, we have good measurements for 14 pulsars. As the dispersion measures of the other two pulsars are well separated, the 14 pulsars form almost a complete sample of pulsars up to a DM of 41 c m $^{-3}$ pc for the purpose of the later analysis.

3. Determination of decorrelation frequencies

The cross-correlation function (CCF), γ'_{1j}, between the intensities in the first and the jth channel is given by

$$\gamma'_{1j} = \frac{\langle I_1(t) I_j(t) \rangle}{\sigma_1 \sigma_j}$$

where I_1 and I_j are the mean subtracted ONPULSE intensities and σ_1^2 and $\sigma_j^2$are the variances of I_1 and I_j respectively. The γ',computed as above, carries errors from the following sources: (a) receiver noise, (b) broadband intensity variations, and (c) finite bandwidth and overlapping of filter passbands.

The noise-corrected CCF, γ_{1j} is given by

$$\gamma_{1j} = \left[\gamma'_{1j} - \beta_{1j} \frac{\sigma_{1n}\sigma_{jn}}{\sigma_1 \sigma_j} \right] \frac{\sigma_1 \sigma_j}{\{\sigma_1^2 - \sigma_{1n}^2\}^{1/2} \{\sigma_j^2 - \sigma_{jn}^2\}^{1/2}} \tag{1}$$

where β_{1j} is calculated from OFFPULSE values in a way similar to γ_{1j}, and σ_{jn}^2 are the variances computed from OFFPULSE values. Not all β_{1j} , $j \neq 1$ are equal to zero as filter passbands overlap. Since for a given filter bank β_{1j} do not depend on the pulsar, we used average values obtained from all the observations done with the filter bank. For the 300 kHz filter bank, the values of β_{1j} so obtained are 0.35,0.12 and 0.07 for j = 2,3 and 4, and 0 for $j \geqslant 5$. For the 50 kHz filter bank, $\beta_{12} = 0.15$ and $\beta_{1j} = 0$ for $j \geqslant 3$. The 50 kHz filters are designed better and hence have less overlap.

It should be noted that Equation (1) takes into account the instrumental correlation introduced through the noise due to the overlap of filter passbands, in addition to correcting the signal variances. As pointed out by Roberts & Ables (1982) and Armstrong & Rickett (1981) the overlap of filter passbands introduces instrumental correlation through the signal also. We take into account this aspect of the instrumental correlation in estimating the decorrelation frequency as discussed in Section 3.1.

The γ_{1j}, in general, do not settle down to zero even for large values of j as would be expected if ISS alone were present. Γ_{1j}, the CCF corrected for the broadband fluctuations giving rise to the non-zero base level (p) in γ_{1j}, are obtained by renormalizing g_{1j} as follows (Sutton 1971):

$$\Gamma_{1j} = (\gamma_{1j} - p)/(1 - p)$$

As discussed in Section 3.1, applying the correction is not easy since getting the value of p is difficult with a limited number of channels.

3.1 *Model Fitting*

We have estimated decorrelation frequencies from Γ_{1j} by a model-fitting procedure. The model Q_{1j} are obtained numerically from the normalized coherence function Γ_D of Lee & Jokipii (1975) for monochromatic waves. As discussed by Lee (1976), the finite bandwidth effects can be incorporated by calculating Q_{1j} as,

$$Q_{1j} = \frac{\int_{\nu} \int_{\nu'} G_1(\nu) G_j(\nu') \Gamma_D^2 \left(\frac{\nu - \nu'}{f_\nu} \right) d\nu \, d\nu'}{\sigma'_1 \sigma'_j} \tag{2}$$

where the band width-affected rms values σ'_j of the intensity fluctuations due to ISS are given by

$$\sigma'_j = \int_{\nu} \int_{\nu'} G_j(\nu) G_j(\nu') \Gamma_D^2 \left(\frac{\nu - \nu'}{f_\nu} \right) d\nu \, d\nu',$$

f_ν is the decorrelation frequency defined as the frequency separation at which the correlation coefficient falls to 0.5 if the observations were done with zero bandwidth, and $G_j(\nu)$ is the intensity response of the filter number j.

In arriving at Equation (2), the effect of pure refraction has been neglected. Lee (1976) shows that refraction is negligible for Gaussian density spectrum and gives justification for neglecting it even for a Kolmogorov spectrum of density fluctuations.

The models are calculated for different f_ν for both the Gaussian and Kolmogorov spectra. A few of the models for the 300 kHz filters and Kolmogorov spectrum are shown in Fig. 1 to illustrate the effect of finite bandwidth on the measurement of f_ν.

It can be seen from the figure that the expected correlation coefficient remains high (say $\geqslant 0.1$) if the frequency separation is less than about four times the decorrelation frequency. It should be noted that the slowness of the fall in correlation is inherent to the scintillation process and is not due to either the overlap or the finite bandwidth of the filters. Since the correlation remains high, unless the frequency separation is large compared to the decorrelation frequency, judging the value of ρ due to non-ISS intensity fluctuations is prone to errors. At the same time, the estimate is unlikely to be grossly wrong as illustrated by the dashed curve in Fig. 1, which shows the

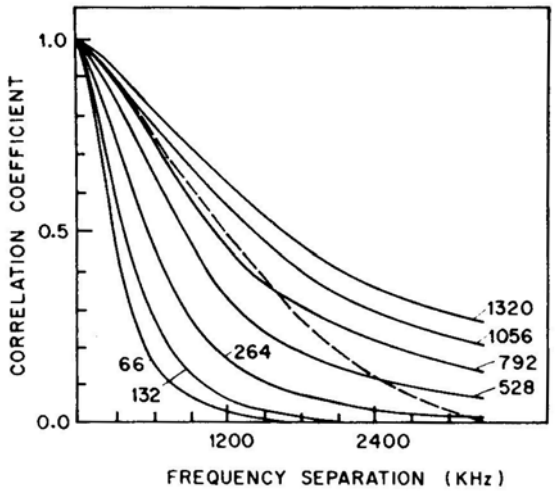

Figure 1. Model correlation functions for various decorrelation frequencies (solid curves). Each function is labelled with the assumed decorrelation frequency. The dashed curve shows the effect of renormalization if a wrong pedestal value is assigned.

renormalized correlation function obtained if the value of ρ for f_v= 1320 kHz is wrongly judged to be 0.28 when it is actually equal to zero. The curve runs across a series of theoretically expected curves and hence a good fit is not possible, indicating that a wrong p is subtracted.

The model fitting is done by minimizing χ^2 which is defined as

$$\chi^2 = \sum_{j=2}^{12} (\Gamma_{1j} - Q_{1j})^2 W_{1j}. \tag{3}$$

One has to be careful in assigning the weights W_{1j}. Purely statistical weights are given by (Johnson & Kotz 1970)

$$W_{1j} = n_c/(1 - Q_{1j}^2)^2 \tag{4}$$

where n_c is the number of ISS cycles in the data. These weights change very rapidly as Q_{1j} changes from close to 1 to lower values. Thus the first few terms of Equation (3), in general, dominate the minimization procedure rendering the procedure insensitive to the correlation values at large frequency separations. This is not a satisfactory situation as any systematic effects present would make f_v estimates erroneous. On the other hand, one cannot assign equal values to all W_{1j} as the statistical errors are widely different. As a compromise we have readjusted the weights such that W_{1j} is not more than $0.5 \sum_{K=j+1}^{12} W_{1K}$. If W_{1j} given by Equation (4) satisfies this condition, it is left unchanged, otherwise it is set equal to $0.5 \sum_{k=j+1}^{12} W_{1K}$. This scheme of modifying the weights is not unique. We adopted it since it modified only W_{12} and sometimes W_{13} (*i.e.,* very few weights) without allowing any single weight to dominate the fit.

We found that the statistical errors on the measured values of Γ_{1j} are too large to distinguish between Gaussian and Kolmogorov spectra. Even if the errors were smaller,

discriminating between the two spectral laws on the basis of f_v would not have been possible as the numerically computed values may carry significant errors (Lerche 1979).

4. Determination of decorrelation times

We define decorrelation time, t_v , as the time lag at which the correlation coefficient due to ISS falls to half its zero lag value if the observations were done with zero bandwidth. Receiver noise, broadband intensity variations and finite bandwidth of the filters affect the measured correlation coefficients. Multiplying the non-zero lag coefficients by $\sigma^2/(\sigma^2 - \sigma_n^2)$, where σ^2 and σ_n^2 are the variances calculated from the ONPULSE and OFFPULSE values respectively, corrects the coefficients for the receiver noise.

The correction for broadband intensity variations depends on the timescale of the variations.If the timescale is either very short or very long compared to that of ISS, then it is possible to correct for broadband variations from single channel observations; otherwise it is not. As pulsars exhibit intensity variations over several timescales ranging from a few microseconds to a few years, they probably also have significant variations with timescales similar to those due to ISS. To overcome this difficulty, Krishnamohan & Balasubramanian (1984) have developed a method to separate the autocorrelation function of ISS from that of broadband intensity variations using multichannel data. The method is based on the assumption that the decorrelation frequency of ISS is much smaller than that of broadband intensity variations. It may not work satisfactorily if narrowband intrinsic intensity variations exist. Such variations are suspected for PSR 0950 + 08 (Roberts & Abies 1982). We have subjected correlation functions of 11 pulsars to this method, after correcting them for the presence of receiver noise. The decorreation times listed in Table 1 are obtained from the correlation functions of ISS as separated out by the above method. They are corrected for finite bandwidth effects also, by multiplying by a correction factor. The correction factor depends on the ratio of the bandwidth used and the decorrelation frequency due to ISS. To obtain these correction factors, we have used the curve in Fig. 7 of Lee (1976), which is appropriate for Kolmogorov spectrum. Corrections appropriate for Gaussian spectra are only marginally different.

5. Results

5.1 *Our measurements*

The measured decorrelation frequencies and times are listed in Table 1. All the quantities have been corrected for finite bandwidth effects. All the decorrelation frequencies and a majority of the decorrelation times have also been corrected for any broadband intensity variations present in the data. Magnetic tapes containing the data on pulsars whose decorrelation times are marked with asterisk (*) were inadvertently erased prior to separating the correlation functions due to broadband and narrowband intensity variations, and hence their decorrelation times are not corrected for broadband variations. Filter widths listed in Col. 3 refer to the bandwidths of individual filters and hence the total bandwidth is 12 times as large. Col. 5 gives the observing time spent on each pulsar. If a pulsar is observed on more than a day, the time

Table 1. Observational parameters and results for 15 pulsars.

PSR	DM (cm^{-3} pc)	Filter bandwidth kHz	Data length min	Decorrelation frequency f_v kHz	Decorrelation time t_v s	Quality factor
0301 + 19	15.7	300	589	65	289	1467
0450 − 18	39.9	50	75	47	149*	362
0628 − 28	34.4	300	170	430	222	385
0818 − 13	41.0	50	169	11	40	3042
0823 + 26	19.5	300	145	58	90	1160
0834 + 06	12.9	300	522	495	219	1040
1133 + 16	4.8	300	487	710	189*	784
1237 + 25	9.3	300	198	595	288	250
1604 − 00	10.7	300	115	165	405	204
1642 − 03	35.7	50	53	8.8	43	887
1749 − 28	50.9	50	154	(2.5)	38*	2918
1919 + 21	12.4	300	1095	330	224	3200
2016 + 28	14.2	300	76	132	498	110
2020 + 28	24.6	50	187	150	190	236
2045 − 16	11.5	300	268	396	146*	1001

* Decorrelation time is not corrected for broadband intensity variations.

listed is the total time the pulsar is observed on all the days. The last column lists quality factor which is the approximate number of independent samples that went into the determination of decorrelation frequency and decorrelation time. It is computed as follows:

$$\text{Quality factor} = \frac{\text{Data length}}{t_v} \times \frac{\text{Total bandwidth}}{\text{Larger of filter bandwidth and } f_v}.$$

Even when f_v is smaller than the filter bandwidth, each filter gives only one independent frequency sample. This is taken into account by using either filter bandwidth or f_v, whichever is larger. We expect the statistical errors on our measurements to be small as the quality factors are large. Though we measured a definite value for the f_v of PSR 1749 – 28 following the method given in Section 3, we enclose it in parentheses as the filter bandwidth used for measuring it is too large compared to f_v. Comparison given in the next section, of our values with those measured by others shows that f_v and t_v can be measured reasonably well even if the filter width is several times f_v.

5.2. *Comparison of our f_v and t_v Values with Others*

In Tables 2 and 3, we compare our measurements of f_v and t_v with those by others. We have included only those authors who had at least four of our pulsars in their list. All measurements are scaled to 326.5 MHz using t he scaling laws: $f_v \propto \nu^4$ and $t_v \propto \nu$ where ν is the frequency at which the observation is done. Use of scaling laws corresponding to a Kolmogorov spectrum ($f_v \propto \nu^{4.4}$, $t_v \propto \nu^{1.2}$) does not change our conclusions. All the values are converted to values where the correlation coefficient falls to 0.5 by assuming a Gaussian shape for the correlation function. Rickett (1970) measured half-visibility bandwidth B_h, *i.e.,* the bandwidth for which the modulation index falls to half of that

Table 2. Comparison of f_v (in kHz) measured by us with those by others.

PSR	BK	AR	RA	LS	R	L
0301 + 19	65			79		
0450 − 18	47	49				
0628 − 28	430		189			
0823 + 26	58			309		559
0834 + 06	495		339	687	229	559
1133 + 16	710	421				2236
1237 + 25	595			1375		782
1604 − 00	165			309		
1642 − 03	8.8	12.3	25.3	48.1		
1749 − 28	(2.5)		4.4		6.3	
1919 + 21	330		817		125	894
2016 + 28	132			62	29	
2020 + 28	150	192		172		
$\left\langle \frac{f_v\ (\mathrm{BK})}{f_v\ (\mathrm{others})} \right\rangle$		1.04	1.01	0.74	2.44	0.49
		±0.23	±0.38	±0.22	±0.85	±0.15

References:
BK: Balasubramanian & Krishnamohan: this paper.
AR: Armstrong & Rickett (1981).
RA: Roberts &Abies (1982).
LS:Lyne & Smith (1982).
R: Rickett (1970).
L: Lang (1971).

Table 3. Comparison of t_v (in seconds) measured by us with those by others.

PSR	BK	RA	LS	B
0301 + 19	289		224	246
0628 − 28	222	244		
0823 + 26	90		133	117
0834 + 06	219	204	320	252
1133 + 16	189		240	167
1237 + 25	288		440	309
1604 − 00	405		841	
1642 − 03	43	65	88	58
1749 − 28	38	143		
1919 + 21	224	238		338
2016 + 28	498		420	374
2020 + 28	190		240	76
$\left\langle \frac{t_v\ (\mathrm{BK})}{t_v\ (\mathrm{others})} \right\rangle$		0.90	0.78	0.95*
		±0.08	±0.10	±2.08

* t_v of PSRs 1237 + 25 and 2020 + 28 are excluded in the computation since Backer's data had less than five scintillation cycles for these pulsars.

References:
B: Backer (1975) See Table 2 for other references.

when observed with zero bandwidth. We have taken the conversion factor from Lee (1976), $B_h \sim 10\ f_v$, taking into account the difference in the definition of the decorrelation frequency also.

The purpose behind the comparison is to check whether the methods followed by different authors for measuring these parameters give results consistent with each other or not. Since the parameters measured at different times for the same pulsar by the same authors could differ by a large factor (Roberts & Abies 1982), it is difficult to check the consistency by comparing the values of a single pulsar. So, we have included in the tables the mean ratio of values measured by us and by others. The errors listed are one standard deviation errors. The f_v measurements by Armstrong & Rickett (1981), Roberts & Abies (1982), and Lyne & Smith (1982) are consistent with ours as the mean ratios are close to one within about a standard deviation. Though the error is large, B_h values of Rickett (1970) seem to underestimate the values of f_v . We do not know whether it is caused by the conversion formula that we adopted from Lee (1976) or by the difficulties in measuring B_h values themselves. Lang (1971) had clearly over-estimated f_v values by a factor of two. This could partly be due to noncompensation of finite bandwidth effects in his procedure. t_v measurements of Roberts & Abies (1982) and Backer (1975) are consistent with ours. Though *tv* of Lyne & Smith (1982) are larger than ours by 20 per cent, the deviation may not be significant.

The larger scatter in the ratios of f_v values compared to the ratios of t_v values is consistent with the observation of Roberts & Abies (1982) that f_v of a pulsar varies by a larger factor than t_v when observed on different days.

6. Discussion

To study the dependence of ISS on DM we have combined our data with the measurements presented in the papers referred to in Tables 2 and 3. These measurements are converted to those corresponding to where the correlation coefficient falls to 0.5 and then multiplied by the average ratios obtained in Tables 2 and 3 to make them mutually consistent. We pooled in all, f_v values for 28 pulsars and t_v values for 31 pulsars including our measurements. In plotting Figs 2 and 3, values obtained by averaging the measurements by different authors rather than our measurements alone have been used. This, we believe, leads to more stable values. The pooled values along with the references to the origin of the data are given in Table 4 for easy reference.

The three points in Fig. 2 corresponding to PSRs 0628 – 28,0833 – 45 (the Vela), and 1933 +16 seem to deviate significantly from the general trend of the other points. It is debatable whether one more point (at f_v = 3400 kHz) corresponding to PSR 0809 + 74 also deviates from the rest. If the three labelled points are excluded, the best fit is given by f_v (kHz) = 18840 $DM^{-1.79\pm0\ 14}$. Log f_v and log DM have a linear correlation coefficient of – 0.90. It is known that the Gum nebula causes excessive scattering in the case of the Vela pulsar. (Backer 1974; Lee & Jokipii1976). In the case of PSR 1933+ 16, the deviation may be due to the steepening of f_v –DM relationship at large DM as discussed later. In the case of PSR 0628 – 28, the scattering is too low. The error bar given in Fig. 2 is on the basis of six independent measurements that are available for this pulsar. If PSR 0628 – 28 is included in the f_v – DM fit, the best fit is given by f_v (kHz) = 16070 $DM^{-1.70\pm0\ 14}$ and the correlation coefficient reduces to – 0.87.

Table 4. Averaged values of f_v and t_v with references to the original data. Refer to Sections 5.2 and 6 for details regarding the selection of pulsars for inclusion in the table and the procedure adopted to make different measurements mutually consistent before taking averages. See Tables 2 and 3 for notations used in references.

PSR	DM cm^{-3} pc	f_v kHz	Ref.	t_v s	Ref.
0301 + 19	15.7	62	BK, LS	232	BK, LS, B
0329 + 54	26.8	49	AR, LS, R	140	LS, B
0355 + 54	57.0	9.4	AR, LS	57	LS
0450 − 18	39.9	49	BK, AR	149	BK
0525 + 21	51.0	...	...	34	LS, B
0540 + 23	77.6	...	...	7.4	B
0611 + 22	96.7	...	...	40	B
0628 − 28	34.4	219	BK, RA	221	BK, RA
0809 + 74	5.8	3412	LS, R	573	LS
0818 − 13	41.0	11	BK	40	BK
0823 + 26	19.5	166	BK, L	102	BK, LS, B
0833 − 45	69.1	0.019	RA	1.53	RA
0834 + 06	12.9	368	BK, RA, LS, R, L	211	BK, RA, LS, B
0950 + 08	3.0	...	...	885	LS
1133 + 16	4.8	748	BK, AR, L	178	BK, LS, B
1237 + 25	9.3	666	BK, LS, L	316	BK, LS
1451 − 68	8.6	215	RA	593	RA
1508 + 55	19.6	110	AR, LS, R	50	LS, B
1604 + 00	10.7	197	BK, LS	531	BK, LS
1642 − 03	35.7	20	BK, AR, RA, LS	58	BK, RA, LS, B
1749 − 28	50.9	9	BK, RA, R	112	BK, RA
1919 + 21	12.4	544	BK, RA, R, L	245	BK, RA, B
1929 + 10	3.1	1242	RA, LS	281	RA, LS
1933 + 16	158.5	0.16	RA	6.6	RA
1944 + 17	16.3	76	LS	281	LS
1952 + 29	7.9	229	LS	468	LS
2016 + 28	14.2	83	BK, LS, R	298	BK, LS, B
2020 + 28	24.6	159	BK, AR, LS	169	BK, LS
2021 + 51	22.6	71	LS	261	LS, B
2045 − 16	11.5	396	BK	396	BK
2217 + 47	43.5	27	AR, LS	88	LS, B
2303 + 30	49.9	31	AR	...	...

It is interesting that the exponent (β) is approximately within the errors of what is expected from a homogeneous ISM. If the density fluctuations have Gaussian spectrum, the value of β is expected to be – 2; if it has a Kolmogorov spectrum β is expected to be – 2.2.

By translating pulse broadening (τ_v) measurements of pulsars with large dispersion measure using the relationship $2\pi f_v \tau_v = 1$, Sutton (1971) inferred that $\beta = -4$ describes his data better. Slee, Dulk & Otrupcek (1980) have shown that the steepening is not caused by the breakdown of $2\pi f_v \tau_v = 1$ relationship by directly verifying it on the Vela pulsar and also by showing that $\beta = -3.3 \pm 0.5$ even if only direct measurement of τ_v are used. Since τ_v values are measured for large DM pulsars, it is possible that the f_v – D M relationship steepens for large DM pulsars. Our conclusion differs from that by Slee, Dulk & Otrupcek (1980) who concluded that the f_v – DM relationship does not

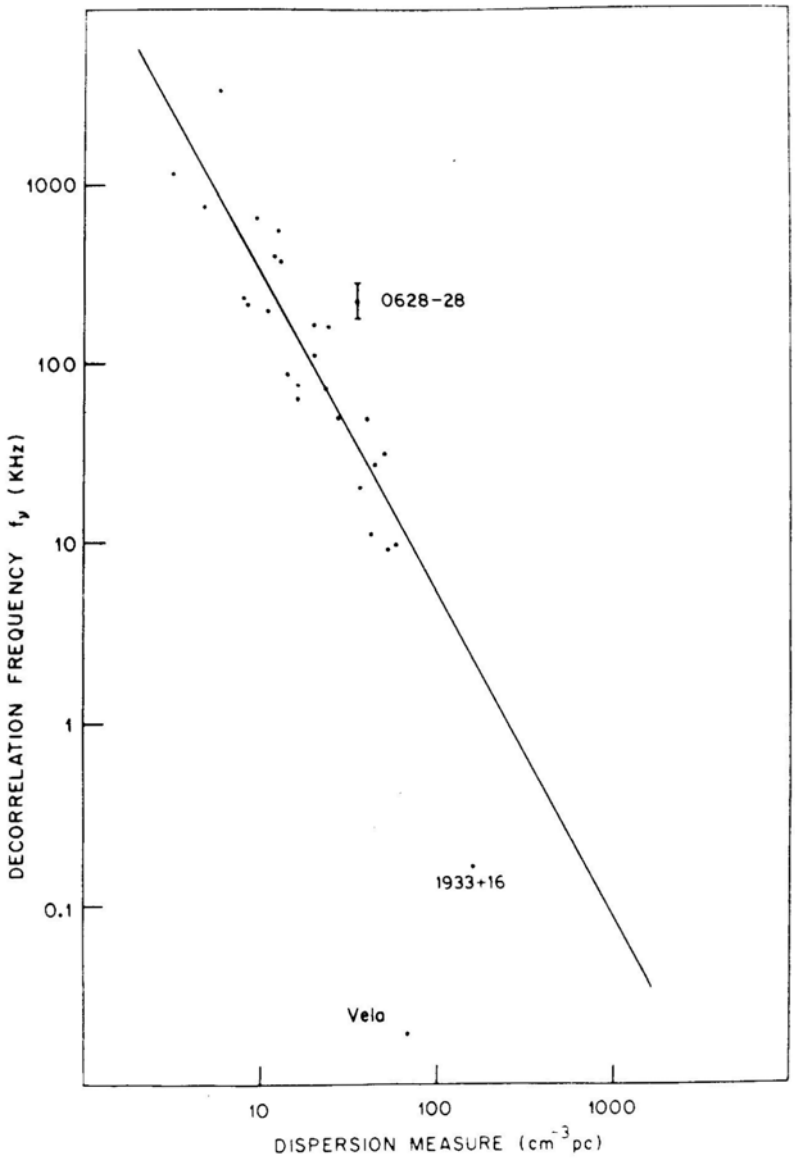

Figure 2. The relationship between the decorrelation frequency and dispersion measure. The three labelled measurements deviate significantly from the general trend shown by others. The best fit obtained by ignoring them, $f_v \propto \mathrm{DM}^{-1.79}$, is shown by a straight line.

depend on the DM range of the pulsars used. Our result implies that the average scattering properties do depend upon the DM range.

The t_v – DM diagram given in Fig. 3 shows that only three pulsars, *i.e.* the Vela, PSRs 0540 + 23 and 1933 + 16 deviate significantly from the general trend. These

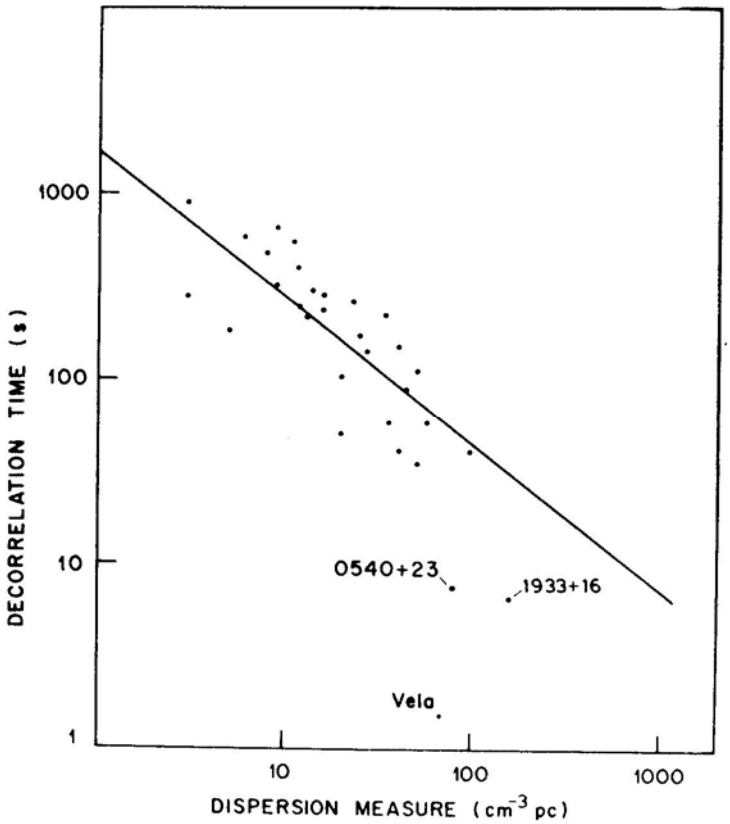

Figure 3. The relationship between the decorrelation time and dispersion measure. The three labelled measurements deviate significantly from the general trend shown by others. The best fit obtained by ignoring them, $t_v \propto \mathrm{DM}^{-0\,80}$, is shown by a straight tine.

three pulsars are excluded in the least-squares fit. The best fit is given by $t_v(s) = 1800\ \mathrm{DM}^{-0\,80\pm0\,15}$. Log t_v and log DM have a linear correlation coefficient of – 0.79. The correlation is less tight in t_v–DM diagram compared to f_v–DM diagram probably due to the difference in the velocity of different pulsars. From an analysis of 28 pulsars, Backer (1975) found that $t_v \propto \mathrm{DM}^{-0s\ \text{to}\ -1\,5}$ Our analysis gives less range to the exponent probably due to our taking average values where more than one independent value is available. The expected relationship is $t_{v.} \propto \mathrm{DM}^{-0\,5}$ for a Gaussian spectrum and $t_v \propto \mathrm{DM}^{-0\,6}$ for a Kolmogorov spectrum. Thus our t_v–DM relationship is also in broad agreement with the theoretical expectations.

The pooled data do not form a complete sample and hence the results obtained from them are likely to be biased. To check the seriousness of the likely bias, we analysed separately the values measured by us on the 14 pulsars. As discussed in Section 2.1, the 14 pulsars form almost a complete sample up to a DM of 41 cm $^{-3}$ pc. The analysis gave f_v (kHz) = $13280\ \mathrm{DM}^{1\,62\pm0\,24}$ with a log f_v, and log DM linear correlation coefficient of – 0.72, and t_v (s) = $1120\ \mathrm{DM}^{0\,66\pm0\,24}$ with a log t, and log DM linear correlation coefficient of – 0.57. As these results agree—within the error limits—with those obtained from the pooled data the biases are unlikely to be serious. The pooled data

used for arriving at DM dependences have pulsars up to a DM of about 60 cm $^{-3}$ pc, with only two pulsars having DM beyond that value.As the relations obtained from the pooled data are likely to hold good at least up to a DM of 60 cm^{-3} pc,the local interstellar medium is homogenious at least up to a distance of about 2 kpc.

Acknowledgements

It is a pleasure to thank the staff of Radio Astronomy Centre Ootacamund for the support they gave during observations and Dr A. Pramesh Rao for several comments.

References

Armstrong, J. W., Cordes, J. M., Rickett, B. J. 1981, *Nature*, **291,** 561.
Armstrong, J. W., Rickett, B. J. 1981, *Mon. Not. R. astr. Soc.,* **194,** 623.
Backer, D. C. 1974, *Astrophys. J*., **190,** 667.
Backer, D.C.1975, *Astr. Astrophys*., **43,** 395.
Cordes, J. M. 1982, in *Low Frequency Variability of Extragalactic Radio Sources*, Eds W. D. Cotton & S. R. Spangler, NRAO, Green Bank, p. 63.
Dennison, B. 1982, in *Low Frequency Variability of Extragalactic Radio Sources,* Eds W. D. Cotton & S. R. Spangler, NRAO, Green Bank, p. 71.
Duffet-Smith, P. J., Readhead, A. C. S. 1976, *Mon. Not. R. astr. Soc.*, **174,** 7.
Johnson, N. L, Kotz, S. 1.1970, *Continuous Univariate Distributions,* Vol. 2, Houghton Mifflin Co.,Boston.
Krishnamohan,. S.,Balasubramanian,V. 1984, *J. Astrophys. Astr.*, **5,** 483.
Lang, K. R. 1971, *Astrophys. J*., **164,** 249.
Lee, L. C.1976, *Astrophys. J*., **206**, 744.
Lee, L. C, Jokipii, J. R. 1975, *Astrophys. J*., **201,** 532.
Lee, L. C, Jokipii, J. R. 1976, *Astrophys. J*., **206,** 735.
Lerche, I. 1979, *Mon. Not R. astr. Soc*., **189,** 137.
Lyne, A. G., Smith, F. G. 1982, *Nature,* **298,** 825.
Mutel, R. L., Broderick, J. J., Carr, T. D., Lynch, M, Desch, M., Warnock, W. W., Klemperer, W. K. 1974,*Astrophys. J*.,**193**,279.
Pramesh Rao, A., Ananthakrishnan, S. 1984, *Nature*, **312,** 707.
Rickett, B. J. 1970, *Mon. Not. R. astr. Soc*.,**150,** 67.
Rickett, B. J. 1977, *A. Rev. Astr. Astrophys*., **15**, 479.
Roberts, J. A., Ables, J. G. 1982, *Mon. Not. R. astr. Soc*., **201**, 1119.
Slee, O. B., Dulk, G. A., Otrupcek, R. E. 1980, *Proc. astr. Soc. Austr.*, **4,** 100.
Sutton, J. M. 1971, *Mon. Not. R. astr. Soc.,* **155**, 51.
Vivekanand, M., Narayan, R. 1982, *J. Astrophys. Astr*., **3,** 399.

J. Astrophys. Astr. (1985) **6,** 49–56

An X-ray Hubble Diagram for Quasi-stellar Objects

A. K. Sapre & V. D. Mishra *Department of Physics, Ravishankar University, Raipur 492010*

Received 1983 January 13; revised 1984 August 17; accepted 1984 November 28

Abstract. To form the Hubble diagram for quasi-stellar objects (QSOs),we have made use of the recently published data on X-ray fluxes of 159 QSOs observed from the Einstein Observatory. The scatter in the Hubble diagram and the lack of an obvious redshift-flux density correlation for these QSOs have been attributed to the observational selection effect that the intrinsically less luminous QSOs can be detected only in the nearby region of space. When the optical, radio and X-ray selection effects are removed, keeping only the intrinsically brighter sources, we obtain a sample of 16 QSOs having a small dispersion in X-ray luminosities ($\langle \log L_x \rangle = 46.12 \pm 0.28$), a statistically significant linear correlation between ($\log f_x$, $\log cz$) pairs and a slope $A = -1.906 \pm 0.061$ of the linear regression of $\log f_x$ on $\log cz$. This slope is consistent, at a confidence level of 95 per cent or greater, with the slope of –2.0 expected theoretically based on the assumption that the redshifts of QSOs are cosmological in nature.

Key words: quasistellar objects—Hubble diagram—cosmology—Xrays

1. Introduction

The Hubble diagram for quasi-stellar objects (QSOs) has been investigated by a number of authors, Sandage (1965) and Schmidt (1968) being among the first. In the optical as well as radio region it turns out to be a scatter diagram, with no obvious correlation between apparent magnitude and redshift for all QSOs. However, the following observational facts complicate the interpretation of the Hubble diagram: (i) some QSOs are variable; (ii) the known QSOs have a broad range of luminosities; and (iii) the intrinsically faint QSOs can be detected only if they are relatively nearby, whereas one needs to sample larger volumes of space to detect the intrinsically brighter ones. All these effects presumably produce the observed scatter in the Hubble diagram. Various attempts have therefore been made to reduce the scatter and obtain evidence for the cosmological interpretation of QSO redshifts. Following the example that the brightest members of clusters of galaxies exhibit a tight Hubble relation (Sandage 1967), McCrea (1972) suggested that the brightest QSOs at each redshift might also display a significant Hubble relation. Attempts to reduce the scatter in the Hubble diagram due to optical variability was made by Usher (1975, 1978) and more recently by Pica & Smith (1983). Bahcall & Turner (1977) and Setti & Zamorani (1978) took account of the large spread in the optical luminosities and the evolution of the luminosity function of QSOs. Kembhavi & Kulkarni (1977) found that the intrinsic

luminosities of the brightest QSOs increases with z for $z < 1$ (volume effect), and that one obtains a consistent Hubble relation for $z > 1$. One concludes from these investigations that the brightest QSOs conform to the Hubble relation, particularly when one corrects for the variability, volume effect and cosmological evolution. Furthermore, Lang *et al.* (1975) and Thakur & Sapre (1978) have emphasized the importance of applying proper *K*-corrections to observed visual magnitudes of QSOs in forming a significant Hubble diagram. Attempts have also been made to isolate subsets of QSOs based on physical properties. Netzer, Yahil & Yaniv (1978) found a strong correlation for QSOs with flat optical continuum whereas Setti & Woltjer (1973) have claimed a Hubble relation for QSOs with steep radio spectra.

Since the QSOs as a class are luminous X-ray emitters (Tananbaum *et al.* 1979), and the X-ray variability by $\Delta \log f_x > 0.3$ is rather rare (Zamorani *et al.* 1984), it would be of interest to examine the Hubble diagram using their X-ray fluxes. We proceed to do so in the following.

2. Data analysis and results

We have compiled the data on X-ray fluxes of QSOs from the available literature. Our sample consists of 19 X-ray selected ('serendipitous') QSOs from Reichert *et al.* (1982), 79 detected QSOs from Zamorani *et al* (1981), 19 X-ray selected QSOs from Grindlay *et al.* (1980),35 detected QSOs from Ku, Helfand & Lucy (1980) and 42QSOs from Tananbaum *et al.* (1979), with some degree of overlap between different lists. We exclude from the sample the QSO 0100 + 0205 of Ku, Helfand & Lucy since its redshift is uncertain,and QSO 1227 + 0224 of Tananbaum *et al.* for which the visual magnitude is not available. Thus we obtain a final sample of 159 QSOs detected in the energy band 0.5–4.5 keV.Of these, 110 are radio-loud QSOs and 49 radio-quiet serendipitous QSOs.

Though the values of observed X-ray fluxes have been given only in Tananbaum *et al.* (1979) and Zamorani *et al.* (1981), the values of L_x (erg s^{-1}) in 0.5–4.5 keV energy band at the source, corrected for galactic absorption, are given for Friedmann cosmological model with H_0 = 50 km s^{-1} Mpc^{-1} and $q_0 = 0$ in all the six references cited above. Therefore, we have obtained the values of corrected f_x (erg cm^{-2} s^{-1}) in the fixed emitted energy band of 0.5–4.5 keV corresponding to the published values of L_x using the relation

$$L_x = f_x \frac{4\pi c^2}{H_0^2} [z(1 + 0.5z)]^2. \quad (1)$$

The resulting Hubble diagram, *i.e.*, the plot of (log *cz*, log f_x) pairs is shown in Fig. 1. The correlation is rather poor, with a coefficient of only 0.536.

Since the scatter in the diagram [σ (log L_x) ~ 0.8] is primarily due to a spread in intrinsic luminosities than the errors in redshifts, it would be more meaningful to analyse the regression of log f_x on log cz. In addition, we have analysed also the regression of log *cz* on log f_x for the sake of comparison with similar analyses found in the literature. If the redshifts of the QSOs are cosmological in nature, then for a Friedmann universe with deceleration parameter $q_0 = 1$, the Hubble diagram should yield a slope of –0.5 for linear regression of log cz on log f_x and –2.0 for linear regression of log f_x on log *cz* The observed slopes of both the regression lines listed in Table 1 are significantly different from the theoretically expected ones. The observed slope results

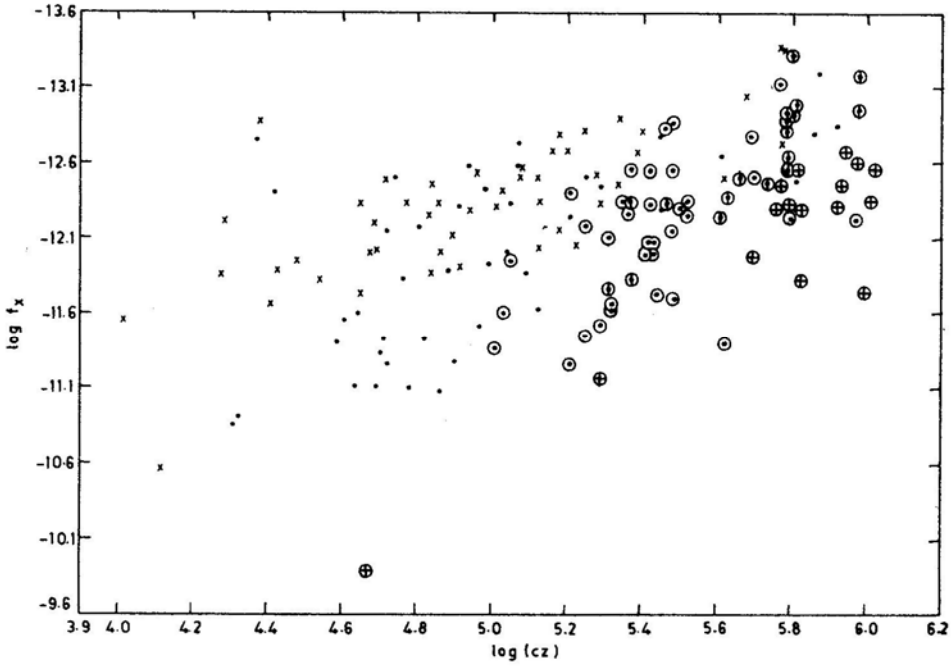

Figure 1. Plot of log f_x against log cz for a sample of 159 QSOs. × : radio-quiet serendipitous X-ray QSOs;⊙ : QSOs free from the optical selection effect; ⊕ :QSOs free from the optical and radio selection effects; ⊕: QSOs free from the optical, radio and X-ray selection effects.

mainly from the exposure effect in the sensitivity limit: the exposure times are raised for high-redshift QSOs, reaching thereby fainter sensitivity limits. Excluding 3C 273, the QSO with the highest f_x, one may note in Fig. 1 that log f_x (max) remains nearly constant with redshift up to log $cz \sim 5.3$, and is in approximate accordance with the Hubble law for higher redshifts. This behaviour mimics the one in optical region noted by Kembhavi & Kulkarni (1977), and certainly results from the volume effect.

The volume effect is seen better in Fig. 2 which shows log L_{X1} (for Friedmann model with $H_0 = 50$ kms^{-1} Mpc^{-1} and $q_0 = 1$) versus log cz. The intrinsically faint X-ray QSOs are clearly seen to have smaller redshifts whereas intrinsically very bright X-ray QSOs, being rare, can be detected only if greater and greater volume of space is sampled, *i.e.*, for larger values of redshifts. Though Fig. 2 is in qualitative agreement with the results of Kembhavi & Kulkarni (1977) in the optical, the X-ray luminosities do not flatten out substantially even at large redshifts. It would appear that there is a larger intrinsic spread in X-ray luminosities than in the optical. In order to correct for the 'volume effect', we should consider only those QSOs which are observable at all redshifts. Following Burbidge & O'Dell (1973), we consider these to be the ones lying to the brighter side of the mean line with a slope of –2.0 in log f versus log z diagram. We apply this criterion in the optical, radio as well as X-rays since all the samples suffer from the volume effect and since fluxes in different wavebands appear to be correlated (see *e.g.,* Zamorani *et al.* 1981).

In the optical region, we have used the corrected visual magnitude m_v and log cz. The observed visual magnitudes have been taken from Hewitt & Burbidge (1980) and are

duly corrected for galactic absorption; also the *K*-correction was applied following the procedure of Thakur & Sapre (1978). The Burbidge–O'Dell procedure, as employed here,implies an optical detectability limit m_v = 21.5 mag, at z = 3.53. This leaves us with a sample of 68 optically bright QSOs which are shown in Figs 1 and 2 by circumscribed circles. Interestingly, all of these 68 are brighter also in the radio and X-rays. For this subset of the sample, the correlation coefficient has improved from 0.536 to 0.671. Furthermore, the slope of the linear regression of log f_x on log cz decreases from – 0.633 to – 1.310, relatively closer to though still significantly different from, the theoretically expected one.

Similarly, in order to remove the radio selection effect we have analysed the corrected radio fluxes f_r (erg cm $^{-2}$ s^{-1}) against redshift. The radio fluxes have been calculated for the 3.1–8.1 GHz band (at the source) from published 1.4 GHz fluxes and spectral indices following the prescription given by Schmidt (1968). With a similar analysis as before, we are left with a sample of 36 radio-bright QSOs which can be observed optically as well as in the radio at all redshifts up to z =3.53 with an implied radio detectability limit of log f_r = –12.67. The correlation coefficient for this sample increases to 0.746, and the slope to –1.670. This sample of 36 QSOs has been displayed in Figs 1 and 2 by circumscribed circles with a vertical diameter. It is seen from Fig. 2 that the removal of radio selection effect further removes X-ray faint QSOs from the Hubble diagram, as expected from the observed correlation between radio and X-ray fluxes.

A similar analysis for the X-ray fluxes leaves us with a sample of 16 QSOs that can be detected in all the three bands at all redshifts up to z= 3.53, with an X-ray detectability limit of log f_x = –12.94. This sample is free from optical, radio and X-ray selection effects and is displayed in Figs 1 and 2 by open circles with an inscribed cross. We find that the sample of 16 QSOs is the sample of intrinsically very bright X-ray QSOs having a small spread in L_{X1}(ergs^{-1}): This sample has a mean $\langle \log L_{Xl} \rangle$ of 46.12 ± 0.28, its only member in the nearby space being 3C 273. It is seen from Table 1 that the correlation coefficient for this sample has increased to 0.912 and the slope of the linear regression of log f_x on log cz has decreased to –1.906 ± 0.061, very close to the theoretically expected one. The *t*-statistic shows at a confidence level of better than 95 per cent that the departure of the calculated slope from the expected one is not significant. On the other hand, the slopes of the linear regressions of log cz on log f_x appear to be rather insensitive to this analysis, possibly since the spread in f_x is still considerably larger than the errors in redshift estimates.

3. Discussion

An inspection of Figs 1 and 2 and Table 1 clearly shows that the X-ray Hubble diagram for the sample of 159 QSOs is a scatter diagram with small correlation. The departure of the slopes of the linear regressions from the theoretically expected slopes (assuming QSO redshifts to be cosmological in origin) is also significant at 0.01 level for this sample. Clearly this is due to the selection effects and a large dispersion in log L_{X1} as seen from the value given in Col.9 of Table 1.As pointed out in Section 2,when the optical, radio and the X-ray selection effects are removed we obtain a smaller sample of QSOs intrinsically brighter in all bands having a smaller dispersion in log L_{X1}.As a result,the values of the correlation cofficient 'r' increases significantly.This sample of 16 QSOs listed in Table 2 covers almost the entire range of redshifts in which QSOs

Table 1. Results of linear regression analyses of $\log f_X$, $\log cz$ pairs for QSOs.

Sample	No. of QSOs	Slope A / A'	Standard deviation in slope σ_A / $\sigma_{A'}$	$t_A = [A-(-2.0)]\sigma_A^{-1}$ / $t_{A'} = [A'-(0.5)]\sigma_{A'}^{-1}$	Significance level 0.05	Significance level 0.01	Correlation coefficient r	$\langle \log L_{X1} \rangle$	$\sigma \log L_{X1}$
1	2	3	4	5	6		7	8	9
All QSOs	159	−0.633	0.006	216.934	Yes	Yes	0.536	44.95	0.796
		−0.454	0.005	10.176	Yes	Yes			
Sample A	68	−1.310	0.022	31.428	Yes	Yes	0.671	45.60	0.45
		−0.343	0.006	27.214	Yes	Yes			
Sample B	36	−1.670	0.044	7.544	Yes	Yes	0.746	45.75	0.41
		−0.334	0.009	19.014	Yes	Yes			
Sample C	16	−1.906	0.061	1.545	No	No	0.912	46.12	0.28
		−0.437	0.014	4.512	Yes	Yes			

Note:
In Columns 3–6, upper values for each sample of QSOs correspond to linear regression of $\log f_X$ on $\log cz$ whereas the lower values correspond to linear regression of $\log cz$ on $\log f_X$.
Sample A: Optical volume effect removed.
Sample B: Optical and radio volume effects removed.
Sample C: Optical, radio and X-ray volume effects removed.

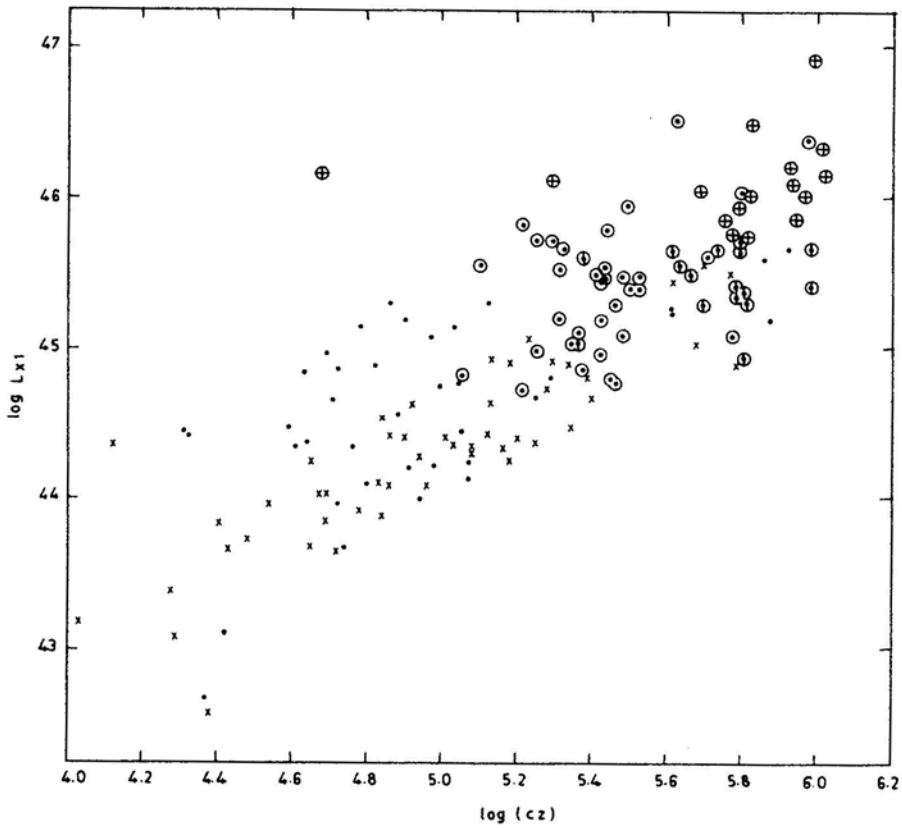

Figure 2. Plot of log L_{X1} against log cz for 159 QSOs. X: radio-quiet serendipitous X-ray QSOs;⊙ :QSOs free from the optical selection effect;: ⊕ QSOs free from the optical and radio selection effects; ⊕ : QSOs free from the optical, radio and Xray selection effects. For these 16 QSOs σ log $L_{X1} = \pm 0.28$.

have been detected, and yields a slope of $\Delta \log f_x / \Delta \log cz$ that agrees with expected value of –2.0 at a confidence level $\geqslant$ 95 per cent. Thus, these QSOs offer the much-needed standard candle in the X-ray luminosities.

The optical, radio and X-ray luminosities (H_0 = 50 km s^{-1} Mpc^{-1}; q_0 = 1) for the sample QSOs are listed in Table 2, along with their mean values and dispersions. It is seen that the dispersions in log L_{V1} and log L_{X1} are small and comparable, whereas the spread in log L_{r1} is still large. This suggests that the correlation between optical and X-ray luminosities of QSOs is better than between either of these and the radio emission, in agreement with the observations of Henriksen, Marshall & Mushotzky (1984). It would thus appear that the X-ray and optical emissions in QSOs may have a common origin.

Acknowledgements

One of us (VDM)would like to thank Professor R. K. Thakur, Head of the Department of Physics, Ravishankar University, Raipur for offering facilities to work in the

Table 2 The Sample of 16 QSQs free from the optical, radio and X-ray volume selection effects.

Coordinate designation of QSOs	Redshift z	log L_{V1} (Visual band)	log L_{r1} (3.1–8.1 CHz band)	log L_{X1} (0.5–4.5 keV band)
0043+008	2.150	46.68	45.86	45.75
0226−038	2.064	46.67	46.32	45.94
0237−2322	2.223	46.85	47.31	46.51
0420−388	3.120	47.00	46.13	46.09
0438−436	2.852	46.19	47.44	46.09
0528−250	2.765	46.65	46.73	46.23
0637−75	0.651	46.36	46.49	46.12
0642+449	3.402	46.56	47.10	46.34
0805+0441	2.877	46.56	46.51	45.88
1011+2504	1.631	47.12	45.89	46.08
1225−317	2.230	47.15	45.91	46.03
1226+023	0.158	46.28	46.25	46.16
1442+1011	3.530	46.72	47.18	46.18
1703.5+609	1.980	46.46	45.68	45.78
2121+0522	1.878	46.45	46.53	45.87
2126−150	3.270	46.38	46.73	46.92
Mean		46.66	46.50	46.12
Standard deviation		± 0.27	± 0.53	± 0.28

department. We would also like to thank the referees for useful comments and suggestions.

References

Bahcall, J. N., Turner, E. L. 1977, in *IAU Symp.* 74: *Radio Astronomy and Cosmology*, Ed. D. L. Jauncey, D. Reidel, Dordrecht, p. 295.
Burbidge, G. R., O'Dell, S. L. 1973, *Astrophys. J.* **183,** 759.
Chanan, G. A., Margon, B., Downes, R. A. 1981, *Astrophys. J.* **243,** L5.
Grindlay. J. E., Streiner, J. E., Forman, W. R. Canizares, C. R., McClintock, J. E. 1980, *Astrophys J.*, **239,** L43.
Henriksen, M. J. Marshall, F. E., Mushotzky, R. F. 1984, *Astrophys J.*, **284**, 491.
Hewitt, A., Burbidge, G. 1980, *Astrophys. J. Suppl. Ser.*, **43,** 57.
Kembhavi, A. K., Kulkarni, V. K. 1977, *Mon. Not. R. astr. Soc.*, **181,** 19P.
Ku, W. H. M., Helfand, D. J, Lucy, L. B. 1980, *Nature,* **288,** 323.
Lang, K. R., Lord, S. D., Johanson, J. M, Savage, P. D. 1975, *Astrophys. J.,* **202,** 583.
McCrea, W. H. 1972, in *IAU Symp.* 44: *External Galaxies and Quasi-Stellar objects,* Ed. D.S. Evans, D. Reidel, Dordrecht, p. 283.
Netzer, H., Yahil, A., Yaniv, R. 1978, *Mon. Not. R. astr. Soc.*, **184,** 21P.
Pica, A. J., Smith, A. G. 1983, *Astrophys. J.*, **272,** 11.
Reichert, G. A., Mason, K. O., Thorstensen, J. R., Bowyer, S. 1982, *Astrophys. J.,* **260,** 437.
Sandage, A. 1965, *Astrophys. J.*, **141,** 1560.
Sandage, A. 1967, *Astrophys. J.*, **150,** L9.
Schmidt, M. 1968, *Astrophys. J.,* **151,** 393.
Setti, G., Woltjer, L. 1973, *Astrophys. J.*, **181,** L61.
Setti, G., Zamorani, G. 1978, *Astr. Astrophys.*, **66,** 249.

Thakur, R. K., Sapre, A. K. 1978, *Astrophys. Space Sci*., **57,** 119.
Tananbaum, H., Avni, Y., Branduardi, G., Elvis, M, Fabbiano, G., Feigelson, E., Giacconi, R., Henry, J. P., Pye, J. P., Soltan, A., Zamorani, G. 1979, *Astrophys. J*., **234,** L9.
Usher, P. D. 1975, *Astrophys. J*., **198,** L57.
Usher, P. D. 1978, *Astrophys. J*., **222,** 40.
Zamorani, G., Giommi, P., Maccacaro, T., Tananbaum, H. 1984, *Astrophys. J.,* **278,** 28.
Zamorani, G., Henry, J. P., Maccacaro, T., Tananbaum, H., Soltan, A., Avni, Y., Liebert, J., Stocke, J., Strittmatter, P. A., Weymann, R. J., Smith, M. G., Condon, J. J, 1981, *Astrophys J*., **245**, 357,

J. Astrophys. Asrt. (1985) **6,** 57–60

A Study of Solar Modulation of Medium Energy Primary Cosmic Ray Nuclei

Projit K. Das *Pandu College, Guwahati 781012*
T. D. Goswami *Department of Physics, Guwahati University, Guwahati 781014*

Received 1984 August 21; accepted 1984 December 6

Abstract. The energy spectra of primary cosmic rays were studied in the energy interval 150 to 450 MeV/nucl by using balloon-borne cellulose-nitrate solid-state plastic detector. Effects of solar modulation were studied using the theoretical spectrum of H_1 nuclei near the solar minimum in 1964 as the demodulated spectrum. The 'force-field' potential which fit the experimental results was estimated to be 270 MeV/nucl.

Key words: cosmic rays, energy spectra—cosmic rays, solar modulation

1. Introduction

The cosmic-ray nuclei suffer modulation due to the physical conditions, mainly electromagnetic, prevailing in the interplanetary space. Of the different variations, the eleven-year cycle of solar activity is of paramount significance in relating the energy spectra outside the interplanetary region to the one observed near earth. The variation of fluxes of heavy cosmic-ray nuclei during a solar cycle is observed to be small above energies of 600 MeV/nucl. In the present investigation, we have studied the solar modulation effect on heavy cosmic ray nuclei by using the 'force-field' solution (Gleeson & Axford 1968), making use of the theoretical demodulated spectrum given by Paruthi *et al.* (1976).

2. Experimental procedure

We have used a stack of Daicell cellulose-nitrate solid-state plastic detector exposed to primary cosmic-ray nuclei for 10.66 h on 1969 June 27 from Fort Churchill, Canada, at a ceiling altitude of 2.8 gm cm $^{-2}$ during the solar maximum. It may be noted that 1969–70 was a period of the polarity reversal of the Sun (Howard 1974). The details of the experimental procedure and the selection criteria are given elsewhere (Das & Goswami 1983).

3. Results and discussion

The differential fluxes of each nucleus from Ne to Fe have been estimated in the energy interval 150 MeV/nucl to 450 MeV/nucl. The differential energy spectra of

H_1 (Z =10–15) nuclei, the most abundant nuclei with $10 \leqslant Z \leqslant 26$ in cosmic rays, are plotted in Fig. 1. The differential fluxes of these nuclei in each energy interval of 50 MeV/nucl are given in Table 1.

Since the first formulation of the cosmic-ray transport equation for interplanetary region, including the effects of diffusion, convection and energy loss (Parker 1965), it has been an accepted fact that the galactic cosmic rays with energies $\leqslant$ 20 GeV/nucl propagating through the interplanetary medium lose energy due to adiabatic deceleration in the expanding magnetic irregularities. Fokker–Planck equation to be satisfied by the cosmic-ray density U (r, T) is given by (Parker 1965),

$$\frac{V}{r^2}\frac{\partial}{\partial r}(r^2U) - \frac{2V}{3r}\frac{\partial}{\partial T}(\alpha TU) - \frac{1}{r^2}\frac{\partial}{\partial r}\left(r^2K\frac{\partial U}{\partial r}\right) = 0 \tag{1}$$

where $U(r, T)$ is the differential number density of cosmic-ray particles at a radial distance r from the Sun in the kinetic energy range T and T+dT, V is the solar wind speed, K is the diffusion coefficient and $\alpha = (T + 2E_0)/(T + E_0) = (E + E_0)/E$ with E_0 the rest mass energy and $E = T+E_0$, the total energy of cosmic-ray particles. The equation describing the effects of convection and scattering of cosmic-ray particles by magnetic scattering centres carried along by the radially moving solar wind is obtained with the assumption that (i) the steady-state condition prevails, (ii) the speed of solar

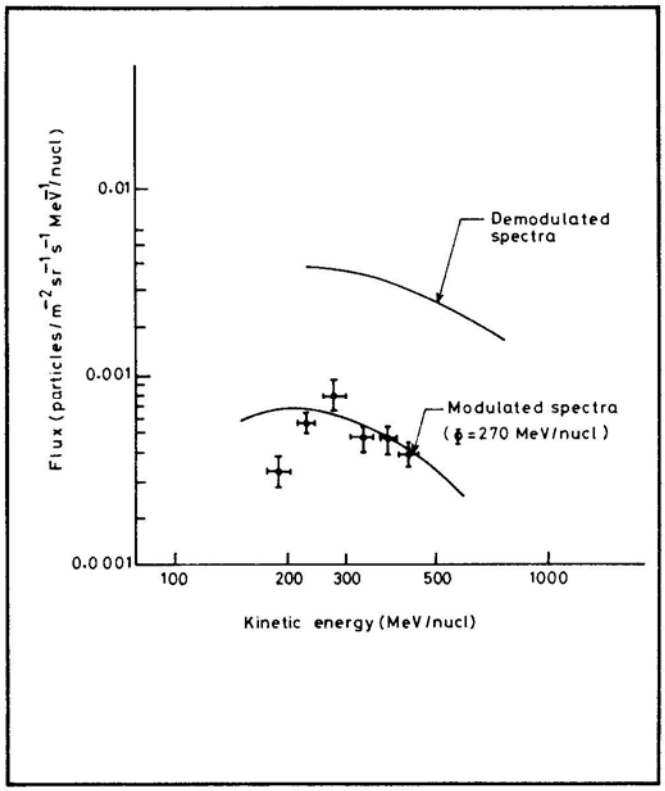

Figure 1. Differential, energy spectra for H_1 nuclei.

Table 1. Differential fluxes of $H_1(10 \leqslant Z \leqslant 15)$ nuclei.

Energy interval MeV/nucl	Fluxes 10^{-4} particles m^{-2} sr^{-1} s^{-1} MeV^{-1}/nucl
151–200	3.19 ± 0.23
201–250	5.89 ± 0.32
251–300	8.38 ± 0.31
301–350	4.78 ± 0.23
351–400	4.79 ± 0.41
401–450	3.90 ± 0.21

wind is spherically symmetric, and (iii) the diffusion coefficient is isotropic. Equation (1) can be solved numerically (Fisk 1971) or by an approximation method (Gleeson & Axford 1968). Gleeson & Axford (1968) showed that if the modulation is small and the diffusion coefficient is a separable function of heliocentric distance r and momentum P, then an approximate solution of Equation (1) will be

$$\frac{J(r,E)}{E^2 - E_0^2} = \frac{J(R, E+\phi)}{(E+\phi)^2 - E_0^2}. \tag{2}$$

Solution (2) is generally known as the 'force-field' solution, where $J(r,E)$ is the differential intensity of the particles of electric charge Z_e at a heliocentric distance r and total energy E, J $(R.E + \phi)$ is the corresponding intensity at the boundary of the modulating volume of radius R corresponding to total energy $(E + \phi)$, E_0 is the rest-mass energy of protons, and ϕ is the so-called 'force-field' potential energy. The parameter ϕ can be identified with the mean energy loss by cosmic-ray particles in penetrating the interplanetary region from the interstellar space, *i.e.* during their traversal from the boundary of modulating region into the point of observation.

The modulated near-earth spectra derived by using the numerical and force-field solutions differ from each other only at very low energies. For kinetic energies $\leqslant$200 MeV/nucl, the two solutions practically give the same result (Fisk 1971; Bhatia, Paruthi & Kainth 1977). We have used the force-field solution in deriving the near-earth modulated spectra.

To study the effects of solar modulation, the theoretical spectrum predicted by Paruthi *et al.*,(1976) for 1964 has been taken as the demodulated spectrum, as this has been found to fit well with the experimental values obtained by Webber & Ormes (1967) and by Durgaprasad & Reames (1967) in different energy intervals ranging from 180 to 3000 MeV/nucl. Using the force-field solution (2), the different energy spectra for different values of ϕ(150–300 MeV/nucl) are predicted. The curve corresponding to ϕ= 270 MeV/nucl is in better agreement with the experimental values. High-energy part of the energy spectra is seen to agree fairly well with the predicted spectra for ϕ = 270 MeV/nucl. The low-energy part indicates predominant solar modulation higher than expected from the force-field solution. The poor fit at low energies may perhaps be due to the uncertainties in the form of the unmodulated cosmic-ray spectrum outside the solar cavity.

A change in cosmic-ray flux occurs during a solar cycle due to solar activity. We have compared our data with those of 1964 (solar minimum) as obtained by Bhatia *et al.* (1967) to find the effect of solar activity on cosmic rays. The ratio J_{64}/J_{69} comes out to

be nearly 3.8 indicating that the flux during the solar minimum (1964) is 3.8 times the flux during solar maximum (1969). This shows that high solar activity in some manner prohibits the galactic cosmic rays from entering the interplanetary space.

Acknowledgements

The authors are grateful to Professor S. Biswas (TIFR) forgiving the stack as a gift. The valuable comments received from Dr N. Durgaprasad (TIFR) and Dr J. N. Goswami (PRL) are also gratefully acknowledged. The financial assistance from the UGC is acknowledged. The facilities provided by the Department of Physics, GU is also acknowledged. We are grateful to Professor P. Dasgupta for going through the manuscript.

References

Bhatia, V. S., Chohan, V. S., Pabbi, S. D., Kainth, P. S., Biswas, S. 1967, in 10*th Symp. on Cosmic Rays, Elementary Particle Physics and Astrophysics*, Aligarh, p.33.

Bhatia, V. S., Paruthi, S., Kainth, G. S. 1977, *J. geophys. Res*., **82,** 2419.

Das, P. K., Goswami, T. D. 1983, *J. Astrophys. Astr*., **4,** 197.

Durgaprasad, R, Reames, D. V. 1967, *Phys. Rev*., **162,** 1296.

Fisk, L. A.1971, *J. geophys. Res. Lett*., **76,** 221.

Gleeson,L. J., Axford, W.I.1968, *Astrophys. J.,* **154,** 1011.

Howard, R. 1974, *Solar Phys*., **38,** 283.

Parker, E. N.1965, *Planet: Space Sci*.,**13,** 9.

Paruthi, S., Bhatia, V. S., Kainth, G. S., Biswas, S., Ramadurai, S. 1976, *Astrophys. Space Sci*., **44**, 167.

Webber, W. R,, Ormes, J. F. 1967, *J. geophys. Res.,* **72,** 5957.

J. Astrophys. Astr. (1985) **6,** 61–70

A Study of the Open Cluster NGC 2374

G. S. D. Babu *Indian Institute of Astrophysics, Bangalore 560034*

Received 1984 September 25; accepted 1985 January 11

Abstract. The results of modified objective grating observations and photoelectric as well as photographic photometry of the open cluster NGC 2374 are presented. The cluster contains at least twenty stars as definite members down to $m_v \approx$ 15mag. There is a uniform extinction of $E(B - V) = 0.175$ mag and the distance is 1.2 ± 0.1 kpc. The most likely age of this cluster is 7.5×10^7 years.

Key words: open clusters—photometry

1. Introduction

The study of young open clusters, especially the estimation of their distances, is very valuable for a better understanding of galactic spiral structure. A search for such young clusters was carried out using the technique of combining the spectral types from the modified objective grating spectra and the transformed V mag from the Palomar Observatory Sky Survey (POSS) Charts (Babu 1983). Out of several clusters observed in the direction of the Monoceros constellation, it was found that NGC2374 ≡ OCI 585 ≡ C0721 –131 (l = 228°.43; b = + 01°.4) has the characteristics of a young cluster. It has, therefore, been selected for further photometric work. Its field is given in Fig. 1 along with the identification numbers.

The details of whatever little is known about this cluster are compiled by Alter, Balazs & Ruprecht (1970) and by Lyngå (1980). These are reproduced in Table 1. Ruprecht (1966) has classified the cluster as II 3p in the Trumpler classification system. The meaning of this classification is that it is a detached cluster with little central concentration of stars which is coded as II. The number 3 means that it is composed of both bright and faint stars, while 'p' indicates that it is a sparsely populated cluster with less than fifty stars.

In this paper, the results of modified objective grating observations and photoelectric as well as photographic photometry are presented.

2. Observations and reductions

The modified objective grating spectra for the stars in the region of the cluster have been obtained using the instrument (Babu 1983) which gives a dispersion of 485 Å mm^{-1} in the second order. The exposure time was 2 hours on a Kodak 103a-O plate, from which the spectral types, with an uncertainty of two subclasses on either side

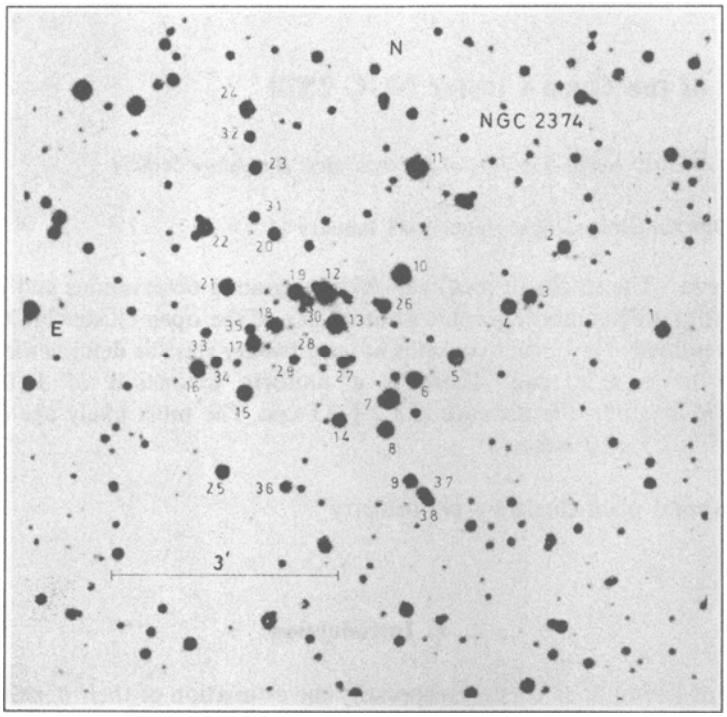

Figure 1. Field of open cluster NGC 2374 reproduced from the Palomar Observatory Sky Survey (Poss) prints. The identification numbers are introduced in the present work.

Table 1. Physical parameters of NGC 2374 known till date.

	Angular diameter arcmin	Distance kpc	No. of stars	$E(B-V)$	Age yr	Source
Trumpler (1930)	4.5	2.6				Alter, Balazs & Ruprecht (1970)
Collinder (1931)	10.0	1.24	40			Alter, Balazs & Ruprecht (1970)
Ba atova (1950)	15.0	0.93				Alter, Balazs & Ruprecht (1970)
Fenkart *et al.* (1972)		1.26	29	0.0	3.5×10^8	Fenkart *et al.* (1972)
Buscombe		1.3		0.0	2×10^9	Lyngå (1980)
Babu		1.2 ± 0.1	20	0.175	7.5×10^7	Present work

of the mean, could be assigned to a total of twenty-four stars around the cluster centre. The spectral type of star no. 20 could not be estimated because of overlapping. These estimates, listed in Table 2, are plotted in Fig. 2 against the *V* mag obtained from the POSS Charts, where star nos 1,2,3,4,5,6 and 24 do not fit into the general sequence of the other stars. Among the rest of the stars, which are considered as possible members of the cluster, the earliest spectral type is found to be B5 for star no. 11. However, due to the uncertainty inherent in the estimation of the spectral types, this could be anywhere between B3 and B7. Thus, since the clusters containing stars of spectral type B3 or earlier are young enough to be used as spiral arm tracers, NGC 2374 has been selected as a marginally young cluster for further studies.

All the above-mentioned stars were then observed photoelectrically, employing the standard *U*, *B* and *V* filters of the Johnson & Morgan system, with a dry-ice-cooled EMI 9558 B photomultiplier mounted on the Kavalur 102-cm telescope. The data collection was done with the help of an on-line computer (TDC-12). After applying the necessary corrections for atmospheric extinction, the instrumental magnitudes were standardized with the help of photometric sequences taken from Landolt (1973). A minimum of three sets of observations were taken for each star and the average *UBV* values are given in Table 2.

In order to reach the fainter members of the cluster, photographs of the cluster region were obtained using the following plate + filter combinations:

Kodak 103a-O + Schott UG 2 for *U*,

Kodak 103a-O + Schott GG 13 for *B*,

Kodak IIa-D + Schott GG 11 for *V*.

The magnitudes of thirteen fainter stars have been established from these plates, using the magnitudes of the photoelectrically observed stars for calibration. These are also

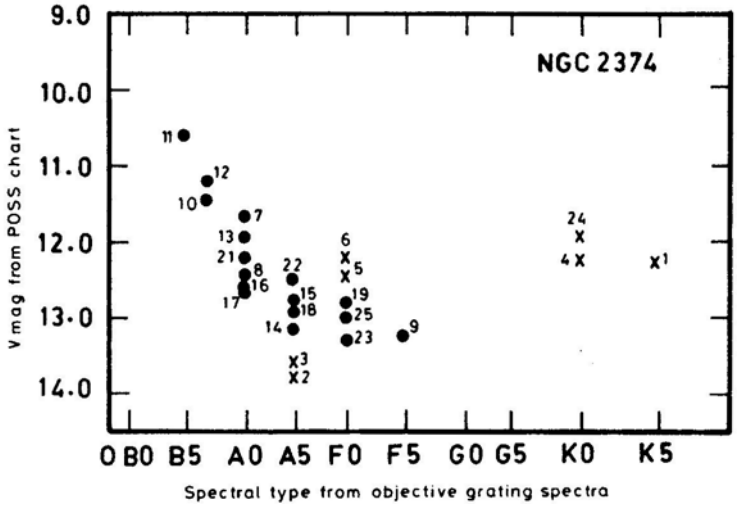

Figure 2. Spectral type obtained from the modified objective grating spectra are plotted against the *V* magnitudes estimated from the POSS Charts, for the stars in the field of NGC 2374. The filled circles denote the probable members and the crosses indicate the probable non-members.

Table 2. The observational data for individual stars in the open cluster NGC 2374.

Star No.	Spectral type	V (POSS)	V	$(B-V)$	$(U-B)$	Membership
Photoelectric photometry:						
1	K5	12.25	11.750	1.340	0.910	m?
2	A5	13.79	13.710	0.312	0.128	m?
3	A5	13.58	13.721	0.255	0.021	m?
4	K0	12.23	11.840	1.099	0.518	m?
5	F0	12.45	12.334	0.469	−0.155	—
6	F0	12.18	12.308	0.606	−0.074	—
7	A0	11.67	11.866	0.179	0.040	m
8	A0	12.44	12.637	0.292	0.109	m
9	F5	13.23	13.380	0.444	0.104	m
10	B7	11.43	11.664	0.128	−0.069	m
11	B5	10.59	10.653	0.449	−0.125	—
12	B7	11.18	11.540	0.080	−0.170	m
13	A0	11.94	12.027	0.177	−0.018	m
14	A5	13.15	13.762	0.241	0.088	m?
15	A5	12.77	12.996	0.246	0.234	m
16	A0	12.58	12.777	0.190	0.136	m
17	A0	12.67	12.604	0.254	0.228	m
18	A5	12.90	13.261	0.315	0.202	m
19	F0	12.81	13.229	0.398	0.179	m
20	—	13.32	13.793	0.485	0.135	m
21	A0	12.23	12.531	0.219	0.213	m
22	A5	12.48	13.038	0.350	0.123	m
23	F0	13.31	13.875	0.376	0.208	m
24	K0	11.89	12.070	1.014	0.552	m?
25	F0	13.01	13.133	0.399	0.173	m
Photographic photometry:						
26			13.80	0.35	0.20	m
27			15.12	0.21	−0.46	—
28			15.04	0.14	0.02	—
29			14.95	0.63	0.07	m
30			14.79	0.15	0.07	—
31			14.92	0.05	−0.82	—
32			15.14	−0.12	−0.12	—
33			14.69	0.56	0.10	m
34			15.02	0.02	−0.05	—
35			15.49	0.00	−0.36	—
37			13.73	0.36	0.06	m
38			14.95	0.07	−0.32	—

Spectral types are from the objective grating technique and V (POSS) are from the image diameters on POSS prints. V, $(B-V)$ and $(U-B)$ are from photometric observations — photoelectric or photographic. The symbol 'm' in the last column denotes positive membership. Doubtful membership is followed by (?)

included in Table 2. A majority of them appear to be around V = 15 mag with an uncertainty of about ± 0.2 mag in B and V, and about ± 0.35 mag in U.

3. Reddening

The ($B - V$) versus ($U - B$) diagram of this cluster is shown in Fig. 3. In this figure, most of the stars seem to follow an apparent sequence and show a general shift from the unreddened main sequence taken from Schmidt-Kaler (1965).

According to Burki (1975), the major causes of dispersion in the colour-colour diagram (CCD) of a cluster are stellar evolution, stellar duplicity, stellar rotation, differences in chemical composition, dispersion in ages, dispersion in distances, presence of non-member stars and limited precision of data. In the absence of differential extinction (across the field of the cluster), all these various physical and observational phenomena put together appear to produce only a small spread in the CCD. In order to find the amount of this spread in the CCD of this cluster, following Burki (1975), the unreddened curve is shifted on to the observed sequence parallel to the reddening line (Hiltner & Johnson 1956) so as to determine the minimum and

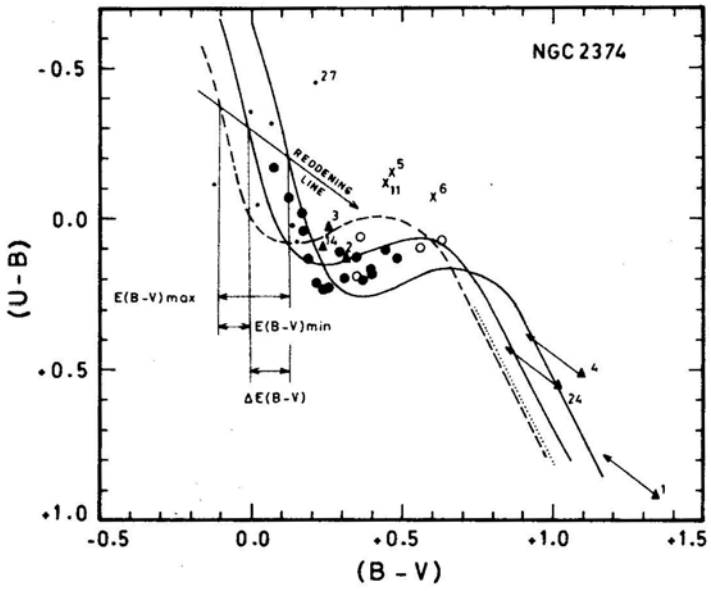

Figure 3. The ($B - V$) versus ($U - B$) diagram of the open cluster NGC 2374. The filled circles, crosses and triangles, respectively, denote the members, nonmembers and doubtful members which are observed photoelectrically. Unfilled circles and small dots indicate the photographically observed members and non-members, respectively. The dashed line is the zero age main sequence (ZAMS) for unreddened stars (Schmidt-Kaler 1965), while the solid lines represent the ZAMS when it is fitted to the observations with maximum and minimum reddening by shifting it parallel to the reddening line (Hiltner & Johnson 1956). The dotted line is the unreddened curve for giants (FitzGerald 1970). The identification numbers of the stars discussed in the text are indicated. Note that the star no. 11 is shown as a nonmember and star nos 1,2, 3,4 and 14 are indicated as doubtful members (see text).

maximum colour excesses as shown in Fig. 3. The difference Δ between $E\ (B\ —V)_{max}$ and $E(B–V)_{min}$ is found to be

$$\Delta E(B-V) = 0.13 \text{ mag.}$$

This value is close to the minimum natural dispersion given by Burki (~ 0.11 mag) and, therefore, indicates an almost non-variable extinction across the field of the cluster. Hence, assuming a uniform extinction, the following mean colour excesses have been adopted.

$$E(B-V) = (B-V)-(B-V)_0$$
$$= \tfrac{1}{2}\left[E(B-V)_{max} + E(B-V)_{min}\right] = 0.175 \text{ mag,}$$

and

$$E(U-B) = (U-B)-(U-B)_0$$
$$= \tfrac{1}{2}\left[E(U-B)_{max} + E(U-B)_{min}\right] = 0.125 \text{ mag.}$$

Earlier, Buscombe (*cf.* Table 1) had given $E(B-V)$ as 0.0 mag.

Using the above-mentioned mean value of $E(B-V)$, the total visual absorption A_υ has been calculated as

$$A_v = V - V_0 = 0.569 \pm 0.009 \text{ mag}$$

from the expression $A_v = R \cdot E(B-V)$, where R is the ratio of total-to-selective absorption, taken to be 3.25 ± 0.05 as suggested by Moffat & Schmidt-Kaler (1976).

A few stars, however, are found to show larger deviations than the general spread. For instance, star nos 5, 6, 11 and 27 indicate some excessive reddening. It is rather peculiar for 5 and 6 to show this type of reddening, when the objective grating observations indicate them to be F stars. However, the photographic measurements of these stars by Fenkart *et al.* (1972) match well with our *UBV* measurements. More detailed spectroscopic observations are needed to understand the nature and membership of these stars better. Nos 1,4 and 24 are at the red end of the curve, away from the rest of the stars.

4. Membership

The observed $(B-V)$ and $(U-B)$ colours are plotted against the corresponding V magnitudes in Figs 4 and 5, respectively. Both figures show fairly well-defined main sequences (MS) formed by a majority of the stars. The respective zero-age main sequence (ZAMS) taken from Schmidt-Kaler (1965) are shifted to match with them. The final cluster membership can now be determined oh the basis of these diagrams, since the extinction has been assumed to be uniform. The location of individual stars in the identification chart (Fig. 1) has been used as an additional criterion.

According to the criteria given by Vogt & Moffat (1972), star nos 5 and 6 are considered as foreground stars, because they appear to be above the MS in one CMD and below it in the other. The same is found by Fenkart *et al.* (1972) for these stars. Star nos 4 and 24, being above the MS in both the CMDs, are possible giant members of the cluster, especially because their brightnesses also appear to be compatible with those of the brightest stars on the MS. A further indication about their likely membership as giants is that when these two stars are dereddened by the amounts of colour excesses obtained for the MS stars, they get much closer to FitzGerald's (1970) unreddened curve for giants, as shown in Fig. 3 by arrows. In this connection, since star no. 1 is seen

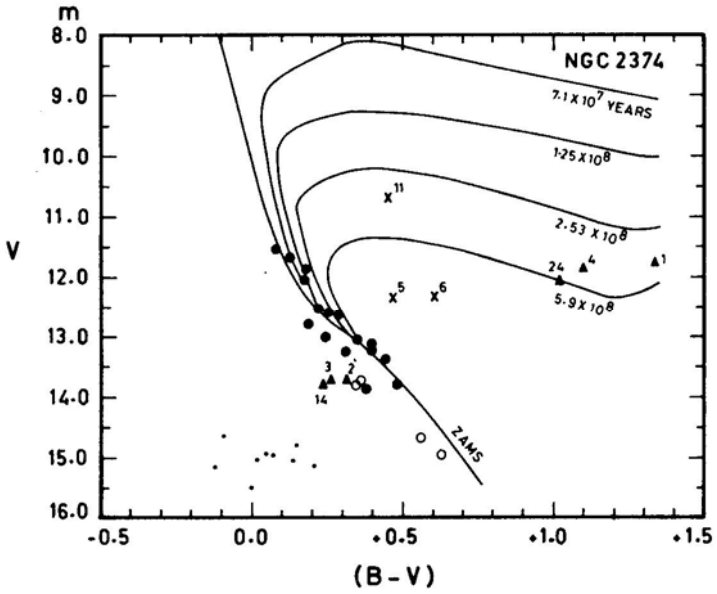

Figure 4. The ($B - V$) versus V diagram of the open cluster NGC 2374. The symbols are the same as in Fig. 3. The solid line is the ZAMS taken from Schmidt-Kaler (1965), but is shifted to match with the observations. The theoretical isochrones are from Barbaro *et al.* (1969). The identification numbers of the stars discussed in the text are indicated.

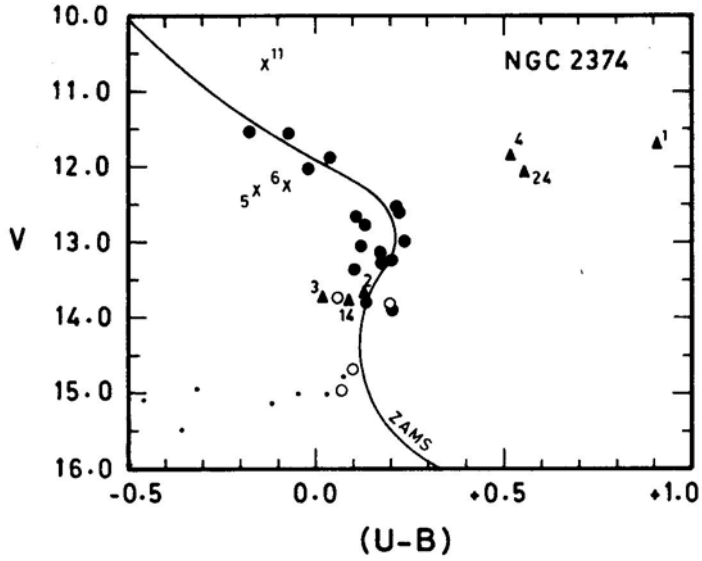

Figure 5. The ($U - B$) versus V diagram of the open cluster NGC 2374. The symbols are the same as in Fig. 3. The solid line is the ZAMS taken from Schmidt-Kaler (1965), shifted to match the observations. The identification numbers of stars discussed in the text are indicated.

closer to star nos 4 and 24 in all the diagrams, it may also be a probable giant member, even though its location is relatively far off from the centre of the cluster (*cf.* Fig. 1).

Star nos 2, 3 and 14 show slight deviations from the ZAMS in Fig. 4 while no. 3 shows it in Fig. 5 as well. However, they show similar colour excesses as those of the MS stars (*cf.* Fig.3).But,while star no. 14 is well inside the physical group of the cluster, star nos 2 and 3 are at the periphery. Therefore, they are considered only as doubtful members, and along with star nos 1, 4 and 24, are denoted by 'm?' in Table 2. Radial velocities and proper motion measurements are required to confirm their membership.

All the stars whose magnitudes are determined by photographic photometry, except star nos 26,29,33 and 37 are considered to be non-members. The reason for this is that seven of them lie below the ZAMS in both CMDs, while the remaining two lie above the ZAMS in one CMD and below it in the other. Thus, they turn out to be background and foreground stars, respectively (*cf.* Vogt & Moffat 1972).

Finally, star no. 11, being the brightest in the physical group, needs special mention. Fig. 2 shows it as a B5 star and its position in that diagram occurs on the extension of the apparent main sequence. However, its position in the CCD shows that it needs a much larger reddening correction (~ 0.60 mag) in ($B - V$) to bring it back into the vicinity of the unreddened curve. Also, its position in Fig. 4 is above the MS, while it is closer to the MS in Fig. 5.Its location is nearer to the periphery than to the centre of the cluster. Thus, all these points make it look more like a reddened, background early-type star than a member of the cluster with some anomalous reddening. Fenkart *et al.* (1972) also have not considered this star as a member.

This brings the total of non-members and doubtful members to eighteen, leaving the other twenty as probable members of the cluster.

5. Distance

The cluster main sequences,composed of the probable members in both the CMDs, are shifted to match with the respective ZAMS. This resulted in a mean true distance modulus of 10.3 ± 0.2 mag, corresponding to a distance to the cluster

$$d = 1.2 \pm 0.1 \text{ kpc}$$

This is in good agreement with the values of distance obtained by Collinder (1931), Fenkart *et al.* (1972) and Buscombe (Lyngå 1980)—*cf.* Table 1.

6. Age

Since no well-evolved stars are seen among the probable members,except for the three doubtful giants, it is not possible to locate the turn-off point on the cluster main sequence in the CMD of Fig. 4. Therefore, the theoretical isochrones given by Barbaro, Dallaporta & Fabris (1969) were superimposed on this figure so as to identify the most likely age of the cluster or at least the upper limit of the age. It is found that the brighter MS stars extend up to the isochrone of 7.1×10^7yr. That is, the age of the cluster could be 7.1×10^7 yr or perhaps somewhat younger. It has also been estimated from $(B - V)_0$ and the spectral type of the brightest star on the MS as 6×10^7 yr and 1×10^8 yr respectively by using the relationships given by Allen (1981) and Hoerner

(1957). This gives a mean value of 8×10^7 yr, which agrees fairly well with the isochrone age of the MS stars. Fenkart *et al.* (1972) estimated the age of this cluster to be 3.5×10^8 yr from the earliest spectral type using Hoerner's (1957) method.

If the three giants are considered as likely members of the cluster, then their apparent fitting to the isochrone of 5.9×10^8 yr might indicate the non-coeval nature of this cluster, as has been shown to be the case in several other open clusters by many previous workers (McNamara 1976; Piskunov 1977; Sagar & Joshi 1979). But the corresponding non-coeval spread by the stars at the turn-off area of the giant-branch isochrone is not found in this diagram.

7. Conclusions

The open cluster NGC 2374 is found to contain at least twenty stars as definite members down to $m_v \simeq 14$ mag. Three of the six doubtful members would be red giants, if they were members. There is a uniform extinction of $E(B - V) = 0.175$ mag due to interstellar matter intervening between the cluster and the observer. The distance of this cluster is found to be 1.2 ±0.1 kpc which places it at the outer edge of the Orion-Cygnus arm in the direction of the Monoceros constellation. The most likely age of this cluster is 7.5×10^7 yr.

Acknowledgements

I am highly grateful to Professor J. C. Bhattacharyya for his guidance and helpful suggestions. My sincere thanks are due to Drs N. Kameswara Rao and R. Rajamohan for many stimulating discussions and useful comments. I wish to thank the referees for their critical comments and very useful suggestions.

References

Allen, C.W. 1981, *Astrophysical Quantities*, 3 edn, Athlone Press, London.
Alter, G., Balazs, B., Ruprecht, J. 1970, *Catalogue of Star Clusters and Associations*, 2nd edn, Akademiai Kiado, Budapest.
Babu, G. S. D. 1983, *J. Astrophys. Astr.*, **4**, 235.
Barbaro, G., Dallaporta, N., Fabris, G. 1969, *Astrophys. Space Sci.*, **3**, 123.
Barhatova, K. A. 1950, *Astr. Zu.*, **27**, 182.
Burki, G. 1975, *Astr. Astrophys.*, **43**, 37.
Collinder, P. 1931, *Ann. Obs. Lund,* **2**, 1.
Fenkart, R. P., Buser, R., Ritter, H., Schmitt, H., Steppe, H., Wagner, R., Weidemann, D. 1972, *Astr. Astrophys. Suppl. Ser.*,**7,** 487.
FitzGerald, M. P. 1970, *Astr. Astrophys.*, **4,** 234.
Hiltner, W. A., Johnson, H. L. 1956, *Astrophys. J.,* **124,** 367.
Landolt, A. U. 1973, *Astr. J.*, **78,** 959.
Lyngå, G. 1980, *A Computer Readable Catalogue of Open Cluster Data*, Stellar Data Centre, Observatoire de Strasbourg, France.
McNamara, B. J. 1976, *Astr. J.*, **81,** 845.
Moffat, A. F. J., Schmidt-Kaler, Th. 1976, *Astr. Astrophys.*, **48,** 115.
Piskunov, A. Eh. 1977, *Nauchn. Inf.*, **37**, 31.
Ruprecht, J. 1966, *Bull. Astr. Inst. Csl.*, **17**, 33.

Sagar, R., Joshi, U. C. 1979, *Astrophys. Space Sci*., **66,** 3.
Schmidt-Kaler, Th. 1965, in *Landolt-Börnstein, Numerical Data and Functional Relationships* in Science and Technology, Group VI, Vol. 1, ed. H. H. Voigt, p. 284.
Trumpler, R. J. 1930, *Lick Obs. Bull.,* **14,**171.
Vogt, N., Moffat, A. F. J. 1972, *Astr. Astrophys. Suppl. Ser*., **7,** 133.
von Hoerner, S. 1957, *Z. Astrophys*., **42,** 273.

J. Astrophys. Astr.(1985) **6,** 71–73

Spectroscopic Binaries near the North Galactic Pole
Paper 11: HD 105982

R. F. Griffin *The Observatories, Madingley Road, Cambridge, England CB3 0HA*

Received 1985 January 4; accepted 1985 January 16

Abstract. Photoelectric radial-velocity measurements show that HD 105982 is a spectroscopic binary with a period of 3.7 years.

Key words: radial velocities—spectroscopic binaries—stars, individual

HD 105982 is near the western margin of the field covered by the Cambridge Galactic-Pole radial-velocity survey ($b > 75°$): it is about 9° north-following β Leo. It is almost bright enough to qualify for an entry in the Bright Star Catalogue, and does in fact feature in the recent Supplement (Hoffleit *et al.* 1983). The magnitudes quoted there, $V = 6.71$ and $(B–V) = 1.04$, are taken from photometry obtained at Uppsala by Häggkvist & Oja (1973). The only spectral type available is the K2 given in the Henry Draper Catalogue (Cannon & Pickering 1920). Unpublished photometry in the Copenhagen system obtained at Palomar Observatory by Dr G. A. Radford and the author and reduced by L. Hansen shows that the object is a giant and that it exhibits no hint of photometric compositeness. Rather surprisingly, the *Supplement to the Bright Star Catalogue* does not record the star's radial velocity: two measurements taken less than 48 hours apart were published by Chériguene (1971) and are listed below at the head of Table 1.

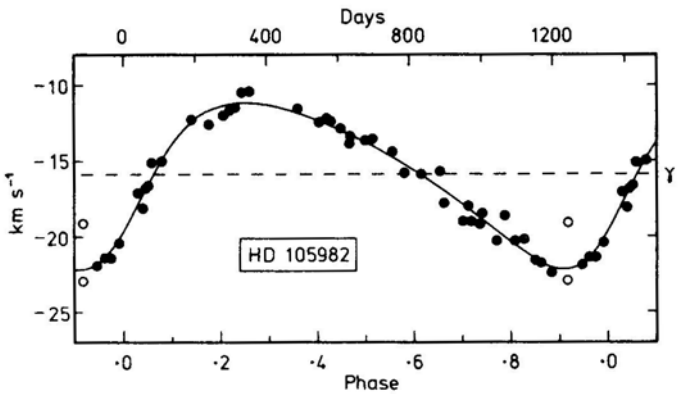

Figure 1. The computed radial-velocity curve of HD 105982, with the measured radial velocities plotted. Photoelectric observations are represented by filled circles; the two photographic velocities (Chériguene 1971), which were not used in the orbital solution, are plotted as open circles.

Table 1. Radial-velocity measurements of HD 105982.

Date	MJD	Velocity km s^{-1}	Phase	$(O–C)$ km s^{-1}
1968 Dec 30.19*	40220.19	0.916	−22.9	−0.7
1969 Jan 1.09*	40222.09	0.917	−19.1	+3.1
1973 Mar 16.00†	41757.00	2.050	−16.6	−0.1
1976 Mar 2.98	42839.98	2.850	−21.6	−0.1
1977 Mar 31.03	43233.03	3.140	−12.3	+0.2
July 15.89	339.89	0.219	−11.7	−0.4
1978 Jan 23.13	43531.13	3.360	−11.6	+0.3
Mar 24.06	591.06	0.404	−12.5	−0.1
Apr 15.05	613.05	0.420	−12.2	+0.4
May 23.19‡	651.19	0.449	−12.9	+0.1
June 18.92	677.92	0.468	−13.4	−0.1
Nov 16.23	828.23	0.579	−15.8	−0.6
1979 Jan 3.21	43876.21	3.615	−15.9	0.0
Feb 25.12	929.12	0.654	−15.7	+1.1
Mar 8.07	940.07	0.662	−17.8	−0.8
Apr 28.95	991.95	0.700	−19.0	−1.1
May 13.94	44006.94	0.711	−18.0	+0.1
June 14.90	038.90	0.735	−19.2	−0.5
Dec 4.22	211.22	0.862	−21.8	0.0
1980 Jan 2.19	44240.19	3.883	−22.4	−0.3
May 3.95	362.95	0.974	−21.4	−0.4
1981 Feb 2.11	44637.11	4.176	−12.6	−0.9
Mar 13.10	676.10	0.205	−12.0	−0.6
Apr 14.97	708.97	0.229	−11.5	−0.3
May 2.95	726.95	0.243	−10.5	+0.7
24.98	748.98	0.259	−10.4	+0.8
1982 Jan 10.15	44979.15	4.429	−12.4	+0.3
Mar 2.07	45030.07	0.467	−13.9	−0.6
Apr 14.96	073.96	0.499	−13.7	+0.1
May 7.02	096.02	0.515	−13.6	+0.4
June 29.91	149.91	0.555	−14.4	+0.4
1983 Feb 4.52§	45369.52	4.717	−19.0	−0.7
Mar 7.06	400.06	0.740	−18.5	+0.3
Apr 15.89	439.89	0.769	−20.3	−0.7
May 9.89	463.89	0.787	−18.6	+1.4
June 6.90	491.90	0.807	−20.3	+0.3
July 2.91	517.91	0.827	−20.2	+0.8
Dec 11.19	679.19	0.946	−21.9	0.0
1984 Jan 2.19	45701.19	4.962	−21.4	0.0
Feb 9.11	739.11	0.990	−20.4	−0.2
Apr 2.04	792.04	5.029	−17.1	+0.8
15.96	805.96	0.039	−18.1	−0.9
23.94	813.94	0.045	−16.8	+0.1
May 10.93	830.93	0.058	−15.1	+1.0
June 8.91	859.91	0.079	−15.0	−0.1

* Photographic observation by Chériguene (1971). Not used in the orbital solution.

† Observed by Dr G. A. Radford with the Cambridge spectrometer.

‡ Observed, in collaboration with Dr J. E. Gunn, with the 200inch telescope (Griffin & Gunn 1974).

§ Observed with the Dominion Astrophysical Observatory 48-inch telescope (Fletcher *et al* 1982).

A discordance of 5 km s^{-1} between the first two photoelectric radial-velocity measurements showed in 1976 that HD 105982 is a spectroscopic binary; since then it has been watched systematically, and the 43 velocities shown in Table 1 (and made in Cambridge by the author (Griffin 1967) except where noted) have been accumulated. They provide the orbit which is shown in Fig. 1 and whose elements are:

$P = 1355 \pm 5$ days
$\gamma = -15.85 \pm 0.10$ km s^{-1}
$K = 5.52 \pm 0.16$ km s^{-1}
$e = 0.297 \pm 0.025$
$\omega = 238 \pm 5$ degrees
$(T)_4 =$ MJD 44398 ± 16
$a_1 \sin i = 98 \pm 3$ Gm
$f(m) = 0.0206 \pm 0.0018\ M_\odot$
rms residual $= 0.6$ km s^{-1}

References

Cannon, A. J., Pickering, E. C. 1920, *Ann. Harv. Coll. Obs.,* **95,** 26.
Chériguene, M. F. 1971, *Astr. Astrophys*., **13,** 447.
Fletcher, J. M., Harris, H. C, McClure, R. D., Scarfe., C. D. 1982, *Publ. astr. Soc. Pacific*, **94,**1017.
Griffin, R. F. 1967, *Astrophys. J*., **148,** 465.
Griffin, R. F., Gunn, J. E. 1974, *Astrophys. J.*, **191,** 545.
Häggkvist, L., Oja, T. 1973, *Astr. Astrophys. Suppl*., **12,** 381.
Hoffleit, D., Saladyga, M., Wlasuk, P. 1983, *A Supplement to the Bright Star Catalogue*, Yale University Observatory, New Haven.

J. Astrophys. Astr. (1985) **6,** 75

Corrigendum

Nonconservation of Baryons in Cosmology—Revisited

Narlikar, J. V. 1984, *J. Astrophys. Astr*., **5,** 67–78.

The adjective ‘late’ appearing before the name of M. H. L. Pryce in the last line of p. 68 in the above paper is regretted. The author is happy to learn that Dr M. H. L. Pryce is alive and well and is at present Honorary Professor in the Department of Physics and Astronomy in the University of British Columbia, Vancouver, Canada. This note records the author’s apology to Professor Pryce.

J. Astrophys. Astr. (1985) **6**, 77–83

Spectroscopic Binaries near the North Galactic Pole
Paper 12:6 Boötis

R. F. Griffin *The Observatories, Madingley Road, Cambridge, England CB30HA*

Received 1984 October 29; accepted 1985 January 28

Abstract. Photoelectric radial-velocity measurements show that 6 Boötis undergoes small periodic variations of velocity. An orbit with a 2.6-year period and a semi-amplitude of little more than 1 km s^{-1} is derived. The amplitude is smaller by a factor of two than that of any plausible orbit previously derived from radial velocities.

Key words: radial velocities—spectroscopic binaries—stars, individual

It is obvious from the frequent occurrence of wide visual binaries—and still more so from that of common-proper-motion pairs—that there must be many binary systems whose radial-velocity amplitudes are so small as to be undetectable with presently available instruments. The wide binaries generally have periods to be reckoned in centuries or millenia rather than in days or years; it is, perhaps, less clear that there is a large class of binaries having relatively short periods and very small amplitudes. However, indications that the frequency of such systems is substantial may be seen in analyses of the characteristics of the many spectroscopic binaries whose orbits have been determined photo electrically in recent years (Griffin 1983b, 1985).

The actual identification of binaries whose velocity fluctuations are scarcely greater than the measuring error is not an easy task. It is a matter of common experience in (for example) stellar photometry, as well as in radial-velocity measurement, that the scatter of the measured quantity is greater for some objects than for other, apparently similar, ones. Statistical tests may be used to indicate whether the differences are significant, but they provide no indication of *what* the significance may be of any variability that is thereby established. Until much more is known about the nature, sizes and distribution of convective cells in late-type stellar atmospheres, one cannot be sure that a statistically verified radial-velocity 'noise' has any relevance to the motion of the star as a whole. The only recourse is to make sufficiently numerous and frequent observations to determine the periodicity (if any) of the variability. No doubt the intelligent application of Fourier techniques would be claimed to permit the identification of periodicities with almost arbitrarily small amplitudes; but in a more conservative approach, in which one requires the periodicity to be discernible when the data are plotted directly against time, the lower limit to the amplitudes admissible as real is probably about equal to the standard deviation of an individual measurement. To approach such a limit would necessitate a very large number of measurements; in the present paper an amplitude of about twice the measuring error is discovered from a set of some 50 observations.

It has been remarked elsewhere (Griffin 1983a) that there are in the literature orbits with very small amplitudes but doubtful authenticity; perhaps the most remarkable is

Table 1. Radial-velocity measurements of 6 Boötis.

Date	MJD	Velocity km s^{-1}	Phase	$(O-C)$ km s^{-1}
1918 June 17.23*	21761.23	−3.1	19.713	0.0
1919 Mar 31.49*	22048.49	−5.0	$\overline{18}$.017	−4.0
Apr 3.48*	051.48	−0.5	.021	+0.5
1921 Mar 24.48†	22772.48	−0.5	$\overline{18}$.785	+2.3
1922 Mar 13.41†	23126.41	+0.6	$\overline{17}$.160	+3.0
13.52*	126.52	−1.8	.160	+0.6
1966 Apr 14.01	39229.01	−2.8	0.221	0.0
24.04	239.04	−5.1:	.232	−2.2
25.01	240.01	−2.3	.233	+0.6
May 15.96	260.96	−3.0	.255	0.0
16.96	261.96	−2.5	.256	+0.5
1973 Mar 31.20‡	41772.20	−0.9	2.916	+0.8
May 11.13‡	813.13	−2.2	.959	−1.0
June 13.15§	846.15	−1.0	.994	0.0
1974 Mar 2.24‡	42108.24	−3.0	3.272	0.0
May 2.05‡	169.05	−4.6	.336	−1.4
8.11‡	175.11	−2.8	.343	+0.4
21.04‡	188.04	−2.2	.357	+1.0
1977 Feb 4.20	43178.20	−3.2	4.406	+0.1
Mar 31.14	233.14	−3.0	.464	+0.3
Apr 26.99	259.99	−3.5	.492	−0.2
May 28.92	291.92	−3.9	.526	−0.6
1978 Jan 13.19	43521.19	−2.9	4.769	0.0
Mar 26.07	593.07	−2.7	.845	−0.3
June 20.92	679.92	−1.1	.937	+0.4
Aug 18.85	738.85	−0.2	5.000	+0.7
1979 Jan 3.30	43876.30	−2.2	5.145	+0.1
Feb 25.19	929.19	−2.7	.201	0.0
Mar 12.10	944.10	−2.9	.217	−0.1
Apr 25.05	988.05	−2.7	.264	+0.3
May 13.99	44006.99	−2.0	.284	+1.0
June 22.96	046.96	−2.7	.326	+0.5
Dec 25.27	232.27	−2.3	.523	+1.0
1980 Jan 24.26	44262.26	−3.6	5.554	−0.3
Feb 23.18	292.18	−3.7	.586	−0.4
Mar 9.12	307.12	−3.7	.602	−0.4
May 3.99	362.99	−3.3	.661	−0.1
July 22.89	442.89	−3.1	.746	−0.1
Dec 7.26	580.26	−2.3	.891	−0.3
1981 Jan 17.26	44621.26	−1.9	5.935	−0.4
Mar 1.16	664.16	−1.0	.980	0.0
Apr 18.03	712.03	−1.4	6.031	−0.3
May 2.97	726.97	−1.0	.047	+0.2
31.97	755.97	−2.2	.077	−0.6
June 28.90	783.90	−1.0	.107	+1.0
July 26.88	811.88	−3.6	.137	−1.4
Aug 16.85	832.85	−2.3	.159	+0.1

Table 1. Continued.

Date			MJD	Velocity km s^{-1}	Phase	$(O-C)$ km s^{-1}
1982	Jan	10.25	44979.25	−3.5	6.314	−0.4
	Mar	4.14	45032.14	−3.5	.370	−0.3
		5.12	033.12	−4.1	.371	−0.9
	Apr	15.04	074.04	−2.6	.414	+0.7
	May	23.96	112.96	−3.1	.456	+0.2
1983	Feb	4.57¶	45369.57	−3.0	6.728	0.0
	Mar	15.14	408.14	−3.0	.768	−0.1
	May	9.97	463.97	−2.1	.828	+0.5
	June	6.95	491.95	−2.2	.857	+0.2
	Dec	11.27	679.27	−1.7	7.056	−0.4
1984	Jan	2.26	45701.26	−1.0	7.079	+0.6
	Apr	2.05	792.05	−2.1	.175	+0.4
		14.05	804.05	−2.9	.188	−0.3
	May	11.93	831.93	−3.0	.217	−0.2
	July	11.89	892.89	−3.4	.282	−0.4

* Lick Observatory photographic observation (Campbell & Moore 1928), not used in orbital solution.

† Mount Wilson Observatory photographic observation (Adams *et al.,* 1929; Abt 1973), not used in orbital solution.

‡ Observed at Cambridge by Dr G. A. Radford.

§ Observed, in collaboration with Dr J. E. Gunn, with the 200 inch telescope (Griffin & Gunn 1974).

¶ Observed with the Dominion Astrophysical Observatory 48-inch telescope (Fletcher *et al.,* 1982).

the orbit (Schaub 1932) with an amplitude K = 0.24 km s^{-1} for the IAU radial-velocity standard α Ari (Pearce 1955). Dworetsky (1983) has identified the orbit given by Aikman (1976) for ϕ Her, with K = 2.39 ± 0.12 km s^{-1}, as the smallest-amplitude reliable orbit derived solely from radial-velocity measurements.

6 Boo is the ninth-brightest of the stars which qualify, by having $b > 75°$ and HD types of G5 or later, for inclusion in the Cambridge radial-velocity survey of the North Galactic Pole field. Its magnitude and colours have been determined on the *UBV* system by Argue (1963), Häggkvist & Oja (1966) and Eggen (1966, 1973), with mean results of V = 4.91, $(B - V)$ = 1.43, $(U - B)$ = 1.65; $(R - I)$ has been found to be near 0.75 by Jacobsen (1970) and Hansen & Kjaergaard (1971). The MK type has been classified as K4 III by Roman (1952), who gave the corresponding absolute magnitude as –0.1. Other absolute-magnitude estimates are + 0.6 (Rimmer 1925) and + 0.3 (Adams *et al.,* 1935) from spectroscopy, +0.2 (Hansen & Kjaergaard 1971) from narrow-band photometry, and + 0.7 (Wilson 1976) from the *K*-line width.

Four measurements of the radial velocity of 6 Boo were made long ago at the Lick Observatory (Campbell & Moore 1928), and two at Mount Wilson (Adams *et al.,* 1929; Abt 1973). They are listed at the head of Table 1 after adjustment by + 0.8 km s^{-1} (Griffin & Herbig 1981). 6 Boo was one of the stars observed in early tests of the photoelectric radial-velocity method at Cambridge, and four measures made in those tests were published then (Griffin 1967). A fifth observation was not published at the time, as it was made on a night other than the five which featured in the paper—only

nights on which a substantial number of observations was made were included. The mean of the five 1966 velocities is 2.9 km s^{-1}.

In 1973 6 Boo was reobserved in the course of the North Galactic Pole programme: two measurements by Dr G. A. Radford with the Cambridge spectrometer and one by Dr J. E. Gunn and the author at Palomar gave a mean of –1.4 km s^{-1} . The discrepancy was just enough to arouse some misgivings, so the star was measured again in 1974; four Cambridge observations by Radford in that year yielded a mean of – 3.2 km s^{-1} Irritated by the uncertainty as to whether or not there really were changes in the radial velocity, the author placed 6 Boo on the Cambridge spectroscopic-binary observing programme in 1977, and has since observed it fairly systematically. The velocity has normally been close to – 3 km s^{-1} but there were distinct indications of a rise to about – 1 km s^{-1} in 1978 and very definite evidence of another in 1981. At that point a periodicity of slightly under 1000 days became apparent, and an orbital solution was obtained; the variability of the velocity was announced, albeit in a very oblique fashion, by Griffin & Herbig [1981 (footnote on p. 42)].

Since the acid test of a preliminary orbit is its predictive power, it was resolved to watch 6 Boo for another cycle and to see whether the velocity maximum predicted for late 1983 actually occurred. In fact it did—although adverse weather and other circumstances conspired to prevent coverage of it being as detailed as one would have wished. There are now 56 photoelectric radial velocities available altogether, and they are set out in Table 1. In Fig. 1 all the measurements made from 1973 onwards are plotted directly against time; the figure is intended to convince the reader that 6 Boo does vary in velocity and that the period of nearly 1000 days is visible immediately in the data.

An anonymous referee has kindly proposed that the fact of velocity variation might be proved by the method suggested by Schlesinger (1915). Schlesinger pointed out that a histogram representing the distribution of observations as a function of radial velocity allows a distinction to be drawn between a spread caused mainly by orbital motion and one arising from observational error. Radial velocities measured for a star in a near-circular orbit are preferentially clustered around the turning points (nodes) of the orbit and therefore form a bimodal distribution, easily distinguished from the *error* distribution obtained for a non-variable object.

Unfortunately the data in Table 1 do not pass Schlesinger's test with much conviction: the measuring error is so nearly comparable with the amplitude of the

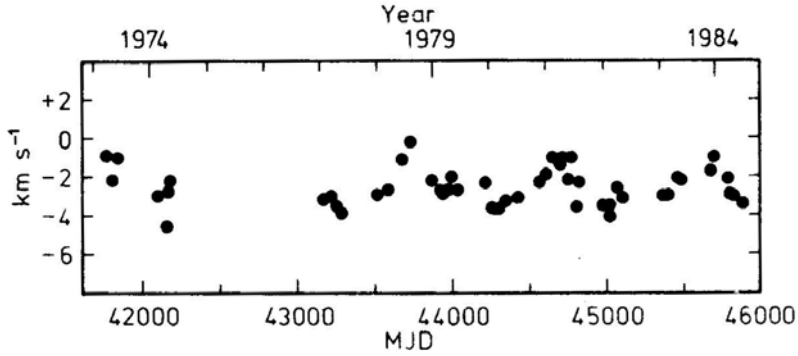

Figure 1. Photoelectric radial velocities of 6 Boo plotted directly against time for the interval 19731984. The periodicity of nearly 1000 days is apparent.

Velocity variation of 6 Boo that the depression in the middle of the bimodal distribution is filled in, whereas in Schlesinger's examples the amplitude of variation is many times the standard error of the observations. Moreover, for an orbit of appreciable eccentricity the height of one of the two maxima is reduced, as Schlesinger himself remarked. In the present case the asymmetry of the maxima, coupled with the blurring caused by the measuring errors, results in a distribution of velocities showing simply a broad and skew single maximum. The exact shape of the distribution depends considerably upon the width and centring chosen for the velocity 'bins' in the histogram. One cannot divide 50-odd observations into very many bins without the population of individual bins becoming too small. To show a velocity histogram here would be to invite at least one of the criticisms that (a) its fairly convincing appearance is due entirely to a skilful choice of bins, and (b) its unconvincing appearance is due to an *un*skilful choice. We therefore refrain from publishing a histogram, but hope instead to provide proof of velocity variation by the statistical discussion below. The principles of the discussion follow those of Bassett's (1978) statistic T_2 for distinguishing between circular and elliptical binary orbits.

The sum of the squares of the residuals from the orbit adopted below is 18.27 (km s^{-1}) ^{2}. That figure is obtained by fitting 6 orbital elements to the set of 56 photoelectric radial velocities, so the number of degrees of freedom is 50. If, instead of accepting the orbit, we make the hypothesis that there is no real change in the velocity of 6 Boo, so all of the scatter in the velocities is attributed to observational error, we obtain a sum of squares of 49.70 (km s^{-1})^2 about a mean velocity of –2.58 km s^{-1}. Here we have fitted just a single parameter (the mean), so the number of degrees of freedom is 55. Fitting the orbit, therefore, brings about a reduction of 31.43 (km s^{-1})^2 in the sum of squares at a cost of the loss of an extra five degrees of freedom, *i.e.* it is associated with a variance estimate of 6.29 (km s^{-1})^2 per degree of freedom. The remaining scatter leads to a variance estimate of 18.27/50, or 0.365, (km s^{-1})^2 per degree of freedom. The ratio of variance estimates is 6.29/0.365, or about 17.2, and its significance can be established by reference to tables of the F-distribution with 5 and 50 degrees of freedom. The ratio $F = 17.2$ is very significant indeed: the 1 per cent point of the F distribution is reached at $F = 3.4$ and the 0.1 per cent point at 4.9. Thus the hypothesis that there is no real change in the radial velocity of 6 Boo is very firmly rejected.

It remains, then, only to give the orbital solution, which is shown in Fig. 2 and has elements as follows:

$P = 944 \pm 8$ days $\qquad (T)_5 = \text{MJD } 44739 \pm 31$

$\gamma = -2.63 \pm 0.09$ km s^{-1} $\qquad a_1 \sin i = 14.1 \pm 1.9$ Gm

$K = 1.19 \pm 0.15$ km s^{-1} $\qquad f(m) = 0.00013 \pm 0.00005\ M_\odot$

$e = 0.41 \pm 0.09$

$\omega = 359 \pm 15$ degrees $\qquad$ rms residual $= 0.6$ km s^{-1}

Despite its small amplitude (a full factor of two less than the previous smallest), this orbit seems quite secure: the amplitude is eight times its own standard deviation, and twice the standard deviation of an individual measurement of the radial velocity. This is about as far as the present author cares to venture in the documentation of orbits of low amplitudes from data of the quality and quantity used here. However, it is quite possible to go further with the aid of more accurate and/or more intensive

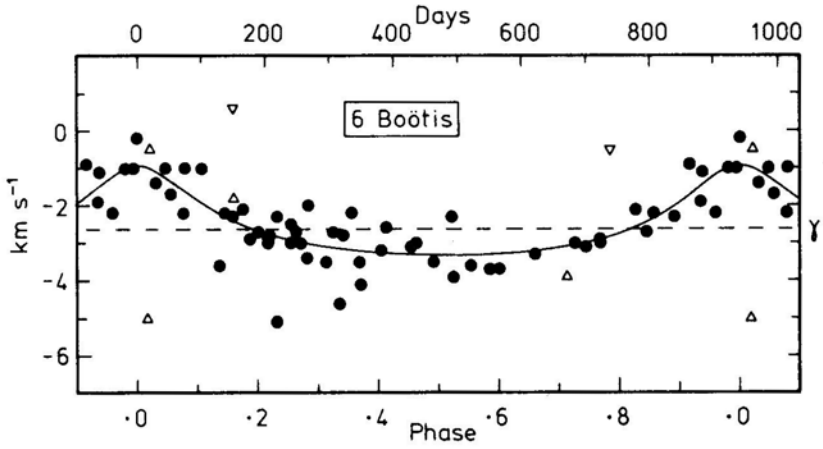

Figure 2. The computed radial-velocity curve of 6 Boo, with the measured radial velocities plotted. Photoelectric observations are represented by filled circles; photographic results, which were not used in the solution of the orbit, appear as open triangles, vertices up for Lick Observatory and vertices down for Mount Wilson.

observations, and cases of apparent orbital motion with $K < 1$ km s^{-1} are already known although not yet ripe for publication.

The astronomical significance of an isolated case of a spectroscopic binary with a very small amplitude is nil, since the low amplitude of any particular system may arise through our viewing the system from very nearly the pole of the orbit; but if—as seems very probable—small amplitudes are commonplace, the conclusion must be that many stars are accompanied by companions of small mass. For giant stars such as 6 Boo, whose masses may be in the range 1–3 $M_\odot$, to have mass functions of the order of 10^{-4} $M_\odot$ implies that the masses of the secondary stars are typically 0.1 $M_\odot$. That mass is indicative of very late-type stars: Allen (1973) attributes it to type M8 V. In terms of luminosity, the components of a K-giant/M8 V binary differ by a factor of a million. Such systems, therefore, are very different from those observable directly as visual binaries. If they prove to be numerous, then the theoretical mechanisms for the formation of binary stars will need to include processes readily permitting the creation of systems in which the masses of the components are very disparate.

Acknowledgement

It is my pleasure to thank Dr E. E. Bassett for checking the statistical discussion in this paper.

References

Abt, H. A, 1973, *Astrophys. J. Suppl.,* **26**, 365.
Adams, W. S., Joy, A. H., Sanford, R. F., Strömberg, G. 1929, *Astrophys. J.,* **70,** 207.
Adams, W. S., Joy, A. H., Humason, M. L, Brayton, A. M. 1935, *Astrophys. J.,* **81**, 187.

Aikman, G. C. L. 1976, *Pub. Dom. astrophys. Obs.,* Victoria, **14**, 379.
Allen, C. W. 1973, *Astrophysical Quantities,* Athlone Press, London, p. 209.
Argue, A. N. 1963, *Mon. Not. R. astr. Soc,* **125**, 557.
Bassett, E. E. 1978, *Observatory,* **98**, 122.
Campbell, W. W., Moore, J. H. 1928, *Publ. Lick Obs.,* **16**, 202.
Dworetsky, M. M. 1983, *Observatory,* **103**, 205.
Eggen, O. J. 1966, *R. Obs. Bull.,* no. 125.
Eggen, O. J. 1973, *Publ. astr. Soc. Pacific,* **85**, 542.
Fletcher, J.M., Harris, H.C., McClure, R. D., Scarfe, C.D.1982, *Publ. astr. Soc. Pacific,* **94**,1017.
Griffin, R. F. 1967, *Astrophys. J.,* **148**, 465.
Griffin, R. F. 1983a, *Observatory,* **103**, 17.
Griffin, R. F. 1983b, *Observatory,* **103**, 273.
Griffin, R. F.1985, in *Proc. NATO Advanced Study Institute on Interacting Binary Stars,* Eds P. P. Eggleton & J. E. Pringle, D. Reidel, Dordrecht, p. 1.
Griffin, R. F., Gunn, J. E. 1974, *Astrophys. J.,* **191**, 545.
Griffin, R. F., Herbig, G. H. 1981, *Mon. Not. R. astr. Soc,* **196**, 33.
Häggkvist, L., Oja, T. 1966, *Ark. Astr.,* **4***,* 137.
Hansen, L., Kjsergaard, P. 1971, *Astr. Astrophys.,* **15**, 123.
Jacobsen, P.-U. 1970, *Astr. Astrophys.,* **4**, 302.
Pearce, J. A. 1955, *Trans, int. astr. Un.,* **9**, 441.
Rimmer, W. B. 1925, *Mem. R. astr. Soc,* **64**, 1.
Roman, N. G. 1952, *Astrophys. J.,* **116,** 122.
Schaub**,** W. 1932, *Z. Astrophys.,* **4**, 35.
Schlesinger, F. 1915, *Astrophys. J.,* **41,** 162.
Wilson, O. C. 1976, *Astrophys. J.,* 2**05**, 823.

J. Astrophys. Astr. (1985) **6**, 85 –100

Energetics of the Kerr-Newman Black Hole by the Penrose Process

Manjiri Bhat, Sanjeev Dhurandhar & Naresh Dadhich
Department of Mathematics, University of Poona, Pune 411 007

Received 1984 September 20; accepted 1985 January 10

Abstract. We have studied in detail the energetics of Kerr–Newman black hole by the Penrose process using charged particles. It turns out that the presence of electromagnetic field offers very favourable conditions for energy extraction by allowing for a region with enlarged negative energy states much beyond $r = 2M$, and higher negative values for energy. However, when uncharged particles are involved, the efficiency of the process (defined as the gain in energy/input energy) gets reduced by the presence of charge on the black hole in comparison with the maximum efficiency limit of 20.7 per cent for the Kerr black hole. This fact is overwhelmingly compensated when charged particles are involved as there exists virtually no upper bound on the efficiency. A specific example of over 100 per cent efficiency is given.

Key words: black hole energetics—Kerr-Newman black hole—Penrose process—energy extraction

1. Introduction

The problem of powering active galactic nuclei, X-raybinaries and quasars is one of the most important problems today in high energy astrophysics. Several mechanisms have been proposed by various authors (Abramowicz, Calvani & Nobili 1983; Rees *et al.,* 1982; Koztowski, Jaroszynski & Abramowicz 1978; Shakura & Sunyaev 1973; for an excellent review see Pringle 1981). Rees *et al.* (1982) argue that the electromagnetic extraction of black hole's rotational energy can be achieved by appropriately putting charged particles in negative energy orbits. Blandford & Znajek (1977) have also proposed an interesting mechanism by considering the electron-positron pair production in the vicinity of a rotating black hole sitting in a strong magnetic field. It is, therefore, important to study the energetics of a black hole in electromagnetic field.

An ingenious and novel suggestion was proposed by Penrose (1969) for the extraction of energy from a rotating black hole. It is termed as the Penrose process and is based on the existence of negative energy orbits in the ergosphere, the region bounded by the horizon and the static surface (Vishveshwara 1968). Though there does not exist an ergosphere for the Reissner-Nordstrϕm black hole, there do exist negative energy states for charged particles (Denardo & Ruffini 1973), which means that the electromagnetic energy can also be extracted by the Penrose process.

Though Penrose (1969) did not consider astrophysical applications of the process, Wheeler (1971) and others proposed that it could provide a viable mechanism for high energy jets emanating from active galactic nuclei. The mechanism envisaged a star-like

body which on grazing a supermassive black hole breaks up into fragments due to enormous tidal forces (Mashhoon 1973; Fishbone 1973). Some fragments may have negative energy orbits and they fall into the black hole resulting in reduction of its rotational energy while the others come out with very high velocities to form a jet. However, this process fell out of favour for its astrophysical applications owing to limits on the relative velocity between the fragments (Bardeen, Press & Teukolsky 1972; Wald 1974): No significant gain in energy results for an astrophysically reasonable orbit of an incident star unless the splitup itself is relativistic, *i.e.* relative velocity between the fragments $\geqslant 1/2$. Very recently, Wagh, Dhurandhar & Dadhich (1985) have shown that these limits can be removed with the introduction of an electromagnetic field around the black hole. The electromagnetic binding energy offers an additional parameter which is responsible for removal of the limits. Thus the Penrose process is revived as a mechanism for high energy sources.

In this paper we wish to study the negative energy states for charged particles in the Kerr-Newman spacetime with a view to extracting energy by the Penrose process. A comparative analysis of negative energy states for charged particles in the Kerr-Newman field and for a Kerr black hole in a dipole magnetic field is done by Prasanna (1983). We study the negative energy states in a greater detail, and set up a Penrose process for energy extraction and also examine its efficiency in this case. It is known (Chandrasekhar 1983) that the maximum efficiency of this process is 20.7 per cent in the case of a Kerr black hole. The presence of charge on the Kerr-Newman black hole decreases the efficiency further when uncharged particles participate in the process while the efficiency is enormously enhanced (as high as over 100 per cent, in fact there is no limit!) when charged particles are involved.

Astrophysically massive bodies are not known to have significant charge on them $[Q/(\sqrt{G}M) \ll 1]$. That means the charge Q on the black hole should be taken as very small. But a small, nonzero Q can have appreciable effect on the test charge orbits due to the Lorentzian force. It is the Coulombic binding energy that contributes significantly to the energy of the test particle. It is not unjustified, therefore, to study the Penrose process with this assumption.

In Section 2, we establish the equations of motion and the effective potential for charged particles in the Kerr-Newman field while in Section 3 the negative energy states are examined. Section 4 deals with the setting up of an energy extraction process and finally in Section 5 we investigate the efficiency of the process.

2. The Kerr-Newman field

The Kerr-Newman spacetime in the BoyerLindquist coordinates is described by the metric

$$\begin{aligned} ds^2 = & -(\Delta/\rho^2)(dt - a\sin\theta d\phi)^2 + (\rho^2/\Delta)dr^2 + \rho^2 d\theta^2 \\ & + (\sin^2\theta/\rho^2)\left[(r^2+a^2)d\phi - a dt\right]^2 \end{aligned} \tag{2.1}$$

where

$$\Delta = r^2 + a^2 - 2mr + Q^2$$

$$\rho^2 = r^2 + a^2\cos^2\theta.$$

Here m is the mass, a is the angular momentum per unit mass and Q is the charge on

the black hole. We have used the geometrised units (c = 1, G = 1). The event horizon is given by the larger root r_+ of $\Delta = 0$, $r_+ = M + (M^2 - a^2 - Q^2)^{1/2}$.

In this spacetime there exists an electromagnetic field due to the presence of charge Q. This field is obtained from the vector potential A_i,

$$A_i = (-Qr/\rho^2, 0, 0, aQr \sin^2\theta/\rho^2). \tag{2.2}$$

That means the rotation of the black hole also gives rise to a magnetic dipole potential in addition to the usual electrostatic potential.

2.1 *The Equations of Motion*

Let a test particle of rest mass μ and electric charge e move in the exterior field of the black hole. Its motion will be governed by the gravitational field of a charged rotating black hole as well as by the Lorentz force due to electromagnetic interaction. The equations of motion of the particle can be derived either from the Lagrangian $\mathscr{L}$

$$\mathscr{L} = \frac{\mu}{2} g_{ij} \dot{x}^i \dot{x}^j + e A_i \dot{x}^i \tag{2.3}$$

or from the Hamiltonian H,

$$H = \tfrac{1}{2} g^{ij} p_i p_j \tag{2.4}$$

where a dot denotes derivative with respect to the affine parameter τ/μ (τ being the proper time) and p_i is 4-momentum of the particle. Since the metric and the electromagnetic field are time independent and axially symmetric, the energy and the φcomponent of the angular momentum will be conserved yielding two constants of motion. Carter (1968) showed that the HamiltonJacobi equation is separable in this system giving the constant related to the θ-motion of the particle. It is known as the Carter constant (Misner, Thorne & Wheeler 1973, hereinafter MTW). Hence all the four first integrals are obtained as the rest mass of the particle is also a constant of motion which gives the remaining integral.

From Equation (2.3) we have

$$\frac{\partial \mathscr{L}}{\partial \dot{t}} = p_t + e A_t = -\mu E \tag{2.5}$$

$$\frac{\partial \mathscr{L}}{\partial \dot{\phi}} = p_\phi + e A_\phi = \mu L \tag{2.6}$$

where E and L are the energy and the ϕ-component of the angular momentum per unit rest mass of the particle as measured by an observer at infinity.

The rest mass μ of the particle gives another first integral

$$-\mu^2 = g^{ij} p_i p_j. \tag{2.7}$$

Now, on substituting Equations (2.5) and (2.6) in (2.7) we obtain

$$\begin{aligned} g_{\phi\phi}(E + eA_t)^2 + 2g_{t\phi}(E + eA_t)(L - eA_\phi) + g_{tt}(L - eA_\phi)^2 \\ + \psi\,(g^{rr} p_r^2 + g^{\theta\theta} p_\theta^2 + \mu^2) = 0, \end{aligned} \tag{2.8}$$

Which gives

$$E = -eA_t + \omega(L - eA_\phi) + (\sqrt{-\psi}/g_{\phi\phi})[(L - eA_\phi)^2 + g_{\phi\phi}(g^{rr}p_r^2 + g^{\theta\theta}p_\theta^2 + \mu^2)]^{1/2}, \tag{2.9}$$

where

$$\psi = g_{tt}g_{\phi\phi} - g_{t\phi}^2 < 0 \quad \text{for} \quad r > r_+ \tag{2.10}$$
$$\omega = -g_{t\phi}/g_{\phi\phi} > 0.$$

The event horizon r_+ is given by the larger root of $\psi = 0$. It can be easily verified that $\psi = 0 \Leftrightarrow \Delta = 0$.

For convenience we introduce the dimensionless quantities

$$\bar{r} = r/m, \quad \bar{a} = a/m, \quad \bar{l} = L/m, \quad \bar{Q} = Q/m$$
$$\bar{A}_t = A_t/m, \quad \bar{A}_\phi = A_\phi/m, \quad \bar{e} = e/\mu$$

and drop the bars on these symbols in further discussion.

2.2 *The Effective Potential*

By the symmetry of the metric and the electromagnetic field, it follows that the particle commencing its motion with $p_\theta = 0$ in the equatorial plane will stay in the plane for all time, *i.e.* $p_\theta = 0$ all through the motion. This can also be verified by considering the equations of motion

$$\ddot{x}^i + \Gamma^i_{kl}\dot{x}^k\dot{x}^l = eF^i_k\dot{x}^k \tag{2.11}$$

for the θ-coordinate. The Lorentz force term on the right gives a force directed in the $\theta = \pi/2$ plane for A_i given in Equation (2.2) and $F_{ik} = A_{k,i} - A_{i,k}$. Henceforth we shall consider motion in the equatorial plane and set $\rho_\theta = 0$. As our main aim in this investigation is to analyse negative energy states, the restriction of motion in the equatorial plane will not matter much.

The effective potential for radial motion could be obtained by putting $p_r = p_\theta = 0$ in Equation (2.9). We write

$$V = -eA_t + \omega(L - eA_\phi) + (\sqrt{-\psi}/g_{\phi\phi})[(L - eA_\phi)^2 + g_{\phi\phi}]^{1/2},$$
$$\omega = -g_{t\phi}/g_{\phi\phi} > 0. \tag{2.12}$$

The positive sign for the radical is chosen to ensure that the 4-momentum of the particle is future directed. The quantity ω represents the angular velocity of a locally nonrotating observer (LNRO) at a given r and θ. That is, a particle with $L = 0$ will have $d\phi/dt = \omega \neq 0$.

Equations (2.8) and (2.12) can be rewritten as

$$\alpha E^2 - 2\beta E + \gamma = 0, \tag{2.13}$$

and

$$V = \frac{\beta + (\beta^2 - \alpha\gamma)^{1/2}}{\alpha}, \tag{2.14}$$

where

$$\alpha = (r^2 + a^2) - \Delta a^2,$$

$$\beta = (r^2 + a^2)(al + eQr) - \Delta al,$$
$$\gamma = (al + eQr)^2 - (r^2 + l^2). \tag{2.15}$$

The effective potential at the horizon reads as

$$V(r_+) = [-eA_t + \omega(l - eA_\phi)](r_+),$$
$$V(r_+) = \frac{eQ}{r_+} + \frac{a}{r_+^2 + a^2}\left(l - \frac{eQa}{r_+}\right), \tag{2.16}$$

where

$$\omega(r_+) = \frac{a}{r_+^2 + a^2}.$$

$V(r_+)$ can become negative if $-eA_t < 0$ and $(l - eA_\phi) < 0$. It should be noted that it is the sign of $(l - eA_\phi)$ which is relevant for V getting negative (Dadhich 1983). The particle rotates slower than the LNRO if $l - eA_\phi < 0$. This can be seen from the following.

The angular velocity $\Omega = d\phi/dt$ of a particle can be obtained by using Equations (2.5) and (2.6),

$$\Omega - \omega = (-\psi/g_{\phi\phi}^2)(l - eA_\phi)[E + eA_t - \omega(l - eA_\phi)]^{-1},$$

which, in view of Equations (2.9) and (2.10), directly relates the sign of $(l - eA_\phi)$ to $\Omega - \omega$. As argued by Dadhich (1985), $\Omega - \omega \gtrless 0$ defines co/counter-rotation relative to an LNRO. It is the LNRO frame that is physically meaningful in these considerations.

3. The negative energy states

In this section we shall discuss the behaviour of the effective potential in relation to the occurrence of negative energy states (NES).

The NES could occur due to the electromagnetic interaction (as in the ReissnerNordstrøm case) as well as due to the counter-rotating orbits (as in the Kerr case). The Kerr-Newman solution represents the gravitational field of a charged and rotating black hole. The rotation of a black hole also gives rise to the magnetic dipole field in addition to the usual electrostatic field. The presence of electromagnetic field will favour the occurrence of NES (Dhurandhar & Dadhich 1984a, b) (i) by allowing larger negative values for energy, and (ii) by increasing the region of occurrence of NES. It is also known to cause in certain situations the splitting of NES region into two disjoint patches (Dhurandhar & Dadhich 1984a, b). However, in the Kerr-Newman field it turns out that NES may occur only in one patch extending upto the horizon (Prasanna 1983) as in the Kerr case. In the following we shall investigate NES with reference to counterrotation and electromagnetic interaction.

3.1 *The Effective Potential Curves*

Let us first look at some typical plots of the effective potential which exhibit its dependence on the parameters l and $\lambda = eQ$. Fig. 1 (a) shows the effective potential V for fixed $\lambda = -5$ and for various values of $l = -100, -50, -10, 0, 5$. It depicts (i) V is large negative for large negative l, (ii) NES region extends beyond the ergosphere

$r = 2$, and (iii) as l becomes less negative, V becomes less negative but NES region enlarges. It is interesting to see that $V < 0$ even for $l = 0$ and $l = 5$. This is in contrast to the Kerr case, and is purely due to the electromagnetic interaction.

In Fig. l(b) V is plotted for fixed $l = -10$ and for various values of $\lambda = -10, -5, -2, 0, 5$. It shows that larger negative λ implies larger negative V as well as enlarged NES region. Hereagain we have the occurrence of NES for $\lambda = 0$ and $\lambda = 5$ which is in contrast with the ReissnerNordstrøm case (Denardo & Ruffini 1973). The contribution due to counter-rotation $(\Omega - \omega)$ dominates over the electrostatic term. These plots are in agreement with Prasanna's results (1983).

3.2 *The Single-Band NES Structure*

The V curves in Figs 1 and 2 exhibit the singleband NES structure as also noted by Prasanna (1983). We establish this character analytically.

From Equations (2.13) and (2.14), $V = 0$ requires $\gamma = 0$ and $\beta < 0$. From Equation (2.15) $\gamma = 0$ gives

$$(al + eQr)^2 - \Delta(r^2 + l^2) = 0 \tag{3.1}$$

We now show that there is only one root for the above equation for $r > r_+ = 1 + (1 -$

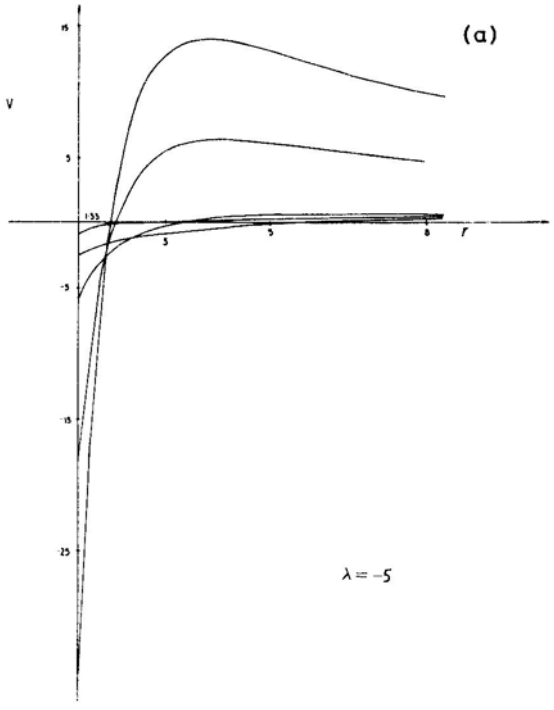

Figure 1. The effective potential V is plotted for $a = 0.8$ and $Q = 0.5$.The vertical axis is drawn at the horizon ($r_+ = 1.33$). (a) l takes the values $-100, -50, -10, 0, 5$; (b) λ ranges through $-10, -5, -2, 0, 5$. The curve corresponding to a particular value of l and a particular value of λ can be picked up from the property that $V(r_+)$ is a monotonically increasing function of l and λ.

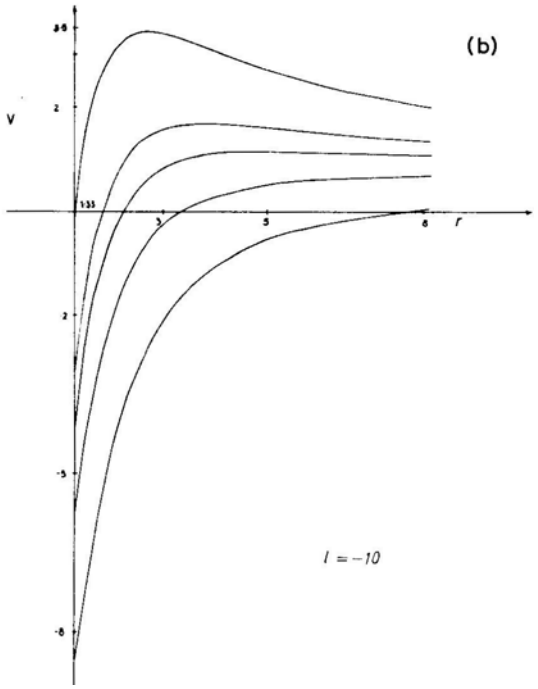

Figure 1. Continued.

$a^2 — Q^2)^{1/2}$· Write $R = r - r_+$. The above equation then reads as

$$R^4 + AR^3 + BR^2 + CR + D = 0, \tag{3.2}$$

where

$$A = 2(1 + 2\sqrt{1 - a^2 - Q^2})$$
$$B = 5r_+^2 - 4r_+ + l^2 - \lambda^2$$
$$C = 2[r_+^3 - r_+^2 + r_+(l^2 - \lambda^2) - l^2 - al\lambda]$$
$$D = -(al + eQr_+)^2.$$

To establish the result we apply Descartes' rule of signs. As $A > 0$ and D < 0, the above equation can have more than one positive root only when $B < 0$ and C > 0. We now show that this is not possible.

Let $B < 0$, which implies

$$\lambda^2 > 5r_+^2 - 4r_+ + l^2, \tag{3.3}$$

which makes

$$C < -2(4r_+^3 - 3r_+^2 + l^2 + al\lambda).$$

If $l\lambda > 0$, then $C < 0$. However, for $l\lambda < 0$, $C < 0$ will require

$$4r_+^3 - 3r_+^2 + l^2 > |al\lambda|.$$

Squaring both sides of the above inequality and using (3.3) we deduce $C < 0$ for this case too. This proves the result. Thus $\gamma = 0$ has only one root $r > r_+$. As $r \to \infty$, $V \to 1$, and hence the NES band will occur only when $V < 0$ at the horizon.

The single-band nature of NES prescribes a linear relationship between l and λ, which could be inferred from $V(r) < 0$. From Equation (2.16) this will imply,

$$l < -\lambda r_+ /a.$$

3.3 *The Extent of the NES Band*

To find the extent of the NES band we consider the quartic Equation (3.1) in various limits as the exact solution is not easily obtainable. We take $|l| \gg 1$ and $|\lambda| \gg 1$ in $V = 0$ for larger r. Then the quartic reduces to a cubic

$$r^3 - 2r^2 + (a^2 + Q^2 + l^2 - \lambda^2)r - 2l(a\lambda + l) = 0 \tag{3.4}$$

by dropping Q^2 terms as $Q^2 \gg 1$.

Case (*i*): Let $|\lambda| \sim |l|$, $l(a\lambda + 1) > 0$. For large r, terms in r^2 and r can be neglected implying

$$r \simeq [2l(a\lambda + l)]^{1/3}$$

Case (ii): $|l - \lambda| \gg 1$, then Equation (3.4) reduces to

$$r^2 \simeq (l^2 - \lambda^2 + a^2 + Q^2)$$

by neglecting r^2 and the constant terms. Since, a, $Q < 1$ and if $l^2 - \lambda^2 > 0$ then $r \sim \sqrt{l^2 - \lambda^2}$

In the general case we need to resort to numerical computations. Table 1 below gives the extent of NES. It gives the root of $V = 0$ for various values of / and λ for fixed a(= 0.8) and Q (= 0.5). The horizon in this case is at $r_+ = 1.3317$.

It is apparent from the table that for a fixed $\lambda < 0$, the value of $r = r_0$, say, where V gets negative, increases as l increases until l becomes positive and dominant, then it drops off below r_+. On the other hand, for $\lambda > 0$, r_0 decreases as / increases and there obviously exists no r_0 for $l > 0$. For fixed $l < 0$, it decreases as X becomes less negative but it slightly increases for $|\lambda|$ small and then steadily decreases as X increases further in the positive range. For $l > 0$, only large negative values of λ give $r_0 > r_+$. The large negative λ favours large values for r_0, as is borne out by the special'cases discussed above.

Table 1. Roots of $V = 0$ for $a = 0.8$, Q = 0.5 and various values of l and λ.

λ \ l	−100	−50	−10	0	10	50
−50	3.6384	>10.0	>10.0	>10.0	>10.0	>10.0
−10	2.0584	2.3020	7.7847	>10.0	3.9459	—
−1	1.8489	1.8318	1.7037	—	—	—
0	1.8659	1.8655	1.8532	—	—	—
1	1.8489	1.8318	1.7037	—	—	—
5	1.7843	1.7107	1.3564	—	—	—
50	1.3538	—	—	—	—	—

3.4 *The Factors Causing NES*

From Equation (2.12) it is seen that V can be negative only when $\lambda = eQ < 0$ (*i.e.* $eA_t < 0$) and /or $(l - eA_\phi) < 0$. Here we wish to compare the contributions of these factors in rendering $V < 0$. There are the following six possible cases.

$$\begin{aligned}
&(1)\ -eA_t < 0 \qquad -eA_\phi > 0 \quad l > 0,\\
&(2)\ -eA_t < 0 \qquad -eA_\phi > 0 \quad l < 0,\\
&(3)\ -eA_t < 0 \qquad -eA_\phi < 0 \quad l > 0,\\
&(4)\ -eA_t < 0 \qquad -eA_\phi < 0 \quad l < 0,\\
&(5)\ -eA_t > 0 \quad (l - eA_\phi) < 0 \quad l > 0,\\
&(6)\ -eA_t > 0 \quad (l - eA_\phi) < 0 \quad l < 0.
\end{aligned}$$

One can immediately see that case (3) is not possible because the conditions put on the parameters are inconsistent in view of Equation (2.2).That is, $\lambda < 0$and $l > 0$ do not permit counter-rotating orbit ($\Omega - \omega < 0$).

The second law of the black hole physics rules out case 5. It implies (MTW),

$$\delta m \geqslant (a\delta J + Q\delta Q r_+)/2r_+,$$

where $\delta m = \mu E$, $\delta J = \mu ml$, $\delta Q = e\mu$.

Clearly $e>0$, and $l > 0$ does not allow $\delta m < 0$, thus ruling out NES. That is, the magnetic field alone cannot make $V < 0$.

The rest of the four cases allow for the NES. In the first case, the electrostatic energy is responsible for the NES while in case 2 it is the electrostatic and rotation, in case 6 the rotation and magnetic field, whereas in case 4 all the three factors join hands.

We shall consider the cases 1, 2 and 6 for $Q \to 0$ but $\lambda = eQ$ finite.

From Equation (2.16), $V(r_+) < 0$ gives

$$\frac{\lambda}{r_+} + \omega\left(l - \frac{a\lambda}{r_+}\right) < 0,$$

Where $\omega(r_+) \simeq \dfrac{a}{2r_+}$ by neglecting Q^2. Then

$$l < -\lambda\left(\frac{2}{a} - \frac{a}{r_+}\right). \tag{3.5}$$

In case 1, the inequality (3.5) gives

$$\frac{l}{-\lambda} < \frac{2}{a} - \frac{a}{r_+}$$

which, in the extreme case $a \to 1$, implies $l < |\lambda|$. In case 2, it will always be satisfied, while in case 6 it gives

$$\frac{l}{\lambda} < \frac{a}{r_+} - \frac{2}{a},$$

which will imply for $a \to 1$, $|l| > \lambda$.

4. The energy extraction

In this section we consider the process of energy extraction from the black hole. In this process proposed by Penrose (1969), it is envisaged that a particle falling onto a black hole splits up into two fragments at some $r > r_+$ where $V < 0$. Then, if one of the fragments has negative energy (relative to infinity), it will be absorbed by the black hole while the other fragment will come out, by conservation of energy, with the energy greater than the parent particle. This will result in extraction of energy from the black hole. In the case of the Kerr-Newman black hole, the extracted energy may be provided by the rotational and/or the electromagnetic energy (Christodoulou 1970). In the following we shall first consider the conservation equations for the 4-momenta of the participating particles, and then give a recipe for energy extraction.

At the point of split, we assume that the 4-momentum is conserved, *i.e.*,

$$P_1 = P_2 + P_3 \tag{4.1}$$

where p_i (i = 1, 2, 3) denotes the 4-momentum of the ith particle. The above relation stands for the following three relations.

$$E_1 = \mu_2 E_2 + \mu_3 E_3 \tag{4.2}$$

$$l_1 = \mu_2 l_2 + \mu_3 l_3 \tag{4.3}$$

$$\dot{r}_1 = \mu_2 \dot{r}_2 + \mu_3 \dot{r}_3 \tag{4.4}$$

where we have set $\mu_1 = 1$. The other conservation relation follows from the conservation of charge,

$$\lambda_1 = \mu_2 \lambda_2 + \mu_3 \lambda_3. \tag{4.5}$$

The quantities μ_i ,l_i; λ_i, E_i r_i refer to the ith particle. These relations contain in all eleven parameters, of which 7 can be chosen freely. The choice of these parameters will be constrained by the requirements that particle 1 should reach the point of split where $V < 0$ for some suitable I, λ values such that particle 2 can have $E_2 < 0$ and particle 3 has an escape orbit. To ensure uninterrupted progress of particle 1 down to the horizon, we set $l_1 = 0 = \lambda_1$. The l and λ parameters for particle 2 should be so chosen that $E_2 < 0$. We further chose $\dot{r}_2 = 0$ which will imply $E_2 = V$ at the point of split. Such a choice is favourable for high efficiency of the process. (For further discussion refer to Dhurandhar & Dadhich 1984b.)

For these calculations we assume $Q \ll$ 1. This assumption is realistic as can be seen from the following relation

$$Q \text{ (metres)} = (G / \varepsilon_0 c^4)^{1/2} Q \text{ (Coulombs)}.$$

Though Q could be small, $eQ = \lambda$ can produce the Lorentz force on a particle of the charge/mass ratio of an electron, comparable to the corresponding gravitational force. So we neglect Q in the metric but retain λ in the equations of motion.

We shall now adopt the scheme for calculations due to Parthasarathy *et al.* (1985). From Equation (2.8) we can readily write the equations for radial motion of the particle,

$$\dot{r}^2 = \frac{1}{r^3}\left[R\bar{E}^2 - 4a\bar{E}\bar{L} - (r-2)\bar{L}^2 - r\Delta\right], \tag{4.6}$$

where

$$R = r(r^2 + a^2) + 2a^2,$$

$$\bar{E} = E + eA_t,$$

$$\bar{L} = l - eA_\phi.$$

Since we have taken $\dot{r}_2 = 0$, which means

$$\dot{r}_1 = \mu_3 \dot{r}_3, \tag{4.7}$$

by writing Equation (4.6) for particles 1 and 3 and using Equations (4.2), (4.3), (4.5) and (4.7) we obtain E_1 as follows

$$E_1 = \frac{[R\bar{E}_2^2 - 4a\bar{E}_2\bar{L}_2^2 - (r-2)\bar{L}_2^2]\mu_2^2 + r\Delta(1-\mu_3^2)}{2\mu_2(R\bar{E}_2 - 2a\bar{L}_2)}. \tag{4.8}$$

For the parent particle to be thrown from infinity $E_1 \geqslant 1$, and Equation (4.8) reduces to the inequality

$$\mu_2^2[R\bar{E}_2^2 - 4a\bar{E}_2\bar{L}_2 - (r-2)\bar{L}_2^2] + r\Delta(1-\mu_3^2) - 2\mu_2(R\bar{E}_2 - 2a\bar{L}_2) \geqslant 0. \tag{4.9}$$

The above inequality can be analysed in $\mu_2 - \mu_3$ plane. The equality sign gives the boundary of the region for the permissible values of μ_2 and μ_3. For the numerical values that we consider, this boundary is a hyperbola given by

$$\mu_2 = \frac{(R\bar{E}_2 - 2a\bar{L}_2) \pm [(R\bar{E}_2 - 2a\bar{L}_2)^2 - r\Delta(1-\mu_3^2)\{R\bar{E}_2^2 - 4a\bar{E}_2\bar{L}_2 - (r-2)\bar{L}_2^2\}]^{1/2}}{R\bar{E}_2^2 - 4a\bar{E}_2\bar{L}_2 - (r-2)\bar{L}_2^2}, \tag{4.10}$$

the relevant branch of which will be decided by the following considerations.

Squaring Equation (4.1), and using $p_2 \cdot p_3 < 0$ (future-pointing timelike vectors) we have,

$$\mu_2^2 + \mu_3^2 < 1. \tag{4.11}$$

This isaregion inside a unitcirclein the $\mu_2 - \mu_3$ plane.The inequality (4.9)requires μ_2 to be greater than the larger root or less than the smaller root given in Equation (4.10). It is the smaller root (*i.e.* with the negative sign for the radical) that gives the nonvoid intersection with the unit circle (4.11). However, μ_2 and μ_3 should be greater than zero. Fig. 2 shows the boundary of the permissible region.

The above prescription ensures that particle 1 from infinity reaches the desired splitting point, and particle 2 has negative energy. By Equation (4.2), particle 3 has greater energy than the incident particle. It now remains to ensure that particle 3 escapes to infinity. This further restricts the allowed region for μ_2 and μ_3. For particle 3 to escape to infinity two conditions must be satisfied. The particle must bounce outside the horizon and then it should continue its motion uninterrupted. That is,

$$\text{(i)}\ E_3 < V_3 \qquad r_0 > r > r_+$$

$$\text{(ii)}\ E_3 > V_3 \qquad r > r_0$$

where r_0 is the point of split. Numerical computations to this effect show that for $0 \leqslant \mu_3 < 1$, and for small values of μ_2, the particle does not escape, while for μ_2 close to the hyperbolic boundary the particle always escapes. Therefore, for a critical value of μ_2, say μ_{2c}, we have the particle escaping to infinity for $\mu_2 > \mu_{2c}$. So the allowed region

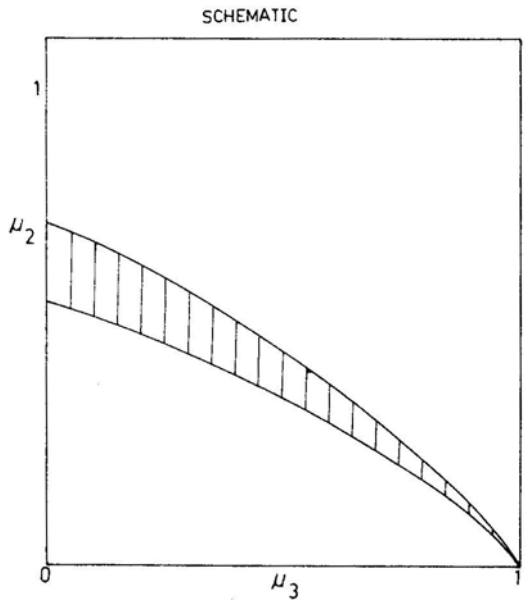

Figure 2. Schematic diagrams for μ_2 (max) and μ_2 (crit) are drawn. Here the numbers involved are too inconvenient to permit a figure to scale. The shaded region lying between μ_2 (max) and μ_2 (crit) is the allowed region.

now shrinks between μ_{2c} and the hyperbola. This is shown in Fig. 2 by the shaded region.

5. Efficiency of the process

The most important question in the black hole energetics is the efficiency of the energy extraction process. It is therefore very pertinent to examine how efficient the Penrose process is. The maximum efficiency of the process in extracting rotational energy of the black hole (Chandrasekhar 1983) turns out to be approximately 20.7 per cent. We shall rederive this result independently following the detailed analysis done by Parthasarathy *et al.* (1985) and show that the presence of charge on the black hole reduces the efficiency of the process. However, it further turns out that there exists no upper limit on the efficiency when one considers the process with electromagnetic interaction. Our numerical results show that there do occur events with more than 100 per cent efficiency.

5.1 *Efficiency in the Absence of Electromagnetic Interactions*

The maximum efficiency is obtained if we take the radial components of the velocities to be zero, the point of split being as close as possible to the horizon (MTW). We first derive the expression for efficiency at some $r > r_+$ and then take the limit as $r \rightarrow r_+$.

Let $U_i(i=1,2,3)$ denote the 4-velocity of the ith particle at the point of split,

$$U_1 = f_1(1, 0, 0, \Omega_1) \tag{5.1}$$

where

$$f_1 = -(g_{tt} + g_{t\phi}\Omega_1)^{-1}, \tag{5.2}$$

$$\Omega_1 = \frac{-g_{t\phi}(1+g_{tt}) + (-\psi(1+g_{tt}))^{1/2}}{g_{t\phi}^2 + g_{\phi\phi}}, \tag{5.3}$$

Ω_1 is the angular velocity of particle 1 with respect to the asymptotic Lorentz frame, and we have taken $E_1 = 1$.f_1 is obtained by considering unit length of the 4-velocity vector U_1.At the point of split, the light cone imposes restrictions on the angular velocity Ω of a future moving timelike particle that $\Omega_- < \Omega < \Omega_+$ where

$$\Omega_\pm = (-g_{t\phi} \pm \sqrt{-\psi})/g_{\phi\phi}. \tag{5.4}$$

The best result will be obtained by choosing the angular velocity of the second particle to be $\Omega_2 \to \Omega_-$ and that of the third to be $\Omega_3 \to \Omega_+$ In the limit,

$$\mu_2 U_2 = k_2(1, 0, 0, \Omega_-), \tag{5.5}$$

$$\mu_3 U_3 = k_3(1, 0, 0, \Omega_+). \tag{5.6}$$

The conservation of 4-momentum can be rewritten as

$$U_1 = \mu_2 U_2 + \mu_3 U_3. \tag{5.7}$$

By algebraically manipulating the above equations we obtain

$$\mu_3 E_3 = \left(\frac{\Omega_1 - \Omega_-}{\Omega_+ - \Omega_-}\right)\left(\frac{g_{tt} + g_{t\phi}\Omega_+}{g_{tt} + g_{t\phi}\Omega_1}\right). \tag{5.8}$$

The efficiency η is defined as

$$\eta = \frac{\text{gain in energy}}{\text{input energy}},$$

$$\eta = \frac{\mu_3 E_3 - E_1}{E_1}$$

$$= \mu_3 E_3 - 1 \quad \text{for} \quad E_1 = 1. \tag{5.9}$$

Now we take the limit as split point tends to r_+. Then

$$\mu_3 E_3 = [(1+g_{tt})^{1/2} + 1]/2. \tag{5.10}$$

For the extreme Kerr-Newman black hole $(a^2 + Q^2 = 1)$, the relevant g_{ij} at the horizon are given as

$$g_{tt} = +(1-Q^2),$$

$$g_{t\phi} = -(2-Q^2)(1-Q^2)^{1/2},$$

$$g_{\phi\phi} = (2-Q^2)^2. \tag{5.11}$$

Putting in these values in Equation (5.10) we obtain

$$\mu_3 E_3 = [1 + (2-Q^2)^{1/2}]/2 \tag{5.12}$$

which will imply

$$\eta = [(2-Q^2)^{1/2} - 1]/2. \tag{5.13}$$

For $Q = 0$

$$\eta = \frac{\sqrt{2}-1}{2} = 0.207$$

which is in agreement with the known result. Thus the presence of charge on the black hole decreases the maximum efficiency of the Penrose process in the absence of electromagnetic interaction (participating particles being uncharged).

5.2 *Efficiency in the Presence of Electromagnetic Interactions*

When we consider the participating particles being charged, the *t*-component of the conservation Equation (5.7) will read as

$$E_1 + e_1 A_t = \mu_2 (E_2 + e_2 A_t) + \mu_3 (E_3 + e_3 A_t). \tag{5.14}$$

Here, the charges on particles can be chosen arbitrarily large and hence this will not give any upper limit on the efficiency (Parthasarathy *et al*., 1985). In fact the term $eA_t = — eQ/r$ can assume arbitrarily large values for large e. This is borne out by the numerical example considered below.

Let us assume $a = 0.8$, $Q = 0.5$. The particle 1 comes from infinity, and has parameters $\mu_1 = 1$, $E_1 = 1$, $l_1 = 0$, $e_1 = 0$. The split is taken to occur at $r = 4.0$. For $l_2 = -10$ and $e_2 = -50$ we give in Table 2 the maximum efficiency for various values of μ_3. For η (max), $\mu_2 = \mu_2$ (max) given by the hyperbolic boundary, and μ_{2c} defines the lower boundary of the permissible region (see Fig. 2). The first row of the table gives an instance when efficiency is 104 per cent.

6. Conclusion

The presence of electromagnetic fields around a black hole (inherent in the metric as in the present case, or externally superposed) influences the behaviour of negative energy states for charged particles in the following two ways (Dhurandhar & Dadhich 1984a, b).

(a) The NES region is enlarged beyond the ergosphere $r = 2M$.
(b) E can have larger negative values.

Table 2. The maximum efficiency of the Penrose process for various values of μ_3, when electromagnetic interactions are included.

μ_3	μ_2 (max)	μ_{2c}	η (max)
0.001	0.2001	0.1199	1.045
0.191	0.1932	0.1930	1.009
0.381	0.1724	0.1723	0.901
0.581	0.1374	0.1373	0.718
0.761	0.0871	0.0870	0.455
0.951	0.0202	0.02019	0.105

Both these factors contribute positively to the energy extraction process. The former brings in NES at comfortable r-values, thereby increasing the probability of larger number of events yielding energy extraction, while the latter tends to increase the energy gain per event resulting in greater efficiency. For the Kerr-Newman black hole, large negative charge on the test particle (*i.e*. large $\lambda < 0$) causes (a), while both λ and l large and negative give rise to (b) (see Fig. 1).

It has been shown that the extraction of energy from the Kerr-Newman black hole is more efficient—in fact, there exists no upper bound on the efficiency when charged particles participate in the process (Table 2 shows an event of over 100 per cent efficiency)—in contrast to when uncharged particles are involved. In the latter case, the charge on the black hole reduces the maximum efficiency which is 20.7 per cent for the Kerr black hole. The electromagnetic extraction of black hole's energy is highly efficient.

As massive bodies cannot have significant charge on them, in our efficiency calculations we have taken $Q/M \leqslant 1$. We have hence neglected it in the metric but have retained its interaction with the test particle in the equations of motion. If a black hole acquires slight charge, our results would apply and will be indicative of the general behaviour of NES and energy extraction process.

Acknowledgement

One of us (S. D.) thanks the Department of Mathematics, Poona University for a visiting fellowship which has facilitated this work. This investigation constitutes the dissertation submitted by one of the authors (M.B.), towards partial fulfilment for the M.Phil, degree, to Poona University.

References

Abramowicz, M. A., Calvani, M., Nobili, L. 1983, *Nature,* **302**, 597.
Bardeen, J. M., Press, W. H., Teukolsky, S. A. 1972, *Astrophys. J.,* **178**, 347.
Blandford, R. D., Znajek, R. L. 1977, *Mon. Not. R. astr. Soc,* 1**79**, 433.
Carter, B. 1968, *Phys. Rev.,* **174**, 1559.
Chandrasekhar, S. 1983,77ie *MathematicalTheory of Black Holes,* Oxford University Press, New York.
Christodoulou, D. 1970, *Phys. Rev. Lett.,* **25**, 1596.
Dadhich, N. 1983, *Phys. Lett.,* **98A**, 103.
Dadhich, N. 1985, in *A Random Walk in Relativity and Cosmology,* Eds N. Dadhich, J. Krishna Rao, C. V. Vishveshwara & J. V. Narlikar, Wiley, Eastern, p. 72.
Denardo, G., Ruffini, R. 1973, *Phys. Lett.,* **45B**, 259.
Dhurandhar, S. V., Dadhich, N. 1984a, *Phys. Rev.,* **D29**, 2712.
Dhurandhar, S. V., Dadhich, N. 1984b, *Phys. Rev.,* **D30**, 1625.
Fishbone, L. G. 1973, *Astrophys.* J., **185**, 43.
Kozfowski, M., Jaroszynski, M., Abramowicz, M, A. 1978, *Astr. Astrophys.,* **63**, 209.
Mashhoon, B. 1973, *Astrophys. J.,* **181**, L65.
Misner, C. W., Thorne, K. S., Wheeler, J. A. 1973, *Gravitation,* W. H. Freeman, San Francisco.
Parthasarathy, S., Wagh, S. M., Dhurandhar, S. V., Dadhich, N. 1985, Astrophys. J., (submitted).
Penrose, R. 1969, *Rev. Nuovo Cimento,* 1 (Special Number), 252.
Prasanna, A. R. 1983, *Astr. Astrophys.,* **126**, 111.

Pringle J E. 1981, *A. Rev. Astr. Astrophys.,* 1**9**, 137.
Reest M. I, Begelman, M. C, Blandford, R. D, Phinney, E. S. 1982, *Nature,* **295**, 17.
Shakura, N. I., Sunyaev, R. A. 1973, *Astr. Astrophys.,* **24**, 337.
Vishveshwara, C. 1968, *J. Math. Phys.,* **9**, 1319.
Wagh, S. M., Dhurandhar, S. V., Dadhich, N. 1985, *Astrophys. J.*, **290**, 12.
Wald, R.. M. 1974, *Astrophys. J.,* **191**, 231.
Wheeler, J. A. 1971, in *Nuclei of Galaxies,* Ed. D. J. K. O'Connell, NorthHolland, Amsterdam, p. 539.

J. Astrophys. Astr. (1985) **6,** 101–112.

Observations of Hydrogen Deficient Binary Upsilon Sagittarii[†]

N. Kameswara Rao *Indian Institute of Astrophysics, Bangalore 560034*

V. R. Venugopal *Radio Astronomy Centre, Tata Institute of Fundamental Research, Post Box 8, Udhagamandalam 643001*

Received 1984 December 12; accepted 1985 February 25

Abstract. The absolute magnitude M_v of the hydrogen deficient binary υ Sgr has been estimated as –4.8 ± 1.0 from the distribution of the interstellar reddening, polarization and interstellar lines of the surrounding stars. From the ANS observations obtained at the time of the secondary eclipse, it appears that the hotter secondary is surrounded by a disc with colours of a B8–B9 star. The λ 1550 CIV absorption line arising in the stellar wind does not show any change in strength during the secondary minimum. The upper limit to the mass-loss rate from the high temperature wind is estimated as $\leqslant 5 \times 10^{-7}\ M_{\odot}\ \mathrm{yr}^{-1}$ from the 2 cm and 6 cm radio observations.

Key words: stars, chemically peculiar—stars, individual—stars, eclipsing—ultraviolet astronomy—mass loss

1. Introduction

Upsilon Sagittarii is the brightest of the small group of hydrogen deficient binaries, the other known members being KS Per (HD 30353) and possibly LSS 4300 (Drilling 1980). All. of them are single-lined spectroscopic binaries consisting of A-type supergiant primaries with optically unseen companions; υ Sgr is probably an eclipsing binary as well (Gaposchkin 1945; Eggen, Krön & Greenstein 1950). The presence of Hα and other emission lines and the infrared excesses with 10 μm emission feature are indicative of extensive mass loss and the presence of circumstellar dust. The observational properties have been summarized by various investigators (Greenstein 1950; Hack, Flora & Santin 1980; Schönberner & Drilling 1983). Further, to explain the Hα absorption components to the emission, Nariai (1967) has presented a model in which the system is surrounded by an expanding tail of gas and dust in which emission and infrared excess occur. Although the presence of a secondary can be inferred from the recent ultraviolet studies (Duvignau, Friedjung &Hack 1979; Hack, Flora & Santin 1980; Hellings *et al.,* 1981; Drilling & Schönberner 1982), the nature of the secondary is not very clear. Hack, Flora & Santin (1980) infer a spectral type of O9 V for the companion from a comparison of IUE spectra of υ Sgr with S2/68 satellite energy distributions of α Cyg and ζ Oph; on the other hand, Drilling & Schönberner (1982)

[†] Based on observations obtained with the Astronomical Netherlands Satellite and VLA. The National Radio Astronomy Observatory's Very Large Array at Socorro, New Mexico is operated by Associated Universities Inc. under contract with the National Science Foundation.

find from the low resolution IUE spectra that the line and continuum can be matched by a companion of type B3 Ib which is about 3–5 mag fainter at V relative to the primary (~ A2 Ia). Furthermore, in order to account for the extreme hydrogen deficiency and high nitrogen abundance Schönberner & Drilling (1983) propose that the primary is a helium star of about $1M_{\odot}$ which has undergone extensive mass loss thereby stripping the outer layers, and the secondary has accreted part of the mass and is thus over luminous for its mass ($\leqslant 4\ M_{\odot}$) . It was pointed out by Hellings *et al.* (1981) and Hack, Flora & Santin (1980) that the strong spectral features seen in the IUE low resolution spectrum of CIV, NV, SiIV, Sim *etc.,* occur in the stellar wind and thus might not really represent the spectral characteristics of the secondary. Although both υ Sgr and KS Per have similar characteristics, their M_vs seem to be different. The M_v of KS Per has been determined by Danziger, Wallerstein & Böhm-Vitense (1967) as – 3.2 ±.7 corresponding to an A2 II star, whereas υ Sgr is usually assumed to be – 7 mostly based on the luminosity classification of Ia. As pointed out by Danziger, Wallerstein& Böhm-Vitense (1967), when the lines are greatly enhanced on account of the low opacity, the approximate spectral type cannot be used to infer the effective temperature or absolute magnitude with high accuracy. A further complication arises regarding the secondary if the primary is assumed to have M_v of –7. Kippenhahn & Meyer-Hofmeister (1977) have computed the radii and the location in H–R diagram of mass-accreting main-sequence stars for various accretion rates. Since the present mass of the secondary is expected to be $\leqslant 4\ M_{\odot}$, and not much different from its original mass (according to Schönberner & Drilling 1983), if we assume the primary has $M_v = -7$, then the secondary occupies a very improbable position in the H–R diagram (B3, $M_v \sim -4$) indicating very high mass accretion rates. Greenstein (1940) earlier estimated M_v as – 7.6 from kinematics. Because of the large uncertainty in distance estimates based on kinematics, a re-examination of M_v of the primary is warranted.

In this paper we rediscuss the determination of the distance and absolute magnitude of υ Sgr in a similar way as was done for KS Per by Danziger, Wallerstein & Böhm-Vitense with the help of Astronomical Netherlands Satellite (ANS) observations. We further discuss the ANS observations—which include observation at the time of the secondary eclipse—with a view of obtaining some constraints regarding the nature of the companion. In addition, we present optical observations in the Hα region. Finally, we present the observations at 2 and 6 cm done with Very Large Array (VLA) and estimate upper limits for the rate of mass loss from the system.

2. ANS observations

A total of eleven photoelectric observations of υ Sgr have been obtained by ANS (kindly supplied by Dr D. P. Gilra) at 1550Å (square-response full-width 150 Å and 50 Å), 1800 Å (150 Å), 2200 Å (200 A) 2500 Å (150 Å), and 3300 Å (100 Å). The entrance aperture had dimensions equivalent to 2.5 × 2.5 arcmin and pointing accuracy was 20 arcsec. The internal accuracy of photoelectric system is supposed to be good to 0.5 to 1 percent. The details of satellite, and method of observations and reductions are given in Wesselius *et al.* (1982). The observations of υ Sgr have been obtained over a period of one year. The individual observations are given in Table 1, with the date of observation, the phase and the magnitude in each wavelength band. The zero magnitude corresponds to 3.64×10^{-9} erg $cm^{-2} s^{-1} A^{-1}$. The phase is calculated from

Table 1. ANS observations of υ Sgr.

Date	Phase	Magnitude* 3300	2500	2200	1800	1550W	1550N
1974 Oct 13.00	0.6885	4.064	4.886	5.326	5.169	5.353	
1974 Oct 13.62	0.6923	4.054	4.850	5.286	5.080	5.256	
1975 Apr 9.13	0.9753	4.226	5.054	5.494	5.294	5.428	5.634
1975 Apr 10.54	0.9866	4.173	5.042	5.479	5.268	5.472	
		4.171	5.044	5.478	5.265	5.468	
1975 Oct 12.86	0.3354	4.115	4.891	5.366	5.198	5.348	
		4.116	4.893	5.369	5.198	5.349	
		4.115	4.901	5.374	5.194		5.532
		4.116	4.906	5.367	5.191		5.548
1975 Oct 14.02	0.3423	4.129	4.917	5.389	5.248	5.393	
		4.128	4.917	5.388	5.234	5.397	

* 0.0 mag corresponds to 3.64×10^{-9} erg cm^{-2} s^{-1} Å^{-1}

the ephemeris given by Hack, Flora & Santin (1980) and corresponds to photometric phase.

2.1 *Reddening, Absolute Magnitude and Distance*

We estimate the distance and M_v of υ Sgr based on the distribution of E (B–V), polarization and interstellar lines with distance. The reddening $E(B - V)$ has been variously estimated ranging from 0.1 to 0.3. Using low-resolution IUE observations, Drilling & Schönberner (1982) estimated the reddening $E(B–V)$ as 0.1 by ironing out the 2200 Å depression using Seaton's (1979) interstellar reddening curve. They matched the energy distribution of the star with a combination of F0 Ib and a visually 5.2 mag fainter B3 Ib star (θ Ara). Later, by fitting the energy distribution longward of 2000 Å with a helium star model of $T_{\rm eff}$= 10500 K, Drilling *et al.* (1984) obtained $E(B - V)$ as 0.12. Earlier, Dyck & Milkey (1972), and Duvignau, Friedjung & Hack (1979), the latter using Copernicus observations, estimated $E(B - V)$ as 0.20.

The ANS observations in Table 1 have been corrected for interstellar reddening using the reddening relations given by Wesselius *et al.* (1980). As can be seen from Fig. 1 these observations normalized to 3300 Å band are not compatible with E ($B - V$) = 0.12. The 2200 Å observation still shows a dip and also the energy distribution does not match the combination of F0 Ib (α Lep or α Car) and a B3 Ib star (θ Ara) which is fainter by 5.2 mag in V. A wide variety of combinations of energy distributions of an A supergiant and a B star can match the ANS observations to roughly equal degree of agreement(or disagreement) although none of the combinations could fit exactly. Fig. 1 also illustrates a combination of an A2 Ia and a B3 Ib star which is fainter by 4.7 mag in V, and an A 2Ib star and a B8 V star which is fainter by 3 mag in V, etc. However, E ($B - V$) of 0.17 to 0.20 seem to be required to explain the 2200 Å observation, and to match with various combinations of ANS energy distributions. We will discuss this aspect further in Section 3. The value of $E(B - V)$ of 0.3 is quite incompatible with these observations. Bohlin & Holm (1984) give correction factors for bringing the ANS fluxes to the IUE flux scale. According to these authors, the IUE fluxes agree with ANS to

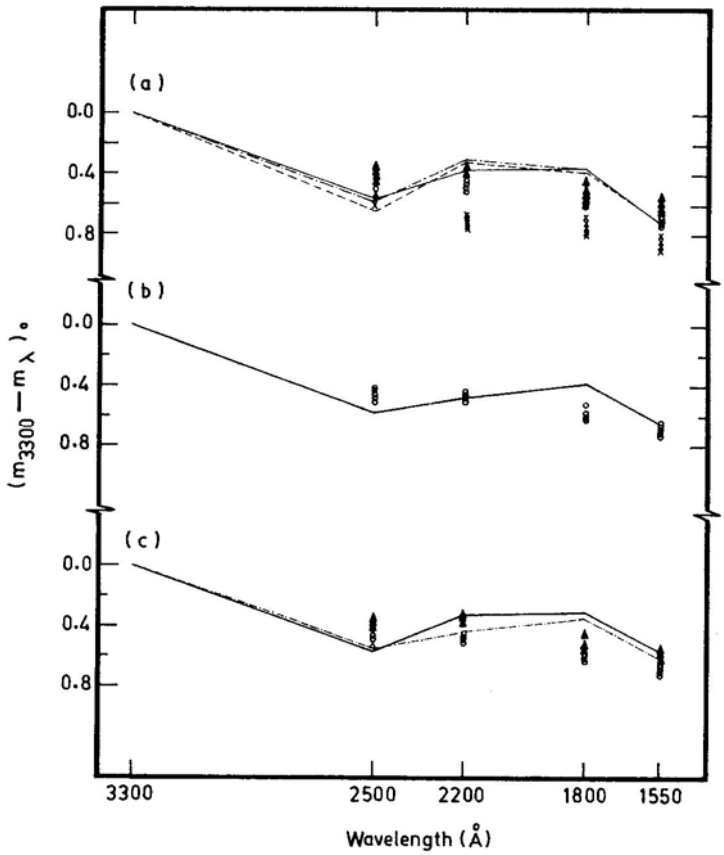

Figure 1. ANS observations of υ Sgr corrected for different values of interstellar reddening. Triangles, open circles and crosses corresponds to $E(B - V)$ = 0.20,0.175 and 0.12 respectively. These observations are fitted to various combinations of standard star energy distributions in a, b, and c. The notation is as follows: (a) Full line: A5 Ib + 5.25 mag visually fainter *B*2 V; dashed line: A2 Ia+ 6.2 mag visually fainter O9 V (10 Lac + α Cyg); dot dashed line: A2 Ia + 4.7 mag visually fainter B3 Ib (θ Ara). (b) Full line: A2 Ib + 6.0 mag visually fainter B3 V. (c) Full line: A2 Ia + 3.0 mag visually fainter B8 Ia; dashed line: A2 Ib + 3.0 mag visually fainter B9 V; dot dashed line: A2 Ib + 3.3 mag visually fainter B9 V.

within 2.5 per cent after applying the correction factors. We converted ANS fluxes to the IUE scale and tried to estimate the reddening by ironing out the 2200 Å depression using Seaton's (1979) reddening curve, which again indicates that the reddening might be around $E(B - V)$ = 0.16 to 0.20. However, because of the crowding of spectral lines, the lower resolution of ANS observations relative to IUE might give a slightly higher value of $E(B - V)$. Since the reddenings estimated by Drilling *et al.* (1984) using a helium star atmosphere and a normal composition atmosphere (Drilling & Schönbemer 1982) do not differ very much, we assume that the uncertainty in the reddening estimate, stemming from hydrogen deficiency is not appreciable. We conclude that $E(B - V)$ value of υ Sgr is between 0.12 and 0.20.

To arrive at the distribution of $E(B - V)$ with distance modulus in the direction of υ Sgr, we have used the B stars (mostly earlier than B5) in the field of less than 6 degrees

(most of them within 3 degrees) around the galactic longitude and latitude of υ Sgr. The *UBV* photometry and spectral types, whenever available, have been gathered from various sources and are given in Table 2. Whenever the MK spectral types are not available, the *Q* method and the relation given by Dworetsky, Whitelock & Carnochan (1982) has been used to derive them from the colours. The intrinsic colours and absolute magnitudes for the spectral type have been taken from FitzGerald (1970) and Lesh (1968, 1979) respectively. Fig. 2 shows the correlation of E $(B–V)$ with $V_o - M_v$ (the line shown in the figure is a mean line drawn by visual inspection) and shows that the reddening increases smoothly with distance modulus—at least until $E(B - V) \sim 0.3$—and can be used to estimate M_v. The reddening value of E $(B - V) = 0.12$ to 0.20 leads to $V_o - M_v = 8.1$ to 10.2. For υ Sgr with $V = 4.61$, using R [$\equiv A_v / E(B - V)$] = 3.2 leads to M_v of –3.9 to – 6.2.

The observations of polarization and interstellar lines of the stars near υ Sgr taken from literature are given in Table 3. The polarization of υ Sgr appears to be variable (Coyne & Gehrels 1967; Coyne 1977), however, most of the contribution seems to come from the interstellar medium. The λ_{max} of polarization and the position angle are close to that determined for κ Aql κ Aql has the same galactic latitude as υ Sgr but is 10 degrees away in longitude, and both υ Sgr and κ Aql have the interstellar components of CaII K (and H) line with the same velocity and roughly equal intensity (Adams 1949, 1943). κ Aql has slightly higher percentage of polarization and also a higher value of $E(B - V)$ (0.28). Thus it appears that υ Sgr is at the same distance as κ Aql, or slightly closer. Assuming the same distance modulus as for κ Aql (Savage & Jenkins 1972) one obtains $M_v = –4.8$ for υ Sgr. The previous estimates of M_v of –7 by McLaughlin (1939) was based on the strengths of the interstellar lines. However, Adams (1943, 1949) has resolved the interstellar CaII lines and both components have roughly the same intensity as in κ Aql. Moreover, the line strength of Na I lines have been

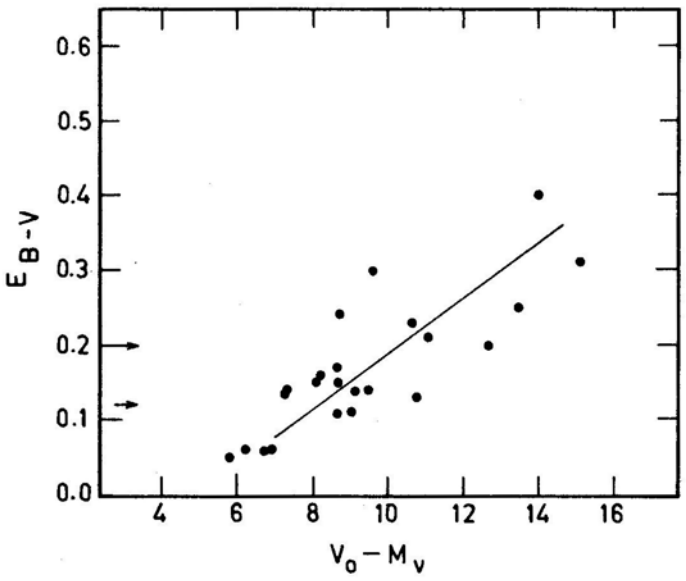

Figure 2 Plot of $E(B - V)$ versus reddening-corrected distance moduls $V_0 - M_v$ for stars around v Sgr. The arrows on the ordinate denote the two values of $E(B - V)$ for υ Sgr.

Table 2. Photometric parameters of B stars in the field of υ Sgr.

HD/BD	l	b	Spectral Type	V	$B-V$	$U-B$	M_v	$E(B-V)$	V_0-M_v
υ Sgr	21.84	−13.77	—	4.61					
175141	15.46	− 9.63	B8	9.23	0.03	−0.32	−0.4	0.14	9.18
175754	16.39	− 9.91	O8 f	7.01	−0.08	−0.96	−4.4	0.23	10.67
175876	15.30	−10.59	O7	6.92	−0.11	−1.00	−4.8	0.21	11.05
177014	16.76	−11.31	B8.5	9.27	0.19	−0.03	0.0	0.24	8.50
177137	18.4	−10.7	(B6)	8.69	0.04	−0.36	−0.5	0.17	8.65
177517	20.44	−10.16	B9 V	5.97	−0.02		0.0	0.05	5.81
177559	16.94	−11.85	B6 Vn	8.1	0.01	−0.66	−0.5	0.15	8.12
177817	20.04	−10.66	B8 IV	6.03	−0.04	−0.36	−0.4	0.06	6.24
177863	17.75	−11.78	B8 III	6.29	−0.04		−0.6	0.06	6.70
177989	17.81	−11.89	B0 III	9.33	−0.05	−0.89	−5.0	0.25	13.53
178070	21.1	−10.4	(B6)	8.67	0.04	−0.36	−0.5	0.17	8.63
178175	17.35	−12.26	B2 V	5.54	−0.11	−0.78	−2.2	0.13	7.32
178487	25.79	− 8.55	B0 Ia	8.66	0.16	−0.78	−6.6	0.40	13.98
179003	21.5	−11.2	(B8)	9.00	0.02	−0.25	−0.4	0.11	9.05
179407	24.03	−10.4	B0.5 Ia	9.41	−0.09	−0.81	−6.7	0.31	15.12
180110	22.25	−12.01	B5	7.79	0.02	−0.40	−0.9	0.16	8.18
180194	21.6	−12.4	(B5)	9.02	0.00	−0.42	−0.9	0.14	9.47
14°5313	22.97	−10.48	B5	8.28	0.0	−0.45	−0.9	0.15	8.70
180629	20.5	−13.3	(B5)	8.10	−0.05	−0.50	−0.9	0.11	8.65
181613	22.9	−13.3	(B4)	10.08	−0.03	−0.50	−1.1	0.13	10.76
181558	18.74	−15.10	B5 V	6.26	−0.10	−0.51	−0.9	0.06	6.97
183133	23.36	−14.92	B5 V	6.79	−0.03	−0.55	−0.9	0.13	7.27
183761	21.6	−16.5	(O8)	8.92	−0.10	−0.98	−4.4	0.20	12.68
183570	22.7	−15.85	(B6)	7.43	−0.01	−0.45	−0.5	0.14	7.38

Table 3. Polarization and interstellar line strengths of stars near υ Sgr.

HD (name)	l deg	b deg	Spectral type	$E(B-V)$	V_0-M_v	λ_{max}	P_{max} per cent	$\theta(P_{max})$ deg	Interstellar lines* km s^{-1}
176162	22	−8	B5 IV	0.12	6.15	0.58	0.91 0.87	120.2	−11.6 (15), −15.0M
179406 20 Aql	28	−8	B3 V	0.33	5.64	0.51	1.39 1.32	183.7 182.5	−13.6 (10), −24.2 (2), −15.2 M
181615 υ Sgr	22	−13		0.15 ±0.03		0.51	1.004 0.78	168.2 170.7	−11.6 (10), 4.2 (4), −13.1 M
183344 U Aql	31	−12	F5–G3 Ib	0.42	9.4	0.50 0.54	2.72 2.76		
184915 K Aql	32	−13	B0.5 III	0.28	8.8	0.58	1.35 1.39	171.5 170.3	−12.1 (8), 8.2 (4)

* Ca II K line components, the number in parenthesis is the intensity as given by Adams (1949). M refers to the molecular lines.
† The polarization measurements are from Coyne & Gehrels (1967); for other stars they are from Serkowski, Mathewson & Ford (1975).

given by Duvignau, Friedjung & Hack (1979) who also plot the relation of Na I D 1 line equivalent width against the hydrogen column density. This relation yields $N_H \sim 5 \times 10^{20}$ cm $^{-2}$ for an equivalent width of 0.186 Å; however, there is a large amount of scatter in the relation. Using the relation $N_H /E (B - V) = 5.3 \times 10^{21}$ leads to $E (B - V) \sim 0.1$ which is compatible with the $E(B — V)$ estimate given earlier. Further, Hack, Flora & Santin (1980) show that the equivalent widths of other interstellar lines in β Lyr and υ Sgr have about the same value. The distance to β Lyr is only 350 pc (Plavec, Weiland & Dobias 1982). Thus we conclude that M_v of υ Sgr is –4.8 ± 0.8 and roughly the same as that estimated for KS Per of – 3.2 ± 0.7 (Danziger, Wallerstein & Böhm-Vitense 1967).

2.2 *The ANS Photometry and the Depth of Secondary Eclipse*

The observations are few and do not cover the complete period. We propose to see how consistent these observations are with the models proposed earlier based on the depth of the secondary eclipse in the ultraviolet (UV). These observations have been phased with the ephemeris of Hack, Flora & Santin (1980). They occur at phases 0.99, 0.98, 0.69, 0.34 and 0.33. These have been plotted in Fig. 3 after normalizing to the averaged flux at phase 0.69 for all the five ANS bands, along with the light curve in the blue region obtained by Eggen, Kron & Greenstein (1949). The coincidence of the minimum of 1947 observations with 1975 ANS observations shows that the period is fairly accurate. The optical observations show that the eclipse is asymmetrical and has a depth of 0.1 mag. As can be seen from the figure and as is anticipated, the depth in UV is higher. Since the ANS observations do not cover the total eclipse to define the shape, we assume the duration of the eclipse to be the same as in blue light in order to extrapolate the eclipse curve from phase 0.99 to phase 0.0 and estimate the depth of the eclipse at phase 0.0. This has been done in two ways with practically the same result for the minimum depth. It is likely that the light is not constant even outside the minima (Cousins 1963). There may even be short-period variations. The ANS observations show that the flux

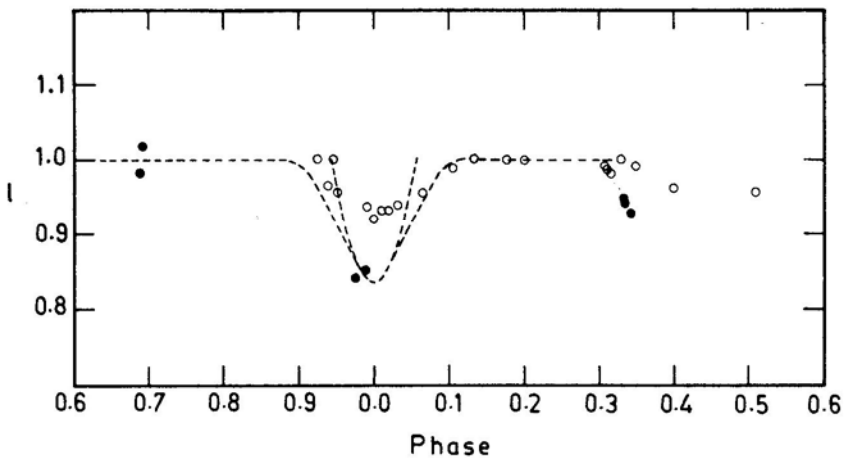

Figure 3. Light curve of υ Sgr, Open circles are the observations of Eggen, Kron & Greenstein (1949) in the blue; the dots are 2200 Å ANS observations.

observed at 0.692 phase differs from that at phase 0.689, particularly at the shorter wavelengths. The depth of the secondary minimum in terms of the light outside eclipse represented by the mean of the fluxes at phase 0.692 and 0.689, and the flux at phase 0.692 separately, are given in Table 4. The eclipse seems to be partial. As can be seen from Table 4, the depth of the eclipse between 2500 Å to 1550 Å is the same or perhaps slightly less at shorter wavelength (*i.e.* 1800 Å and 1550Å). This behaviour is similar to that reported by Duvignau, Friedjung & Hack (1979). With the assumption that the secondary eclipse is an occultation, the differential depth can give an indication of the luminosity of the secondary. Within the uncertainty of the exact shape of the minimum, the α_0^∞ is estimated to be 0.96 ± 0.03 for the assumed limb-darkening coefficient of 0.5 (Irwin 1960).Further, assuming α_0^∞ is the same in all the wavelengths, the luminosity of the secondary [i.e.$(1 - l)^\infty = \alpha_0^\infty L_s$] is estimated. Taking the value of $E(B - V) \simeq 0.2$ and the mean fluxes of phase 0.689 and 0.692 as representing the total light outside the eclipse, the magnitudes in the ANS bands inferred for the secondary are quoted in Table 4. The colours thus determined for the secondary do not correspond to any single spectral type (Wesselius *et al.* 1980,1982),but vary between B8 to A3 (as the wavelength decreases). This behaviour is similar to that described by Duvignau, Friedjung & Hack (1979) from the energy distribution of S2/68 observations. The UV colours obtained from the secondary eclipse depth certainly do not indicate a spectral type of B3 Ib.

Table 4. The depth of the secondary minimum, and the estimated magnitude of the secondary.

λ	4340	3300	2500	2200	1800	1550
depth*	0.075	0.13	0.16	0.167	0.165	0.165
depth†		0.13	0.182	0.182	0.185	0.195
$M_{\text{secondary}}$		5.30 ±0.10	5.31 ±0.08	5.23 ±0.05	5.33 ±0.10	5.46 ±0.10

* Assuming that the average flux at phase 0.692 and 0.688 represents the light outside the eclipse.
† Assuming that the average flux at phase 0.692 represents the light outside the eclipse.

The inclination of the orbit can be estimated as between 66° to 84.7° depending on the shape of the eclipse. From this, the mass function of 1.677 $M_\odot$ (Hack, Flora & Santin 1980) leads to $m_2^3 / (m_1 + m_2)^2 = 2.2$ and 1.7 respectively. Further, assuming the mass ratio m_p / m_s to be around 0.3 as proposed by Plavec (1973) and Schönberner & Drilling (1983), one has $m_p \sim 1\ M_\odot$ and m_s about 3 $M_\odot$. This leads to a spectral type of B 9 , if the secondary obeys the mass- luminosity relation of the main sequence. The estimate of K, the ratio of radii (r_s / r_p) is quite uncertain—it could even be as large as 0.9. Adopting $M_v = -4.8$ and T_{eff} of 10500 K the latter leads to $R_p \sim 29.7\ R_\odot$, $\log L / L_\odot = 4.01$.

3. Spectra in the Hα region

Spectra in the red region were obtained monitoring the Hα profile. A spectrogram obtained in September 1976 with the 1 m telescope at Kavalur at 17 Å mm^{-1} dispersion at phase 0.28, shows an emission feature at 6583.6 Å probably due to [N II], in addition to the Hα and Fe II lines. The profile of Hα appears to be very similar to that quoted by

Greenstein & Merrill (1946). The 6584 Å feature seems to have the same radial velocity as the other emission lines. The other line of [NII], at 6548 Å, could not be detected with certainty. The presence of [NII] lines indicates circumstellar material of low density. Danziger, Wallerstein & Böhm-Vitense (1967) have also detected [NII] 6584 Å in KS Per.

4. VLA observations

The resonance lines due to high temperature gas indicate a considerable mass loss (Hack, Flora & Santin 1980). This is to be expected from stellar evolution as the primary must either have lost or is still losing mass at a high rate. To derive the mass-loss rate from the free-free continuum of the circumstellar material, we observed υ Sgr at 2 and 6 cm with the Very Large Array (VLA) on 1983 December 12. No emission was detected, the upper limits (3 σ) to the flux density being 0.9 mJy at 2 cm and 0.3 mJy at 6 cm, and hence only an upper limit of $\dot{M}$ can be derived. Following Wright & Barlow (1975), the mass loss rate $\dot{M}$ of a star with a flux density S_ν at frequency ν. can be expressed as

$$\dot{M} = \frac{0.095 \mu S \nu^{3/4} D^{3/2} V_\infty}{z \gamma^{1/2} g^{1/2} \nu^{1/2}} \quad M_\odot \, \mathrm{yr}^{-1}$$

where S_ν is in Jy, ν is in Hz and D the distance is in kpc and V_∞ is the wind terminal velocity in km s^{-1}. μ, z and γ are the mean molecular weight per ion, the rms ionic charge and the mean number of electrons per ion respectively, g is the Gaunt factor at radio frequency obtained from the formula of Spitzer (1962). Taking the abundance ratio H/He as 0.1, and temperature of 10^5 K for the wind as indicated by the lines of CIV, Nv, Si IV, we adopt μ = 4.1, γ = 2.0, z = 2.0 and g(6 cm) = 7.2. Adopting the distance 0.6 kpc as obtained earlier and V_∞ = 700 km s^{-1}, as inferred from the CIV, Si IV lines, from IUE spectra (Hack, Flora & Santin 1980), we obtain an upper limit to the mass-loss rate of about 5.4×10^{-7} $M_\odot \mathrm{yr}^{-1}$. This rate is far too low to account for the evolutionary state of the system. Hence we conclude that the mass loss rate was probably much higher in the past, as the primary was estimated to have lost 5 to 12 $M_\odot$ in its earlier evolution (Schönberner & Drilling 1983).

5. Discussion

The depth of the secondary eclipse in the UV and the energy distribution indicate a spectral type later than B3 Ib for the secondary, contrary to that proposed by Drilling & Schönberner (1982), whose classification is based on the strength of tue UV resonance lines. Several explanations for this discrepancy are conceivable.

First we discuss the-possibility that the UV secondary minimum is filled in by additional light which becomes observable, at least partially, during the eclipse. This additional source may arise from circumbinary gas clouds with multi-component emission lines in the UV, or it might arise from a disc (or a hot spot) around the B star. The IUE spectra Obtained by Hack, Flora &Santin(1980) and Drilling & Schönberner (1982) show that there are no strong emission lines present in the UV spectrum, which fact points to a disc. With the mass ratio m_p/m_s = 0.3 (see Section 3) the radii of the

Roche lobes around the primary and secondary are about 38 $R_\odot$ and 70 $R_\odot$, respectively. Within the uncertainties of M_v, the primary just about fills its Roche lobe, and hence mass transfer seems to occur. Blue-shifted absorption components of – 300 km s^{-1} around the time of the primary minimum seen occasionally (Bidelman 1949; Nariai 1967)also indicate mass transfer. The presence of absorption components at 0.5 phase (Hα ,Al III) has been interpreted (Hack, Flora & Santin 1980) as due to a jet or stream of material from the secondary to the primary. The variability of the spectral features as evidenced from the changes in the profile of Hα (Greenstein & Adams 1947) show similar behaviour to that seen in Algol type systems like U Cep.

Then we have to discuss whether the classification B3 Ib based on UV resonance lines really pertains to the photosphere of the secondary. These lines, through their P-Cygni profiles, manifest that they are formed mostly in the wind material . However, the only true photospheric line may be 1183.7 Å of NIII(20), seen in the Copernicus spectrum. It indicates a spectral type of B3 or earlier (Duvignau, Friedjung & Hack 1979);however, this identification is regarded as uncertain. Hence the spectral classification of the secondary remains open. The compromise is a B3. star surrounded by a disc whose colour temperature corresponds to a B8–B9 star, which may come close to a realistic model.

6. Conclusion

The absolute magnitude of the primary seems to be close to M_v of –4.8 ± 1.0 which is similar to the value derived for KS Per of 3.7 ± 0.7 by Danziger, Wallerstein & Böhm-Vitense (1967). From the ANS observations of depth of the secondary eclipse, it appears that the hotter secondary is surrounded by a disc which makes the colours of the secondary similar to a B8–B9 star. The strength of the stellar (or systemic) wind lines of C IV 1550 Å do not change even during the secondary eclipse indicating that the wind is not affected by the orbital motion. The appearance of [N II] 6583 Å indicates a low density envelope. Finally, from radio observations an upper limit to the mass loss rate is estimated as 5×10^{-7} $M_\odot yr^{-1}$. To understand the system fully a complete phase coverage is needed in the UV as well as in the optical.

Acknowledgements

We would like to thank Drs D. P. Gilra and P. R. Wesselius for providing the ANS observations. We would like to express our appreciation to Mr Alok Patnaik for help with reductions of VLA data and Ms Peggy Perley for carrying out the VLA observations for us. Thanks are also due to Dr R. Rajamohan for going through the manuscript. We also would like to thank the referees for their comments.

References

Adams, W. S. 1943, *Astrophys. J.,* **97**, 105.
Adams, W. S. 1949, *Astrophys. J.,* **109**, 354.
Bidelman, W. P. 1949, *Astrophys. J.,* **109**, 544.

Bohlin, R. C, Holm, A. V. 1984, *IUE News Letter NASA,* **24**, 73.
Cousins, A. W. J. 1963, *Mon. Not. R. astr. S. Africa,* **22**, 151.
Coyne, G. V. 1976, *Astr. Astrophys.,* **49**, 89.
Coyne, G. V., Gehrels, T. 1967, *Astr. J.,* **72**, 887.
Danziger, I. J., Wallerstein, G., Böhm-Vitense, E. 1967, *Astrophys. J.,* **150**, 239.
Drilling, J. S. 1980, *Astrophys. J.,* **242**, L43.
Drilling, J. S., Schönberner, D. 1982, in *Advances in Ultraviolet Astronomy,* Eds Y. Kondo, M. J. Mead & R. D. Chapman, NASA, CP-2238, p. 546.
Drilling, J. S., Schönberner, D., Heber, U., Lynas-Gray, A. E. 1984, *Astrophys. J.,* **278,** 224.
Duvignau, H., Friedjung, M., Hack, M. 1979, *Astr. Astrophys.,* **71,** 310.
Dworetsky, M. M., Whitelock, P. A., Carnochan, D. J. 1982, *Mon. Not. R. astr. Soc.* **201**, 901.
Dyck, H. M., Milkey, R. W. 1972, *Publ. astr. Soc. Pacific,* **84**, 597.
Eggen, O. J., Krön, G. E., Greenstein, J. L. 1950, *Publ. astr. Soc. Pacific,* **62**, 171.
FitzGerald, M. P.197O*, Astr. Astrophys.,* **4**, 234.
Gaposchkin, S. 1945, *Astr. J.,* **51**, 109.
Greenstein, J. L. 1940, *Astrophys. J.,* **91**, 438.
Greenstein, J. L. 1950, *Astrophys.* J., **111**, 20.
Greenstein, J. L., Adams, W. S. 1947, *Astrophys. J.,* **106**, 339.
Greenstein, J. L., Merrill, P. W. 1946, *Astrophys.* J., **104**, 177.
Hack, M., Flora, U., Santin, P. 1980, in *IAU Symp.* 88: *Close Binary Stars: Observations and Interpretation,* Eds M. J.Plavec, D.M.Popper &R. K.Ulrich, D. Reidel,Dordrecht, p.271.
Hellings, P., de Loore, C, Burger, M., Lamers, H. J. G. L. M. 1981, *Astr. Astrophys.,* **101**, 161.
Irwin, J.B.1960, *Astronomical Techniques,* Ed. W.A. Hiltner, University of Chicago Press, p.584.
Kippenhahn, R., Meyer-Hofmeister, E. 1977, *Astr. Astrophys.,* **54**, 539.
Lesh, J. R. 1968, *Astrophys. J. Suppl,* **17**, 371.
Lesh, J. R. 1979, in *IAU Coll.* 47: *Spectral Classification of the Future,* Eds M. F. McCarthy, A. G. D. Philip & G. V. Coyne, Vatican Observatory, p. 81.
McLaughlin, D. P. 1939, *Publ. Am. astr. Soc.,* **9**, 224.
Nariai, K. 1967, *Publ. astr. Soc. Japan,* **19**, 564.
Plavec, M. 1973, in IAU Symp. 51: *Extended Atmospheres and Circumstellar Matter in Spectroscopic Binary Systems,* Ed. A. H. Batten, D. Reidel, Dordrecht p. 216.
Plavec, M. J.,Weiland, J.L., Dobias, J.1982, *Advances in Ultraviolet Astronomy,* Eds Y. Kondo, M. J. Mead & R. D. Chapman, NASA CP-2238, p. 550.
Savage, B. D., Jenkins, E. B. 1972, *Astrophys. J.,* **172**, 491.
Schönberner, D., Drilling, J. S. 1983, *Astrophys. J.,* **268,** 225.
Seaton, M. J. 1979, *Mon. Not. R. astr. Soc,* **187,** 73p.
Serkowski, K., Mathewson, D. S., Ford, V. L. 1975, *Astrophys. J.,* **196,** 261.
Spitzer, L. 1962, *Physics of Fully Ionized Gases,* Interscience, New York, p. 148.
Wesselius, P. R., van Duinen, R. J., Aalders, J. W. G., Kester, D. 1980, *Astr. Astrophys.,* **85,** 221
Wesselius, P. R., van Duinen, R. J., de Jonge, A. R. W., Aalders, J. W. G., Luinge, W., Wildeman, K. J. 1982, *Astr. Astrophys. Suppl. Ser.,* **49,** 427.
Wright, A. E., Barlow, M. J. 1975, *Mon. Not. R. astr. Soc,* **170,** 41.

J. Astrophys. Astr. (1985) **6**, 113-130

Yields of Nucleosynthesis from Massive and Intermediate Mass Stars and Constraints on their Final Evolution

D. C. V. Mallik & Sushma V. Mallik *Indian Institute of Astrophysics, Bangalore 560 034*

Received 1984 December 11; accepted 1985 May 21

Abstract. Nucleosynthetic yields and production rates of helium and heavy elements are derived using new initial mass functions which take into account the recent revisions in O star counts and the stellar models of Maeder (1981a, b) which incorporate the effects of massloss on evolution. The current production rates are significantly higher than the earlier results due to Chiosi & Caimmi (1979) and Chiosi (1979), and a near-uniform birthrate operating over the history of the galactic disc explains the currently observed abundances. However, the yields are incompatibly high, and to obtain agreement it is necessary to assume that stars above a certain mass do not explode but proceed to total collapse. Further confirmation of this idea comes from the consideration of the specific yields and production rates of oxygen, carbon and iron and the constraints imposed by the observational enrichment history in the disc as discussed by Twarog & Wheeler (1982). Substantial amounts of ^{4}He and ^{12}C, amongst the primary synthesis species, are contributed by the intermediate mass stars in their wind phases. If substantial numbers of them exploded as Type I SN, their contribution to the yields of ^{12}C and ^{56}Fe would be far in excess of the requirements of galactic nucleosynthesis. Either efficient massloss precludes such catastrophic ends for these stars, or the current stellar models are sufficiently in error to leave room for substantial revisions in the specific yields. The proposed upward revision of the ^{12}C $(\alpha, \gamma)^{16}$O rate may produce the necessary changes in stellar yields to provide a solution to this problem. Stars that produce most of the metals in the Galaxy are the same ones that contribute most to the observed supernova rate.

Key words: stars, nucleosynthesis — stars, birthrate—stars, intermediate mass — Supernovae, Type I

1. Introduction

Our understanding of the chemical enrichment of the interstellar medium is critically dependent upon our knowledge of the processes of nucleosynthesis, mass ejection and final evolution of stars. Recent evolutionary computations of massive as well as low and intermediate mass stars include the effects of massloss via stellar winds and contain the details of nucleosynthetic yields as a function of the initial stellar mass. Along with the

theoretical developments, new and vastly improved observational data have become available, and a meaningful comparison of theoretical results with what is actually observed is now possible. Such comparisons are crucial in limiting theoretical possibilities, and they provide important constraints for the models of chemical evolution of galaxies.

In an earlier paper (Mallik 1981), we had investigated the rate of element production in the solar neighbourhood using the stellar nucleosynthesis data from Arnett (1978, hereinafter A78) and the birthrate function determined by Lequeux (1979). The essential new feature of Lequeux's birthrate function was a correction applied to the O star counts based on the belief that a significant fraction of them belonged to an older, evolved population. When the observed surface densities were corrected for the presence of this population, the numbers dropped considerably for masses above 24 $M_{\odot}$ 8. The derived birthrate function was fairly steep (with a slope of – 2.1, compared to the Salpeter function with its slope of – 1.35). As a result, the current element production rate turned out to be rather low. If the observed abundances in the disc were assumed to be a result of nucleosynthesis in massive stars, the past star formation rate had to be much higher. The inferred high star formation rate in the past would violate the continuity constraint on the initial mass function (Tinsley 1977a; Miller & Scalo 1979, hereinafter MS).

It is now fairly certain that Lequeux had overcorrected for the OB 'runaway' stars and, if at all, one should use the surface densities obtained by him with the 'runaways'. Moreover, Lequeux possibly underestimated the effects of interstellar extinction and arrived at rather low surface densities (see Garmany, Conti & Chiosi 1982). For both these reasons the birthrate function determined by Lequeux is deemed unreliable. There have been important revisions to the IMF for the massive stars, correcting for the earlier incompleteness of the data, and using better evolutionary models that take into account the effects of massloss. They imply a higher birthrate for the massive stars and therefore, a higher current rate of nucleosynthesis, and hence a slower variation of the stellar birthrate during the lifetime of the galactic disc. From an observational study of the ages and metallicity distribution of F and G dwarfs, Twarog (1980) concluded that the stellar birthrate had been more or less uniform.

A related problem in the chemical evolution of galaxies is the ratio of helium to heavy element enrichment. From a theoretical point of view, a linear correlation is expected. Peimbert (1977), Lequeux *et al.* (1979) and Rayo, Peimbert & Torres-Peimbert (1982) find a steep linear correlation with $\Delta Y / \Delta Z \sim 2.0$–$3.0$. Shaver *et al.* (1983) conclude, from a study of radio recombination lines in galactic H II regions that $\Delta Y / \Delta Z$ is close to 0.8, a value much smaller than those quoted by Peimbert and coworkers. The steep slope of helium to heavy-element enrichment, if confirmed, would pose a serious theoretical problem, since no combination of any reasonable IMF and the available stellar nucleosynthesis data is able to produce this slope (Hacyan *et al.* 1976; Gingold 1977; Mallik 1980). Chiosi and coworkers (Chiosi & Caimmi 1979; Chiosi 1979) argued that if massloss from massive stars were taken into account in the evolutionary models, the mass of the helium core M_{α}, for a given initial mass $M$of the star, would be greatly reduced and subsequent evolution of the core would, then, generate heavier elements in much smaller quantities. Using A 78 but a modified M (M_{α}) relation, they computed a much higher $\Delta Y / \Delta Z$. They further noted that this was a lower limit since the loss of He-rich material by stellar wind, during the core H- and He-burning phases, was not taken into account. However, the reduced ability of massive stars to produce heavy elements

was reflected in a derived low rate of nucleosynthesis. The past star formation rate was inferred to be higher by a factor of 25-30.

New evolutionary models have since been computed by Maeder (1981a, b) who includes the effects of massloss and follows the evolution beyond He-burning to core carbon ignition. Maeder has studied the M (M_α) relation implied by his models and finds that it is more in agreement with the one used in A78. Maeder (1981b) computed the stellar yields of helium and heavy elements as a function of the stellar mass from his models and used the same to calculate nucleosynthetic yields from a generation of stars. Using MS and the new stellar data, he found that a maximum variation of a factor of 3 in the SFR over the history of the disc is sufficient to explain the observed abundances. This result is in near perfect agreement with the earlier estimate by Wheeler, Miller & Scalo (1980, hereinafter WMS). Maeder (1981b) obtained a $\Delta Y / \Delta Z \sim 0.75$ which is similar to the previous estimates, when no massloss was taken into account, and concluded that massloss in massive stars does not alter this ratio significantly. None of these authors took into account the contribution of the intermediate mass stars although these stars are known to produce significant amounts of He and CN elements (Renzini & Voli 1981), and may also contribute to Fe enrichment should they explode finally as Type I SN (Iben 1981).

The rate of nucleosynthesis depends on the current SFR and the upper portion of the initial mass function. The yield is independent of the former and depends on the complete mass range of the IMF since, by definition, it is the ratio of the mass of a certain species newly formed and ejected by a generation of stars to the mass of that generation that remains locked up in unevolved stars and stellar remnants. The ratio $\Delta Y / \Delta Z$, on the other hand, depends only on the IMF of the evolving stars and most critically on its slope, since it determines the relative numbers of helium and heavy-element producing stars. Twarog & Wheeler (1982, hereinafter TW) have compared the data obtained by Twarog (1980) and Clegg, Lambert & Tomkin (1981) with model predictions based on the production rates of WMS and the assumption of a uniform SFR. They discovered that the Fe production rate had to be reduced to match the age-metallicity relation of Twarog. Secondly, even when the Fe yield was fixed at the value dictated by the observations, the enrichment history of other elements could be faithfully reproduced if the integrated yields of these elements relative to Fe were reduced by fixed amounts compared to the WMS values. This led TW to investigate into the possible alterations of the IMF that would result in reduced yields and reduced element production rates without jeopardizing the constraint on the variation of SFR. They concluded that observations could be reconciled with the theory, if the IMF were cut off at some upper limit so that stars that are more massive do not explode at all. For example, on the assumption that oxygen came entirely from massive stars, they found that a cut-off at 25 $M_\odot$ was required by the observations for a slope of the IMF similar to the MS value of – 2.3, and in this case both Fe and C were underproduced in massive stars. They suggested that these deficiencies could be made up by contributions from intermediate mass stars (IMS, $2.5 < M / M_\odot \lesssim 9$) although this possibility was not explored in detail by these authors. They, however, put rather stringent limits on the production of C and Fe from IMS.

In the present paper, we address ourselves to many of the questions regarding stellar nucleosynthesis and chemical evolution of the disc. The recent modifications of the O star counts have been taken into account to derive new consolidated IMFs. The current SFR is then fixed on the basis of the continuity constraint. These IMFs have been used

in conjunction with the stellar models of Maeder to estimate the nucleosynthetic yields from massive stars, the current rate of nucleosynthesis and $\Delta Y / \Delta Z$. Nucleosynthesis by the intermediate mass stars has also been calculated from the models of Renzini & Voli (1981). The net production rates and yields are compared with observations to infer the variation of SFR and place constraints on nucleosynthesis from massive stars.

To study the nucleosynthesis pattern of the individual species further, the stellar data from A78 have been used. The limits imposed by the galactic abundance data on the production of the major nucleosynthesis species ^{12}C, ^{16}O and ^{56}Fe require upper mass cut-offs to the IMF. The effect of such a procedure on the yields and the helium to heavy-element ratio has been investigated in some detail. On the assumption that ^{16}O is produced almost exclusively by massive stars, our calculations indicate that substantial amounts of ^{12}C and small amounts of ^{56}Fe are required to be produced by other sources which brings into focus the role of the intermediate mass stars in galactic nucleosynthesis. These stars produce and eject varying amounts of ^{4}He, ^{12}C, ^{13}C, ^{14}N and s-process elements during their quasi-static evolution. If the IMS end their lives as white dwarfs after ejecting their residual envelopes as planetary nebulae, they add little to the production of other primary species. However, the possibility of a more catastrophic end, where some of these stars explode as carbon detonation or deflagration Supernovae, has been extensively discussed in the literature (Arnett 1969; Tinsley 1977b, 1980a; Wheeler 1978, 1981; Nomoto 1981, 1984). In such an event, copious amounts of ^{56}Fe, other iron-peak elements, some intermediate mass elements (^{40}Ca, ^{28}Si, ^{32}S *etc.*) as well as ^{12}C and ^{16}O may be produced from the disrupted cores of these stars. The occurrence of such an eventuality is principally controlled by the quiescent massloss phenomenon during the red giant phases of evolution of these stars and may be prevented altogether in case of efficient massloss. In Section 3 of this paper we calculate the magnitude of enrichment due to this process and discuss the rather drastic effects this should have on the observed abundances.

2. Nucleosynthetic yields, current production rate of metals and the ratio of helium to heavy element enrichment

2.1 *Initial Mass Function and the Current Star Formation Rate*

The essential first step in determining the IMF is to obtain from counts of stars reliable surface densities of main sequence stars as a function of their mass, the so-called present day mass function (PDMF). Since massive stars are fewer in number, the errors in the derived PDMF are rather large. The poor luminosity designation of O stars posed a further problem in the earlier determinations. It has also been known for some time that the hydrogen-burning main-sequence for massive stars is much wider than previously assumed, and B type supergiants should also be included in the derivation of the PDMF. Owing to these drawbacks the PDMFs of Miller & Scalo (MS) and Lequeux (1979) are increasingly unreliable at larger masses. Improvements in O star catalogues with large data sets and proper luminosity identification of these stars have corrected for these deficiencies. Using larger volume-limited samples of OB stars, several authors, in the last couple of years, have rederived the PDMFs for massive stars in the Galaxy (Garmany, Conti & Chiosi 1982; Bisiacchi, Firmani & Sarmiento 1983). The surface densities in the different mass intervals arc considerably larger than the

corresponding values in MS and the PDMFs extend to higher masses. Fig. 1 displays the PDMFs determined by the different authors. The uncertainties in the numbers are much less than the differences produced by the new data on O stars. The most recent determination is due to Humphreys & McElroy (1984). Their derived IMFs are very similar to that of Bisiacchi *et al.* In our calculations the data from Garmany *et al.* and Bisiacchi *et al.* have been used.

While the IMF is generally assumed to be independent of time, the time variation of SFR is explicitly considered, since the presently observed number of main-sequence stars at any mass contains stars of this mass formed at different times but within one main-sequence lifetime of the present corresponding to this mass. For the massive stars, which are shortlived compared to the age of the Galaxy, the PDMF divided by the main-sequence lifetime yields directly the current birthrate. For stars with long lifetimes, the history of the birthrate appears in the relation between PDMF and IMF (see Tinsley 1980a, for details). MS has emphasized that a choice of an IMF with an arbitrary choice of SFR will not, in general, reproduce the PDMF and a consistent choice has to be always made in this regard. Further, the continuity of the IMF near the present turn-off mass of the Galaxy provides a fundamental constraint on the variation of SFR with time. We follow the procedure laid down in MS and derive consolidated new IMFs using the counts from MS for stars less than 20 $M_{\odot}$, and the new counts from Garmany *et al.* and Bisiacchi *et al.* for stars more massive than 20 $M_{\odot}$. The quantity finally obtained, after satisfying the continuity constraint for a time-varying birthrate, is ξ (log m) which is defined as the total number of field stars that have ever

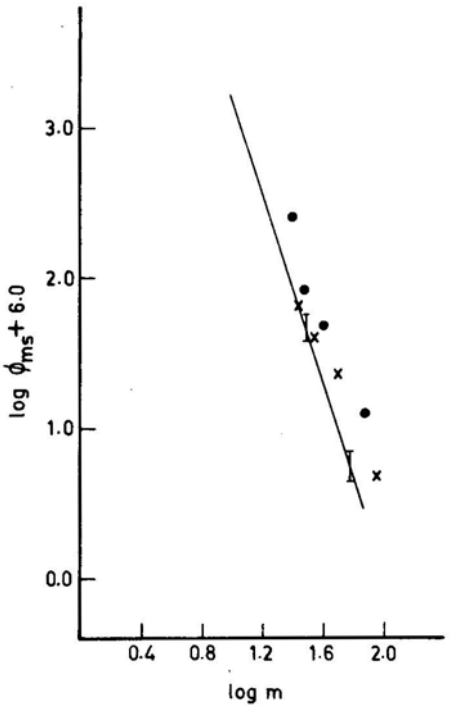

Figure 1. The present day mass functions (PDMF) from MS (solid line), Garmany *et al.* (crosses) and Bisiacchi *et al.* (filled circles).

formed per pc^2 per logm in the solar neighbourhood. This is related to the normalized field star IMF $\phi(m)$ through

$$m\phi(m)\psi_1 = \log e \frac{\xi(\log m) b(T_0)}{T_0}. \quad (1)$$

Here ψ_1 is the current SFR, T_0 the age of the Galaxyand $b(T_0)$ the birthrate at T_0 in units of the average birthrate. All through the paper m will denote the initial main-sequence mass in solar units. If SFR decreased with time, for an assumed T_0 of 12×10^9 yr, the extreme present birthrate satisfying the continuity constraint (MD birthrate in MS parlance) is given by $b(T_0) = 0.24$. For a uniform birthrate $b(T_0) = 1$. We have integrated Equation (1) to obtain ψ_1 for the prescription of a uniform birthrate and a maximum allowable decreasing birthrate. Simple power-law fits to these IMFs and the derived values of ψ_1 are summarized in Table 1. It is seen that ψ_1 is relatively insensitive to the changes at the upper end of the IMF brought about by the new counts on O stars. The $\phi(m)$'s for the uniform birthrate are somewhat different from the $\phi(m)$'s for the MD birthrate. We emphasize that the use of an arbitrary ψ_1 with any $\phi(m)$ will, in general, lead to erroneous results.

2.2 *Production Rates and Nucleosynthetic Yields from Massive Stars*

Once $\phi(m)$ and ψ_1 are known, it is straightforward to obtain the current production rates of elements and the nucleosynthetic yields. Arnett (A78) computed the absolute yields of abundant nuclei as a function of the helium core mass, M_a, which was related to the initial main-sequence mass M of the star through a M (M_α) transformation based on conservative evolutionary sequences. Since then, Maeder (1981a, b) has evolved models with massloss and obtained stellar yields as a function of the stellar mass. An important feature of the mass-losing models is the evaluation of the separate contributions to the enrichment from the stellar wind and the final supernova event. The stellar wind contribution is important during the longer-lived H and He-burning phases and for helium and some of the CNO elements. Maeder's models thus provide an opportunity to study in greater detail the production of helium and also the ratio of helium to heavy-element enrichment. We have used Maeder's models to compute the

Table 1. The initial mass function and the current star formation rate.

Data	Birthrate prescription	$\phi(m)$	Current SFR ψ_1 $M_\odot$ pc^{-2} Gyr^{-1}	Reference in text
MS for $m < 20$, and Garmany *et al.* for $m > 20$	Maximum, decreasing	$0.40m^{-2.82}$, $m < 10$ $0.10m^{-2.21}$, $m \geqslant 10$	3.0	1(a)
	Uniform	$0.42m^{-2.68}$	4.6	1(b)
MS for $m < 20$, and Bisiacchi *et al.* for $m > 20$	Maximum, decreasing	$0.38m^{-2.6}$	3.0	1(c)
	Uniform	$0.50m^{-2.69}$, $m < 10$ $1.00m^{-3.01}$, $m \geqslant 10$	4.6	1(d)

nucleosynthetic yields and the current production rates. We have considered his case B results only. In Maeder's work the stellar yields are given by mp_{ym} and mp_{ym} which are the respective masses of newly synthesized helium and metals ejected into the interstellar medium from a star of initial mass m. Both p_{ym} and p_{zm} are the sums of the contributions from the stellar wind(p_{im}^{wind})and the supernova event(p_{im}^{sn}). While p_{Ym}^{wind} is substantial for all masses, Maeder's work shows that p_{Zm}^{wind} is important only for certain special cases when Wolf-Rayet stars of the type WC may form.

The production rate of newly synthesized metals at time t is then

$$\int_{m_t}^{\infty} mp_{Zm}\phi(m)\psi(t-\tau_m)\mathrm{d}m \tag{2}$$

where $\psi(t)$ is the SFR, τ_m the lifetime of the star of mass m and m_t the turn-off mass. To evaluate the current production rate, t is replaced by the age of the Galaxy and m_t by m_1, the present turn-off mass. Since most of the synthesis is effected by rather massive stars for which $\tau_m < T_0$, expression (2) is simplified further by the use of the instantaneous recycling approximation to

$$\dot{\Sigma}_Z = \psi_1 \int_{m_1}^{\infty} mp_{Zm}\phi(m)\mathrm{d}m \tag{3}$$

where ψ_1 is the current SFR. If a star of mass m leaves a remnant of mass r_m, the fractional mass returned to the interstellar medium per generation is given by

$$R = \int_{m_1}^{\infty} (m - r_m)\phi(m)\mathrm{d}m. \tag{4}$$

Therefore, the heavy element yield

$$y_Z = \frac{1}{1-R}\int_{m_1}^{\infty} mp_{Zm}\phi(m)\mathrm{d}m. \tag{5}$$

Similarly, for helium

$$\dot{\Sigma}_Y = \psi_1 \int_{m_1}^{\infty} mp_{Ym}\phi(m)\mathrm{d}m \tag{6}$$

and

$$y_Y = \frac{1}{1-R}\int_{m_1}^{\infty} mp_{Ym}\phi(m)\mathrm{d}m.$$

For evaluating R, we have used the prescription of Iben & Truran (1978) for the mass of the white dwarf as a function of the initial main-sequence mass and have assumed $r_m = 1.4$ for $m > 8$.

The results are presented in Table 2a. The rate of nucleosynthesis is estimated to be much higher than the earlier estimates (Chiosi & Caimmi 1979; Chiosi 1979; Mallik 1981). The earlier low values are attributable to the use of a wrong IMF in the case of Mallik (1981) and to the use of a wrong M (M_a) transformation in the case of Chiosi & Caimmi (1979) and Chiosi (1979). Thus, massloss in massive stars does not seem to produce any major effect on the final rate of nucleosynthesis. The rate is a bit higher than the WMS rate partly due to the use of a different IMF and partly due to different stellar yields. The ratio of helium to heavy-element enrichment is uniformly low and, contrary to the assertion of Chiosi and Caimmi, we conclude that massloss has little effect on this ratio even though the wind contribution to He-enrichment has been explicitly taken into account here.

2.3 *Contribution of Intermediate Mass Stars*

Although massive stars are generally held responsible for element synthesis, the intermediate mass stars make significant contribution to the enrichment of ^{4}He, ^{12}C, ^{14}N, ^{13}C and s-process elements. We have used the stellar yields from Renzini & Voli (1981) to estimate the enrichment rate of helium and CNO elements. The dredge-up and mixing of enriched material into the envelopes of these stars and hence the final enrichment of the interstellar medium are sensitively dependent on the massloss parameter η, and the ratio of the mixing length to the pressure scale height, denoted by the parameter α. Higher rates of massloss reduce the time spent by these stars on the asymptotic-giant branch and therefore the growth of the core is also reduced and the total amount of matter dredged up is less. In the absence of any massloss, enormous amounts of ^{12}C and s-process elements would be produced by these stars, far in excess of the requirements of galactic nucleosynthesis (Iben 1981). The effect of the parameter α is to induce burning at the base of the convective envelope which causes further processing of the material dredged up following each He-shell flash episode. The consequence of this is to produce fresh ^{14}N and ^{13}C in CNO cycle at the expense of ^{12}C and ^{16}O which were produced in He-burning. Some amounts of ^{4}He are also produced in this case. To have representative estimates of the enrichment caused by intermediate mass stars we have chosen three of the cases considered by Renzini & Voli: Case a, with $\eta = \frac{1}{3}$ $\alpha = 0$, case e with $\eta = \frac{1}{3}$, $\alpha = 2$, and case f with $\eta = \frac{2}{3}$ $\alpha = 0$. In Table 2b, the results are given. It is obvious that intermediate mass stars are an important source of ^{4}He and they add to the metals mostly in the form of CNO elements. The approximation of instantaneous recycling used here for the IMS is still justified because the bulk of the contribution comes from $m > 3.0$ with peaks around $m = 5$ or 6, and the main-sequence lifetime of a 3 $M_{\odot}$ star is only 0.3 Gyr.

Table 2a. Production rates and yields from massive stars.

IMF	R	$\dot{\Sigma}_Y$ ($M_\odot$ pc^{-2} yr^{-1})	$\dot{\Sigma}_Z$ ($M_\odot$ pc^{-2} yr^{-1})	y_Y	y_Z	$\Delta Y/\Delta Z$
1(a)	0.352	3.90(−11)	5.86(−11)	0.020	0.030	0.48
1(c)	0.389	4.08(−11)	5.61(−11)	0.022	0.031	0.51

Table 2b. Contribution from intermediate-mass stars.

IMF	η	α	$\dot{\Sigma}_Y$ ($M_\odot$ pc^{-2} yr^{-1})	$\dot{\Sigma}_{CNO}$ ($M_\odot$ pc^{-2} yr^{-1})
1(a)	1/3	0	1.30(−11)	4.62(−12)
		2	1.51(−11)	8.72(−12)
	2/3	0	1.08(−11)	3.18(−12)
1(c)	1/3	0	1.84(−11)	6.33(−12)
		2	2.14(−11)	8.86(−12)
	2/3	0	1.53(−11)	4.44(−12)

The total production rates are the sums of the contributions from massive stars and intermediate mass stars. These along with the yields are given in Table 3 The proportionate increase in helium production due to the contribution of intermediate-mass stars is larger. These yields imply $\Delta Y / \Delta Z = 0.58 - 0.69$, for an initial $Y = 0.28$ The ratio is somewhat increased over the values obtained when only massive stars were considered *(vide* Table 2a). However, it is less than unity.

It should be noted that in the absence of massloss, the vast majority of these stars ($2 \lesssim m \lesssim 8$) would proceed to thermonuclear disintegration following carbon ignition in their degenerate cores. As the cores disrupt totally, large amounts of Fe-peak elements as well as carbon and oxygen should be added to the galactic pool. In our discussion so far, the rather drastic effects of core disruption have not been considered. For the massloss parameters used here, the maximum initial mass of a star becoming a white dwarf is either 4.75 ($\eta = \frac{1}{3}$) or 6.0 ($\eta = \frac{2}{3}$). Thus a crucial gap is left open, between a 4.75 or 6.0, and 8.0 or 9.0 solar masses, for core disruption Supernovae to occur. We postpone a discussion of this possibility to Section 3.

2.4 *The Yield*

The heavy element yields presented in column 6 of Table 2a and column 5 of Table 3 are rather high. Pagel & Patchett (1975) were the first to analyse in detail the abundance data in the solar neighbourhood and they arrived at a value of the yield between 0.004 and 0.006. Since then, several other studies have been made and somewhat higher values of yields have been obtained. Twarog (1980), in his study of the age-metallicity relation of the disc stars, determined the present value of $\Delta Z / y_z$ to be 1.76, which, for a value of $\Delta Z = 0.02$ leads to a $y_z = 0.0114$. Peimbert & Serrano (1982) have derived yields from observational data on a number of galaxies and in a variety of galactic objects. The range in the yields is rather narrow with all the values lying between 0.002 and 0.014. Their value for the solar neighbourhood is 0.007, almost a factor of two lower than Twarog's. Tinsley (1980b) has emphasized that all consistent models for the solar neighbourhood predict that the mean metallicity of disc stars lies within 20 per cent of the yield. Thus, assuming that the mean metallicity $\Delta Z = 0.8 Z_{\odot}$, one obtains for the heavy element yield a range 0.013–0.019. All these values are lower than the computed yields based on the IMF we have advocated. From a detailed analysis of the data from Clegg, Lambert & Tomkin (1981) with the help of a standard infall model, Twarog & Wheeler (TW) came to the conclusion that the theoretical yields in WMS were too high.

Table 3. Total production rates and yields.

IMF	$\dot{\Sigma}_Y$ ($M_\odot$ pc^{-2} yr^{-1})	y_Y	$\dot{\Sigma}_Z$ ($M_\odot$ pc^{-2} yr^{-1})	y_Z
1(a)	5.20(−11)	2.68(−2)	6.32(−11)	3.25(−2)
	5.41(−11)	2.78(−2)	6.73(−11)	3.46(−2)
	4.98(−11)	2.56(−2)	6.18(−11)	3.18(−2)
1(c)	5.92(−11)	3.23(−2)	6.24(−11)	3.40(−2)
	6.22(−11)	3.39(−2)	6.50(−11)	3.55(−2)
	5.61(−11)	3.06(−2)	6.05(−11)	3.30(−2)

The IMFs used here are derived from higher stellar surface densities than those obtained in MS. Therefore, it is not surprising that the yields determined here are even higher. Unless the stellar yields are in error by large factors, there is no escape from the fact that the theoretical yields computed here are incompatible with observations.

2.5 *Effect of Cutoffs in the IMF*

As anticipated in the introduction, the nucleosynthetic yields per generation can be reduced without altering the IMF or the stellar yields if we assume that stars beyond a certain upper mass limit evolve to total collapse. This would help reduce the net contribution by massive stars to metal production.

The upper mass cutoffs in the IMF will also have the effect of reducing the current production rates. This leads to the following problem. A low current rate of nucleosynthesis implies that the past SFR was much higher to produce the currently observed abundances. However, other evidences (Twarog 1980) and the continuity constraint on the IMF require that the SFR is more or less uniform. The revised IMFs and Maeder's stellar yields used above, make the current production rate sufficiently high such that the need for a higher SFR in the past is precluded. With the introduction of the cutoffs in the IMF now, are we violating the constraint of uniform birthrate? In an effort to find an answer, we have introduced cutoffs to the IMF and recomputed $\dot{\Sigma}_z$, $\dot{\Sigma}_Y$, y_z, y_Y, R and derived $\langle \psi \rangle / \psi_1$ in each case. The results are displayed in Fig. 2, where m_u denotes the upper limit on the main-sequence mass beyond which stars are presumed to proceed to total collapse without adding to the enrichment of the ISM. As m_u increases, $\dot{\Sigma}z$ goes up and so does y_z. $\langle \psi \rangle / \psi_1$ decreases. We find that there is a range in m_u for which y_z lies in the range of observed values and $\langle \psi \rangle / \psi_1$ is within the limits consistent with a near uniform birthrate. With the IMF 1 (a) a cutoff at $m_u = 48$ produces an yield $y_z = 0.015$. The production rate of metals is 0.029 $M_\odot$ pc^{-2} Gyr^{-1} and $\langle \psi \rangle / \psi_1 = 2.7$. For $m_u = 39$, $y_z = 0.011$ and $\langle \psi \rangle / \psi_1 = 3.5$. This value is marginally consistent with a near uniform birthrate. Similar cutoffs are obtained for the IMF l(c).

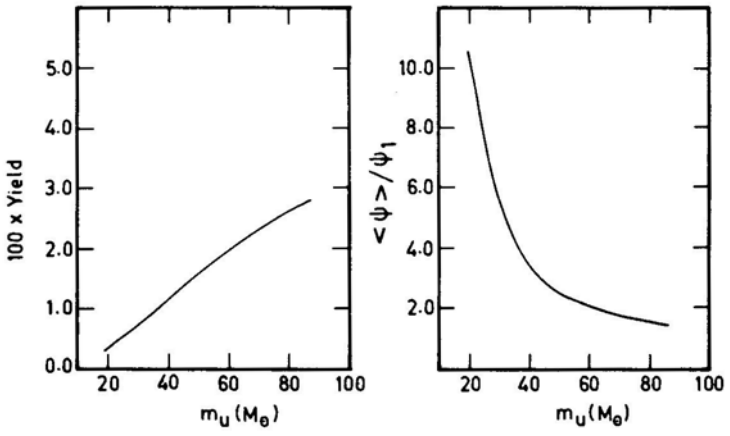

Figure 2. Yield and the variation of the star formation rate as a function of m_u. A value of $\Sigma = 50\ M_\odot$ pc^{-2} has been used.

A further effect of introducing the cutoffs in the IMF is to change the value of $\Delta Y / \Delta Z$. Since helium production is weighted heavily towards the lower masses, y_Y is, in general, less sensitive to the choice of m_u. Moreover, stars with $m > m_u$ evolve through the H-and He-burning phases before collapsing to black holes and $p_{Ym}^{\text{wind}}$is non zero for them. Thus y_y/y_z dramatically increases with decreasing m_u and $\Delta Y / \Delta Z$ is increased. For $m_u = 40$, $y_y/y_z = 1.76$ while for $m_u = 30$, it goes up to 2.47. We suggest that the large values of helium to heavy-element enrichment are an indirect indication of the massive stars evolving to black holes instead of producing Supernovae and not an effect caused by internal adjustments in the star as a result of massloss (*cf.* Chiosi & Caimmi 1979).

3. The element enrichment pattern and the effect of carbon deflagration Supernovae

In the previous section we discussed the metal production rate and heavy-element yield based on the stellar models of Maeder. Individual species were not considered. However, to gain a clearer understanding of the pattern of nucleosynthesis, it is more useful to consider the individual species. This is best done with the data from A78 where specific yields of He, C, O, Ne, Mg, Fe + Si as a function of the stellar mass are given. Observations as well as theory have suggested different enrichment histories for the primary elements like C, O and Fe (Clegg 1977; Tinsley 1979; Sneden, Lambert & Whitaker 1979). TW showed that a standard infall model with uniform birthrate was capable of reproducing this varied history of enrichment provided the yields were substantially reduced. Through this analysis they put limits on the contribution to element enrichment by IMS. The production of carbon in progenitors of planetary nebulae is a well-established fact. The important recent observation by Wu *et al.* (1983) of strong Fe II absorption lines in what is believed to be the stellar ejecta from SN 1006 and the earlier discovery by Kirshner & Oke (1975) of overabundance of iron in SN 1972e in NGC 5253 provide evidence of iron production in Type I Supernovae which are believed to be the result of core disruption of relatively low-mass stars. We now investigate in some detail the contribution of IMS to galactic carbon production and the impact of Type I SN nucleosynthesis on the production of carbon, oxygen and iron.

3.1 *Constraints on Specific Production Rates*

Based on the abundance data of Clegg, Lambert & Tomkin (1981), and the age-metallicity relation of disc stars (Twarog 1980), Twarog & Wheeler were able to derive the net yield of iron and the ratio of the yields of carbon, neon, magnesium and iron to that of oxygen. The absolute production rates of oxygen, carbon and iron obtained by them are

$$\dot{\Sigma}_{\mathrm{O}} = 1.44 \times 10^{-11} M_{\odot}\,\mathrm{pc}^{-2}\,\mathrm{yr}^{-1}, \qquad \dot{\Sigma}_{\mathrm{C}} = 7.47 \times 10^{-12} M_{\odot}\,\mathrm{pc}^{-2}\,\mathrm{yr}^{-1},$$
$$\dot{\Sigma}_{\mathrm{Fe}} = 3.92 \times 10^{-12} M_{\odot}\,\mathrm{pc}^{-2}\,\mathrm{yr}^{-1}. \tag{3.1}$$

The solar abundances of Cameron (1973) have been used in arriving at these numbers. These absolute rates have a 30-40 per cent uncertainty in them. In the following

analysis, we shall accept as observed the values in (3.1). We further assume that the birthrate has been uniform during the evolutionary lifetime of the disc, and the IMFs we use accordingly are l(b) and (d) from Table 1. The production rates of carbon, oxygen and iron as a function of m_u are displayed in Fig. 3. Here, m_u has the same significance as in Section 2. An examination of the figure reveals the following:

(i) For the IMF 1 (b), at $m_u = 28$, the production rate of oxygen equals the net galactic production rate. The corresponding production rates of carbon and iron are respectively $6.26 \times 10^{-12}\ M_\odot\ \mathrm{pc}^{-2}\ \mathrm{yr}^{-1}$ and $3.96 \times 10^{-12}\ M_\odot\ \mathrm{pc}^{-2}\ \mathrm{yr}^{-1}$. Carbon is marginally underproduced in massive stars while the iron production rate seems adequate. Since A78 yields refer to Fe + Si and not Fe alone, it is possible that a part of the contribution here comes from unburned Si. Moreover, if a higher iron production rate of $4.9 \times 10^{-12}\ M_\odot\ \mathrm{pc}^{-2}\ \mathrm{yr}^{-1}$ were assumed (see Nomoto, Thielemann & Wheeler 1984), there is a predicted deficiency of 18 per cent in iron production from massive stars. On the assumption that oxygen is produced entirely in massive stars, the combination of our birthrate function and the stellar yield data from A78 precludes the participation of stars more massive than 28 $M_\odot$ in nucleosynthesis. At $m_u = 28$ the relative yields of carbon and iron are 0.43 and 0.28 respectively. The corresponding solar values are 0.42 and 0.22.

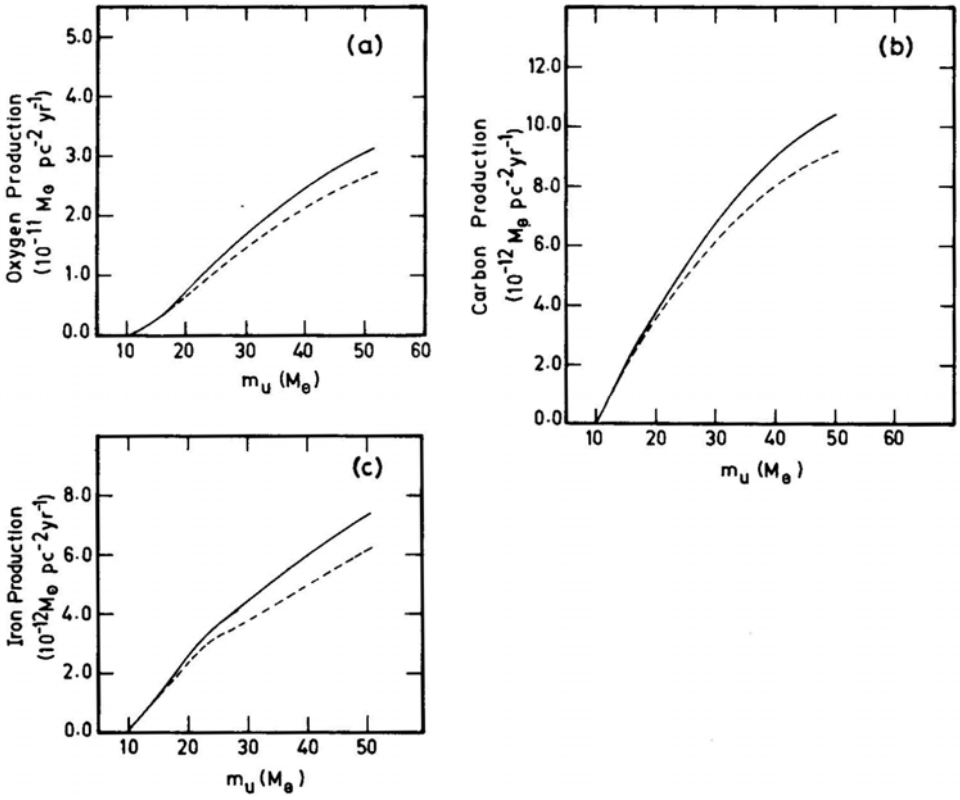

Figure 3. (a) Oxygen, (b) carbon, and (c) iron production rates as a function of m_u. The upper line in each case is calculated with the IMF 1 (b) and the lower one with 1(d).

(ii) For the IMF 1 (d), the oxygen production rate from massive stars equals the galactic production rate at m_u = 30. The corresponding production rates of carbon and iron are 6.1×10^{-12} $M_\odot$ pc $^{-2}$ yr^{-1} and 3.6×10^{-12} $M_\odot$ pc $^{-2}$ yr^{-1} respectively. This leads to a deficiency of 19 per cent in carbon production and a maximum deficiency of 27 per cent in iron production. These deficiencies are significant as they provide constraints on the production of iron and carbon from alternative sources, in particular, the IMS.

3.2 *Carbon Production in Planetary Nebulae*

The intermediate-mass stars contribute to element enrichment through the three dredge-up episodes which were first enumerated and quantified by Iben & Truran (1978). The eventual journey of these stars to the stellar graveyard of white dwarfs is critically dependent upon the massloss rate during the final evolutionary stages which controls their ability to reduce themselves below the Chandrasekhar mass limit just prior to carbon ignition in their degenerate core. There is compelling observational evidence to the fact that white dwarfs in many clusters have evolved from stars as massive as 5–8 $M_\odot$ (Romanishin & Angel 1980; Weidemann 1977; Anthony-Twarog 1982; Weidemann & Koester 1983). Planetary nebulae, which represent a transitory phenomenon in the final evolution of these stars, show enhancements of He, C and N (See Torres-Peimbert 1984 for details). French (1983) has derived carbon abundances in a large number of planetary nebulae and concluded that carbon was enhanced in the progenitors by a factor of 2 at the time of ejection of the envelopes. According to him, the enhanced carbon mass in the nebulae observed is 3.6×10^{-3} $M_\odot$ per nebula. The observed birthrate of planetary nebulae depends sensitively on the adopted distance scale but all the derived birthrates lie in the range $2.4–12.0 \times 10^{-10}$ pc^{-2} yr^{-1} (Mallik 1984). Thus the total carbon production rate from planetary nebulae amounts to $0.87–4.3 \times 10^{-12}$ $M_\odot$ pc^{-2} yr^{-1}. Therefore, planetary nebulae alone can provide 10-50 per cent of the galactic carbon. If massive stars produced carbon at the predicted efficiency, carbon would be over-produced. The models of Renzini & Voli may also be used to derive carbon production rates in the wind phases and planetary nebula ejection phases of stars in the interval $2.5 \leqslant m \leqslant 8$. A variety of values of η and α are used. The results are presented in Table 4. The production rates are too high to be compatiable with observations when $\eta = \frac{1}{3}$ and α = 0 and 1; they are in the range of observed values when $\eta = \frac{1}{3}$ and α =2 or $\eta = \frac{2}{3}$ and α = 1.5. Thus, whether the observed carbon production rate in planetary nebulae indicates a high massloss rate or an efficient burning at the base of the convective envelope, cannot be decided by looking at carbon production alone. However, the stellar models with appropriate choices of η and α are

Table 4. Carbon production in IMS.

IMF	SFR ($M_\odot$ pc^{-2} Gyr^{-1})	Rate (10^{-12} $M_\odot$ pc^{-2} yr^{-1}) $\eta = 1/3, \alpha = 0$	$\eta = 1/3, \alpha = 1.5$	$\eta = 1/3, \alpha = 2$	$\eta = 2/3, \alpha = 1.5$
1(b)	4.6	9.87	4.87	1.50	3.00
1(d)	4.6	. . .	6.30	2.10	3.75

successful in producing the right amount of carbon required by the observations of planetary nebulae. Further, carbon production in massive stars is constrained to perhaps half the observed galactic production rate.

3.3 *The Iron Production Rate and Carbon Deflagration Supernovae*

The situation is quite different with iron. First, apart from the two observations mentioned in the beginning of the section, there is no unambigous identification of iron production in any supernova event (Woltjer 1984). Yet the most plausible model for producing the uniform exponential tail of SN I light curves is the radioactive decay model involving the parent ^{56}Ni whose eventual decay product is ^{56}Fe (Arnett 1979; Colgate & Petschek 1980). Since SN I account for roughly 50 per cent of the net supernova rate, this would make them a major source of iron. Second, although it is generally recognized that SN I originate from relatively low mass stars, the exact nature of their progenitors is not known. It has often been contended that they are terminal explosions of those intermediate-mass stars which ignite carbon in their degenerate cores (see for example Tinsley 1979). On the other hand, observations of planetary nebulae and cluster white dwarfs suggest that few intermediate-mass stars may actually evolve to the point of carbon ignition. However, there are alternative scenarios for producing SN I involving accreting white dwarfs in binary systems with red supergiant companions, which appear to be quite plausible. The theoretical production rate of these events on the assumption that they are carbon detonation of single stars is consistent with the observed rate. Thus, based on the algorithm of Renzini &Voli with $\eta = \frac{1}{3}$, the deathrate of stars becoming Supernovae of this type equals 0.059 pc^{-2} Gyr^{-1} and for $\eta = \frac{2}{3}$ it equals 0.027 pc $^{-2}$ Gyr^{-1}. The observed SN I rate from Tammann (1982) is 0.029 pc^{-2} Gyr^{-1}. If SN I were all carbon detonation Supernovae releasing 1.4 $M_\odot$ of iron per event (Arnett 1969), the iron production rate from this source alone would be 4.06×10^{-11} $M_\odot$ pc $^{-2}$ yr^{-1} which is a factor of ten higher than the net galactic production rate given in (3.1). For a uniform birthrate this would lead to an iron abundance of 0.01. It is impossible that the observations are in error by any factor like this. This problem with the overproduction of iron practically rules out the occurrence of carbon detonation Supernovae.

In recent years an alternative model for the explosion has been developed principally by Nomoto (1981) in which a deflagration wave rips through the star incinerating the inner portion of the core to iron but ejecting the outer layers of the core as unburned ^{12}C and ^{16}O. The carbon deflagration models have been successful in reproducing the light curves of Type I Supernovae. Numerous deflagration models have been computed by Nomoto and collaborators (see Nomoto 1984) and by Woosley, Axelrod & Weaver (1984). The crucial feature of these models relevant to the present discussion is that although the fraction of iron ejected is less, moderate to large amounts of carbon and oxygen are also ejected by them. We have considered only two representative models, Model W7 of Nomoto (1984) and Model 5 of Woosley, Axelrod & Weaver (1984). They provide two extremes of carbon and oxygen production while the mass of iron ejected is roughly similar. These models serve our purpose of highlighting the problems of galactic nucleosynthesis when such events occur at the observed SN I rate. The production rates and the yields of carbon, oxygen and iron are tabulated for both W7 and M5 (Table 5)where we have used the observed SN I rate for the calculation. When

Table 5. Carbon, oxygen and iron production in carbon deflagration models.

SN I rate: 0.029 $pc^{-2}\,Gyr^{-1}$						
	$\dot{\Sigma}_i$ ($M_\odot\,pc^{-2}\,yr^{-1}$)		Yield		X/O	
Species	W7	M5	W7	M5	W7	M5
^{12}C	9.28(−13)	9.86(−12)	2.86(−4)	3.03(−3)	0.23	0.95
^{16}O	4.06(−12)	1.04(−11)	1.25(−3)	3.2 (−3)	1	1
^{56}Fe	1.77(−11)	1.42(−11)	5.45(−3)	4.37(−3)	4.36	1.37

these are compared with the results of the previous sections and the constraints imposed by the observations [*cf.* (3.1)], it is obvious that the iron production rate greatly exceeds the requirements. Even if carbon deflagration Supernovae were the only source of iron in the Galaxy, at the currently observed SN I rate they would produce several times (2–3) the observed abundance of iron. In reality, things are worse since massive stars also contribute to iron production. Almost all of the galactic carbon could also come from the carbon deflagrations alone which contradicts the results from Section 3.2 that at least half is produced in PN progenitors. This is true of all those models that eject several tenths of solar mass of carbon per event. It is also seen that these models predict reasonable amounts of ^{16}O production, although they may not produce enough to maintain the net galactic production rate. Even then oxygen production in these models is something of an embarassment for nucleosynthesis since all our considerations were based on the assumption that ^{16}O is entirely produced by massive stars. Oxygen has always been regarded as a signature of massive star nucleosynthesis. Observations of Cas A and some other SNR tend to support this view (Kirshner 1982). Theoretically, an examination of the stellar mass fractions returned in the form of various species clearly shows the preponderance of oxygen in the ejecta from massive stars (*cf* Fig. 2, Audouze & Tinsley 1976). Therefore, substantial oxygen production by lower mass stars will upset many seemingly well-established facts, besides violating our specific assumption here that all oxygen comes from massive stars. The carbon deflagration events clearly infringe upon one or more constraints imposed by observations and conventional wisdom on galactic nucleosynthesis.

A simple-minded solution would be not to have such events at all. However, this is not really a solution since (i) Supernovae of Type I do occur in nature and (ii) the carbon deflagration models reproduce a number of key characteristics of observed SN I events without violating any of their observational features (Sutherland & Wheeler 1984). One could perhaps ask by what factor the iron yield from these models should be reduced to satisfy the constraints on the production rates. To choose a particularly favourable case if we assumed that only 50 per cent of the Fe + Si yield as estimated in A78 was ejected as true iron, the rest being unburned silicon, our calculations show that massive stars would still contribute $2.0 \times 10^{-12}\ M_\odot\ pc^{-2}\ yr^{-1}$ to the iron production rate. If the remainder came from SN I and specifically from carbon deflagrations, the required contribution of these events should amount to at most $2.9 \times 10^{-12}\ M_\odot\ pc^{-2}\ yr^{-1}$. Thus, the expected amount of iron per deflagration event is 0.0029/0.029 or 0.1 $M_\odot$. This is about a sixth of what the models predict. However, Sutherland & Wheeler assert that the kinematics of the SN I event requires a minimum of 0.7 $M_\odot$ of incinerated material in the explosion to generate the observed ejecta velocities. Also the problem

with excess carbon from these events will still remain. It is unlikely that the SN I rate is grossly overestimated.

A glimmer of hope has been provided recently by the proposed revision of a crucial nuclear reaction rate, namely the rate for the reaction ^{12}C $(\alpha, \gamma)^{16}O$. Arnett & Thielemann (1984) quote recent experiments which suggest an enhancement of this reaction rate by a factor of 3-5 over the conventional value and discuss the implications of this upward revision. An enhanced ^{12}C $(\alpha, \gamma)^{16}O$ rate enhances the $^{16}O/\ ^{12}C$ ratio after core helium burning and therefore, during the subsequent thermonuclear phases one obtains less carbon-burning products and more oxygen-burning products. It seems logical that in the final yields of massive stars, more oxygen and less carbon would be present as the contribution from zones processed through helium burning. We already found that the yields from A 78 required an upper mass cut off to the IMF at 28-30 $M_\odot$ to have the theoretical oxygen production rate equal the observed rate in the solar neighbourhood. The same considerations with an enhanced oxygen yield should now lead to an upper mass cut off which is lower than 28 $M_\odot$ It is difficult for us to say, at the moment, how the iron yield from massive stars is affected. But the contribution of the massive stars to the production of ^{12}C would surely be considerably reduced such that, even if almost all of the galactic carbon originates in lighter stars through carbon deflagration and planetary nebula events, no serious overproduction problem would be encountered.

Finally, if the bulk of the nucleosynthesis in the Galaxy be effected by stars in the mass range 530 $M_\odot$, the death rate of these stars is found to be 0.073 pc^{-2} Gyr^{-1} or a galactic average of 10.3 yr^{-1}. The observed supernova rate from Tammann (1982) is 0.063 pc^{-2} Gyr^{-1}. These rates are equal within the limits of observational uncertainties. Therefore, a typical supernova event is also a typical nucleosynthesis event.

4. Summary and conclusions

In this paper we have attempted to arrive at a consistent picture of galactic nucleosynthesis based on improved data on stellar yields and new determinations of the IMF and the current stellar birthrate. The current rate of nucleosynthesis is high enough to obviate the need for a higher star formation rate in the past to explain the currently observed abundances. The effect of massloss on nucleosynthetic yields is negligible. However, the observed yields are low and to be consistent it is required that stars above a certain mass do not participate in nucleosynthesis. The observed large values of the helium to heavy-element enrichment ratio may be an indirect indication that this actually happens.

If the observational constraints on the current production rates of iron, oxygen and carbon are to be believed, then, stars heavier than 28–30 $M_\odot$ do not effectively participate in nucleosynthesis. Observations of planetary nebulae as well as theoretical dredge-up models of IMS indicate that nearly half the galactic carbon comes from PN progenitors. If carbon deflagration models correctly represent the Type ISN event, substantial amounts of galactic carbon and oxygen could come from them. At the observed SN I rate these models would overproduce iron by a factor of 2 to 3. The role of massive stars in element synthesis is even more suppressed in that case. While there does not seem to be any known way of preventing production of iron in massive stars, the proposed enhancement of the rate of $^{12}C(\alpha, \gamma)^{16}O$ works in the right direction for

carbon. This will certainly reduce the carbon production in massive stars considerably and enhance their oxygen yield. The galactic oxygen production rate may then be matched by synthesis in stars up to a mass m_u which is even less than 28 $M_\odot$ which, in turn, will help reduce the iron yield from massive stars. While the carbon production in deflagration events could then account for most of the galactic production, the problem of overproduction of iron due to these events is not totally solved. We have only considered the element synthesis pattern in the galactic disc. Similar considerations may not apply to the halo at all. Observations indicate a very different enrichment history for the halo.

References

Anthony–Twarog, B. J. 1982, *Astrophys. J.*, **255,** 245.
Arnett, W. D. 1969, *Astrophys. Space Sci.*, **5,** 180.
Arnett, W. D. 1978, *Astrophys. J.*, **219,** 1008 (A78).
Arnett, W. D. 1979, *Astrophys. J.*, **230,** L37.
Arnett, W. D., Thielemann, F.-K. 1984, in *Stellar Nucleosynthesis*, Eds C. Chiosi & A. Renzini, D. Reidel, Dordrecht, p. 145.
Audouze, J., Tinsley, B. M. 1976, *A Rev. Astr. Astrophys.*, **14,** 43.
Bisiacchi, G. F., Firmani, C, Sarmiento, A. F. 1983, *Astr. Astrophys.*, **119,** 167.
Cameron, A. G. W. 1973, in *Explosive Nucleosynthesis*, Eds D. N. Schramm & W. D. Arnett, Univ. Texas Press, p. 3.
Chiosi, C. 1979, *Astr. Astrophys.*, **80,** 252.
Chiosi, C, Caimmi, R. 1979, *Astr. Astrophys.*, **80,** 234.
Clegg, R. E. S. 1977, *Mon. Not. R. Astr. Soc*, **181,** 1.
Clegg, R. E. S., Lambert, D. L., Tomkin, J. 1981, *Astrophys. J.*, **250,** 262.
Colgate, S. A., Petschek, A. G. 1980 in *Type I Supernovae*, Ed. J. C. Wheeler, Univ. Texas, p. 42.
French, H. B. 1983, *Astrophys. J.*, **273,** 214.
Garmany, C. D., Conti, P. S., Chiosi, C. 1982, *Astrophys. J.*, **263,** 777.
Gingold, R. A. 1977, *Mon. Not. R. Astr. Soc.*, **178,** 569.
Hacyan, S., Dultzin-Hacyan, D., Torres-Peimbert, S., Peimbert, M. 1976, *Rev. Mex. Astr. Astrofis.*, **1,** 355.
Humphreys, R. M., McElroy, D. B. 1984, *Astrophys. J.*, **284,** 565.
Iben, I., Jr. 1981, in *Effects of Mass loss on Stellar Evolution*, Eds C. Chiosi & R. Stalio, D. Reidel, Dordrecht, p. 373.
Iben, I. Jr., Truran, J. W. 1978, *Astrophys. J.*, **220,** 980.
Kirshner, R. P. 1982, in *Supernovae: A Survey of Current Research*, Eds M. J. Rees & R.J. Stoneham, D. Reidel, Dordrecht, p. 1.
Kirshner, R. P., Oke, J. B. 1975, *Astrophys. J.*, **200,** 574.
Lequeux, J. 1979, *Astr. Astrophys.*, **80,** 35.
Lequeux, J., Peimbert, M., Rayo, J. F., Serrano, A., Torres-Peimbert, S. 1979, *Astr. Astrophys.*, **80,** 155.
Maeder, A. 1981a, *Astr. Astrophys.*, **99,** 97.
Maeder, A. 1981b, *Astr. Astrophys.*, **101,** 385.
Mallik, D. C. V. 1980, *Astrophys. Space Sci*, **69,** 133.
Mallik, D. C. V. 1981, *J. Astrophys. Astr.*, **2,** 171.
Mallik, D. C. V. 1984, *Astrophys. Lett.*, **24,** 173.
Miller, G. E., Scalo, J. M. 1979, *Astrophys. J. Suppl.*, **41,** 513 (MS).
Nomto, K. 1981, in *I AU Symp.* 93: *Fundamental Problems in the Theory of Stellar Evolution*, Eds D. Sugimoto, D. Q. Lamb, & D. N. Schramm, D. Reidel, Dordrecht, p. 295.
Nomoto, K. 1984, in *Stellar Nucleosynthesis*, Eds C. Chiosi & A. Renzini, D. Reidel, Dordrecht, p. 205.
Nomoto, K., Thielemann, F.-K., Wheeler, J. C. 1984, *Astrophys. J.*, **279,** L23
Pagel, B. E. J., Patchett, B. E. 1975, *Mon. Not. R. Astr. Soc*, **172,** 13.

Peimbert, M. 1977, in *Topics in Interstellar Matter*, Ed. H. van Woerden, D. Reidel, Dordrecht, p. 249.
Peimbert, M., Serrano, A. 1982, *Mon. Not. R. Astr. Soc.*, **198,** 563.
Rayo, J. F., Peimbert, M., Torres-Peimbert, S. 1982, *Astrophys. J.*, **255,** 1.
Renzini, A., Voli, M. 1981, *Astr. Astrophys.*, **94,** 175.
Romanishin, W., Angel, J. R. P. 1980, *Astrophys. J.*, **235,** 992.
Shaver, P. A., McGee, R. X., Newton, L. M., Danks, A. C, Pottasch, S. R. 1983, *Mon. Not. R. astr. Soc.*, **204,** 53.
Sneden, C, Lambert, D. L, Whitaker, R. W. 1979, *Astrophys. J.*, **234,** 964.
Sutherland, P. G, Wheeler, J. C. 1984, *Astrophys. J.*, **280,** 282.
Tammann, G. A. 1982, in *Supernovae: A Survey of Current Research*, Eds M. J. Rees & R.J. Stoneham, D. Reidel, Dordrecht, p. 371.
Tinsley, B. M. 1977a, *Astrophys. J.*, **216,** 548.
Tinsley, B. M. 1977b, in *Supernovae*, Ed. D. N. Schramm, D. Reidel, Dordrecht, p. 117.
Tinsley, B. M. 1979, *Astrophys. J.*, **229,** 1046.
Tinsley, B. M. 1980a, *Fundam. Cosmic Phys.*, **5,** 287.
Tinsley, B. M. 1980b, *Astr. Astrophys.*, **89,** 246.
Torres-Peimbert, S. 1984, in *Stellar Nucleosynthesis*, Eds C. Chiosi & A. Renzini, D. Reidel, Dordrecht, p.3.
Twarog, B. A. 1980, *Astrophys. J.*, **242,** 242.
Twarog, B. A., Wheeler, J. C. 1982, *Astrophys. J.*, **261,** 636 (TW).
Weidemann, V. 1977, *Astr. Astrophys.*, **59,** 411.
Weidemann, V., Koester, D. 1983, *Astr. Astrophys.*, **121,** 77.
Wheeler, J. C. 1978, *Mem. Soc. astr. Ital.*, **49,** 349.
Wheeler, J. C. 1981, *Rep. Prog. Phys.*, **44,** 85.
Wheeler, J. C, Miller, G. E., Scalo, J. M. 1980, *Astr. Astrophys.* **82,** 152 (WMS).
Woosley, S. E., Axelrod, T. S., Weaver, T. A. 1984, in *Stellar Nucleosynthesis*, Ed. C. Chiosi & A. Renzini, D. Reidel, Dordrecht, p. 263.
Woltjer, L. 1984, in *Proc. Workshop Supernovae, their Progenitors and Remnants*, Eds V. Radhakrishnan & G. Srinivasan, Indian Acad. Sci., Bangalore (in press).
Wu, C-C, Leventhal, M., Sarazin, C. L., Gull, T. R. 1983, *Astrophys. J.*, **269,** L5.

J. Astrophys. Astr. (1985) **6,** 131-135

Higher-Dimensional Bianchi Type-VI$_h$ Cosmologies

D. Lorenz-Petzold *Fakultät für Physik, Universität Konstanz, D-7750 Konstanz, FRG*

Received 1985 February 18; accepted 1985 May 28

Abstract. We present the higher-dimensional perfect fluid generalizations of the extended Bianchi type-VI$_h$ vacuum space-times discussed recently by Demaret & Hanquin (1985). It is shown that the Chodos-Detweiler mechanism of cosmological dimensional-reduction is possible in these cases.

Key words: cosmology, Bianchi type—cosmology, higher dimensional

1. Introduction

The topic of higher-dimensional cosmologies has recently received much attention (Chodos & Detweiler 1980; Freund 1982; Sahdev 1984; Lorenz-Petzold 1984a, b; 1985a-d). It has been suggested that such cosmologies play an important role in the very early universe (Chodos 1984; Chodos & Myers 1984; Appel & Dresden 1984). In the course of time, the influence and effect of extra dimensions $D \geqslant 1$ (N=1+d+ D) must have diminished or changed. An easy way to visualize this process is that in the course of time, the usual $d = 3$ dimensions kept on expanding, while the extra dimensions $D \geqslant 1$ contracted very rapidly to distances of the order of the Planck length. Such MN=$\|R \otimes M^d \otimes M^D$ space-time models were first constructed by Chodos & Detweiler (1980) (see also Belinskii & Khalatnikov 1972; Forgacs & Horvath 1979; Barrow 1983; Tosa 1984; Mann & Vincent 1985).

An interesting paper in this respect has been recently published by Demaret & Hanquin (1985). Most of the studies done so far are of the higher-dimensional generalization of the anisotropic (1 + 3)-dimensional Bianchi type-I model (see Lorenz-Petzold 1985c). However, no generalization of the Petrov-Bianchi classification exist in (1 + n)-dimensions ($n = N - 1$) (Petrov 1969; Sahdev 1984). A simple definition was given by Demaret & Hanquin (1985). A N-dimensional spatially homogeneous model is defined as a N-dimensional space-time possessing a (N – 1)-dimensional group of isometry acting simply transitively on (N – 1)-dimensional space-like hyper-surfaces. This definition does not probably recover all possible cases of spatially homogeneous models in (1+3)-dimensions (Ryan & Shepley 1975; Kramer *et al.* 1980). However, the definition given by Demaret & Hanquin is already sufficiently rich as to recover a large set of spatially homogeneous models.

In this paper we discuss the higher-dimensional perfect fluid field equations of a generalization of the (1 + 3)-dimensional Bianchi type-VI$_h$ space-time, which includes also the Bianchi type-V and the Bianchi type-Ill as special cases. Only the vacuum case was discussed by Demaret & Hanquin (1985).

2. Field equations and solutions

We consider the metrics

$$ds^2 = -dt^2 + R_1^2 (dx^1)^2 + \exp(2p_i x^1) R_i^2 (dx^i)^2, \tag{1}$$

where $R_j = R_j(t) (j = 1,\ldots, N-1; n = N-1)$ are the cosmic scale functions and P_i = const. The corresponding perfect fluid field equations to be solved are given by

$$H_1' + H_1 (\ln u)' - \sum p_i^2 = \varepsilon(2-\gamma) R_1^2/(N-2), \tag{2a}$$

$$H_i' + H_i (\ln u)' - p_i \sum p_i = \varepsilon (2-\gamma) R_1^2/(N-2), \tag{2b}$$

$$H_1 \sum p_i - (\ln g)' = 0, \tag{2c}$$

$$(\ln u)'^2 + 2(\ln u)' H_1 - \sum H_i^2 - \sum p_i^2 - (\sum p_i)^2 = 2\varepsilon R_1^2, \tag{2d}$$

$$\varepsilon' + \gamma\varepsilon(\ln R_1 u)' = 0, \tag{2e}$$

$$p = (\gamma - 1)\varepsilon, \qquad 1 \leqslant \gamma \leqslant 2, \tag{2f}$$

where $H_j = (\ln R_j)'$ are the Hubble parameters, $u = R_2 \ldots R_{N-1}$, $g = R_2^{p_2} \ldots R_{N-1}^{p_{N-1}}$, $dt = R_1 d\eta$, $( )' = d/d\eta$, $i = 2,\ldots, N-1$ and ρ and ε are, respectively, the pressure and energy density of the perfect fluid matter. In cosmology, we are mainly interested in the cases $\varepsilon = 0$ (vacuum), $y = 1$ (dust), $y = 2$ (stiff matter) and $\gamma = N/(N-1)$ (radiation). From Equation (2e) we obtain the conservation equation $\varepsilon = M(R_1 \ldots R_{N-1})^{-y}$, M = const.

We first consider the cases $\varepsilon = 0$ and $y = 2$. From the linear combination of Equations (2b) we obtain

$$u'' - p^2 u = 0, \qquad p = \sum p_i, \tag{3}$$

with the general solutions

(i) $$u = \sinh p\eta, \qquad p \neq 0, \tag{4a}$$

(ii) $$u = \eta, \qquad p = 0, \tag{4b}$$

and the special solution

(iii) $$u = \exp p\eta, \quad p \neq 0. \tag{4c}$$

Equations (2a) and (2b) can now be easily integrated (Equation 2d is nothing but the constraint equation on the constants of integration) to give:

(i)
$$R_1 = (\sinh p\eta)^{(1/p^2)\sum p_i^2} \left(\tanh \frac{p}{2}\eta\right)^{(1/p)\sum c_i p_i},$$

$$R_i = (\sinh p\eta)^{p_i/p} \left(\tanh \frac{p}{2}\eta\right)^{c_i},$$

$$\sum c_i = 0, \qquad p^2 + \sum p_i^2 = p^2 \sum c_i^2 + 2M, \tag{5a}$$

(ii)
$$R_1 = \eta^a \exp\left(\frac{1}{4}\sum p_i^2\right),$$

$$R_i = \eta^{c_i},$$

$$\sum c_i = 1, \qquad \sum c_i p_i = 0, \qquad 2a = \sum c_i^2 - 1 + 2M, \tag{5b}$$

(iii)
$$R_1 = \exp\left(\frac{1}{p}\sum p_i^2 \eta\right),$$
$$R_i = \exp p_i\eta, \qquad M = 0, \tag{5c}$$

where c_j, a = const.

The stiff matter solutions ($M \neq 0$) are new. By setting $M = 0$ we rediscover the vacuum solutions ($p = 1$, if $p \neq 0$ without loss of generality) discussed by Demaret & Hanquin (1985). The four-dimensional solutions (5a) ($i = 2, 3$) are due to Collins (1971) (in a somewhat different form) and Ruban (1978a) (see also Wainwright, Ince & Marshman 1979), which include the Bianchi type-VI_h vacuum solutions of Ellis & MacCallum (1969) and the Bianchi type-V solution given by Joseph (1966) ($p_i = 1$). The special solution (5b) has no analogue in (1 + 3)-dimensions. Our solution (5c) has been discussed in four-dimensions by Lifshitz & Khalatnikov (1963a, b), Collins (1971, 1977), Evans (1974, 1978), Siklos (1981), Ruban (1978a, b), Siklos (1981), Ruban, Ushakov & Chernin (1981), Belinskii, Khalatnikov & Lifshitz (1982), Wainwright (1983) and Wainwright & Anderson (1984) (see also the recent paper by Rosquist & Jantzen 1985).

We next consider the special power law perfect fluid solutions:

$$R_1 = \exp a\eta, \qquad R_i = \exp c_i\eta, \tag{6}$$

where a, c_i — const. It follows that

$$a = c\gamma/(2-\gamma), \qquad \gamma \neq 2, \qquad c = \sum c_i,$$
$$c_i = a + [\gamma/a(2-\gamma)]\,[pp_i - \sum p_i^2], \tag{7a}$$

and thus a can be re-expressed in terms of p_i:

$$a^2 = \gamma^2[p^2 - (N-2)\sum p_i^2]/[(2-\gamma)(2-\gamma(N-1))], \tag{7b}$$

which yields in addition to $\gamma \neq 2$ the condition $y \neq 2\ \ (N-1)$. According to Equation (2c) we have also

(i)
$$p \neq 0:$$
$$a = \sum c_i p_i/p, \tag{8a}$$

(ii)
$$p = 0:$$
$$\sum c_i p_i = 0, \tag{8b}$$

and the value of M is determined by Equation (2d).

Our solutions (6–8) are the higher-dimensional special perfect fluid generalizations of the (1 + 3)-dimensional solutions first given by Collins (1971). Such solutions are of much interest in cosmology and have been discussed recently in (1 + 3)-dimensions by Ruban, Ushakov & Chernin (1981), Barrow (1982, 1984), Wainwright (1983, 1984) and Wainwright & Anderson (1984) (see also the recent paper by Lorenz-Petzold 1985e). By setting $a = c_2 = c_3$, $c_4 = b$, we obtain the isotropic solution in (1+4)-dimensions with

$$b = a(2-3\gamma)/\gamma, \qquad a > 0, \tag{9}$$

leading thus to a contraction of the physical unobservable dimension and an expansion of the three physical dimensions.

We finally consider the space-times defined by $p_i = 1$, which are the higher-dimensional generalization of the (1 + 3)-dimensional Bianchi type-V cosmologies. Exact solutions (besides the ones given by Equation 5) can be obtained in the cases $y = N/(N-1)$ (radiation) und $\gamma = 1$ (dust). Without going into all the details we present only the results (see Lorenz-Petzold 1985f for derivation):

$$u = a\sinh^2 q\eta + b\sinh 2q\eta, \tag{10a}$$

$$\begin{aligned} R_1 &= u^{1/(N-2)} \\ R_i &= u^{1/(N-2)}\left[1 + (2b/a)\coth q\eta\right]^{c_i/(N-2)}, \\ a &= 2M/(N-2)(N-1), \qquad q = (N-2)/2, \\ \sum c_i &= 0, \qquad \sum c_i^2 = (N-1)(N-2), \end{aligned} \tag{10}$$

where b, c_i = const. By setting $i = 2, 3$, we rediscover the (1 + 3)-dimensional Bianchi type-V radiation solution first given by Ruban (1977a, b) (Note that these papers are not quoted by Kramer *et al.* 1980).

The dust case can be reduced to the solution of a generalized Friedmann equation:

$$\begin{aligned} R'^2 &= R^2 + (a^2/(N-1)(N-2))\sum c_i^2 R^{2(1-N)} + (2M/(N-1)(N-2))R^{5-N}, \\ S &= \exp\left[a\int R^{1-N}\mathrm{d}\eta\right], \end{aligned}$$

where a = const., $R = R_1$ $R_i = RS^{c_i}$, $\sum c_i = 0$, c_i = const. The case $N = 4$ is nothing but the (1 + 3)-dimensional Bianchi type-V dust solution first given by Schucking & Heckmann (1958), which can be solved explicitly in terms of elliptic functions. This completes our study of the higher-dimensional Bianchi type-VI_h perfect fluid field equations. According to the relations Σc_i = const., it is always possible to construct solutions such that d = 3-dimensions are expanding while the extra dimensions $D \geqslant 1$ are contracting to an unobservable scale.

References

Appel, D., Dresden, M. 1984, in *Proc. Johns Hopkins Workshop*; *Particles and Gravity*, Eds G. Domokos & S. Kovesi-Domokos, World Scientific, Singapore, p. 229.

Barrow, J. D. 1982, *Q.* J. *R. astr. Soc*, **23,** 344.

Barrow, J. D. 1983, *Phil. Tram. R. Soc. London*, **310,** 337.

Barrow, J. D. 1984, *Mon. Not. R. astr. Soc*, **211,** 221.

Belinskii, V. A., Khalatnikov, I. M. 1972, *Zh. Eksp. Teor. Fiz.*, **63,**1121; 1973, *Sov. Phys. JETP*, **36,** 591.

Belinskii, V. A., Khalatnikov, I. M. 1972, *Adv. Phys.*, **31,** 639.

Chodos, A. 1984, in *Workshop on Kaluza-Klein Theories: An Introduction to Kaluza Klein Theories*, Ed. H. C. Lee, World Scientific, Singapore, p. 256.

Chodos, A., Detweiler, S. 1980, *Phys. Rev.* **D21,** 2167.

Chodos, A, Myers, E. 1984, *Ann. Phys.*, New York, **156,** 412.

Collins, C. B. 1971, *Commun. Math. Phys.*, **23,** 137.

Collins, C. B. 1977, *Phys. Lett.*, **60A,** 397.

Demaret, J., Hanquin, J.-L. 1985, *Phys. Rev.* **D31,** 258.

Ellis, G. F. R., MacCallum, M. A. H. 1969, *Commun. Math. Phys.*, **12,** 108.

Evans, A. B. 1974, *Nature*, **252,** 109.

Evans, A. B. 1978, *Mon. Not. R. astr. Soc*, **183,** 727.

Forgäcs, P., Horväth, Z. 1979, *Gen. Relativ. Gravitation*, **11,** 205.

Freund, P. G. O. 1982, *Nucl. Phys.*, **B209,** 146.

Joseph, V. 1966, *Proc. Cambridge Phil. Soc*, **62,** 87.
Kramer, D., Stephani, H., MacCallum, M. A. H., Herlt, E.1980, *Exact Solutions of Einstein's Field Equations*, Cambridge Univ. Press.
Lifshitz, E. M., Khalatnikov, I. M. 1963a, *Usp. Fiz. Nauk*, **80,** 391; 1964, *Sov. Phys. Usp.*, **6,**495.
Lifshitz, E. M., Khalatnikov, I. M. 1963b, *Adv. Phys.*, **12,** 185.
Lorenz-Petzold, D. 1984a, *Phys. Lett.*, **148B,** 43.
Lorenz-Petzold, D. 1984b, *Phys. Lett.*, **149B,** 79.
Lorenz-Petzold, D. 1985a, *Phys. Lett. B.*, **151B,** 105.
Lorenz-Petzold, D. 1985b, *Phys. Lett. B.*, **153B,** 134.
Lorenz-Petzold, D. 1985c, *Phys. Rev.*, **31D,** 929.
Lorenz-Petzold, D. 1985d, *Prog. Theor. Phys.*, **73,** 533.
Lorenz-Petzold, D. 1985e, *Acta phys. pol.*, **B16,** 171.
Lorenz-Petzold, D. 1985f, *Lett. Math. Phys.* (Submitted).
Mann, R. B., Vincent, D. E. 1985, *Phys. Lett.*, **107A,** 75.
Petrov, A. Z. 1969, *Einstein Spaces*, Pergamon Press, Oxford.
Rosquist, K., Jantzen, R. T. 1985, *Phys. Lett.*, **107A,** 29.
Ruban, V. A. 1977a, *Zh. Eksp. Teor. Fiz.*, **72,** 1201; 1977, *Sov. Phys. JETP*, **45,** 629.
Ruban, V. A. 1977b, Leningrad Institute of Nuclear Phys., B. P. Konstantinova, Preprint No. 327.
Ruban, V. A. 1978a, Leningrad Institute of Nuclear Phys., B. P. Konstantinova, Preprint No. 412.
Ruban, V. A. 1978b, Leningrad Institute of Nuclear Phys., B. P. Konstantinova, Preprint No. 411.
Ruban, V.A., Ushakov, Yu. A., Chernin, A. D.1981, *Zh. Eksp. Teor. Fiz.*, **80,** 816; 1981, *Sov. Phys. JETP*, **53,** 413.
Ryan, Jr. M. P., Shepley, L. C. 1975, *Homogeneous Relativistic Cosmologies*, Princeton Univ. Press.
Sahdev, D. 1984, *Phys. Rev.*, **D30,** 339.
Schucking, E., Heckmann, O. 1958, in *Institute International de Physique, Onzieme Conseil de Physique, Editions Stoops*, Brussels.
Siklos, S. T. C. 1981, *J. Phys. A.: Math. Gen.*, **14,** 395.
Tosa, Y. 1984, *Phys. Rev.*, **D30,** 339.
Wainwright, J. 1983, *Phys. Lett.*, **99A,** 301.
Wainwright, J. 1984, *Gen. Relativ. Gravitation*, **16,** 657.
Wainwright, J., Anderson, P. J. 1984, *Gen. Relativ. Gravitation*, **16,** 609.
Wainwright, J., Ince, W. C W., Marshman, B. J. 1979, *Gen. Relativ. Gravitation*, **10,** 259.

J. Astrophys. Astr. (1985) **6,** 137-144

Higher-Dimensional Vacuum Bianchi-Mixmaster Cosmologies

D. Lorenz-Petzold *Fakultät für Physik, Universität Konstanz, D-7750 Konstanz, FRG*

Received 1985 February 19; accepted 1985 May 28

Abstract. We derive some new exact 7-dimensional cosmological solutions $| R \otimes \mathrm{I} \otimes N$, where N = I, II, VI_0, VII_0, VIII and IX are the various 3-dimensional Bianchi models. The solutions given are higher-dimensional generalizations of the mixmaster cosmologies. There is a strong influence of the extra spaces N, which results in a fundamental change of the 3-dimensional cosmology.

Key words: cosmology, vacuum Bianchi type — cosmology, higher dimensional

1. Introduction

The topic of higher-dimensional cosmologies is of much interest in view of the modern Kaluza–Klein picture of the universe (Lee 1984). In this approach the basic world manifold is of type $M^n = | R \otimes P^d \otimes Q^D$, where P^d, Q^D are some d, D-dimensional spaces. By taking $d = 3$, $D \geqslant 1$, the three-space P^3 should be identified with one of the isotropic Friedmann–Robertson–Walker (FRW) models or with one of their anisotropic generalizations of the various Bianchi types I–IX (Ryan & Shepley 1975; Kramer *et al.* 1980). The internal (or extra) space Q^D must be some higher-dimensional generalization of the Kaluza–Klein S^1 sphere. For instance, in $d = 11$ supergravity a natural candidate for Q^D is one of the various S^7-spheres (Lorenz-Petzold 1985; Alvarez 1984; Fujii & Okada 1984; Gleiser, Rajpoot & Taylor 1984). However, there are an embarassingly large number of other solutions with other topologies (Bais, Nicolai & van Nieuwenhuizen 1983; Castellani, Romans & Warner 1984).

Recently, some 1 + 3 + 3 = 7-dimensional Bianchi–mixmaster cosmologies of types I ⊗ IX (Furusawa & Hosoya 1984) and IX ⊗ IX (Tomimatsu & Ishihara 1984) have been constructed on the basis of higher-dimensional gravity. In (1+3)-dimensions, type-I leads to the well-known Kasner solution while type-IX is known as the mixmaster model (Misner 1969; Barrow 1984). It is well known that the original mixmaster model shows a chaotic behaviour near the initial singularity (Barrow & Tipler 1979; Barrow 1981; 1982; 1984; Chernoff & Barrow 1983; Elskens 1983; Zardecki 1983; Lifshitz *et al.* 1983). However, there are also some controversial results concerning the possibility of 'mixing' (Doroshkevich & Novikov 1970a, b; MacCallum 1971; Doroshkevich, Lukash & Novikov 1971). It is now interesting to see that the influence of the extra dimensions may prevent the chaotic behaviour near the initial singularity (Furusawa & Hosoya 1984; Tomimatsu & Ishihara 1984).

In view of this it becomes interesting to study some more general higher-dimensional cosmologies of type I ⊗ *N*, where *N* denotes one of the Bianchi types I, II, VI_0, VII_0, VIII and IX with different topologies (The (1 + 3)-dimensional type-VIII has been first considered by Lifshitz & Khalatnikov 1970; for types VI_0, VII_0 see Khalatnikov & Pokrovski 1972; Lukash 1974; Ruban 1978; Belinskii, Khalatnikov & Lifshitz 1982; Lorenz-Petzold 1984; Jantzen 1984). In this paper we solve the corresponding field equations in 7-dimensions.

2. Field equations and solutions

In choosing a local orthonormal basis σ^μ, we can put the metric on $R \otimes I \otimes N$ in the form

$$ds^2 = \eta_{\mu\nu}\sigma^\nu\sigma^\mu, \tag{1a}$$

where $\eta_{\mu\nu} = (-1, 1, \ldots, 1)$ is the seven-dimensional Minkowski metric tensor. We have

$$\sigma^0 = \omega^0 = dt, \quad \sigma^i = r_i\omega^i, \quad \sigma^j = R_j\omega^j \text{ (no sum)}, \tag{1b}$$

where $r_i = r_i(t)$ are the cosmic scale functions on type-I, $R_i = R_i(t)$ are defined on type-*N*, ω^i — dx^i, $\omega^i(i,j = 1, 2, 3)$ are time-independent differential forms for the Bianchi types I, II, VI_0, VII_0, VIII and IX (see Kramer *et al.* 1980). The corresponding vacuum field equations to be solved are given by

$$(\ln r_i)'' = 0, \tag{2a}$$

$$(\ln R_i^2)'' = r^6[(n_jR_j^2 - n_kR_k^2)^2 - n_i^2R_i^4], \tag{2b}$$

$$\begin{aligned} 9hH + h_1h_2 + h_1h_3 + h_2h_3 + H_1H_2 + H_1H_3 + H_2H_3 \\ = (1/4R^6)[n_1^2R_1^4 + n_2^2R_2^4 + n_3^2R_3^4 \\ - 2\{n_1n_2(R_1R_2)^2 + n_1n_3(R_1R_3)^2 + n_2n_3(R_2R_3)^2\}], \end{aligned} \tag{2c}$$

where $r_i = ri(t)$, $R_i = R_i(t)$, $h_i = (\ln r_i)$, $H_i = (\ln R_i)$, $3h = \Sigma h_i$, $3H = \Sigma H_i$, $r^3 = r_1r_2r_3$, $R^3 = R_1R_2R_3$, $dt = (rR)^3\, d\eta$, $(\,)^{\cdot} = d/dt$, $(\,)' = d/d\eta$, n_i are the structure constants of the various Bianchi types given by

n_1	n_2	n_3	
0	0	0,	I
1	0	0,	II
1	−1	0,	VI_0
1	1	0,	VII_0
1	1	−1,	VIII
1	1	1,	IX

and *i, j, k* are in cyclic order.
The general solutions of Equation (2a) are of the Kasner-type:

$$r_i = r_{i0}\exp(k_i\eta), \quad \Sigma k_i = k, \tag{3}$$

where r_{i0}, k_i, k = const. We obtain the following results:

(1) N = I:

$$r_i = \tilde{r}_{i0} t^{p_i}, \quad R_i = \tilde{R}_{i0} t^{q_i}, \quad \tilde{r}_{i0}, \quad \tilde{R}_{i0} = \text{const}, \tag{4a}$$

$$[\Sigma(p_i + q_i)]^2 = \Sigma(p_i^2 + q_i^2) = 1, \; p_i, \; q_i = \text{const}. \tag{4b}$$

This is the seven-dimensional generalization of the Kasner-solution in four dimensions. Equation (2b) yields $R_i = R_{i0} \exp(K_i \eta)$ and (4a) is obtained by setting $p_i = k_i / (k + K)$, $q_i = K_i / (k + K)$, where $\Sigma K_i = K$. Our solution (4a) turns out to be identical with the IX ⊗ IX solution (Tomimatsu & Ishihara 1984) when the spatial curvature terms of the right-hand side of (2b) are ineffective, which is characteristic for the original Bianchi type-IX mixmaster cosmology.

(2) N = II:

$$R_1 R_2 = R_{12} \exp(p\eta), \quad R_1 R_3 = R_{13} \exp(q\eta), \tag{5a}$$

$$r^3 = a \exp(k\eta), \tag{5b}$$

$$\tilde{H}_1^2 + k\tilde{H}_1 - b^2 + (1/4) r^6 R_1^4 = 0, \tag{5c}$$

$$2b^2 = k^2 + 2[k(p+q) + pq] - \Sigma k_i^2, \tag{5d}$$

where R_{12}, R_{13}, p, q, a = const, and $H_i = (\ln R_i)'$. We obtain two different kinds of solutions:

(i) the general solution with $k = 0$;

$$\begin{aligned} R_1^2 &= (2b/a)(\cosh 2b\eta)^{-1}, \\ R_2^2 &= \tilde{R}_2 \exp(2p\eta)(\cosh 2b\eta)^2, \\ R_3^2 &= \tilde{R}_3 \exp(2q\eta)(\cosh 2b\eta)^2, \\ r_i &= \tilde{r}_{i0} \exp(k_i \eta), \end{aligned} \tag{6a}$$

(ii) the special power-type solution

$$\begin{aligned} & r_i = \tilde{r}_{i0} t^{p_i}, \quad R_i = \tilde{R}_{i0} t^{q_i}, \\ & p_i = \frac{2k_i}{2(p+q)+3k}, \quad q_1 = \frac{-k}{2(p+q)+3k}, \\ & q_2 = \frac{2p+k}{2(p+q)+3k}, \quad q_3 = \frac{2q+k}{2(p+q)+3k}, \\ & a^2 c^4 = 4b^2 + k^2, \end{aligned} \tag{6b}$$

where $\tilde{R}_2$, $\tilde{R}_3$, $\tilde{R}_{i0}$, c = const.

Our solution (6a) is the generalization of the vacuum Bianchi type-II solution in four dimensions first given by Taub (1951) (see also Lorenz 1980a). Our solution (6b) obeys the relation $q_1 + 1 = q_2 + q_3$, from which it follows that no Kasner conditions are satisfied if $k \neq 0$.

We now turn to the spaces I ⊗ VI_0 and I ⊗ VII_0. In considering first the LRS case (see Ellis & MacCallum 1969) $R = R_1 = R_2$, $S = R_3$, the Bianchi type-VII_0 model reduces to a special Bianchi type-I model. We thus consider only the Bianchi type-VI_0

space. The corresponding field equations to be solved are

(3) $N = \mathrm{VI}_0$:

$$(\ln R^2)'' = 0, \tag{7a}$$

$$(\ln S^2)'' - 4r_6 R_4 = 0. \tag{7b}$$

From (7a) we obtain the solution

$$R^2 = \exp \mathrm{b}\eta, \tag{8a}$$

where b = const, and (7 b) gives now

$$(\ln S^2)'' = 4\alpha^2 \exp 2(\mathrm{k} + \mathrm{b})\eta \tag{8b}$$

It can be shown that the case $k + b = 0$ is not compatible with Equation (2c). For $k + b \neq 0$ it is more convenient to consider Equation (2c) instead of (8b). The field equation to be solved is given by

$$\tilde{H}_3 = [1/(b+k)]r^6R^4 - [1/4(b+k)][b(b+4k) - 2(\Sigma k_i^2 - k^2)], \tag{9}$$

where $\tilde{H}_3 = (\mathrm{In}\ S)'$, $(\ ) = \mathrm{d}/\mathrm{d}\eta$. The solutions can now be easily completed in terms of the generalized Ellis-MacCallum (1969) parameter $u = r^3R^2$:

$$\begin{aligned} R^2 &= ur^{-3}, \\ S^2 &= u^{-A^2/[2(b+k)]} \exp((a^2/(b+k))u^2, \\ r_i &= r_{i0}\,(ur^{-3})^{k_i/b}, \\ r^3 &= a \exp k\eta, \end{aligned} \tag{10}$$

where

$$A^2 = b(b+4k) - 2(\Sigma k_i^2 - k^2). \tag{11}$$

By setting $k_i = 0$, $a = b = 1$, we rediscover the (1 + 3) dimensional solution first given by Ellis & MacCallum (1969) (Note that this solution is incorrectly given by Kramer *et al.* 1980; in Ellis & MacCallum (1969) q_0 should be replaced by q_0^2).

We next consider the non-LRS case $R_1 \neq R_2 \neq R_3$. Introducing the new variables $u_i = u_i(\eta)$ by

$$R_i = \exp u_i, \quad u = 2(u_1 - u_2), \tag{12}$$

the corresponding field equations can be decoupled and partially integrated to give

$$u_1 + u_2 = b(\eta - \eta_0), \tag{13a}$$

$$u'' + 4a^2 \exp[2(k+b)\eta - 2b\eta_0] \sinh u = 0, \tag{13b}$$

$$u_3'(k+b) = -u_1'u_2' - kb + \tfrac{1}{2}(\Sigma k_i^2 - k^2) + \tfrac{1}{4}[\exp 2u_1 - \delta \exp 2u_2]^2, \tag{13c}$$

where b, η_0 = const. and $\delta = (n_2) = -(\mathrm{VI}_0)$, $\delta = 1$ (VII0). After solving Equation (13b) to give $u = \imath\imath(\eta)$ the most general Bianchi type-VI_0 and type-VII_0 solutions would arise. We will now show how the solutions can be expressed in terms of a particular form of the third Painleve transcendents (Ince 1956). Introducing the time variable ζ by

$$\zeta = \frac{2a}{k+b} \exp[(k+b)\eta - b\eta_0], \tag{14}$$

can transform the system (13) to obtain

$$\ddot{u} + \frac{1}{\zeta}\dot{u} + \sinh u = 0, \tag{15a}$$

$$u_1 = \ln\left[\frac{k+b}{2a}\zeta \exp(-k\eta_0)\right]^{b/2(k+b)} + \frac{u}{4}, \tag{15b}$$

$$u_2 = \ln\left[\frac{k+b}{2a}\zeta \exp(-k\eta_0)\right]^{b/2(k+b)} - \frac{u}{4}, \tag{15c}$$

$$\dot{u}_3 = \frac{\zeta}{16}(\dot{u}^2 - 4b^2) - \frac{1}{(k+b)^2\zeta}\left[kb + \frac{1}{2}(k^2 - \Sigma k_i^2)\right]$$

$$+ \frac{1}{4a(k+b)}\left[\frac{(k+b)}{2a}\zeta\right]^{(b-k)/(b+k)} [\cosh u + \delta] \exp\left[-\frac{2kb\eta_0}{k+b}\right], \tag{15d}$$

where $\dot{(\ )} = \mathrm{d}/\mathrm{C}.\zeta$ In the limit $k = k_i = 0$ we rediscover the field equations first given by Belinskii & Khalatnikov (1969) (for type-IX) and Lifshitz & Khalatnikov (1970) (for type-VIII) and later by Khalatnikov & Pokrovski (1972). The connection with the Bianchi type-VI_0 and type-VII_0 spaces has been first observed by Lorenz-Petzold (1984) and independently by Jantzen (1984) (Note that there are some errors in the papers of Belinskii & Khalatnikov, Lifshitz & Khalatnikov, and Lorenz-Petzold).

If we put

$$w = \exp u, \quad z = \frac{\zeta^2}{4}, \quad w = w(z), \quad (\ )' = \mathrm{d}/\mathrm{d}z, \tag{16}$$

Equation (15a) becomes

$$w'' = \frac{w'^2}{w} - \frac{1}{z}\left[w' + \frac{1}{2}(w^2 - 1)\right]. \tag{17}$$

This equation is a particular form of the nonlinear equation of second order which defines the third Painleve transcendent (Ince 1956). The Bianchi types-VI_0, VII_0 solutions are completed by Equations (15b), (15c) and (15d) to give $u_i = u_i$ (w(z)). A solution of Equation (15a) in terms of elliptic function was given by Khalatnikov & Pokrovski (1972). The scale functions r_i are given by

$$r_i = r_{i0}\left[\frac{k+b}{2a}\zeta \exp(b\eta_0)\right]^{k_i/(k+b)} \tag{18}$$

We finally consider the spaces I ⊗ VIII and I⊗ IX. By setting $R = R_1 = R_2$, $S = R_3$, $g = RS$, $f = (RV$, $d = n_3$, $z = S^2$, the field equations (2a-2c) can be decoupled to give

(4) N = VIII, IX:

(i) $k = 0$:

$$\ddot{g} + \delta a^2 g = 0, \tag{19a}$$

$$z'^2 - 2[2(\dot{g}^2 + \delta a^2 g^2) - \Sigma k_i^2]z^2 + a^2 z^4 = 0, \tag{19b}$$

where d $\tau = g d\eta$, ( )' = d / dτ, ( )' =d/dη and

(ii) $k \neq 0$:

$$f'' = \frac{f'^2}{f} - \frac{1}{\zeta}(f' + \delta c^2 f^2), \tag{20a}$$

$$z'^2 + \frac{1}{\zeta} z z' + \frac{c^2}{2} z^4 + 2[(\ln f)' - \frac{1}{2(k\zeta)^2}(k^2 - \Sigma k_i^2)] z^2 = 0, \tag{20b}$$

where $\zeta = \exp(2k\eta)$, d$\zeta = 2k\zeta d\eta$, ( )' = d/dζ. From Equation (19a) we obtain the solutions

$$g = A \sin(a\tau), \quad \delta = 1, \tag{21a}$$

$$g = A \sinh(a\tau), \quad \delta = -1, \tag{21b}$$

where A = const. It is now an easy matter to solve Equation (19b) to give $S = S(\tau)$. The results are

$$\begin{aligned} R^2 &= (A^2 a/2D) \sin^2(a\tau) \cosh\left[\ln\left(\tan\frac{a}{2}\tau\right)^{2D/Aa}\right], \\ S^2 &= (2D/a) \cosh^{-1}\left[\ln\left(\tan\frac{a}{2}\tau\right)^{2D/Aa}\right], \\ r_i &= r_{i0}\left(\tan\frac{a}{2}\tau\right)^{k_i/Aa}, \qquad \text{type-VIII}, \end{aligned} \tag{22a}$$

$$\begin{aligned} R^2 &= (A^2 a/2D) \sinh^2(a\tau) \cosh\left[\ln\left(\tanh\frac{a}{2}\tau\right)^{2D/Aa}\right], \\ S^2 &= (2D/a) \cosh^{-1}\left[\ln\left(\tanh\frac{a}{2}\tau\right)^{2D/Aa}\right], \\ r_i &= r_{i0}\left(\tanh\frac{a}{2}\tau\right)^{k_i/Aa}, \qquad \text{type-IX}, \end{aligned} \tag{22b}$$

where

$$2D^2 = 2A^2 a^2 - \Sigma k_i^2.$$

Our solutions (22) are the generalizations of the (1 + 3)-dimensional vacuum solutions first given by Taub (1951) (only the type-IX solution was given explicitly by Taub; for type-VIII see Lorenz 1980b). No such explicit solutions are possible in the more general case $k \neq 0$. Equation (20a) defines a special kind of a third Painleve transcendental function (Ince 1956) $f = f(\zeta)$, which also determines $z = z(\zeta)$ *via* Equation (20b).

3. Conclusions

We have given a complete discussion of the higher-dimensional vacuum Bianchi-mixmaster cosmologies of types $|R \otimes \mathrm{I} \otimes N$, N = I, II, VI_0, VII_0, VIII, IX. Only the

Kasner solution I⊗I (4) was known (Tomimatsu & Ishihara 1984). There is a strong influence of the spaces N on the Bianchi type-I model and vice versa. This can be seen explicitly by our new solutions of types-II (Equation 6b), VI_0 (Equations 10, 15), VII_0 (Equation 15), VIII and IX (Equation 20). However, due to the great numbers of solutions it remains a problem for the near future to discuss our solutions in adequate detail. A next step into some more general cosmologies would be to construct some perfect fluid solutions. It is also worth investigating the mixmaster cosmologies of type-$N \otimes N$ (besides the IX ⊗ IX model of Tomimatsu & Ishihara 1984).

References

Alvarez, E. 1984, *Phys. Rev*., **D30,** 1394; Errata: 1984, *Phys. Rev*., **D30,** 2695.

Bais, F. A., Nicolai, H., van Nieuwenhuizen, P. 1983, *Nucl. Phys*., **B288,** 333.

Barrow, J. D. 1981, *Phys. Rev. Lett.*, **46,** 963; Errata: 1981, *Phys. Rev. Lett.*, **46,** 1436.

Barrow, J. D. 1982, *Phys. Rep*., **85,** 1.

Barrow, J. D. 1984, in *Classical General Relativity*, Eds W. B. Bonnor, J. N. Isham & M. A. H. MacCallum, Cambridge Univ. Press.

Barrow, J. D., Tipler, F. J. 1979, *Phys. Rep*., **56,** 372.

Belinskii, V. A, Khalatnikov, I. M., Lifshitz, E. M. 1982, *Adv. Phys*., **31,** 639.

Castellani, L., Romans, L. J., Warner, N. P. 1984, *Ann. Phys*., New York, **157,** 394.

Chernoff, D. F., Barrow, J. D. 1983, *Phys. Rev. Lett*., **50**, 134.

Doroshkevich, A. G, Lukash, V. N., Novikov, I. D. 1971, *Zh. Eksp. Teor. Fiz*., **60,**1201; 1971, *Sov. Phys. JETP*, **33,** 649.

Doroshkevich, A. G., Novikov, I. D. 1970a, *Astr. Zh*., **47,** 948.

Doroshkevich, A. G., Novikov, I. D. 1970b, USSR Academy of Sciences, Institute of Applied Mathematics, Moscow, Preprint. No. 20.

Ellis, G. F. R., MacCallum, M. A. H. 1969, *Commun. Math. Phys*., **12,** 108.

Elskens, Y. 1983, *Phys. Rev*, **D28,** 1033.

Fujii, Y., Okada, Y. 1984, Univ, Tokyo, Preprint UT-Komaba 84-18.

Furusawa, T., Hosoya, A. 1984, Hiroshima Univ. Preprint R R K 84-20.; 1985, *Prog. Theor. Phys*., **73,** 467.

Gleiser, M., Rajpoot, S., Taylor, J. G. 1984, *Phys. Rev*., **30D,** 756.

Ince, E. L. 1956, *Ordinary Differenial Equations*, Dover, New York.

Jantzen, R. T. 1984, in *Cosmology of the Early Universe*, Eds L. Z. Fang & R. Ruffini, World Scientific, Singapore.

Khalatnikov, I. M., Pokrovski, V. L. 1972, in *Magic without Magic*, Ed. J. R. Klauder, Freeman, San Francisco, p. 289.

Kramer, D., Stephani, H., MacCallum, M. A. H., Herlt, E. 1980, *Exact Solutions of Einstein's Field Equations*, Cambridge Univ. Press.

Lee, H. C. 1984, *An Introduction to Kluza-Klein Theories*, World Scientific, Singapore.

Lifshitz, E. M., Khalatnikov, I. M. 1970, *Pisma Zh. Eksp. Teor. Fiz*., **11,** 200; 1970, *J ETP Lett.*, **11,** 123.

Lifshitz, E. M., Khalatnikov, I. M.$_s$ Sinai, Ya. G., Khanin, K. M., Shchur, L. N. 1983, *Pisma Zh. Eksp. Teor. Fiz*., **38,** 79; 1983, *JETP Lett*., **38,** 91.

Lorenz, D. 1980a, *Phys. Lett*., **79A,** 19.

Lorenz, D. 1980b, *Phys. Rev*., **22D,** 1848.

Lorenz-Petzold, D. 1984, *Acta phys. Pol*., **B15,** 117.

Lorenz-Petzold, D. 1985, *Phys. Lett.*, **151B,** 105.

Lukash, V. N. 1974, *Astr. Zh*., **51,** 281;1974, *Sov. Astr*., **18,** 164.

MacCallum, M. A. H. 1971, *Nature*, **29,** 112.

Misner, C. W. 1969, *Phys. Rev. Lett*, **22,** 1071.

Ruban, V. A. 1978, Leningrad Institute of Nuclear Physics, B. P. Konstantinova, Preprint No. 411.

Ryan, Jr. M. P., Shepley, L. C. 1975, *Homogeneous Relativistic Cosmologies*, Princeton Univ. Press.
Taub, A. H. 1951, *Ann. Math.*, **53,** 472.
Tomimatsu, A., Ishihara, H. 1984, Hiroshima Univ. Preprint R R K 84-20.
Zardecki, A. 1983, *Phys. Rev.*, **D28,** 1235.

J. Astrophys. Astr.(1985) **6,** 145–151

VLA Observations of Three M 33 Supernova Remnants at 20 cm

W. M. GOSS *Kapteyn Astronomical Institute, Postbus 800, 9700 AV, Groningen, The Netherlands*

F. Viallefond *Observatory of Meudon, F-92190 Meudon, France*

Received 1985 May 21; accepted 1985 June 1

Abstract. Three supernova remnants (SNR) have been mapped in the galaxy M33 with the Very Large Array* (VLA) at 20 cm. The angular resolution is ~ 1.3 arcsec or ~ 4 pc at a distance of 600 kpc and the rms noise is ~ 0.04 mJy /beam. One of the radio sources shows evidence for a shell structure with a size of ~ 15 pc, confirming the SNR nature of this source. The second object is extended and may well be a thick-shell SNR of size ~ 12 pc. The third object is a small, presumably young SNR with a size of ~ 4 pc.

Key words: supernova remnants, radio observations — external galaxies, individual — radio sources, VLA observations

1. Introduction

Radio investigations of conventional supernova remnants (SNR) in nearby galaxies are only possible within the local group of galaxies. Extensive investigations of the SMC and LMC have recently been completed with the Molonglo Observatory Synthesis Telescope (MOST) at 843 MHz with a resolution of ~ 43 arcsec (~ 10 pc) (Mills 1983; Mills & Turtle 1984; Mills *et al.* 1984). In M 31 and M 33, the radio emission from SNR is quite weak. As an example, an intense young galactic SNR such as Tycho (3C 10; 43 Jy at a distance of ~ 4 kpc) would have a flux density of only ~ 2 mJy at a distance of 600 kpc corresponding to the distance of M 33 (Humphreys 1980). A radio survey of M 31 SNR using the VLA has been carried out by Dickel *et al.* (1982), who detected five SNR at 20 cm with flux densities in the range 1 to 3.4 mJy. In addition, Dickel & D'Odorico (1984) have determined the non-thermal nature of several of the SNR in M 31 based on 6 cm VLA observations.

The directed radio observations of M 33 SNR began with observations by Goss *et al.* (1980, GEDI) of three of the SNR previously found in an optical survey by D'Odorico, Benvenuti & Sabbadin (1978) and confirmed to be SNR by spectroscopic studies of Danziger *et al.* (1979). These three (SN-1, 2, 3) were detected in a 21 cm continuum Westerbork Synthesis Radio Telescope (WSRT) map. Two of the objects (SN-2,3) were detected at 6 cm with maps made with the partially completed VLA in 1978 (resolution

* The Very Large Array of the National Radio Astronomy Observatory is operated by Associated Universities, Inc., under contract with the National Science Foundation

~ 1.5 arcsec and rms noise ~ 0.25 mJy /beam). Based on a more extensive optical survey of SNR in M 33 by D'Odorico, Dopita & Benvenuti (1980) (19 objects, DDB list), D'Odorico, Goss & Dopita (1982, DGD) looked for radio emission from these SNR using the WSRT at 21 cm. Five certain and three possible detections were reported, including the original three (SN-1, 2, 3). Viallefond *et al.* (1985) have also investigated the radio properties of the faint, extended SNR candidate DDB-1 (size ~ 18 arcsec); a weak radio source of 0.8 ± 0.3 mJy was detected. Blair & Kirshner (1985) have confirmed the SNR nature of this source based on optical spectroscopic measurements.

We have used the VLA in the A-array at 20 cm with an angular resolution of ~ 1.3 arc sec (4 pc) and an rms noise six times more favourable than the 1978 VLA observations. Three of the objects studied by GEDI (SN-1 = DDB-7; SN-2 = DDB-8; SN-3 = DDB-9) were observed.

The purpose of these observations was to use the highest possible resolution and sensitivity to study the radio morphology of these SNR. In particular, these observations have revealed a shell structure for one of the SNR, and a possible shell structure for a second.

2. Observations

The three SNR in M 33 were observed on 1983 November 14 during a period of 12 hours. The observing frequencies were 1465 and 1515 MHz with a total of four 50 MHz bands in both senses of circular polarization. The angular resolution was ~ 1.3 arcsec. Each object was observed separately since the delay beam of the VLA in the A-array is ~ 1 arcmin and the sources have typical separations of 3–4 arcmin. The observing time per field ranged from 1.7 to 2.7 hours with rms noises in the range 0.04 to 0.03 mJy /beam (Table 1). The maps were 'cleaned' to correct for distortions due to sidelobes.

3. Results

The 20 cm maps of the objects DDB-7, 8 and 9 are shown in Figs 1, 2 and 3. In these maps 1 mJy/beam corresponds to ~ 330 K full beam brightness temperature Fig. 1(a) shows the SNR DDB-7 and 1 (b) shows the source D, 40 arcsec to the southwest. Source D is probably an extragalactic background source (Israel & van der Kruit 1974; Viallefond *et al.* 1985) as it has no optical counterpart in M 33. In addition, the radio morphology (Fig. 1b) suggests that it could be an extragalactic double (size ~ 3 arcsec) with an unequal flux density ratio between the two radio lobes.

The source parameters are summarized in Table 1. The positions for the extended sources refer to the centroid of the emission. The optical sizes in column 8 are taken from GEDI, DGD and Viallefond *et al.* (1985). Very uncertain values are indicated by(:).

The VLA flux densities at 20 cm given in Table 1 are less than the WSRT values at 21 cm (GEDI) by 3.1 ±1.0 mJy (source D), 0.4 ± 0.3 mJy (DDB-7), 2.9 ± 0.5 mJy (DDB-8) and 2.5 ± 0.5 mJy (DDB-9). This difference is probably due to confusion problems in the WSRT data. Source D, DDB-7 and DDB-9 are located in the

Table 1. 20 cm observations of M 33 sources.

Name	Type	Observing time hr	rms noise mJy/beam	α (1950)	δ (1950)	θ radio arcsec	θ H α arcsec	S_{tot} mJy
				h m s s	° ′ ″ ″			
Source D*	BG**	2.1	0.042	01 30 39.65 ± 0.01	30 17 47.2 ± 0.1	< .3	...	9.4 ± 0.3
DDB-7	SNR	2.1	0.042	01 30 42.11 ± 0.01	30 18 11.1 ± 0.1	1.5	2.5†, < 2.5‡	1.3 ± 0.1
B 33	HII	2.7	0.038	01 30 45.7 ± 0.1	30 21 44 ± 1	3:	4§	1.0 ± 0.3
DDB-8*	SNR	2.7	0.032	01 30 46.79 ± .03	30 21 05.7 ± 0.3	~4	3.6†, 2.5‡	2.9 ± 0.2
...	...	2.7	0.038	01 30 47.95 ± .02	30 20 31.4 ± 0.2	< 1	...	0.4 ± 0.1
DDB-9	SNR	1.7	0.043	01 31 05.75 ± .03	30 17 49.3 ± 0.3	~5	3.3†, 3.2‡	4.5 ± 0.2

• Position and size refer to prominent peak. Flux density refers to entire source. ** BG = background source. † GEDI. ‡ DDB. § Viallefond *et al.* (1985).

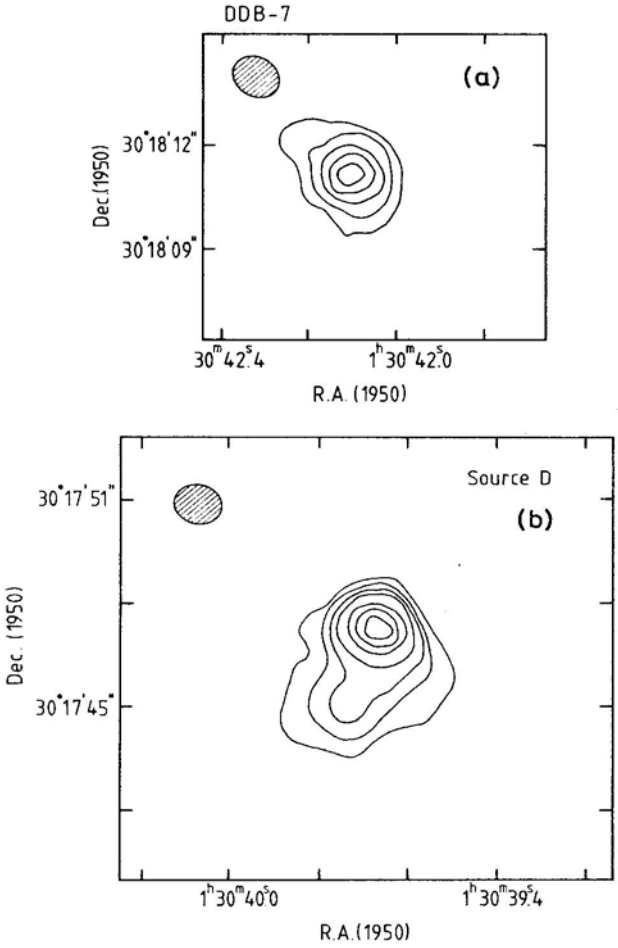

Figure 1. (a) DDB-7 (SN-1) at 20 cm as observed with the VLA in the A-array. The angular resolution is 1.38 arcsec × 1.18 arcsec at a position angle of 78°. The contour units are 0.1, 0.2, 0.3, 0.4, 0.5 mJy/beam. The rms noise is 0.042 mJy/beam. (b) Source D, to the southwest of DDB-7, a probable background source. The beamwidth is the same as for DDB-7 and the contour units are 0.2, 0.4, 0.6, 1,2,3,4 mJy/beam.

prominent, southern spiral arm of M 33 (Viallefond *et al.* 1985); at these low flux density levels (< 5 mJy), it is difficult to perform a precise separation of source emission from spiral arm emission. For DDB-8 the presence of nearby HII emission (see below) is a probable cause of confusion.

4. Discussion

Two of the detected SNR (DDB-8, 9) are clearly resolved with angular sizes in good agreement with the earlier 6 cm VLA observations and in reasonable agreement with the optical determinations (GEDI, DGD).

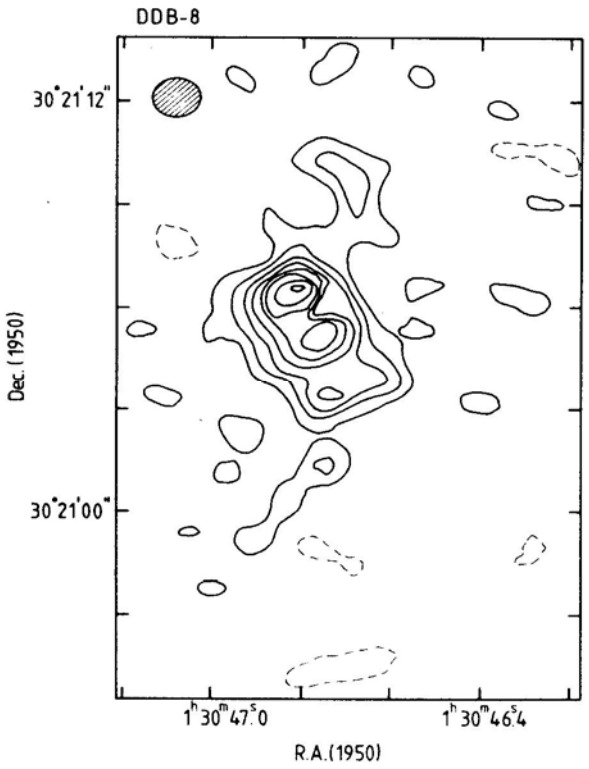

Figure 2. DDB-8(SN-2) at 20 cm. The beamwidth is 1.5 arcsec × 1.14 arcsec at position angle 87°. The contour units are – 0.06, 0.06, 0.12, 0.18, 0.24, 0.30, 0.36, 0.42, 0.48 mJy/beam. The rms noise is 0.032 mJy/beam.

The shell structure for DDB-9 (SN-3) suggested by GEDI is confirmed by the present data (Fig. 3) and is further evidence that this source is in fact a SNR. The shell size of ~ 5 arcsec corresponds to a diameter of 15 pc. By comparing with the results of GEDI, the rather flat spectral index of 0.2 ± 0.1 ($S \propto \nu^{-\alpha}$) is derived between 6 and 20 cm.

The object DDB-8 is a radio source with a complex morphology (Fig. 2). This morphology could be caused by thick shell structure with a size of ~ 4 arcsec or 12 pc. We cannot, however, exclude that some of the radio structure is caused by the crowding of several individual sources. D'Odorico, Benvenuti & Sabbadin (1978), DDB, and Danziger *et al.* (1979) remark on the presence of faint HII emission adjacent to DDB-8. The total emission from the radio source (above the 4 σ level) in Fig. 2 is 2.9 ± 0.2 mJy while the major radio source of flux density ~ 2.5 mJy has a position within 1.5 arcsec of the optical position of DDB-8 (DGD) and is thus probably related to the optical SNR. The weak emission (flux density ~ 0.4 mJy) 4–5 arcsec to the NW could be related to HII emission. Two other sources are also present in the DDB-8 field: 40 arcsec to the NW there is a source of 1.0 + 0.3 mJy (Table 1) which coincides with the H α nebula B 33 (Boulesteix *et al.* 1974). To the SE of DDB-8 there is an additional source (Table 1) which might be related to B1004; however the radio position is ~ 7 arcsec NE of the optical position and thus the identification is far from certain. In addition, the radio source is compact (< 1 arcsec) in contrast to the H α nebula (~ 12 arcsec). Thus,

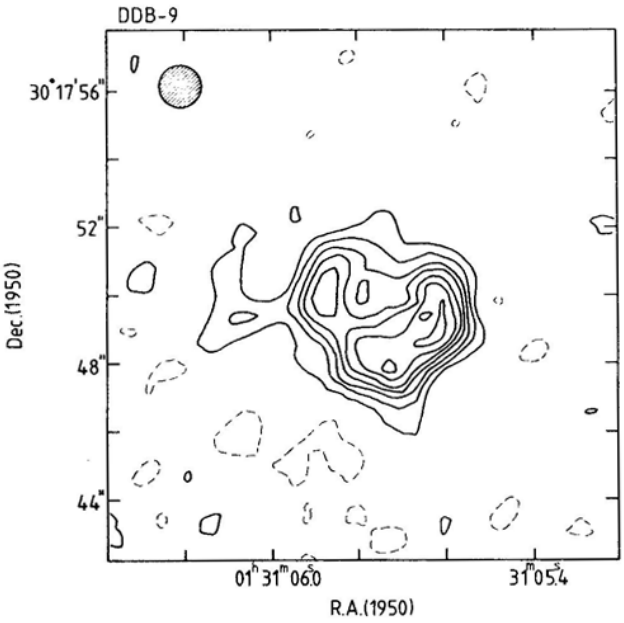

Figure 3. DDB-9 (SN-3) at 20 cm. The beamwidth is 1.28 arcsec x 1.15 arcsec at a position angle of 98°. The contour units are: – 0.08, 0.08, 0.16, 0.24, 0.32, 0.40, 0.48, 0.56 mJy/beam. The rms noise is 0.043 mJy/beam.

the WSRT 21 cm observation of DDB-8, which shows an extended source at position angle 150°, is affected by confusion arising from nearby HII regions. The spectral index of the major source in Fig. 2 can be derived using the 6 cm VLA data from GEDI and the 6 cm VLA data described by Viallefond *et al.* (1985); both results are in good agreement and indicate a spectral index between 6 and 20 cm of 0.0 ± 0.15. Thus the identification of DDB-8 as a SNR must rest entirely on the optical spectroscopy of Danziger *et al.* (1979), Dopita, D'Odorico & Benvenuti (1980) and Blair & Kirshner (1985).

The SNR DDB-7 is much more compact, with an optical size of 2.5 arcsec (GEDI) or < 2.5 arcsec (DGD) and a slightly extended radio source with a deconvolved size of 1.5 arcsec or 4 pc. This must be a young SNR with a surface brightness at 20 cm, Σ, of 300×10^{-21} W m^{-2} Hz sr^{-1}.

SNR in M 33 are faint radio sources. Even with the full sensitivity of the VLA, mapping large numbers of M 33 SNR is difficult. Of the 112 radio sources identified with H α nebulosities by Viallefond *et al.* (1985), only at most nine sources can be identified with SNR in the various optical catalogues. Thus a large fraction of the SNR have flux densities < 1 mJy and the HII catalogue of Viallefond *et al.* (1985) does not suffer from substantial SNR contamination. It is still clear that optical searches (DDB) and spectroscopic follow-up observations (*e.g.* Dopita, D'Odorico & Benvenuti 1980; Blair & Kirshner 1985) are the most efficient method to discover SNR in local group galaxies beyond the Magellanic Clouds. Radio observations are, however, useful in studying individual objects.

References

Blair, W. P., Kirshner, R. P. 1985, *Astrophys. J.*, **289,** 582.
Boulesteix, J., Courtes, G., Laval, A., Monnet, G., Petit, M. 1974, *Astr. Astrophys.*, **37,** 33.
Danziger, I. J., Murdin, P. G., Clark, D. H., D'Odorico, S. 1979, *Mon. Not. R. astr. Soc.*, **186,** 555.
Dickel, J. R., D'Odorico, S., Felli, M., Dopita, M. 1982, *Astrophys. J.*, **252,** 582.
Dickel, J. R., D'Odorico, S. 1984, *Mon. Not. R. astr. Soc.*, **206,** 351.
D'Odorico, S., Benvenuti, P., Sabbadin, F. 1978, *Astr. Astrophys.*, **63,** 63.
D'Odorico, S., Dopita, M. A., Benvenuti, P. 1980, *Astr. Astrophys. Suppl.*, **40,** 67 (DDB).
D'Odorico, S., Goss, W. M., Dopita, M. A. 1982, *Mon. Not. R. astr. Soc.*, **198,** 1059 (DGD).
Dopita, M. A., D'Odorico, S., Benvenuti, P. 1980, *Astrophys. J.*, **236,** 628.
Goss, W. M., Ekers, R. D., Danziger, I. J., Israel, F. P. 1980, *Mon. Not. R. astr. Soc.*, **193,** 901 (GEDI).
Humphreys, R. M. 1980, *Astrophys. J.*, **241,** 587.
Israel, F. P., van der Kruit, P. C. 1974, *Astr. Astrophys.*, **32,** 363.
Mills, B. Y. 1983, in *IAU Symp.* 101: *Supernova Remnants and their X-ray Emission*, Eds J. Danziger & P. Gorenstein, D. Reidel, Dordrecht, p. 551.
Mills, B. Y., Turtle, A. J. 1984, in *IAU Symp.* 108: *Structure and Evolution of the Magellanic Clouds*, Eds S. van den Bergh & K. S. de Boer, D. Reidel, Dordrecht, p. 283.
Mills, B. Y., Turtle, A. J., Little, A. G., Durdin, J. M. 1984, *Aust. J. Phys.*, **37,** 321.
Viallefond, F., Goss, W. M., van der Hulst, J. M., Crane, P. C. 1985, *Astr. Astrophys. Suppl.* (in press).

J. Astrophys. Astr. (l985) **6,** 153–157

VLA* Observations of Extreme Hydrogen Deficient Stars

N. Kameswara Rao *Indian Institute of Astrophysics, Bangalore 560034*

V. R. Venugopal *Radio Astronomy Centre, Tata Institute of Fundamental Research, Post Box 8, Udhagamandalam 643001*

A. Patnaik *Radio Astronomy Centre, Tata Institute of Fundamental Research, Bangalore 560012*

Received 1985 April 24; accepted 1985 June 25

Abstract. VLA observations at 2 and 6 cm have been obtained for six hydrogen-deficient stars R CrB, HD 160641, BD – 9°4395, V348 Sgr, MV Sgr and Sgr *v* Upper limits to the massloss rates have been estimated for some of these using the upper limits to the radio flux density.

Key words: Stars, hydrogen-deficient—stars, radio observations—stars, massloss— stars, individual— VLA observations

1. Introduction

Massloss in extreme hydrogen-deficient stars is an important phenomenon in understanding their evolution (Renzini 1983; Iben 1984) as well as in understanding the physical mechanism responsible for massloss (Hamann, Schönberner & Heber 1982). Extreme hydrogen-deficient stars comprise both hot and cool stars as well as variable and nonvariables. Hamann, Schönberner & Heber have obtained the rates of massloss for three nonvariable hot hydrogen-deficient stars from the profiles of ultraviolet resonance lines. They find that the massloss rates are similar to those of normal stars of the same luminosity and seem to decrease with increasing radius. However, these analyses arc strongly model dependent. The radio detection of free-free emission from ionized mass outflows probably provides the most accurate method for the determination of massloss rates. Therefore, we have observed a sample of hydrogen deficient stars with VLA at 2 and 6 cm. Although we could not detect any radio emission, we could set upper limits to the flux density which enabled setting upper limits to the massloss rates for some of these objects.

2. Observation

The observations of six of the hydrogen deficient stars were obtained with the VLA (Napier, Thompson & Ekers 1983) in the A configuration on 12 December 1983. Each

* National Radio Astronomy Observatory's Very Large Array is operated by Associated Universities Inc. under contract with National Science Foundation, USA

source was observed in snapshot mode at 6 cm (C-band) and 2 cm (U-band) with a bandwidth of 50 MHz in each band. The data were acquired in both AC and BD IFs (4835 MHz and 4885 MHz in C-band; 14915 and 14965 MHz in U-band). The data from two IFs were combined to make maps. A region of about 1 arcmin × 1 arcmin was mapped at 6 cm and 20 arcsec × 20 arcsec at 2 cm. As the positions of the stars were known quite accurately the regions searched for detection of radio emission were considered adequate. The maps were cleaned and restored using the standard software package AIPS. The results are tabulated in Table 1 along with other stellar data.

3. Massloss rates

Write & Barlow (1975) and Panagia & Felli (1975) have derived simple relations between the rate of massloss $\dot{M}$ and radio flux density S_ν at frequency ν when the flow is uniform and spherically symmetric with a velocity V_∞ independent of radius and time. The majority of the radio emission should originate far from the star so that the velocity can be approximated by the terminal value and the density is assumed to vary as r^{-2}. The Wright & Barlow formulation gives

$$\dot{M} = \frac{0{\cdot}095\ \mu\ V_\infty\ S_\nu^{3/4}\ D^{3/2}}{z\,\gamma^{1/2}\,g^{1/2}\,\nu^{1/2}} \qquad M_\odot\ \mathrm{yr}^{-1}$$

where V_∞ the terminal velocity in km s^{-1}, S_ν in Jy, ν in Hz, D the distance in kpc. The remaining parameters depend on composition, kinetic temperature T and ionization equilibrium in the radiating gas; μ is the mean atomic weight per nucleon, γ is the number of electrons per ion, z is the rms average charge of the ion, and $g(\nu, T)$ is the Gaunt factor (Spitzer 1962). Since spectral analyses of many of these objects indicate that their atmospheres are rich in helium (Cottrell & Lambert 1982; Dahari & Osterbrock 1984; Drilling *et al.* 1984), we adopt helium as the major constituent of the wind.

3.1. *Programme Stars*

RCrB: Altenhoff *et al.* (1976) give an upper limit of 5 mJy at 10·6 GHz from the observations obtained in 1973. The present estimate is more sensitive (< 0.3 mJy at 5 GHz). We adopt μ = 4, y = l and z = 1. The estimation of terminal velocity of the gas is uncertain. The massloss is indicated by the absorption components of Mg II lines of – 55 and – 28 km s^{-1} relative to the stellar absorption spectrum (Rao, Nandy & Bappu 1981). However, at the time of light minimum emission linewidths indicate expansion velocity of 250 km s^{-1}. If we adopt the terminal velocity as 100 km s^{-1}, then the upper limit to the massloss rate of ionized gas is < 7·9 × 10^{-7} $M_\odot$ yr^{-1}. However, the presence of low-density circumstellar material is indicated by the presence of emission lines of λ3727 of [OII] when the star is faint (> 13 mag). From the infrared flux, the massloss rate has been estimated as ~ 10^{-5} $M_\odot$ yr^{-1} (Forrest 1974) which is far in excess of our upper limit.

HD 160641: We adopt μ= 4, z = 2 and y= 2 as well as the distance and terminal velocity from the analysis of Hamann, Schonberner & Heber (1982). The present estimate of the massloss rate < 8·9 × $10^7 M_\odot$ yr^{-1} (Table 1) is consistent with their estimate.

Table 1. Upper limits to flux density and massloss.

Star	Spectral type	T_{eff} K	Distance pc	2 cm		6 cm		V km s^{-1}	(Upper limit) M $M_\odot$ yr^{-1}
				Beam size arcsec	Upper limit (3σ) flux density mJy	Beam size arcsec	Upper limit (3σ) flux density mJy		
R CrB	F8Ib	7000 (6)	1380 (1)	0.45 × 0.14	0.66	1.08 × 0.39	0.28	(100)	7.9×10^{-7}
BD −9°4395	B0	24000 (4)	1860 (2)	0.44 × 0.20	0.81	1.48 × 0.55	0.28	600	2.4×10^{-6}
HD160641	O	32500 (4)	1000 (2)	0.43 × 0.23	1.14	1.38 × 0.64	0.34	550	8.9×10^{-7}
V348 Sgr	B0–B1	23000 (3)	2200 (3)	0.44 × 0.26	0.84	1.37 × 0.74	0.34	(100)	1.8×10^{-6}
MV Sgr	B2	18000 (4)	2690 (4)	0.44 × 0.24	0.93	1.46 × 1.20	0.34	(500)	1.2×10^{-5}
υ Sgr	Ap + B3	10500 (4)	600 (5)	0.44 × 0.21	0.88	1.16 × 1.13	0.30	700	5.4×10^{-7}

References to columns 3 and 4:
(1) Assuming $M_v = -5$ (Rao, Nandy & Bappu 1981)
(2) Hamann, Schönberner & Heber (1982)
(3) Rao & Nandy (1985)
(4) Drilling *et al.* (1984); Rao & Nandy (1982)
(5) Rao & Venugopal (1985)
(6) Cottrell & Lambert (1983)

BD – 9°4395: The terminal velocity again is taken from Hamann, Schönberner & Heber, $\mu = 4$, z = 2 and $y = 2$ have been adopted. The distance is estimated by adopting $\log L_*/L_\odot = 4.0 \pm 0.5$ and $E(B-V) = 0.31$.

MV Sgr: We adopt $\mu = 4$, z = 1, $y = 1$. The distance is estimated by adopting $M_v = -1$ and $E(B-V) = 0.5$. The terminal velocity is very uncertain, lack of line-shifts in the low-resolution IUE spectra gives a velocity < 500 km s^{-1}. The upper limit to the massloss rate is quoted in Table 1. The ultraviolet spectra show changes in line strengths of Fe II, Al II *etc* (Rao & Nandy 1982) indicating massloss.

V 348 Sgr: We adopt $\mu = 4$, $y = 1$ and $z = 1$. The emission linewidths indicate an expansion velocity of ~ 50 km s^{-1} (Houziaux 1968; Dahari & Osterbrock 1984). If we adopt the terminal velocity of ~ 100 km s^{-1} then $\dot{M} \lesssim 1.8 \times 10^{-6}\ M_\odot$ yr^{-1} for the ionized gas (Table 1). The star is known to be surrounded by an optical nebulosity extending to 8–10 arcsec. The distance has been estimated as 2.2 kpc by Rao & Nandy (1985) which leads to a $N_e \sim 2 \times 10^3$ cm^{-3} estimated from nebular Hβ emission and which agrees well with the value of N_e independently estimated from forbidden lines. The analysis of Dahari & Osterbrock (1984) show that the star's CII emission-line region is characterised by $T \sim 2 \times 10^4$ K.

υ Sgr: This is one of the three known hydrogen-deficient binary stars. It has a period of 138 days. The IUE spectrum shows resonance lines due to NV, CIV, SiIV *etc.* strongly in absorption, indicating massloss with a terminal velocity of 700 km s^{-1}. The observational aspects have been discussed by Rao & Venugopal (1985). We adopt $\mu = 4$, $z = 2$, $\gamma = 2$, $T_e \sim 10^5$ K. The present upper limit to the radio flux density indicates a massloss rate $\leqslant 5.4 \times 10^{-7}\ M_\odot$ yr^{-1} (Table 1). In the evolution scheme proposed by Plavec (1973) and Schönberner & Drilling (1983), the system is supposed to have lost or to be losing 4 to 12 $M_\odot$ from the primary star. The present rate of massloss is not sufficient to have reduced the primary to a hydrogen-deficient star of 1 $M_\odot$. Most of the matter must have been lost, to the system already in an earlier phase of evolution.

4. Discussion

The upper limits to the rate of massloss obtained for HD 160641 and BD – 9° 4395 are in agreement with the upper limits $10^{-7\,2}$ and $10^{-7\,7}\ M_\odot$ yr^{-1}, respectively, determined earlier by Hamann, Schönberner & Heber (1982) from ultraviolet spectral lines.

Acknowledgements

We would like to thank Ms Peggy Perley for obtaining the VLA observations for us and the referees for their comments.

References

Altenhoff, W. J.; Braes, L. L. E, Olnon, F. M, Wendker, H. J. 1976, *Astr. Astrophys.*, **46,** 11.
Cottrell, P. L, Lambert, D. L. 1982, *Astrophys. J.*, **261,** 595.
Dahari, O., Osterbrock, D. E. 1984, *Astrophys. J.*, **277,** 648.

Drilling, J. S., Schönberner, D., Heber, U., Lynas-Gray, A. E. 1984, *Astrophys. J*., **278,** 224.
Forrest, W. J. 1974, *Ph.D. Thesis*, Univ. California, San Diego.
Hamann, R., Schönberner, D., Heber, U. 1982, *Astr. Astrophys*., **116,** 273.
Houziaux, L. 1968, *Bull. astr. Inst. Csl*., **19,** 265.
Iben, Jr. I. 1984, *Astrophys. J*., **277,** 333.
Napier, P. J., Thompson, A. R., Ekers, R. D. 1983, *Proc. IEEE*, **71,** 1295.
Panagia, N., Felli, M. 1975, *Astr. Astrophys*., **39,** 1.
Plavec, M. J. 1973, in *IAU Symp.* 51: *Extended Atmospheres and Circumstellar Matter in Spectroscopic Binary Systems*, Ed. A. H. Batten, D. Reidel, Dordrecht, p. 216.
Rao, N. K., Nandy, K. 1982, *J. Astrophys. Astr.*, **3,** 79.
Rao, N. K., Nandy, K. 1985, Preprint.
Rao, N. K., Venugopal, V. R. 1985, *J. Astrophys. Astr.*, **6,** 101.
Rao, N. K., Nandy, K., Bappu, M. K. V. 1981, *Mon. Not. R. astr. Soc*, **195,** 71P.
Renzini, A. 1983, in *IAU Symp.* 103: *Planetary Nebulae*, Ed. D. R. Flower, D. Reidel, Dordrecht, p. 267.
Schönberner, D., Drilling, J. S. 1983, *Astrophys. J*., **268,** 225.
Spitzer, L. 1962, *Physics of Fully Ionized Gases*, Interscience, New York, p. 148.
Wright, A. E., Barlow, M. J. 1975, *Mon. Not. R. astr. Soc.*, **170,** 41.

J. Astrophys. Astr. (1985) **6,** 159–164

Spectroscopic Binaries near the North Galactic Pole
Paper 13: HD 110195

R. F. Griffin* *The Observatories, Madingley Road, Cambridge, England CB30HA*

Received 1985 June 5; accepted 1985 June 27

Abstract. Photoelectric radial-velocity measurements show that the tenth–magnitude object HD 110195 is a double-lined spectroscopic binary. It consists of two very similar late-G dwarfs in an orbit having high eccentricity and a period of 18 days.

Key words: radial velocities—spectroscopic binaries—stars, individual

HD 110195 is a late-type star about 3° following γ Com, At a Galactic latitude of more than 87°, it is closer to the Galactic Pole than any spectroscopic binary whose orbit has been determined previously, either in this series of papers or elsewhere. It is amongst the faintest *Henry Draper Catalogue* stars in the North Galactic Pole field, being fainter than tenth magnitude.

Two photoelectric determinations have been made of the magnitude of HD 110195: Harris & Upgren (1964) found $V = 10.14$, $(B - V) = 0.74$, $(U - B) = 0.34$, whereas McClure & Crawford (1971) found $V = 10.04$, $(B - V) = 0.74$. The latter authors did not comment on the discrepancy between their own determination of the V magnitude and the earlier one. The V magnitude derived from Geneva photometry (Rufener 1980) is 10.13.

There is an equally serious discordance between the two MK types to be found in the literature: Stock & Wehlau (1956) obtained G3 V, but Woolley *et al.* (1981) preferred G8 V. McClure & Crawford (1971) inferred a type of G9 V from narrow-band photometry, but their result is not an actual classification of the spectrum.

HD 110195 is the first binary shown in the present series of papers to be double-lined. Its faintness, together with the splitting of the 'dip' on radial-velocity traces into two nearly equal parts (each, of course, only about half as deep as a single star of the same spectral type would give) makes it a difficult object to observe with the Cambridge radial-velocity instrument (Griffin 1967). This paper accordingly relies to an unusual extent on observations made with the spectrometer (Griffin & Gunn 1974) at the Palomar 200-inch telescope, where HD 110195 has been observed as a matter of some priority in recent seasons; and observations made with the Dominion Astrophysical Observatory instrument (Fletcher *et al.* 1982) have also been helpful.

* Guest Investigator, Palomar Observatory; Visiting Observer, Dominion Astrophysical Observatory, Victoria

A recent Palomar radial-velocity trace, illustrating the double-lined nature of HD 110195 at a time when the components of the binary exhibited a mutual difference of velocity of more than 100 km s^{-1}, is shown in Fig. 1. There is seen to be a difference of about 10 per cent between the depths of the two dips. Within observational error, such an inequality is shown by all Palomar traces of the object, its mean value being 12.7 ± 1.6 per cent. The difference is sufficient to permit unambiguous identification of the respective components from Palomar traces; but the same is not true of traces obtained at Cambridge or the DAO, for which the component assignments often had to be made retrospectively after the orbital period was discovered. Because the intrinsic depth of the dip increases towards later spectral types throughout the G-dwarf sequence, the difference in luminosity of the components of HD 110195 (in the wavelength range used by the radial-velocity spectrometers, ~ *B*) is somewhat greater than the difference in dip depths; it may be estimated at 16 per cent or 0.16 mag, and corresponds (Allen 1973) to a difference in spectral type of rather less than one sub-class. The sum of the absolute depths of the dips is consonant with the depth expected for a late-G dwarf but (like the broad-band colour indices) is too great to correspond to the type of G3 V favoured by Stock & Wehlau.

There is one measurement of the radial velocity of HD 110195 in the literature, made photographically in 1970 by Woolley *et al.* (1981) at Kottamia. The dispersion (66 Å mm^{-1}) was too small to resolve the components, and the velocity obtained was close to the γ-velocity derived below. The first photoelectric observation was made at Cambridge in 1973; unfortunately it was at a phase when the two dips in the trace were juxtaposed but not *super*posed, and the double-lined nature of the object was not recognized although it did confuse the measurement of the trace. The discovery of the double lines was made when HD 110195 was next observed, at Palomar in 1978. Altogether 12 Palomar observations have now been made, and 12 Cambridge and 4 DAO measurements at times when the traces were not seriously compromised by juxtaposition or blending of the dips. All the radial velocities are collected in Table 1.

In other papers, in the present series no special weighting has been accorded to Palomar observations, notwithstanding that they are normally more accurate than Cambridge ones. The ideas behind this policy are (*a*) to avoid the attribution of a great

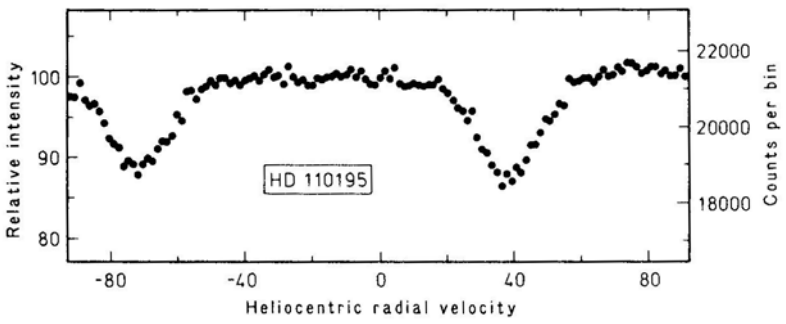

Figure 1. Palomar radial-velocity trace of HD 110195, observed on 1984 December 2. The points represent the photon counts in a set of independent 'bins' corresponding to a uniformly spaced set of longitudinal displacements of a specially constructed mask upon which the stellar spectrum is focussed. A more complete description of the equipment and procedure is given by Griffin & Gunn (1974).

Table 1. Photoelectric radial-velocity measurements of HD 110195.

Date			MJD	Velocity (km s^{-1}) Prim.	Sec.	Phase	$(O-C)$ (km s^{-1}) Prim.	Sec.	Obs.*
1973	Mar	31.03†	41772.03	−11.7:		0.021			C
1978	May	23.28	43651.28	+2.7	−29.2	105.724	+2.7	+3.5	P
1981	May	4.93	44728.93	−43.4:		166.339	+0.3		C
		17.35‡	741.35	−24.8	−12.8	167.038	−1.7	−3.1	P
		19.20	743.20	−56.6	+22.4	.142	+0.1	−1.3	P
	Dec	4.55	942.55	−42.6	+10.6	178.355	−0.2	+1.1	P
		6.55	944.55	−32.7	−2.0	.467	−1.0	−0.9	P
1982	Jan	21.18†	44990.18	−14.8		181.034			C
	Mar	4.08	45032.08	−39.2:	+5.8	183.391	−0.1	−0.4	C
		8.14†	036.14	−20.6		.619			C
		13.05	041.05	+38.2:		.895	−1.9		C
		16.09	044.09	−45.9:	+10.0	184.066	−2.1	−0.9	C
	Nov	23.57	296.57	−49.7	+16.4	198.268	+0.2	−0.6	P
		24.57	297.57	−45.5	+13.1	.324	−0.4	+0.9	P
		25.55	298.55	−40.0	+5.5	.379	+0.2	−1.8	P
		26.56	299.56	−34.5	+2.2	.436	+0.3	+0.2	P
1983	Feb	3.49	45368.49	−46.6	+14.0	202.313	−0.5	+0.8	V
		4.49	369.49	−42.1	+8.6	.369	−1.0	+0.4	V
		15.38	380.38	+44.9	−81.1	.982	−1.1	−2.7	V
		23.11	388.11	−36.5	+5.5	203.417	+0.1	+1.7	C
		28.10§	393.10	−7.7::	−34.7::	.697	−3.4	−6.3	C
	Mar	15.08§	408.08	−27.9::	−16.6::	204.540	−3.7	−8.0	C
	May	15.92	469.92	−0.9	−35.4:	208.018	−2.1	−1.6	C
	June	6.92	491.92	−52.4	+18.8	209.256	−1.6	+0.9	C
		18.92	503.92	+52.6	−80.4	.931	+1.6	+2.9	C
		19.92	504.92	+41.4	−77.3	.987	−0.3	−3.2	C
1984	Apr	17.01	45807.01	+47.2	−82.7	226.979	−1.0	−2.1	C
		20.99	810.99	−55.2	+23.1	227.202	−0.6	+1.4	C
	Nov	29.57	46033.57	+0.7	−31.6	239.722	+1.1	+0.7	P
		30.53	034.53	+8.7	−42.0	.776	−0.6	−0.1	P
	Dec	2.53	036.53	+38.2	−71.3	.889	+0.3	−0.9	P
		21.24	055.24	+51.2	−84.3	240.941	−2.2	+1.4	C
1985	Feb	17.44	46113.44	−50.7	+21.9	244.214	+3.1	+1.0	V

* Observatory code:
C = Cambridge 36-inch telescope (Griffin 1967)
P = Palomar 200-inch telescope (Griffin & Gunn 1974)
V = Dominion Astrophysical Observatory 48-inch telescope (Fletcher *et al.* 1982)

† Blended dips. Not used in orbital solution.

‡ Blended dips, but on Palomar trace can be split (Griffin 1982) Used in solution with weight 1.

§ Closely juxtaposed dips; attempts to read both velocities From them were manifestly unsuccessful, and the results have been rejected.

deal of weight to just a very few isolated observations, and (*b*) since there are so few Palomar observations their weighting will not make much difference to the orbital solution anyway. A different attitude seems to be called for in the case of HD 110195, where the two principal sources have provided similar numbers of observations of manifestly different quality, the Palomar ones being perfectly satisfactory whereas the Cambridge ones are mostly rather marginal. In principle the proper weighting should

be determined by the orbital solution itself, through successive iterations; but it is difficult to apply such a principle in the present case, where the result hinges upon the retention or rejection of one particular observation whose seemingly 'wild' residuals provide two-thirds of the total variance of all the Palomar measurements. In other cases where Cambridge observations have been obtained only with difficulty (*e.g.* Griffin *et al.* 1985), weights of Palomar 4, Cambridge 1 have been found to do reasonable justice to the respective sources, and those weights are adopted here. Then, on the proper basis of the orbital residuals, Victoria measures have been given the same weight as Cambridge ones, and all observations of the secondary have had their weights multiplied by 0.6.

The final orbital solution derived from the data given in Table 1 on the basis of the adopted weighting is illustrated in Fig. 2 and has the following elements:

$$P = 17.7786 \pm 0.0005 \text{ days} \qquad (T)_{198} = \text{MJD } 45291.812 \pm 0.023$$

$$\gamma = -16.36 \pm 0.19 \text{ km s}^{-1} \qquad a_1 \sin i = 11.28 \pm 0.10 \text{ Gm}$$

$$K_1 = 55.8 \pm 0.5 \text{ km s}^{-1} \qquad a_2 \sin i = 11.22 \pm 0.17 \text{ Gm}$$

$$K_2 = 55.5 \pm 0.8 \text{ km s}^{-1} \qquad f(m_1) = 0.181 \pm 0.005\ M_\odot$$

$$q = 0.995 \pm 0.012\ (= m_1/m_2) \qquad f(m_2) = 0.178 \pm 0.008\ M_\odot$$

$$e = 0.563 \pm 0.005 \qquad m_1 \sin^3 i = 0.72 \pm 0.04\ M_\odot$$

$$\omega = 60.4 \pm 0.8 \text{ degrees} \qquad m_2 \sin^3 i = 0.72 \pm 0.02\ M_\odot$$

R.m.s. residual (unit weight) = 1.7 km s^{-1}

The HD 110195 system is very reminiscent of the Hyades binary system van Bueren 117 (Griffin & Gunn 1978) in the nature of the components, the period and the high

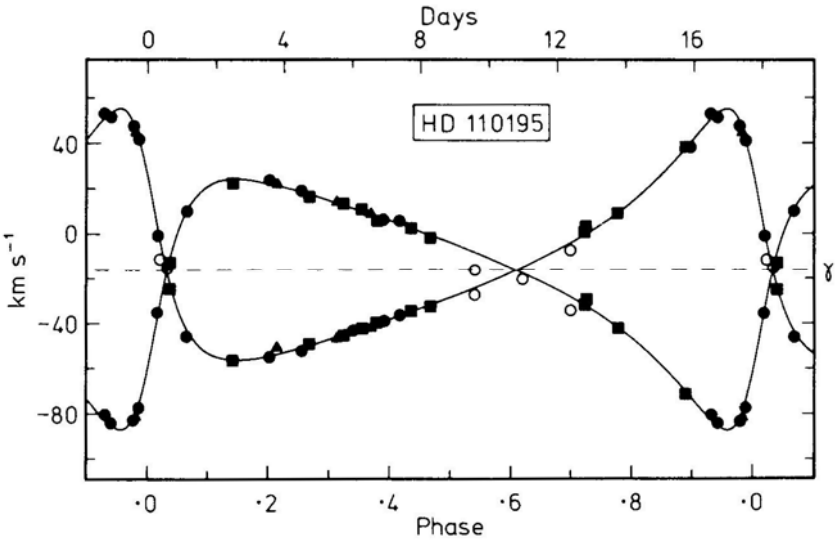

Figure 2. The computed radial-velocity curve for HD 110195, with the measured radial velocities plotted. Palomar observations are plotted as squares, Cambridge as circles and Victoria as triangles. Open symbols indicate observations not used in the orbital solution.

eccentricity. Van Bueren 117 exhibits BY Dra variability with a period considerably shorter than the orbital period (Bopp, Noah & Klimke 1980), and it would now be of interest to know whether HD 110195 is also a BY Dra variable. The discordance of 0.10 mag between the two published photoelectric *V* magnitudes (Harris & Upgren 1964; McClure & Crawford 1971) might well encourage that interest; on the other hand, the somewhat earlier spectral type and longer orbital period of HD 110195 reduce the *a priori* likelihood that that object is a BY Dra system. Moreover, the radial-velocity traces of HD 110195 show little rotational broadening; the minimum equatorial velocity of 5 km s^{-1} which has been repeatedly suggested (e.g. Bopp, Noah & Klimke 1980) as a necessary condition for BY Dra variability is close to the upper limit of the rotation that is compatible with traces such as that shown in Fig. 1.

The values of m_1, $\sin^3 i$ and $m_2 \sin^3 i$ derived from the orbital elements suggest that $0.90 < \sin i < 0.95$, corresponding approximately to $64° < i < 72°$. It is therefore unlikely that HD 110195 will be found to exhibit eclipses, which would only take place if $i \gtrsim 84°$.

A disconcerting feature of Table 1 is the unacceptable residuals, for both components, shown by the Palomar observation of 1978 May 23. They are far too large to be understood as random errors, and adjacent observations of other stars confirm their systematic correctness. The question arises as to how they are to be regarded. To accept the corresponding observation fully would be to imply that HD 110195 has a variable *y*-velocity and is therefore a triple system; the author is not prepared to do that on the basis of one observation, although it is true that that is the only way in which the 1978 observation can be reconciled with the others. To reject the observation without any better reason than discomfiture over its residuals would be too arbitrary. To retain it in the solution, where it does not seem to belong— it contributes more than a third to the sum of the (weighted) squares of the deviations of all the observations—is perhaps equally unsatisfactory; but there is some justice in its causing the solution to be less certain than would otherwise be the case, and that is the course that has been followed here. The possibility of variation in the γ-velocity, like that of photometric variability, is one that warrants investigation in the future.

Acknowledgements

It is a pleasure to acknowledge the guest-investigator privileges accorded me by the Palomar Observatory and the Dominion Astrophysical Observatory. Dr J. E. Gunn kindly collaborated in the Palomar observations.

References

Allen, C. W. 1973, *Astrophysical Quantities*, Athlone, London, p. 206.
Bopp, B. W., Noah, P. V., klimke, A. 1980, *Astr. J.*, **85,** 1386.
Fletcher, J. M., Harris, H. C, McClure, R. D., Scarfe, C. D. 1982, *Publ. astr. Soc. Pacific*, **94,** 1017.
Griffin, R. F. 1967, *Astrophys. J.*, **148,** 465.
Griffin, R. & R. 1982, *Observatory*, **102,** 217.
Griffin, R. F., Gunn, J. E. 1974, *Astrophys J.*, **191,** 545.
Griffin, R. F., Gunn, J. E. 1978, *Astr. J.*, **83,** 1114.
Griffin, R. F., Gunn, J. E., Zimmerman, B. A., Griffin, R. E. M. 1985, *Astr. J.*, **90,** 609.

Harris III, D. L., Upgren, A. R. 1964, *Astrophys. J.*, **140,** 151.
McClure, R. D., Crawford, D. L. 1971, *Astr. J.*, **76,** 31.
Rufener, F. 1980, *Third Catalogue of Stars Measured in the Geneva Observatory Photometric System*, Observatoire de Geneve, Geneva.
Stock, J., Wehlau, W. H. 1956, *Astr. J.*, **61,** 80.
Woolley, R., Penston, M. J., Harding, G. A., Martin, W. L., Sinclair, J. E., Haslam, C. M., Asian, S., Savage, A., Aly, K., Asaad, A. S. 1981, *R. Obs. Ann.*, no. 14, p. 73.

J. Astrophys. Astr. (1985) **6,** 165–169

Temperature Dependent Variation of Pulsar Periods

M. C. Padmaraj & S. C. K. Nair *Physics Department, Calicut University, Calicut 673635*

Received 1984 December 18; in revised form 1985 June 24; accepted 1985 June 28

Abstract. Changes in the radii of neutron stars due to variations in core temperature are studied qualitatively in a simple model. The resulting irregular changes in pulsar periods are compared with observed values. For the millisecond pulsar PSR 1937 + 214 the random changes in period due to temperature variation is estimated to be of the order of 10^{-14} s yr^{-1} which is two orders of magnitude smaller than the steady variation due to loss of energy by radiation.

Key words: Pulsars, period variations—neutron stars, cooling—stars, interiors

1. Introduction

Three classes of period variations have been observed in pulsars: steady secular changes, unpredictable period discontinuities, and small random fluctuations (Manchester & Taylor 1977), The experimental results of Boynton *et al.* (1972) suggest that random fluctuations in pulsar periods can be described as a random walk in frequency. This implies random changes in the stellar moment of inertia. Several possible mechanisms have been suggested (see Manchester & Taylor 1977 and references therein). In particular, Greenstein (1979) proposes that a heat pulse would slow down the neutron star interior, and spin up the crust. We investigate here a somewhat different mechanism of period variations induced by changes in temperature: the temperature variations produce small changes in radius, which in turn produce changes in the pulsation period. We make here a qualitative estimate of the random fluctuations in period caused by variations in the temperature.

2. The model

The structure of neutron stars is governed by the Tolman-Oppenheimer-Volkoff equation (Baym, Pethick & Sutherland 1971)

$$\frac{dP}{dr} = \frac{-[P(r)+\rho(r)][m(r)+4\pi r^3 P(r)]}{r^2[1-2m(r)/r]}, \tag{1}$$

$$\frac{dm}{dr} = 4\pi r^2 \rho(r), \tag{2}$$

Where $P(r)$ is the pressure, $m(r)$ is the mass within the radius r, and $\rho(r)$ is the energy density. Here, and in what follows, we set $G = c = h = 1$. Assuming adiabatic condition, the neutron number density n is related to p by (Misner, Thorne & Wheeler 1973)

$$\frac{\partial \rho}{\partial n} = \frac{P+\rho}{n}. \tag{3}$$

The core of the neutron star is assumed to be spherical with uniform energy density. It is also assumed to be isothermal and we ignore the crust. Under these assumptions, Equations (1) and (2) could be easily solved to give the radius

$$R = \left(\frac{3P^2}{\pi\rho^3} + \frac{3P}{2\pi\rho^2}\right)^{1/2} (1 + 3P/\rho)^{-1} \tag{4}$$

where P is the pressure at the centre.

The equation of state is found in the temperature dependent Hartree-Fock approximation with the Skyrme interaction. We use the SII set (Vautherin & Brink 1971) with the following parameters: $t_0 = -1169.9$ MeV fm^2, $t_1 = 586.6$ MeV fm^5, $t_2 = 0.27$ MeV fm^5, and $x_0 = 0.34$. The three-body term does not contribute to the energy of neutron matter. A modified form of the density dependence could contribute, but we ignore it here. The effective mass m^* and the single particle potential v are given by

$$\frac{1}{2m^*} = \frac{1}{2m_n} + \frac{1}{8}(t_1 + 3t_2)n, \tag{5}$$

$$v = \frac{1}{2}t_0(1 - x_0)n + \frac{1}{8}(t_1 + 3t_2)\tau, \tag{6}$$

where n and τ are the number and kinetic energy densities at a given distance from the centre. The entropy S per unit volume is calculated from

$$S = \frac{-1}{n\pi^2}\int_0^\infty K^2\,\mathrm{d}K[f(K)\log f(K) + \{1 - f(K)\}\log\{1 - f(K)\}], \tag{7}$$

with

$$f(K) = \left[1 + \exp\left\{\frac{1}{K_B T}\left(\frac{K^2}{2m^*} + v - \mu\right)\right\}\right]^{-1} \tag{8}$$

and μ is the chemical potential, K_B is the Boltzman's constant and K is the magnitude of the neutron momentum in units of h. The total energy per unit volume is then evaluated as

$$E = \frac{\tau}{2m_n} + \frac{1}{4}t_0(1 - x_0)n^2 + \frac{1}{8}(t_1 + 3t_2)n\tau \tag{9}$$

and the pressure ($P = TS - E + \mu n$) is given by

$$P = \left(\frac{5}{6m^*} - \frac{1}{2m_n}\right)\tau + \frac{1}{4}t_0(1 - x_0)n^2 \tag{10}$$

Where

$$n = \frac{(2m^*K_B T)^{3/2}}{2\pi^2}\int_0^\infty \frac{x^{1/2}\,\mathrm{d}x}{(e^{x-\eta} + 1)}, \tag{11}$$

and
$$\tau = \frac{(2m^* K_B T)^{5/2}}{2\pi^2} \int_0^\infty \frac{x^{3/2} dx}{(e^{x-\eta}+1)} \tag{12}$$

with
$$\eta = (\mu - v)/K_B T.$$

When η is large (as is the case here), the above Fermi-integrals could be evaluated by the Sommerfeld approximation (Landau & Lifshitz 1958) as

$$\int_0^\infty \frac{x^{1/2} dx}{(e^{x-\eta}+1)} \simeq \frac{2}{3}\eta^{3/2}\left(1+\frac{\pi^2}{8\eta^2}\right), \tag{13}$$

$$\int_0^\infty \frac{x^{3/2} dx}{(e^{x-\eta}+1)} \simeq \frac{2}{5}\eta^{5/2}\left(1+\frac{5\pi^2}{8\eta^2}\right). \tag{14}$$

Thus, we have

$$P = \left(\frac{5}{6m^*} - \frac{1}{2m_n}\right)\frac{(3\pi^2 n)^{5/3}}{5\pi^2}\left[1+\frac{5\pi^2(2m^*)^2 K_B^2 T^2}{12(3\pi^2 n)^{4/3}}\right]. \tag{15}$$

This, together with Equation (4), gives us the explicit temperature dependence of R.

Using the fact that pR^3 is a constant, we find the change in R due to a change in T, the temperature of the star, as

$$\dot{R} = \frac{\frac{\partial R}{\partial P}\frac{\partial P}{\partial T}\dot{T}}{1+\frac{3\rho}{R}\left(\frac{n}{P+\rho}\frac{\partial R}{\partial n}+\frac{\partial R}{\partial \rho}\right)}, \tag{16}$$

where $\dot{R}$ and $\dot{T}$ are the time derivatives of R and T respectively.

Assuming that the moment of inertia of the rotating neutron star is proportional to R_2, the angular momentum conservation gives us

$$\frac{\dot{P}_1}{P_1} = \frac{\dot{\omega}}{\omega} = \frac{2\dot{R}}{R}, \tag{17}$$

where P_1 is the pulsation period and ω is the angular frequency; superscript dots indicate corresponding time derivatives.

3. Results

We now make a few numerical estimates of the change in radius. Calculations are carried out for two values of density. The computed values of radius, mass and $\dot{R}/T\dot{T}$ are enumerated in Table 1. In what follows we use the 1 $M_\odot$ results for illustrative purposes.

According to observational upper limits from the Einstein observatory, the surface temperature of younger neutron stars (10^3 yr old) is 3×10^6 K (Tsuruta 1980, 1981; Nomoto & Tsuruta 1981). The corresponding interior temperature is 10^9 K and the rate of cooling 10^5 K yr^{-1} (Tsuruta 1979). In addition to normal cooling, some heating mechanisms are also thought to be at work in neutron stars (Tsuruta 1979). In the case of radio pulsars, accretion of positrons, friction between crust and core, plastic flows *etc.* are the possible heating mechanisms. There is observational evidence that older radio pulsars are heated to almost 10^6 K (Helfand 1981). Since there is heating as well as

Table 1. Temperature dependent changes in the radius of a neutron star.

Density g cm^{-3}	Radius R km	Mass $M_\odot$	$\dot{R}/(T\dot{T})$
0.98×10^{15}	7.9	1.0	2.1×10^{-24}
1.72×10^{15}	7.1	1.3	0.3×10^{-24}

cooling, the star may reach a steady state. The rate of cooling at this surface temperature is 10^5 K yr^{-1} (Tsuruta 1974) which would equal the rate of heating at steady state. In order to arrive at some order-of-magnitude estimates, we will assume in the following that there exist irregular fluctuations of the order 10^5 K yr^{-1} in the core, though we do not have any observational evidence for this number.

For the Crab pulsar, $\omega = 2 \times 10^2$ s^{-1}. Taking $T = 10^9$ K, $\dot{T} = 10^5$ K yr^{-1} = 10^3 K day^{-1}, we find the magnitude of the possible change in ω in one day as 10^{-10} s^{-1}. In the case of older radio pulsars, surface temperature is 10^6 K. Taking $\omega = 10$ s^{-1}, $T = 10^8$ K and $\dot{T} = 10^3$ K day^{-1}, we find the magnitude of the change in ω in one day as 10^{-12} s^{-1}.

Analysis of Crab pulsar arrival times by Boynton *et al.* (1972) shows that the data are consistent with frequency noise, *i.e.*, a random series of frequency jumps with $R \langle \Delta\omega^2 \rangle \gtrsim 4 \times 10^{-21}$ s^{-3}, where R is the rate at which frequency jumps occur and $\langle \Delta\omega^2 \rangle$ is their variance. Since individual frequency jumps are not resolved with daily observations $R \gtrsim 10^{-4}$ s^{-1} and hence rms size of frequency jumps $\langle \Delta\omega^2 \rangle^{1/2} \lesssim 6 \times 10^{-9}$ s^{-1} Groth (1975), using a more sophisticated procedure, found $\langle \Delta\omega^2 \rangle^{1/2} \lesssim 5 \times 10^{-9}$ s^{-1} These values are to be compared with our result of $\sim 10^{-10}$ s^{-1}.

For older pulsars of longer period, Manchester & Taylor (1974) find that $\langle \Delta\omega^2 \rangle^{1/2} \lesssim 4 \times 10^{-12}$ s^{-1}, which is of the same order as that of our result. For the millisecond pulsar PSR 1937 + 214, friction between crust and core could be a major heating mechanism (Backer, Kulkarni & Taylor 1983). If rotation is sufficiently fast, heating mechanisms can keep the surface temperature around 10^6 K even if the object is old (Tsuruta 1979). Taking $T = 10^8$ K and $\dot{T} = 10^5$ K yr^{-1}, we find $\dot{P}_1 \simeq 10^{-14}$ s yr^{-1} ($\dot{\omega} \simeq 10^{-9}$ s yr^{-1}). These fluctuations would be superimposed on the steady increase in period $3{\cdot}8 \times 10^{-12}$ s yr^{-1}, due to loss of energy by radiation.

In the case of binary X-ray pulsars, matter is being accreted from the companion. For typical accretion rates, the stellar surface may be heated to temperatures of the order of 10^7 K, and the whole star to an average value of 10^6 K. For $T = 10^8$ K, $P_1 = 1$ s and $\dot{T} = 10^5$ K yr^{-1}, we find $\dot{P}_1 \simeq 10^{-12}$ s yr^{-1} ($\dot{\omega} \simeq 10^{-11}$ s yr^{-1}).

In summary, possible temperature variations of $\sim 10^5$ K yr^{-1} in the interior of neutron stars could produce daily random frequency variations of the order of 10^{-10} s^{-1} in young pulsars and 10^{-12} s^{-1} in older long period pulsars. The observed daily random fluctuations in frequency are $\simeq 5 \times 10^{-9}$ s^{-1} and $\simeq 4 \times 10^{-12}$ s^{-1} respectively. For the millisecond pulsar PSR 1937 + 214, the expected random fluctuations in period is two orders of magnitude less than the steady increase due to loss of energy by radiation.

Acknowledgements

This work was financially supported by a grant BRNS/37/11 80–83 from the Department of Atomic energy, Government of India. We are very grateful to Professor S. Tsuruta for several valuable suggestions which have been incorporated in the present version of this paper. We also wish to thank C. Radhakrishnan for many critical discussions.

References

Backer, D. C, Kulkarni, S. R., Taylor, J. H. 1983, *Nature*, **301,** 314.
Baym, G., Pethick, C, Sutherland, P. 1971, *Astrophys. J.*, **170,** 299.
Boynton, P. E., Groth, E. J., Hutchinson, D; B., Nanos, G. P., Partridge, R. B., Wilkinson, D. T. 1972, *Astrophys. J.*, **175,** 217.
Greenstein, G. 1979, *Astrophys. J.*, **231,** 880.
Groth, E. J. 1975, *Astrophys. J. Suppl. Ser.*, **29,** 431.
Helfand, D. J. 1981, in *IAU Symp.* 95: *Pulsars*, Eds W. Sieber & R. Wielebinski, D. Reidel, Dordrecht, p. 343.
Landau, L. D., Lifschitz, E. M. 1958, *Statistical Physics*, Pergamon Press, London, p. 164.
Manchester, R. N., Taylor, J. H. 1974, *Astrophys. J.*, **191,** L63
Manchester, R. N., Taylor, J. H. 1977, *Pulsars*, Freeman, San Francisco.
Misner, C. W., Thorne, K. S., Wheeler, J. A. 1973, *Gravitation*, Freeman, San Francisco, pp. 557–562.
Nomoto, K., Tsuruta, S. 1981, *Astrophys. J.*, **250,** L19.
Tsuruta, S. 1974, *Physics of Dense Matter*, D. Reidel, Dordrecht, p. 209.
Tsuruta, S. 1979, *Phys. Rep.*, **56,** 237.
Tsuruta, S. 1980, in *X-ray Astronomy*, Eds R. Giacconi & G. Setti, D. Reidel, Dordrecht, p. 73.
Tsuruta, S. 1981, in *IAU Symp.* 95: *Pulsars*, Eds W. Sieber & R. Wielebinski, D. Reidel, Dordrecht, p. 331.
Vautherin, D., Brink, D. M. 1972, *Phys. Rev. C*, **5,** 626.

J. Astrophys. Astr. (1985) **6,** 171–175

On a Nonlinear and Lorentz-Invariant Version of Newtonian Gravitation—II

J. V. Narlikar & T. Padmanabhan *Tata Institute of Fundamental Research, Homi Bhabha Road, Bombay 400005*

Received 1985 June 18; accepted 1985 August 6

Abstract. This paper gives a full nonlinear version of Newtonian gravity in which the gravitational energy acts as a source of the gravitational field. The generalized field equation for the scalar gravitational potential is solved for a spherically symmetric localized distribution of matter. It is shown that the perihelia of orbits of test particles in such a field precess steadily. The effect is, however, too small to account for the observed shift in the perihelion of planet Mercury. Further, the bending of light in this theory is zero. It is suggested that these inadequacies of the quasi-Newtonian framework call for more sophisticated approaches to gravity.

Key words: Newtonian gravitation, nonlinear—Lorentz-Invariant gravitation

1. Introduction

This paper forms a sequel to an earlier paper by Rawal & Narlikar (1982, hereafter referred to as Paper I) in which an attempt was made to combine the essentials of special relativity with those of Newtonian gravity to construct a scalar Lorentz invariant theory of gravity. Paper I was limited to discussing first order effects in which the mass-equivalent of gravitational energy acts as a source of the scalar gravitational potential ϕ. Here we generalize the framework to all orders in which the feedback of gravitational energy on ϕ in turn modifies the energy which further modifies ϕ and so on. We will then apply the field equation of the modified theory to study the gravitational effects of spherical distributions of matter. As in Paper I, the approach will be Lorentz invariant.

It will be shown that the above problem can be solved exactly and that the motion of a test particle in the field can be applied to study the orbits of planets around the Sun.

2. The field equations

As in Paper I we will begin by formulating the action. We first do so in an iterative fashion and later obtain the final answer in a closed form by a self-consistency argument. We choose units in which $c = 1$ and $\hbar = 1$. Thus

$$l_{\mathrm{P}} = \sqrt{4\pi G} \tag{2.1}$$

has the dimensions of length

The zero'th order action is written as

$$J^{(0)} = J_{\phi}^{(0)} + J_{\mathrm{Int}}^{(0)} + J_{m}. \tag{2.2}$$

Following the sign-convention of Paper I we have (with $\phi_i = \delta\phi/\delta x^i$),

$$J_{\phi}^{(0)} = \frac{1}{2l_{\mathrm{P}}^2}\int \phi^i \phi_i \, \mathrm{d}^4x, \quad J_{\mathrm{Int}}^{(0)} = \int \phi \, T_{\mathrm{m}} \, \mathrm{d}^4x, \quad J_{\mathrm{m}} = -\sum_{\mathrm{a}} \int m_{\mathrm{a}} \, \mathrm{ds}_{\mathrm{a}} \tag{2.3}$$

where m_a is the rest mass of typical particle 'a' and ds_a the element of its proper time. T_m is the trace of the matter energy tensor. $\delta J^{(0)}/\delta\phi = 0$ gives us the zero'th order Lorentz invariant Poisson equation

$$\Box \, \phi = l_{\mathrm{P}}^2 T_{\mathrm{m}}. \tag{2.4}$$

To begin the iteration we must add to T_m. the trace of the energy tensor of the ϕ field. To calculate this energy tensor at any order of iteration we use the procedure outlined below (for a rationale, see, for example, Landau & Lifshitz 1975).

Given the action in flat spacetime as J, write it covariantly in a Riemannian spacetime with the flat spacetime metric η_{ik} replaced by g_{ik} ($i, k = 0, 1, 2, 3$; 0 timelike) and ordinary derivatives by covariant derivatives. Then consider the variation $g_{ik} \rightarrow g_{ik} + \delta g_{ik}$. suppose that

$$\delta J = -\tfrac{1}{2}\int T^{ik} \delta g_{ik} \sqrt{-g} \, \mathrm{d}^4x. \tag{2.5}$$

Then T^{ik} is the required energy tensor. It can then be written down for flat spacetime.

For the ϕ-field using $J_{\phi}^{(0)}$ in place of J above we get

$$T_{\phi}^{ik} = \frac{1}{l_{\mathrm{P}}^2}(\phi^i\phi^k - \tfrac{1}{2}\eta^{ik}\phi^l\phi_l). \tag{2.6}$$

Therefore to T_m we must add

$$T_{\phi} = -\frac{1}{l_{\mathrm{P}}^2}\phi^l\phi_l. \tag{2.7}$$

However, addition of T_ϕ to T_m. in the interaction term J_{int}^{0} further modifies T_{ϕ}^{ik} by our prescription (2.5). This is where the iteration begins. So we write the complete action as

$$J = J_{\phi} + J_{\mathrm{Int}} + J_{\mathrm{m}} \tag{2.8}$$

where J_m is unchanged but

$$J_{\phi} \equiv \int L \mathrm{d}^4x \equiv \int \sum_{n=0}^{\infty} L^{(n)} \mathrm{d}^4x. \tag{2.9}$$

Here the term $L^{(n)}$ arises from the interaction term:

$$\int \phi \, T_{\phi}^{(n-1)} \mathrm{d}^4x \equiv \int L^{(n)} \mathrm{d}^4x \tag{2.10}$$

where $T^{(n-1)}$ is obtained from $L^{(n-1)}$ by the prescription (2.5)

The following ansatz gives us the iterative solution. Write

$$L^{(n)} = \tfrac{1}{2} a_n \phi^n \phi^i \phi_i, \quad a_0 = \frac{1}{l_{\mathrm{P}}^2}. \tag{2.11}$$

This gives us from (2.5)

$$T_{\phi}^{(n)} = -a_n \phi^n \phi^i \phi_i. \tag{2.12}$$

But from (2.10) we get

$$-a_{n-1} = \tfrac{1}{2} a_n; \quad i.e., \, a_n = \frac{(-2)^n}{l_{\mathrm{P}}^2}. \tag{2.13}$$

Therefore

$$L = \frac{1}{2l_P^2}\sum_{n=0}^{\infty}(-2\phi)^n\phi_i\phi^i$$
$$= \frac{1}{2l_P^2}(1+2\phi)^{-1}\phi_i\phi^i. \tag{2.14}$$

Thus we get

$$J_\phi = \frac{1}{2l_P^2}\int(1+2\phi)^{-1}\phi_i\phi^i\,\mathrm{d}^4x. \tag{2.15}$$

The situation is actually more complicated than we have so far anticipated; for there is another iteration involved! Consider $J^{(o)}_{int}$. It can be expressed in the form

$$J^{(0)}_{\mathrm{Int}} = \int\phi T_m\,\mathrm{d}^4x = \sum_a\int\phi m_a\,\mathrm{d}s_a. \tag{2.16}$$

When we apply (2.5) to the above action, it yields additional contribution to T_ϕ :

$$\delta\sum_a\int\phi m_a\,\mathrm{d}s_a = \tfrac{1}{2}\int\phi T^{ik}_m\delta g_{ik}\sqrt{-g}\,\mathrm{d}^4x \tag{2.17}$$

which gives the additional contribution as $-\phi T_m$. This generates further terms $+\phi^2T_m$,$-\phi^3T_m$ *etc.* in the same manner as obtained earlier for J_ϕ. Therefore we get on summation

$$J_{\mathrm{Int}} = \sum_a\int\frac{\phi}{1+\phi}m_a\,\mathrm{d}s_a. \tag{2.18}$$

Putting all three terms of (2.8) together we get

$$J = \frac{1}{2l_P^2}\int(1+2\phi)^{-1}\phi_i\phi^i\,\mathrm{d}^4x - \sum_a\int(1+\phi)^{-1}m_a\,\mathrm{d}s_a \tag{2.19}$$

as the complete nonlinear action.

It is possible to derive this expression by a short-cut route using the consistency argument. Let J be written in the form

$$J = \frac{1}{2l_P^2}\int f(\phi)\phi^i\phi_i\,\mathrm{d}^4x + \sum_a\int m_a g(\phi)\,\mathrm{d}s_a - \sum_a\int m_a\,\mathrm{d}s_a \tag{2.20}$$

where the three terms are respectively J_ϕ, J_{int} and J_m. Then from (2.5) we get

$$T_\phi = -\frac{f(\phi)}{l_P^2}\phi^l\phi_l - g(\phi)T_m. \tag{2.21}$$

Now rewrite (2.20) in the form

$$J = \frac{1}{2l_P^2}\int\phi_i\phi^i\,\mathrm{d}^4x - \int(T_m+T_\phi)\phi\,\mathrm{d}^4x - \sum_a\int m_a\,\mathrm{d}s_a. \tag{2.22}$$

A variation of ϕ in this action can lead to a Poisson-type equation if T_ϕ in the second term is kept unchanged like T_m. With this interpretation (2.20) may be equated to (2.22)

$$f(\phi) = (1+2\phi)^{-1}, \quad g(\phi) = \phi(1+\phi)^{-1} \tag{2.23}$$

and (2.19) is obtained.

This argument illustrates the fact that although T_ϕ may be looked upon as a source of ϕ in much the same way as T_m, it hides the nonlinearity inherent in the gravitational interaction. This nonlinearity is seen in the correct field equation obtained from $\delta J = 0$ by a free variation of ϕ:

$$(1+2\phi)^{-1} \Box \phi - (1+2\phi)^{-2}\phi_i\phi^i = l_P^2(1+\phi)^{-2}T_m. \tag{2.24}$$

This generalized Poisson equation is simplified by the transformation

$$\Omega^2 = 1+2\phi \tag{2.25}$$

to the form

$$\Box \Omega = \frac{4l_P^2\Omega}{(1+\Omega^2)^2} T_m. \tag{2.26}$$

3. Spherically symmetric potential

To solve (2.26) in the empty spacetime outside a spherical distribution is easy. Since $T_m = 0$ we get the solution as

$$\Omega = A + \frac{B}{r} \tag{3.1}$$

where A, B are arbitrary constants.

The potential f is then given by

$$\phi = \frac{1}{2}(A^2-1) + \frac{AB}{r} + \frac{B^2}{2r^2}. \tag{3.2}$$

If we assume that the matter is localized and at large r there is no 'cosmological' contribution to ϕ then a comparison with the Newtonian theory in the 'weak field approximation at large r' gives

$$A = 1, \quad AB = \frac{l_P^2}{4\pi} M. \tag{3.3}$$

Restoring G, c, $\hbar$ to the cgs units we therefore get

$$\phi = \frac{GM}{r}\left\{1 + \frac{GM}{2c^2r}\right\}. \tag{3.4}$$

A word of caution is needed here. As we shall shortly show, the constants A and B are not so trivial in the present nonlinear theory as they are in the linear Newtonian theory. This is seen by considering the equations of motion of a test particle 'a'.

The variational principle $\delta J/\delta s_a = 0$ gives the equations of motion of 'a'. Writing r as the position vector of 'a', we get the 'energy integral' as

$$\dot{\mathbf{r}}^2 = 1 - \frac{k^2}{(1+\phi)^2}, \quad k = \text{constant}. \tag{3.5}$$

Here $\dot{\mathbf{r}}$ denotes the velocity of the test particle in the rest frame of the source distribution. The appearance of the $(1+\phi)^2$ term in the denominator underscores the need for fixing A and B unambiguously.

Consider for example the effect of A and B on the precession of the perihelion of a planet around the Sun. A straightforward calculation gives the answer for the rate of

precession of the perihelion as

$$\omega = \omega_E \cdot \frac{1}{6} \cdot \frac{1 - 5A^2}{A^2(1 + A^2)} \tag{3.6}$$

where ω_E is the Einstein value for the precession rate in general relativity. In (3.6) we have already fixed B by the requirement $AB = GM$, M being the mass of the Sun.

Thus for $A = 1$ and the potential (3.4) we get a retardation of perihelion. This result corrects the earlier erroneous conclusion of Paper I based on only the first term of the iterative process. However, we also see that if asymptotic conditions at infinity require $A \neq 1$ then a different value of the perihelion precession is found.

R. Nityananda & A. Samuel (1984, private communication) have pointed out that there is no bending of light in a coupling of the type ϕT_m since for photons (or for electromagnetic fields in general) $T_m = 0$. An analysis of particle trajectories with non-zero restmass but with $|\dot{\mathbf{r}}| \simeq c$ at infinity also shows that as the relativistic parameter

$$\gamma \equiv \left(1 - \frac{|\dot{\mathbf{r}}|^2}{c^2}\right)^{-1/2} \tag{3.7}$$

tends to infinity the bending angle drops off as γ^{-2}.

4. Conclusion

The preceding sections describe a logically complete and mathematically consistent theory of gravity. However, this theory cannot claim to have anything to do with reality because it fails to explain correctly (i) the bending of light and (ii) the precession of planetary orbits. Nevertheless the above exercise has the advantage in that it demonstrates the need for a more sophisticated theory, as a generalization of the Newtonian law of gravitation. In view of the fact that the next possible generalization of the Newtonian concept of matter density is to the second rank tensor T_{ik}, we expect the theory to be a tensorial one. Whether such a theory, satisfying the present observational tests can be constructed within a flat spacetime, is currently under investigation. If such a theory also fails we have a strong reason why general relativity, a tensorial theory in curved spacetime is needed to describe gravity.

Acknowledgement

We thank Rajaram Nityananda and A. Samuel for discussions.

References

Landau, L. D., Lifshitz, E. M. 1975, *Classical theory of fields*, Pergamon, Oxford.
Rawal, J. J., Narlikar, J. V. 1982, *J. Astrophys. Astr.*, **3**, 393.

J. Astrophys. Astr. (1985) **6**, 177–201

A Survey of Recombination Line Emission from the Galactic Plane at 325 MHz

K. R. Anantharamaiah *Raman Research Institute, Bangalore 560080*

Received 1985 June 21; accepted 1985 August 9

Abstract. A survey of the H 272α recombination line at 325 MHz has been made towards 53 directions in the galactic plane using the Ooty Radio Telescope (ORT). 34 of these directions correspond to well-known HII regions, 12 to SNRs and 6 to 'blank' areas selected so that the 5 GHz continuum is a minimum over the telescope beam of 2° × 6 arcmin. Observing procedure and spectra of 47 sources towards which lines are detected are presented. Hydrogen recombination lines have been detected towards all the observed directions having $l < 40°$. Carbon recombination lines are identified in 12 of the directions. The hydrogen line intensities are found to correlate well with the total continuum intensity (which includes the nonthermal galactic background) indicating that most of the lines arise due to stimulated emission by the background radiation. A preliminary discussion on the nature of the line-emitting regions is also presented.

Key words: Galaxy, radio recombination lines—radio observations, low-frequency—stimulated emission

1. Introduction

In a heterogeneous medium, recombination line observations at different frequencies sample conditions in different components of the ionized gas (Brocklehurst & Seaton 1972; Brown, Lockman & Knapp 1978). In particular, recombination line emission at low frequencies (< 1 GHz) is expected to be dominated by low-density ionized gas and those at high frequencies by high-density gas typical of HII regions prominent in most radio continuum surveys *(e.g.* Altenhoff *et al.* 1978). This is because at low frequencies line emission from high density gas is expected to be suppressed by opacity and pressure broadening. On the other hand, recombination line emission from low-density ionized gas is expected to be enhanced at low frequencies due to stimulated emission. Calculations by Shaver (1975) have shown that at frequencies below 500 MHz stimulated emission from low-density regions can be important due to the presence of strong background continuum sources or even the nonthermal galactic background. At these frequencies, particularly strong lines can be expected from cold, partially ionized gas. Fortuitously, it is at these frequencies that both nonthermal sources and the galactic background are most intense. It appears therefore that frequencies below 500 MHz are best suited to study the conditions in cold partially ionized gas (provided the ionization is adequate) and in large low-density ionized regions for which beam dilutions are not important.

Most existing largescale recombination line surveys of the Galaxy have been carried out at frequencies higher than 1 GHz (see Wilson 1980 and references therein). Below 500 MHz there are only a handful of observations made towards a few selected sources in the galactic plane (see Pedlar & Davies 1980 and references therein). Weak centimetric wavelength recombination lines have been detected at several positions along the galactic ridge (at $l \leqslant 40°$) apparently free of discrete continuum sources (Gottesman & Gordon 1970; Gordon & Cato 1972; Matthews, Pedlar & Davies 1973; Jackson & Kerr 1975; Lockman 1976; Hart & Pedlar 1976). There are no comparable observations of these lines at frequencies below 500 MHz. The only attempt at a large-scale survey for such lines along the galactic ridge was done at 408 MHz (Batty 1976), but with very low sensitivity and which consequently did not detect any lines.

In this paper we present a survey of the H 272α recombination line (324.99 MHz) made towards 53 directions in the galactic plane using the Ooty Radio Telescope. In the next section we discuss the observing frequency and the source positions. In Section 3 we describe the equipment and observing procedure. The results of the survey and a comparison with existing low-frequency observations are presented in Sections 4 and 5. A preliminary discussion on the origin of these lines is presented in the final section.

2. Observing frequency and source positions

The rest frequency of the H 272α recombination line falls at 324.9915 MHz. A knowledge of this frequency alone allows us to put constraints on the density and emission measure of the ionized gas sampled by these observations. At this frequency the continuum optical depth of the ionized gas exceeds unity and the lines merge with the continuum when the emission measure exceeds $1.15 \times T_e^{1.35}$ pc cm^{-6}, where T_e is the electron temperature. For an electron temperature of 8000 K and a path length of about 100 pc this condition is satisfied for densities $N_e > 50$ cm^{-3}. Further, at this frequency, pressure broadening which is independent of pathlength and virtually independent of temperature (Griem 1967; Brocklehurst & Leeman 1971) considerably weakens the line intensities for $N_e > 50$ c m $^{-3}$. The brightness temperature of the nonthermal galactic background is about 600 K at this frequency and can be expected to enhance the recombination line intensities by stimulated emission in ionized gas if the density is less than a few tens cm^{-3} (Shaver 1975).

The source positions for these observations were selected from the galactic plane continuum surveys of Shaver & Goss (1970a) and Altenhoff *et al.* (1978). Most of the positions selected are in the first quadrant of the Galaxy. The galactic longitude l is restricted to < 60° due to the limited declination coverage of the Ooty Radio Telescope ($-30° < \delta < 30°$).

Due to the long integration times necessary for detecting recombination lines at this frequency, a complete coverage of all the sources in the plane would require an impractical amount of telescope time. Directions were therefore selected at somewhat coarser angular intervals, but chosen so as to provide a variety of physical conditions in which to study the recombination lines. The directions selected for observations can be classified into three types.

1. *H II regions:* 34 directions corresponding to well-known HII regions of different densities and temperatures as determined by high frequency studies (*e. g.* Shaver & Goss

1970b). For reasons discussed above, the higher density HII regions are unlikely to produce detectable recombination lines at these frequencies. However, these observations can sample conditions in either low-density outer envelopes of these HII regions or low-density ionized gas which happens to be present along the line of sight.

2. *Supernova remnants:* 12 directions corresponding to well-known strong SNRs in the galactic plane. These directions are particularly suited for studying the effect of stimulated emission at low frequencies due to the strong background continuum source. There is ample evidence for the existence of substantial amounts of ionized gas along the line of sight to these sources. For example, a turnover in their continuum spectra at low frequencies has been observed (Dulk & Slee 1975). In addition, high-frequency recombination lines have been detected towards a few of these sources *(e.g.* Downes & Wilson 1974).

3. *Blank regions:* The high-resolution continuum map at 5 GHz by Altenhoff *et al.* (1978) was used to select six regions in the galactic plane devoid of any strong discrete source within the beam used for these observations. Observations in these directions are expected to provide complementary information to the galactic ridge recombination lines detected at centimetric wavelengths as mentioned above.

For comparison purposes a few positions were also selected in the anticentre direction where the nonthermal background is considerably weaker. Table 1 gives all the observed source positions in galactic and equatorial coordinates. Well-known names of the sources, where available, are indicated in column 4. The nature of the source in the direction of observation is given in column 5.

The high density of sources in the galactic plane introduces confusion. In some of the directions chosen above, the 2° × 6 arcmin beam intercepts more than one source. Arguments such as comparison of velocities with measurements at higher frequencies with better angular resolution should be used to identify the source of an observed line.

3. Equipment, observing procedure and data reduction

Observations were made using the 530 m × 30 m Ooty Radio Telescope (ORT) (see Swarup *et al.* 1971 for a detailed description). Since these are the first major spectral line observations carried out with the ORT, we describe in some detail below the equipment, observing procedure and the difficulties encountered in using such a phased-array telescope for line studies. We begin with a brief description of the ORT.

The ORT operates at a nominal centre frequency of 326.5 MHz and has an angular resolution of 2° in RA and 5.6 sec δ arcmin in declination. The telescope is equatorially mounted and mechanically steerable to track a source continuously for about 9 hours, a feature particularly suited for these observations since long integration times are required. The beam is steered in declination using phase shifters at RF of 326.5 MHz and delays and phase shifters at an IF of 30 MHz (Sarma *et al.* 1975). With the new RF amplifiers and phase shifters installed recently, the system temperature at the input of the RF amplifier is now about 300 K when the antenna is pointed towards a cold region in the sky. A source of 1 Jy in the beam of the antenna produces an increase of about 1.8 K in this system temperature.

The back-end is a 128 channel one-bit autocorrelator which can analyse total bandwidths of 500 kHz, 250 kHz and 125 kHz. After Hanning smoothing of the

Table 1. Source positions and continuum temperatures.

Galactic coordinates l b	RA(1950) h m s	DEC(1950) ° ′ ″	Source name	Source type	Telescope[2] configuration	Total Continuum Temperature[1] K
(1)	(2)	(3)	(4)	(5)	(6)	(7)
357.7 −0.1	17 36 57	−30 56 41	...	SNR	A	930
359.9 −0.0	17 42 27	−28 59 04	SGR A	Gal. centre	A	2330
0.7 −0.0	17 44 10	−28 21 59	SGR B2	H II	A	1100
2.1 −0.0	17 47 27	−27 07 29	...	Blank	B	740
2.3 +0.2	17 46 56	−26 49 35	...	H II	B	750
4.2 −0.0	17 52 14	−25 18 49	...	Blank	B	690
4.4 +0.1	17 52 13	−25 04 52	AMW 35	H II	A	700
6.0 −1.2	18 00 33	−24 23 25	M 8	H II	D	660
6.6 −0.1	17 57 54	−23 21 17	W 28	SNR	D	900
7.0 −0.3	17 59 17	−23 02 54	M 20	H II	A	720
8.1 +0.2	17 59 55	−21 48 17	...	H II	A	770
9.4 +0.1	18 03 03	−20 45 22	...	Blank	C	730
10.2 −0.3	18 06 25	−20 19 42	W 31	H II	D	610
10.3 −0.2	18 05 60	−20 05 52	...	H II	B	680
11.2 −0.3	18 08 31	−19 26 31	...	SNR	A	760
12.8 −0.2	18 11 10	−17 57 56	W 33	H II	A	730
14.0 −0.1	18 13 26	−16 51 55	...	H II	A	680
15.1 −0.7	18 17 35	−16 12 22	M 17	H II	D	810
15.7 −0.0	18 16 24	−15 17 58	...	Blank	C	610
16.9 +0.7	18 16 08	−13 51 41	M 16	H II	C	610
17.6 −0.3	18 21 17	−13 44 04	...	Blank	C	630
18.9 −0.5	18 24 21	−12 44 28	...	H II	A	660
19.6 +0.0	18 23 56	−11 52 40	...	H II	D	550
20.7 −0.1	18 26 26	−10 54 53	...	H II	A	590
21.2 −0.0	18 27 01	−10 28 09	...	Blank	B	580
21.8 −0.6	18 30 25	−10 12 46	...	SNR	A	790
23.0 −0.3	18 31 27	−08 57 27	W 41	SNR	A	770

23.4	−0.2	18 31 57	−08 35 51	...	H II	A	750
24.8	+0.1	18 33 29	−07 13 10	...	H II	A	660
25.4	−0.2	18 35 31	−06 50 32	3C 385	H II	A	650
27.3	+0.2	18 37 53	−05 00 47	...	H II	A	640
28.8	+3.5	18 28 48	−02 07 37	W 40	H II	A	450
29.9	+0.0	18 43 30	−02 44 01	...	H II	B	650
29.9	−0.2	18 43 25	−02 43 47	...	H II	A	680
30.8	+0.0	18 44 50	−01 59 04	W 43	H II	C	830
31.9	+0.0	18 46 51	−00 58 52	3C 391	SNR	A	680
34.6	−0.6	18 53 57	+01 06 20	W 44	SNR	A	830
34.7	−0.6	18 54 13	+01 14 24	W 44	SNR	A	950
35.1	−1.6	18 58 43	+01 08 24	W 48	H II	A	460
37.8	−0.2	18 58 30	+04 09 54	W 47	H II	D	480
39.2	−0.3	19 01 35	+05 21 35	3C 396	SNR	A	570
39.7	−2.2	19 09 21	+04 53 48	W 50	SNR	B	360
43.2	−0.1	19 08 16	+08 59 54	W 49	SNR	A	690
45.4	+0.1	19 11 57	+11 03 41	...	H II	B	360
49.0	−0.3	19 20 17	+14 02 01	W 51B	H II	A	650
49.0	−0.6	19 21 23	+13 51 51	W 51C	SNR	D	490
49.5	−0.4	19 21 27	+14 24 22	W 51A	H II	A	450
51.4	+0.0	19 23 42	+16 14 17	...	H II	A	290
54.1	−0.1	19 29 27	+18 35 52	...	H II	A	210
59.8	+0.2	19 40 24	+23 42 32	...	H II	A	120
206.0	−2.1	06 28 29	+05 13 25	W 16	H II	A	100
206.8	−16.4	05 39 11	−01 55 50	NGC 2024	H II	A	120
209.2	−19.4	05 32 50	−05 25 09	Orion A	H II	A	420

Notes:

1. Total beam-averaged brightness temperature. Error on the measurement of this quantity is estimated to be 15 per cent.

2. The 530 m × 30 m Ooty radio telescope is divided into 22 equal modules along the north-south direction. Starting from the middle the northern modules are designated as N1, N2 ... N11 and southern modules as S1, S2 ... S11. Signals from each of the modules are brought independently into the receiver room and combined with proper phases and delays to form the final beam. There is provision to switch off any of the modules thereby removing their contribution to the final output. These observations were made during the period when the telescope was undergoing major modifications. Therefore many sources in this list were observed with one or more modules switched off. Switching off modules starting from either end reduces the collecting area and broadens the beam. Switching off intermediate modules creates a hole in the aperture, reducing the collecting area and introducing low-level side lobes. For the purpose of this table the designations in this column mean the following: A—All modules on, B—N1 module off, C—N1 and N2 modules off, and D—Modules S6 to S11 off.

autocorrelation function, these bands can provide frequency resolutions of 7.8 kHz, 3.9 kHz and 2.0 kHz respectively. Any required frequency band at the RF can be placed in the autocorrelator band by changing the frequency of a synthesizer used as the first local oscillator (FLO).

Observations were made in the total power mode in several sessions during the period from August 1980 to May 1982. During this period the ORT was undergoing several modifications in its front-end system. Therefore some of the observations were made with some sections of the telescope missing, and sometimes with slightly different sensitivity. Column 6 of Table 1 indicates the configuration of the telescope during the different observations. However during all the observing sessions the line intensities were measured with respect to the adjacent continuum, which to first order removes the dependence on system parameters. A bandwidth of 500 kHz (which corresponds to ~ 461 km s^{-1} at the H 272α frequency) was used during all the observations providing a velocity resolution of 7.2 km s^{-1}. Double frequency switching was employed for all the observations; the FLO was switched between the line frequency (ON) and two reference frequencies (REF1, REF2), one on either side in the sequence ON-REF1-ON-REF2-ON-*etc*, spending 0.25 seconds at each frequency. Depending on the direction of observation, the line frequency was chosen such that the expected LSR velocity of hydrogen and carbon 272α lines fell within the observing band.

The different frequency settings of the FLO and switching between them which is necessary for these observations, introduces many complications in the performance of the antenna and the receiver. When the frequency of the FLO is changed from the nominal setting of 296.5 MHz by an amount Δf, the north-south pointing of the antenna changes by an amount $\Delta\delta = (\Delta f/f) \tan \delta$, where f is the nominal RF centre frequency (326.5 MHz) of the system. Therefore, when the central frequency of observation is changed from the nominal setting (for example to the H 272α frequency) a set of systematic phase corrections have to be applied in order to point the antenna in the desired direction. We find that a change in the centre frequency also decreases the sensitivity of the system; the sensitivity drops by about 20 per cent at the frequency of the H 272α line. This may be partly due to problems in applying phase corrections in the system.

A further complication is introduced when the FLO is switched between the line and reference frequency. The corresponding beamshift produces a change in the total system temperature whose magnitude depends on the strength, size and angular distribution of the source being observed. A mere change in the total system temperature, which only introduces a change in the input signal level, does not change the response of a one-bit correlator. However, this change in the system temperature is really a function of frequency even within the bandwidth of 500 kHz. This produces a curved baseline in the final spectrum obtained by subtracting the line and reference band shapes and dividing by the reference band shape. The curvature of the baseline is therefore a function of the continuum distribution of the source being observed. This being so, we cannot use observations towards a reference region to remove the instrumental baseline as is done in many single-dish spectral-line observations. We were able to minimize the baseline curvature by using double frequency switching as described above. We tried to reduce the curvature further by also switching in phase corrections, as mentioned above, corresponding to the line and reference frequencies. Phase correction switching considerably reduced the total system temperature variation but failed to improve the baseline; in fact in some cases the curvature in the

baseline deteriorated. Several test observations towards a cold region in the sky showed that the instrumental baseline introduced only by the frequency response of the RF amplifiers is minimal.

In Fig. 1 we show examples of two baselines. SgrA, the strongest source in these observations, has a sharply peaked continuum distribution and is an example of the most unfavourable baseline. A fourth-order polynomial has been fitted to channels devoid of line emission to determine the instrumental baseline. However, the baseline for most of the sources are intermediate between SgrA and W 41 shown in Fig. 1. Polynomials up to third order were fitted to determine the baselines in most of the cases. In a few cases a fourth-order polynomial was necessary.

Each source was observed in three to four sessions either on successive days or separated by several days depending on the availability of telescope time. Data were acquired in stretches of 1 to 1.5 hours while tracking the source position over an hour-angle range generally between -4^h and $+4^h\ 30^m$. Individual scans were combined, after

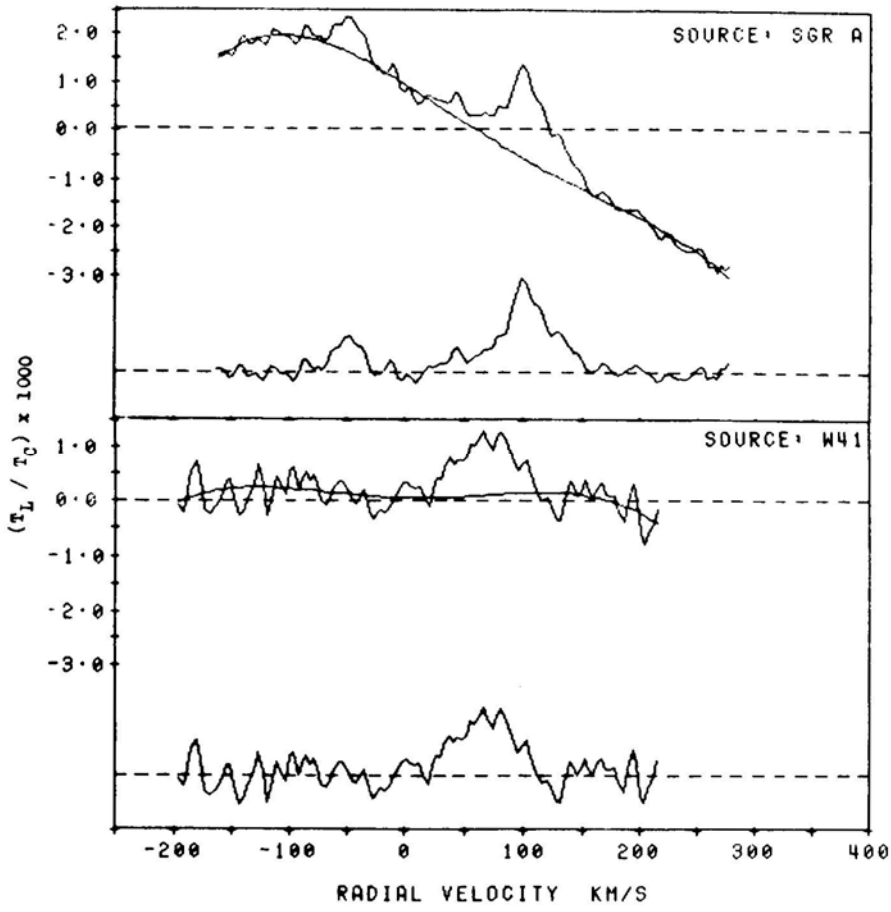

Figure 1. Observed spectra and the fitted instrumental baseline towards two sources Sgr A and W 41. The spectrum in the lower part of both the frames is obtained after subtracting the baseline shown as a solid line

editing out interference, to form a one day's spectrum for the source. A one-bit auto-correlator only measures a normalized spectrum (Weinreb 1962). At the beginning of each day's observing session the increase in the total system temperature at the source position was measured with respect to a region generally about $1^h.5$ to 2^h away in right ascension. This was used to calibrate each day's spectrum in terms of the line to continuum ratio. These one day spectra for each source were averaged with weighting functions proportional to their integration times to obtain the final spectrum for the source. Instrumental baselines were fitted and removed from these final spectra as described above. For some sources the data were further smoothed to improve the signal-to-noise ratio. It was ensured that the smoothing process did not affect any narrow feature. For most of the sources, gaussian components were fitted to the line profiles using a standard least-square technique and the line parameters were determined. In Fig. 2 we show an example of a gaussian fit and the residuals after subtracting the fitted components from the final spectrum. In all the cases, the residuals obtained this way showed rms noise fluctuations consistent with that expected for a one-bit correlator (Weinreb 1962). The source G 359.9 – 0.1 (SgrA) was observed several times during the one-and-half year period of these observations to monitor the satisfactory functioning of the system at all times. This resulted in a particularly long integration time and therefore the best signal-to-noise ratio for this source.

One of the major difficulties in spectral-line-observations at low frequencies is the presence of CW interference. Low-level CW interference from equipment in the laboratory, low-level oscillations in one of the RF amplifiers, harmonics of transmissions in the communication bands from nearby ground-based transmitters and satellites, can all seriously affect the quality of the data. In fact, for some period during

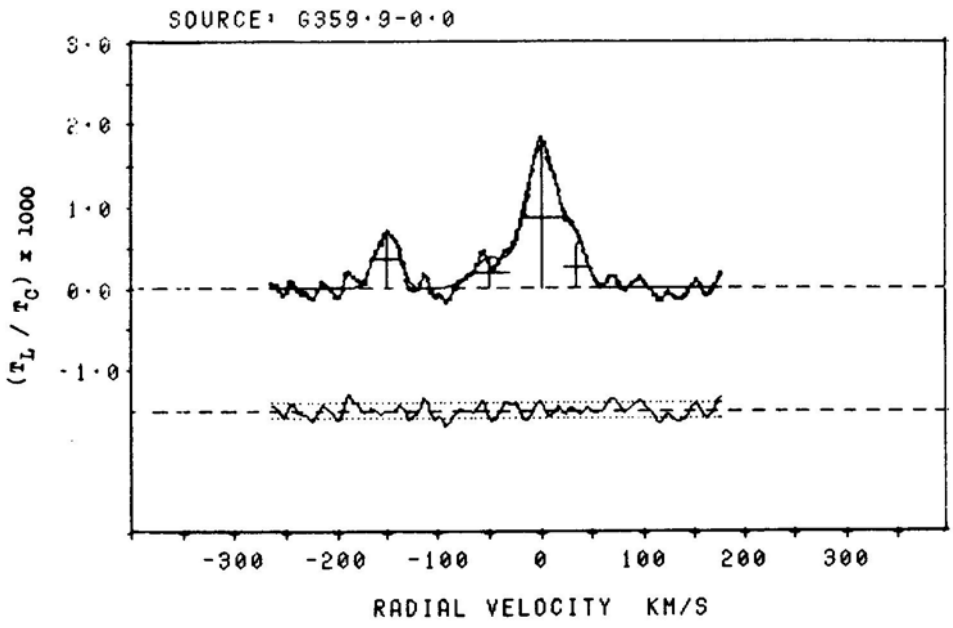

Figure 2. An example of a gaussian fit to the final spectrum. The crosses indicate the amplitude and width (FWHM) of the fitted components. The residuals after removing the gaussians are also shown. The dotted lines indicate the expected 1σ amplitude of the residuals.

these observations, strong interference through the image band of the ORT receiver (266.5 MHz) was coming from a geostationary satellite. Because of this, after some initial observations at the H 271α recombination line frequency (328.6 MHz), we switched to the H 272α line at 324.99 MHz. The interference usually manifests itself as an increase in the rms noise in the spectra, or as sharp spikes in either one-minute data or in the averaged spectrum depending on the strength and duration. The 'lines' due to interference can generally be easily distinguished from those due to an astronomical source by their peakiness and confinement to one or two channels only. In the final analysis, all such stretch of data containing this type of interference were deleted. Up to 30 per cent of the total acquired data had to be discarded due to the presence of such interference. We have carefully examined all the individual pieces of data making up the final spectrum for each source to ensure that the line emission attributed to an astronomical source is not due to the presence of interference in some individual stretches of data. Except for the sources W 51B and Orion, we believe that all the data presented here are free of interference to a high degree.

Continuum measurements of all the sources observed for recombination lines were made in a separate session in 1983 April. Even though the observed lines were already calibrated in terms of line-to-continuum ratios, the continuum measurements were necessary for interpretation since the total background radiation can cause stimulated emission of these lines as discussed before. For each of the source positions the increase in total system temperature was measured with respect to a cold region about $2^h.5$ to 3^h away in right ascension. This was compared with the increase in system temperature due to the sources 3C 283 and Her-A. The flux density of 3C 283 at 327 MHz was taken to be 20.6 Jy and that of Her-A as 200 Jy. Necessary corrections were applied for the deviation of the total power detector characteristic from a true square law. The resulting equivalent flux in the beam was converted to average beam brightness temperature using the measured main-beam solid angle of the ORT. No attempt was made to separate the contributions from the source in the beam and the background. The measured beam brightness temperature for each source is given in Column 7 of Table 1.

4. Results

Out of the 53 directions observed, recombination lines have been detected in 47 directions. The observed spectra corresponding to directions in which lines were detected are presented in Fig. 3 in which the ratio of line to total underlying continuum intensities have been plotted against radial velocity with respect to LSR calculated using the rest frequency of the H 272α recombination line. The line parameters obtained from a least-squares gaussian fit to the observed profiles are given in Columns 2 to 4 of Table 2. Columns 5 and 6 of this table give the velocity resolution of the spectra and the integration time respectively. The peak brightness temperature of the line T_{BL} is given in Column 7. This was obtained by multiplying the quantity in Column 2 by the measured continuum beam brightness temperature for the source indicated in Column 7 of Table 1. For many of the sources (particularly those with very wide lines), the individual line parameters obtained from gaussian fits can only be used as indicators of the strength and extent of the line; a single gaussian component may not accurately represent the true line shape. A more meaningful parameter would be the integrated

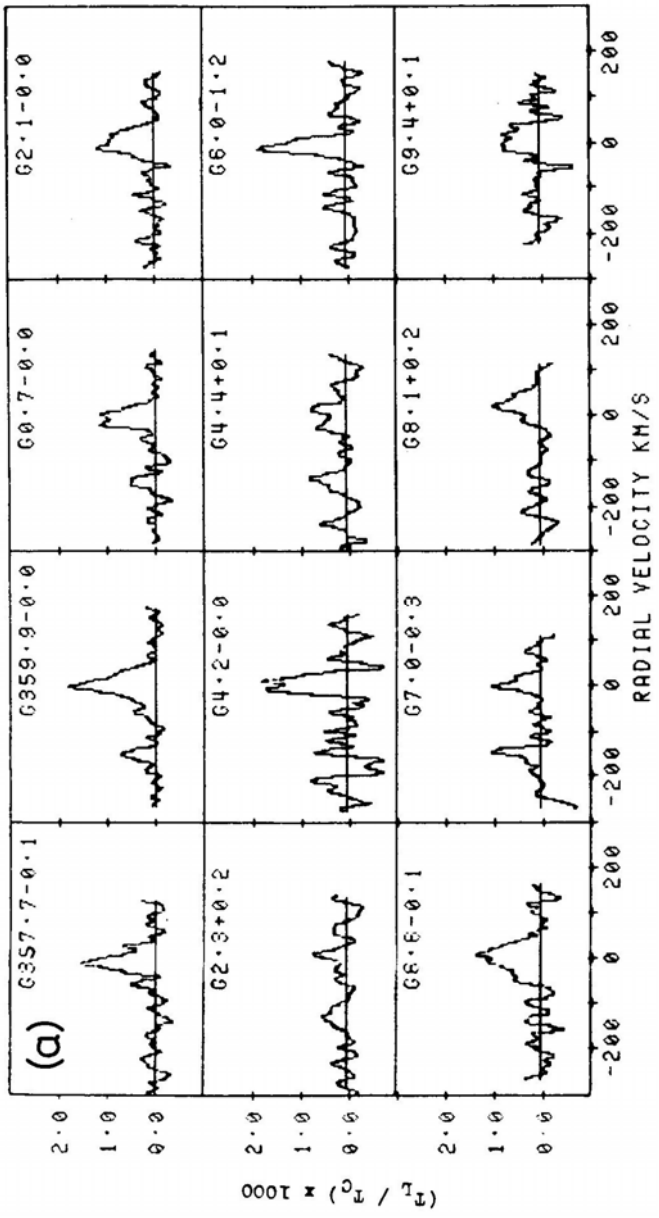
(a)
G357·7-0·1
G359·9-0·0
G0·7-0·0
G2·1-0·0
G2·3+0·2
G4·2-0·0
G4·4+0·1
G6·0-1·2
G6·6-0·1
G7·0-0·3
G8·1+0·2
G9·4+0·1
2·0
1·0
0·0
-200
0
200
RADIAL VELOCITY KM/S
(TL / TC) x 1000

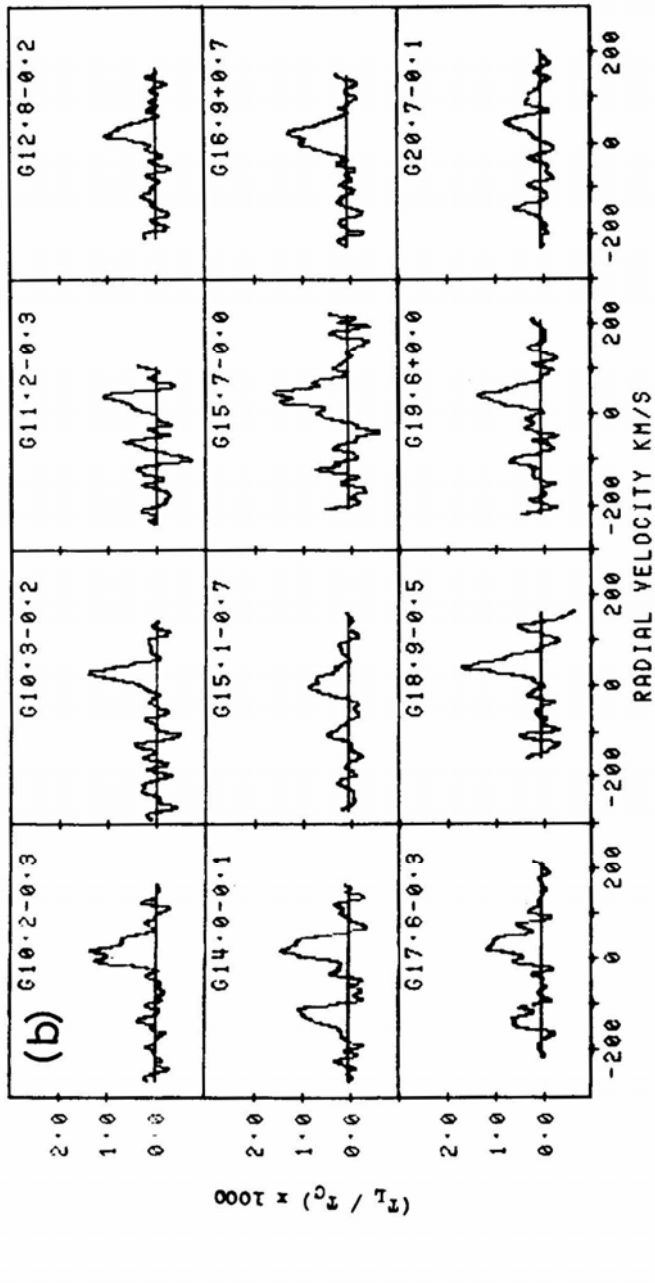

Figure 3. H 272*α* spectra of sources towards which lines were detected. The radial velocity is with respect to LSR. T_L is the antenna temperature in the line and T_C is that in the continuum which includes the nonthermal galactic background.

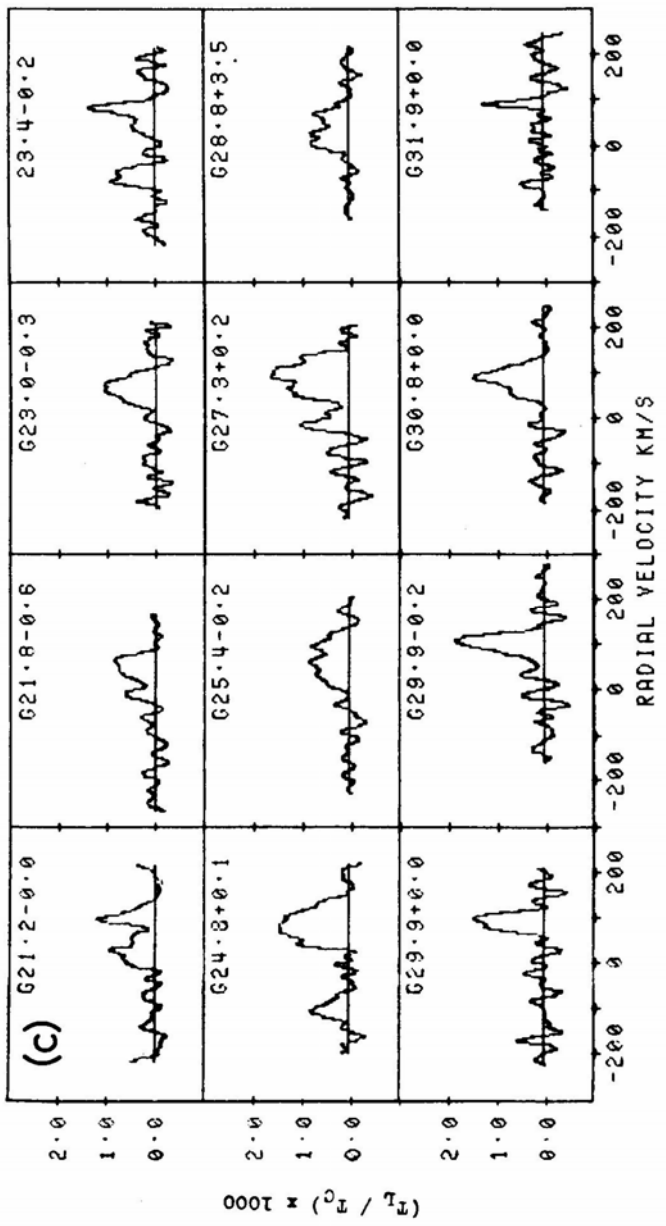
(c)
G21·2-0·0
G21·8-0·6
G23·0-0·3
23·4-0·2
G24·8+0·1
G25·4-0·2
G27·3+0·2
G28·8+3·5
G29·9+0·0
G29·9-0·2
G30·8+0·0
G31·9+0·0
2·0
1·0
0·0
-200
0
200
RADIAL VELOCITY KM/S
(T_L / T_C) x 1000

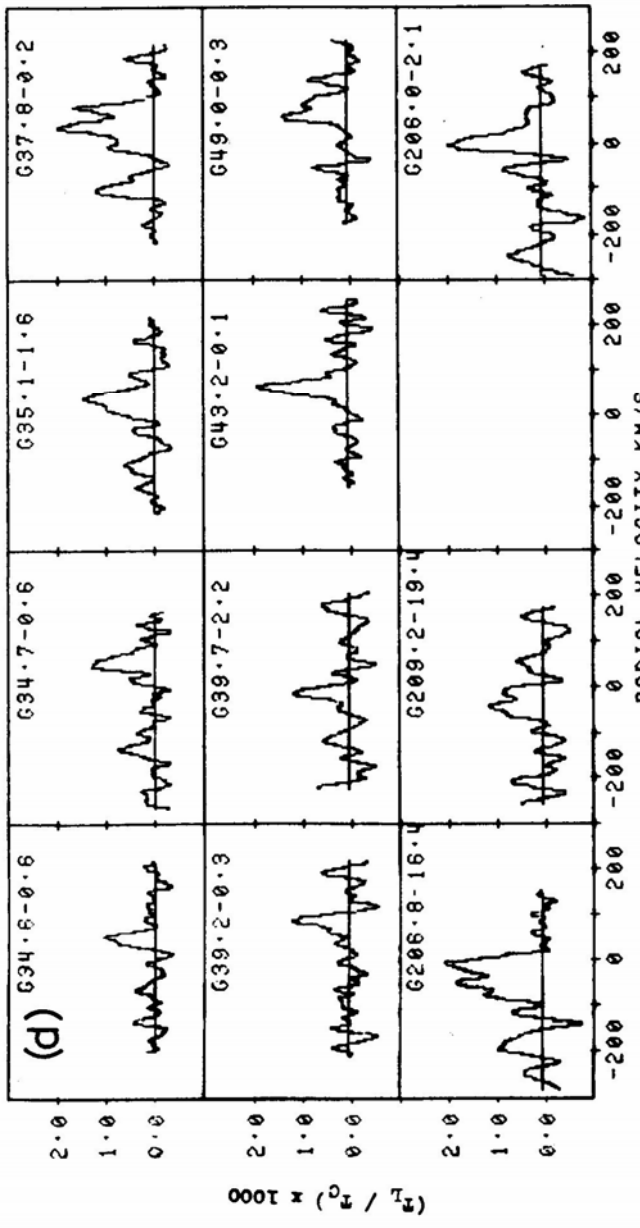

Figure 3. Continued. The ordinate scale for the source G 206.0 – 2.1 is $(T_L/T_C) \times 500$.

Table 2. Observed line parameters and integration times.

Source	H 272α gaussian parameters: Peak $T_L/T_C \times 10^3$	Width (FWHM) km s^{-1}	Velocity (LSR) km s^{-1}	Spectral Resolution km s^{-1}	Integration time hours	Peak line temperature T_{BL}(K)	$\int T_{LB}\,dv$ K kHz	Velocity of H 110α[1] km s^{-1}	$V_{110\alpha} - V_{272\alpha}$ km s^{-1}
1	2	3	4	5	6	7	8	9	10
G 357.7 – 0.1	1.39(09)	40(3)	−7.9(1.3)	10	25.9	1.3(2)	60(11)	...	...
G 359.9 – 0.0	1.59(04)	51(1.5)	4.7(0.6)	10	62.5	3.7(6) }	238(35)	18	13
	0.36(06)	21(4.5)	−57(2)			0.8(2) }			
	0.71(06)	24(2.5)	−149.5(1.0)*			1.7(3)	46(9)		
G 0.7 – 0.0	1.13(06)	43(3)	−4.4(1.2)	12	22.9	1.24(20)	62(11)	64.6	69
	0.58(09)	20(4)	−146(2)*			0.64(14)	15(4)		
G 2.1 – 0.0	1.10(07)	47(4)	5(2)	12	33.8	0.81(13)	44(8)	...	...
G 2.3 + 0.2	0.64(13)	18(5)	9(2)	15	19.3	0.48(12)	10(4)	5.0	−4
	0.48(10)	36(9)	−127(4)			0.36(09)	15(5)		
G 4.2 – 0.0	1.9(2)	33(5)	7(2)	12	12.0	1.28(24)	49(11)	...	...
G 4.4 + 0.1	0.56(09)	66(13)	4(5)	15	19.0	0.39(09)	30(9)	5.7	2
	0.70(13)	26(7)	−141(3)*			0.49(12)	15(5)		
G 6.0 – 1.2	1.83(14)	26(3)	−4(1)	15	11.9	1.2(2)	36(7)	3.0	7
G 6.6 – 0.1	1.2(1)	43(4)	11(2)	12	14.4	1.1(2) }	69(12)	12.5	2
	0.36(10)	41(13)	−27(6)			0.32(10) }			
G 7.0 – 0.3	0.87(13)	30(6)	6(2)	15	10.0	0.63(13)	22(6)	14.0	8
	1.0(2)	14(4)	−144(2)*			0.73(16)	12(4)		
G 8.1 + 0.2	0.83(09)	47(7)	25(3)	20	16.0	0.64(12)	35(8)	22	−3
G 9.4 + 0.1	0.83(12)	42(7)	10(3)	12	24.6	0.61(13)	30(8)	...	...
G 10.2 – 0.3	1.27(08)	51(4)	15(2)	15	13.6	0.77(13)	45(8)	13.0	−2
G 10.3 – 0.2	1.36(12)	29(3)	32(2)	15	12.0	0.92(16)	31(6)	12.0	−20
G 11.2 – 0.3	1.1(2)	23(6)	37(2)	15	8.3	0.8(2)	22(7)	...	...
G 12.8 – 0.2	1.0(1)	32(4)	26(2)	15	12.0	0.72(13)	27(6)	30.0	4
G 14.0 – 0.1	1.4(1)	38(3)	24.1(1.5)	15	11.7	1.0(2)	43(8)	31.5	7
	1.1(1)	29(4)	−122(2)*			0.74(14)	25(6)		
G 15.1 – 0.7	0.83(07)	41(5)	9(2)	20	18.7	0.67(12)	32(7)	11.5(3)	

G 15.7 − 0.0	1.4(1)	58(5)	43(2)	12	19	0.86(14)	58(11)	...	...
G 16.9 + 0.7	1.19(06)	53(3)	20(1)	12	27.8	0.73(11)	45(7)	28.0	8
G 17.6 − 0.3	1.07(08)	47(4)	30(2)	15	20.4	0.67(11)	36(7)	...	...
	0.32(08)	50(15)	−129(6)*			0.20(06)	12(5)		
G 18.9 − 0.5	1.6(2)	32(4)	48(2)	15	13.2	1.0(2)	38(9)	67	19
G 19.6 + 0.0	1.3(1)	35(3)	41(2)	15	16.7	0.71(12)	29(6)	55.3	14
	0.67(14)	13(5)	−100(2)*			0.37(09)	6(2)		
G 20.7 − 0.1	0.77(14)	19(6)	47(3)	20	9.9	0.45(11)	10(4)	57	10
G 21.2 − 0.0	1.11(10)	26(3)	98.6(1.3)	15	20.5	0.64(11) } 0.46(08) }	48(7)	...	...
	0.80(07)	54(6)	25(3)						
G 21.8 − 0.6	0.89(08)	44(5)	54(2)	20	13.7	0.70(12)	43(8)	...	...
	0.62(12)	13(5)	−9(2)			0.49(12)			
G 23.0 − 0.3	1.09(07)	55(4)	68(2)	12	18.7	0.84(14)	53(10)	78.0	10
G 23.4 − 0.2	1.30(14)	27(4)	85(2)	15	14.5	1.0(2)	31(7)	104.0	19
	0.93(13)	30(6)	−64(2)*			0.70(14)	24(7)		
G 24.8 + 0.1	1.51(06)	77(4)	83(2)	15	15.4	1.00(15)	89(14)	107.0	24
	0.73(09)	34(5)	−104(2)*			0.48(09)	19(5)		
G 25.4 − 0.2	0.78(06)	95(9)	64(4)	20	14.7	0.51(09)	56(11)	59.0	−5
G 27.3 + 0.2	1.53(09)	85(6)	93(2)	15	14.1	0.98(16) } 0.65(15) }	110(18)	33.0	−60
	1.0(2)	18(5)	−12(2)						45
G 28.8 + 3.5	0.61(06)	35(4)	72(2)	15	17.5	0.27(05) } 0.36(06) }	29(4)	0.7[2]	−72
	0.79(05)	44(4)	19(2)						−19
G 29.9 + 0.0	1.51(13)	35(4)	91(2)	15	13.0	1.0(2)	40(8)	98.5	8
G 29.9 − 0.2	1.86(12)	37(3)	105(2)	15	21.8	1.26(21)	54(10)		
G 30.8 + 0.0	1.42(08)	41(3)	95(1)	15	20.5	1.2(2) } 0.46(12) }	64(11)	90.0	−5
	0.55(12)	16(5)	54(2)						
G 31.9 + 0.0	1.3(2)	10(2)	98(1)	12	22.2	0.9(2)	10(3)	103[4]	5
G 34.6 − 0.6	1.05(11)	21(3)	48(1)	12	13.0	0.87(16)	21(5)	53.0	5
G 34.7 − 0.6	1.24(10)	37(4)	59(2)	12	14.3	1.2(2)	50(10)	50.3[3]	−9
	0.69(13)	20(5)	−132(2)*			0.7(2)	15(5)		
G 35.1 − 1.6	1.33(12)	55(6)	34(3)	15	13.4	0.61(11)	39(8)	43.0	9
G 37.8 − 0.2	1.59(11)	81(6)	48(3)	15	16.9	0.76(13)	71(13)	61.0	13
	1.2(2)	26(5)	−96(2)*			0.57(12)	17(5)		
G 39.2 − 0.3	1.15(14)	21(5)	84(2)	15	11.3	0.66(13)	16(5)	...	...
G 39.7 − 2.2	1.1(2)	18(6)	−11(3)	20	17.5	0.4(1)	9(4)	...	...
G 43.2 − 0.1	1.72(11)	35(3)	63(1)	12	28.1	1.2(2)	48(9)	10.0	−53

Table 2. Continued.

Source	H 272α gaussian parameters: Peak $T_L/T_C \times 10^3$	Width (FWHM) km s^{-1}	Velocity (LSR) km s^{-1}	Spectral Resolution km s^{-1}	Integration time hours	Peak line temperature T_{BL}(K)	$\int T_{LB} dv$ K kHz	Velocity of H 110α[1] km s^{-1}	$V_{110\alpha} - V_{272\alpha}$ km s^{-1}
1	2	3	4	5	6	7	8	9	10
G 45.4 + 0.1	< 1.6	...	...	15	15.5	< 0.6	...	54.5	...
G 49.0 − 0.3†	1.1(1)	55(6)	75(3)	15	15.8	0.75(15)	46(10)	60.5	−14
G 49.0 − 0.6	<1.3	...	...	15	11.3	<0.7	...	...	...
G 49.5 − 0.4	< 1.0	...	...	15	22.5	< 0.5	...	57.1	...
G 51.4 + 0.0	< 2.1	...	...	20	11.0	< 0.6	...	53.3	...
G 54.1 + 0.2	< 1.6	...	...	20	10.0	< 0.3	...	43.0	...
G 59.8 + 0.2	< 4.0	...	...	20	12.2	< 0.8	...	−6	...
G 206.0 − 2.1	4.0(5)	28(5)	5(2)	20	32.3	0.4(1)	13(3)	7(3)[5]	2
G 206.8 − 16.4†	1.78(12)	84(7)	−36(3)	15	112.9	0.21(04)	20(4)	7.0[2]	43
	1.0(2)	26(7)	−187(3)*			0.12(03)	4(1)		
G209.2 − 19.4†	1.0(2)	53(11)	−34(5)	20	23.2	0.43(10)	26(8)	−2.7[2]	31

Notes:

1. From Downes *et al.* (1980)
2. Velocity of 109α line form Reifenstein *et al.* (1970)
3. Velocity of 166α line form Bignell (1973)
4. Velocity of 92α line form Cesarsky & Cesarsky (1973)
5. Velocity of 100α line from Viner, Vallée & Hughes (1979)

* Possible carbon line

† Observations affected by interference

line intensity. This quantity computed from the gaussian parameters for each source is given in Column 8 of Table 2. Possible carbon lines have been excluded when obtaining this quantity. The errors quoted in Table 2 are equal to one standard deviation. These errors are obtained from the rms noise of the residuals after gaussian fit and using the formulae relating this noise to the error of the parameters as discussed by Rieu (1969).

The main results of this survey can be summarized as follows.

1. In the first quadrant of the Galaxy, for the longitude range $l \leqslant 40°$, hydrogen recombination lines were detected towards every direction irrespective of whether it corresponded to an HII region or an SNR or a blank region. Outside this range the line was detected only towards two strong sources W 49 and W 51. The line was also detected towards the three HII regions in the anticentre direction.

2. The line intensities are typically about 0.1 per cent of the total continuum intensity, and required integration times ranging from 10 hours to 30 hours for detection with a signal-to-noise ratio between 5 and 10.

3. There is no marked difference in the line to total continuum intensity ratio between directions of HII regions, SNRs and blank regions.

4. Typical widths of the lines (FWHM) are 20–50 km s^{-1}. However, the spectrum is much wider (60–80 km s^{-1}) or has more than one component for many sources, particularly those in the longitude range 20° to 30°. The line towards 3C 391 (G 31.9 + 0.0) is particularly narrow; the FWHM is only about 11 km s^{-1} after correction for instrumental broadening.

5. The strongest H 272α line detected is towards the galactic centre. The line profile clearly shows three components; one centred at 0 km s^{-1} one around – 50 km s^{-1} and the other at a positive velocity.

6. Judging by the frequency shift (~ 162 kHz $\simeq$ 149 km s^{-1}) with respect to the hydrogen line, carbon lines can be identified in about 12 cases. These lines are however somewhat wider (20–30 km s^{-1}) than the carbon lines observed at higher frequencies (5–15 km s^{-1}).

5. Comparison with other low-frequency observations

Recombination lines from a few individual sources in this survey have been observed before by other workers using other telescopes at frequencies below 500 MHz. For comparison we have selected all those sources in Table 1 which have been observed at frequencies close to that of this survey. The frequency of observation, angular resolution, observed line parameters and references are given in Table 3. Comparison of these parameters with those given in Table 2 for the same sources show that the observed line intensities and centroids are in good agreement for most of the sources; the slight differences in these quantities could be the result of the very different beam sizes employed for the two observations. Some noticeable differences between the two sets of observations are described below.

The width of the line towards the SNR 3C 391 (G31.9 + 0.0) observed at this frequency is much smaller than at higher frequencies. On the other hand, the lines towards SgrA and M 17 are somewhat broader. The observations towards W 5IB at 325 MHz seem to show additional components at higher velocities. But these components have to be treated with, caution since, as noted earlier, observations towards this source were affected by interference. Further, we have not detected any

Table 3. Parameters from other observations for comparison.

Source	Name	Frequency MHz	Size arcmin	T_L/T_C $\times 10^3$	T_C K	T_L K	Width km s^{-1}	V_{LSR} km s^{-1}	Reference
G 359.9 − 0.0	SGR A	328	50	1.5	1770	2.6(0.4)	26(5)	2.1(1.5)	1
G 15.1 − 0.7	M17	386	35	1.0	527	0.5(0.2)	24(17)	15	2
				1.1		0.6(0.1)	34(20)	51	
G 30.8 − 0.0	W 43	328	50	2.4	380	0.9(0.4)	48(11)	102(10)	1
G 31.9 + 0.0	3C 391	428	11	2.5	466	1.15	63	90	3
G 43.2 + 0.0	W 49A	318	16	3.0	250	0.75(0.2)	25(8)	62(6)	4
G 49.0 − 0.3	W 51B	318	16	2.3	860	2.0(0.3)	25(9)	60(7)	4
G 49.0 − 0.6	W 51C	430	9	3.2(0.8)			15(4)	56(2)	5
G 49.5 − 0.4	W 51A	428	11	1.8(0.3)	530		31(7)	55(3)	6
G 206.1 − 2.3	W 16	386	36	3.8	89	0.34(0.12)	38(15)	16	2

1. Pedlar *et al.* (1978)
2. Gordon, Gordon & Lockman (1974)
3. Pankonin (1975)
4. Parrish, Conklin & Pankonin (1977)
5. Terzian & Pankonin (1974)
6. Pankonin *et al.* (1974)

lines towards W 51C and W 51A and our upper limits are somewhat lower than the intensities reported by Terzian & Pankonin (1974). Again, some of these differences may be due to the different angular resolution, frequency and sensitivity of the two sets of observations.

6. Discussion

Detailed interpretation of the data presented in this paper in terms of the distribution and properties of the gas responsible for the observed lines will appear in subsequent publications. Here we discuss only the broad characteristics of the data and their implication for the nature of the line-emitting regions.

6.1 *Hydrogen Lines*

6.1.1 *Line Intensities*

As discussed earlier, there combination lines observed at this frequency can only sample conditions in relatively low-density ionized regions. Macroscopic properties of a large selection of HII regions in the galactic plane have been studied by Shaver & Goss (1970b). Most of the HII regions common to the present H 272α recombination line survey and the continuum survey of Shaver & Goss (1970b) have electron densities greater than 100 cm^{-3} and angular sizes less than 10 arcmin. With these densities and sizes, effects of pressure broadening, optical depth and beam dilution make the recombination lines at this frequency virtually undetectable from these HII regions. The recombination lines measured here must therefore arise from much lower-density gas in regions of much larger angular size. The gas can either be associated with the HII region, for example as an outer envelope, or just lying along the line of sight. Further, the intensity and width of the recombination lines detected in this survey are very similar in all directions observed, irrespective of whether the direction corresponds to that of an HII region, an SNR or a blank region. The intensities of the lines are found to correlate well with the total continuum intensity. In the galactic plane where most of these observed sources lie, the continuum radiation at this frequency is mainly nonthermal in origin. Therefore, the line and continuum radiation originate in different regions along the line of sight. The HII regions and SNRs only add to the background continuum radiation, and the lines themselves must arise in low-density ionized regions distributed along the line of sight. The ORT beam of 2° × 6 arcmin and the low observing frequency are probably well suited for studying the properties of such low-density ionized gas not prominent in the continuum. At higher frequencies, where better angular resolutions are available and where the expected intensity of recombination lines from the HII regions themselves are much higher, it would be difficult to separate the contribution from lower-density gas.

6.1.2 *Stimulated Emission*

Stimulated emission of recombination lines due to non-LTE populations of high principal quantum number levels is expected to be important at low frequencies (Shaver 1975). The presence of a strong background source or even the nonthermal

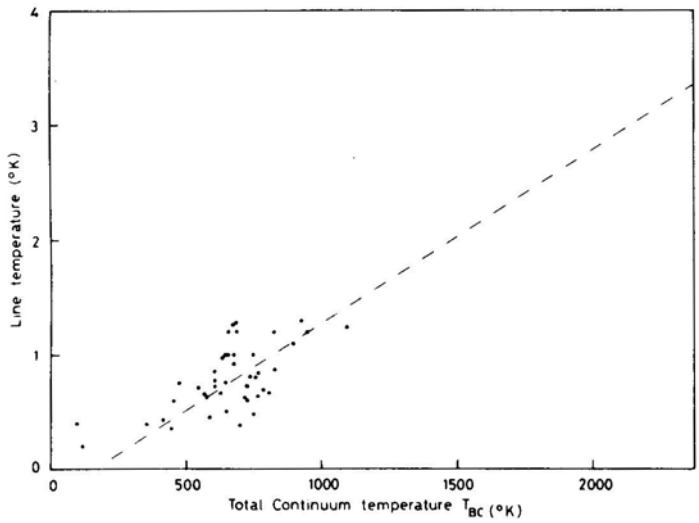

Figure 4. Correlation of the line temperature with the total continuum temperature which includes the nonthermal galactic background. The dashed line indicates the least squares fit. Correlation coefficient is 0.8.

galactic background is expected to have considerable influence on the line intensities Pedlar *et al.* (1978) have demonstrated that the intensity of the low-frequency recombination line towards the galactic centre is enhanced by the background continuum sources in that direction. In Fig. 4 we have plotted the peak line brightness temperature T_{BL}, observed in different directions, against the total continuum temperature T_{BC} which includes the nonthermal galactic background. There is a good correlation between them (correlation coefficient = 0.8) indicating that the line intensities are enhanced by the background radiation. It may be noted here that such a correlation between line and continuum intensity has been observed even at 5 GHz (Jackson & Kerr 1975). But at this frequency the continuum is mainly thermal, and the correlation is expected even in the absence of stimulated emission. However, at low frequencies (< 500 MHz) the continuum intensity is dominated by the nonthermal emission and any correlation between T_{BL} and T_{Bc} can only be due to stimulated emission.

6.1.3 *The Line Velocities*

The radial velocity with respect to LSR for all the observed lines is given in Column 4 of Table 2. The measured radial velocity of an object in the galactic plane is an indicator of its location along the line of sight. It is useful to compare the velocity of the H 272α line observed here with that of a higher-frequency recombination line, as the latter arises preferentially in the relatively high-density HII regions along the line of sight. Column 9 of Table 2 gives the velocity of the H 110α observed by Downes *et al.* (1980) in the same directions. Column 10 is the difference between the observed H 272α velocity and the H 110α velocity. A histogram of these differences is shown in Fig. 5. These differences are an indication of the separation along the line of sight between the HII

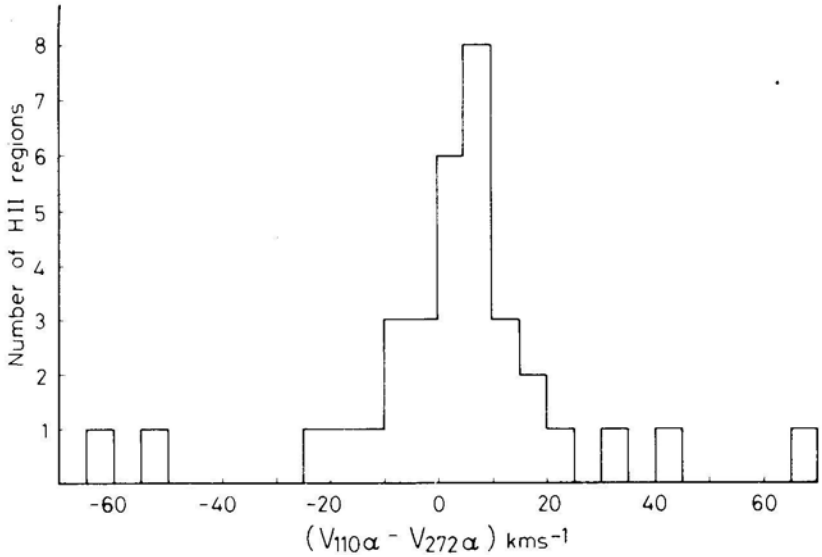

Figure 5. Histogram of the difference between the observed velocity of the H 272α line and the H 110α line in the same direction (see Column 10 of Table 2).

regions from which the H 110α line is observed and the lower-density gas from which the H 272α line is observed. The histogram in Fig. 5 shows that in the 60 per cent of the cases the difference in velocity is within 10 km s^{-1}. Within the observational errors (which are 2–5 km s^{-1} for both) the velocities are in good agreement. In any case there is always a substantial emission of the H 272α line at the velocity of the HII region (as seen in H 110α line) in more than 90 per cent of the cases. This clearly suggests that the low-density gas responsible for the H 272α line is associated with the dense HII region in that direction. In those cases where the velocity difference is large the two regions must be physically widely separated, unless there is differential motion between the higher- and lower-density regions.

6.1.4 *The l–v Diagram*

The longitude velocity (*l–v*) diagram of the lines observed is an indicator of the distribution of the gas responsible for the lines in the galactic disc. Fig. 6 is the *l–v* diagram of the H 272α lines observed in this survey in the range l = 0° to 50°. This can be compared with *l–v* diagram for the 21 cm HI emission in the galactic plane (*e.g.* Lockman 1976). The HI emission occupies a much larger velocity range in such a diagram. It is therefore clear that the gas responsible for the low-frequency recombination line is not distributed like neutral hydrogen. This rules out the possibility that the line emitting regions are partially-ionized neutral-hydrogen clouds. This could be because ionization in the cold HI clouds is not adequate to produce detectable recombination lines at this frequency. Further, the width of these lines, which is in the range of 20–50 km s^{-1}, indicates that these lines do not arise from a distributed component of the interstellar medium.

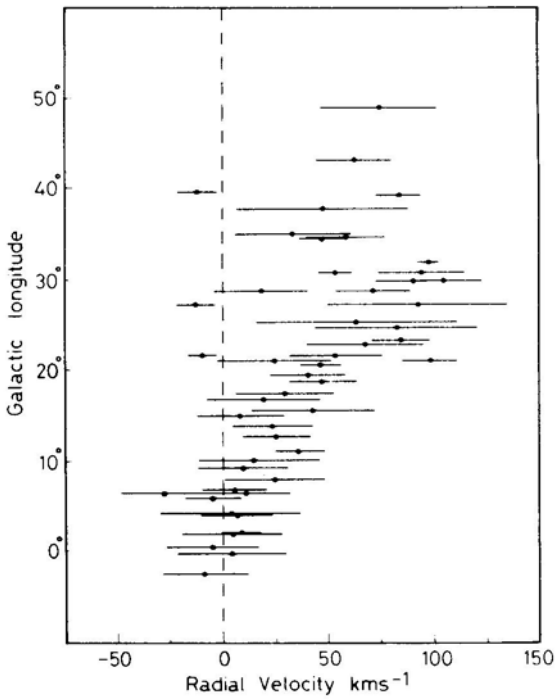

Figure 6. Longitude-velocity diagram of the observed H 272α lines. The extent of the horizontal lines indicates the observed half-power width and the dot indicates the centroid of the line.

On the other hand the *l*–*v* diagram in Fig. 6 is similar to those of HII regions seen in the H 110α survey (see Wilson 1980), the ionized galactic ridge seen in the H 166α survey (Lockman 1980), and molecular clouds seen in the CO surveys (Burton & Gordon 1978). The distributions of both HII regions and molecular clouds in the galactic disc show a peak between 4 kpc and 8 kpc from the galactic centre (Wilson 1980; Sanders 1983). While most of the recombination lines observed here do not arise in the HII regions seen in the H 110α survey, for reasons discussed earlier, the *l*–*v* diagram in Fig. 6 indicates that the lower-density gas responsible for these lines is distributed in a manner similar to HII regions and molecular clouds in the inner part of the Galaxy. As the H 272α recombination line is detected in every direction observed for $l < 40°$ representative quantities of low-density ionized gas must be present in every direction in this range.

6.2 *Carbon Lines*

Recombination lines of carbon are not as widespread as those of hydrogen. They have been detected at other frequencies in only 15 to 20 sources . To date these lines have been identified as coming from three types of regions. These are, the partially-ionized medium adjacent to HII regions (see Pankonin 1980), dark clouds surrounding early B-type stars (see Brown 1980) and possibly diffuse neutral hydrogen clouds (Konovalenko & Sodin 1981; Anantharamaiah, Erickson & Radhakrishnan 1985). The

Table 4. Observed parameters of carbon lines.

Source	T_L/T_C $\times 10^3$	Half-power width km s^{-1}	V_{LSR} km s^{-1}	Peak line temperature T_L(K)
G 359.9 − 0.0	0.71(06)	24(2.5)	0.0(1.0)	1.7(3)
G 0.7 − 0.0	0.58(09)	20(4)	3.5(2)	0.64(14)
G 4.4 + 0.1	0.70(13)	26(7)	8.5(3)	0.49(12)
G 7.0 − 0.3	1.0(2)	14(4)	5.5(2)	0.73(16)
G 14.0 − 0.1	1.1(1)	29(4)	27.5(2)	0.74(14)
G 17.6 − 0.3	0.32(08)	50(15)	20.5(6)	0.20(06)
G 19.6 + 0.0	0.67(14)	13(5)	49.5(2)	0.37(09)
G 23.4 − 0.2	0.93(13)	30(6)	85.5(2)	0.70(14)
G 24.8 + 0.1	0.73(09)	34(5)	45.5(2)	0.48(09)
G 34.7 − 0.6	0.69(13)	20(5)	17.5(2)	0.7(2)
G 37.8 − 0.2	1.2(2)	26(5)	53.5(2)	0.57(12)
G 206.8 − 16.4*	1.0(2)	26(7)	− 37.4(3)	0.12(03)

* Observation affected by interference.

carbon lines therefore arise in predominantly neutral and cool regions in contrast to hydrogen lines, most of which come from the hot fully-ionized HII regions.

In the present survey, C 272α line has been tentatively identified in 12 cases. The observed parameters are separately given in Table 4. For many of the sources, this is the first detection of a carbon line. The observed width of the lines (15–30 km s^{-1}) are much larger than those at higher frequencies (see for example Dupree 1974; Parrish & Pankonin 1975). If the large line widths are due to pressure broadening then electron densities of 50–100 cm^{-3} are implied for the regions. These in turn imply hydrogen densities of 2–3 × 10^5 cm^{-3}, if the cloud has normal interstellar abundance and all the carbon atoms are ionized. We note here that Silverglate & Terzian (1978) also report widths in excess of 25 km s^{-1} for carbon lines at 1400 MHz.

7. Summary

A survey of the H 272α recombination line has been made towards 53 directions in the galactic plane, consisting of 34 HII regions, 12 SNRs and 6 regions where the continuum is a minimum. Observed spectra and line parameters of the hydrogen lines detected towards 47 directions, and possible carbon lines towards 12 of these directions, are presented.

The H 272α line is seen in every direction observed with galactic longitude less than 40°. The line intensities are typically 0.1 per cent of the total continuum and there is no marked difference between directions of HII regions, SNRs and blank regions. Typical widths of the lines are 20–50 km s^{-1} but the lines are much wider in the longitude range 20° to 30°

The observed line temperatures show a good correlation with the total continuum temperature which is dominated by the nonthermal radiation at this frequency, indicating that the line intensities are enhanced by stimulated emission.

It is argued that these lines are unlikely to arise from typical HII regions (densities

> 100 cm^{-3}) which are prominent in many radio continuum surveys, due to the effects of pressure broadening, optical depth and beam dilution. These lines can arise only from much-lower-density gas. Judging from the velocity differences between H 110α lines, observed by Downes *et al.* (1980), and the present H 272α lines detected towards the same directions, there seems to be a physical association between the higher-density HII regions seen in H 110α and the lower-density gas responsible for the H 272α lines. The *l*–*v* diagram for these lines show that the distribution of this low-density gas is similar to that of HII regions and molecular clouds in the inner galactic disc, and is unlike that of neutral hydrogen which occupies a much larger velocity range. The widths of the lines indicate that the gas responsible for them is not a distributed component of the interstellar medium.

The observed widths of the carbon lines at 325 MHz are much larger than those at higher frequencies indicating that pressure broadening may have become important.

A more detailed and quantitative interpretation of the data presented in this paper will appear in the following paper (Anantharamaiah 1985).

Acknowledgements

I am grateful to the Radio Astronomy Centre, Ooty for generous allotment of telescope time for this project and to the telescope operators and maintenance staff for help and active support during observations. I thank G. Swarup for his keen interest in the project, V. Radhakrishnan for invaluable advice, K. M. Chandrakumar for construction and testing of the autocorrelator used for these observations, and B. V. Nataraja for help in the development of software. I also thank W. M. Goss for useful comments on the manuscript.

This paper is based on a part of the doctoral thesis submitted to the Bangalore University.

References

Altenhoff, W. J., Downes, D., Pauls, T., Schraml, J. 1978, *Astr. Astrophys. Suppl.*, **35**, 23.
Anantharamaiah, K. R. 1985, *J. Astrophys. Astr.*, **6**, 203.
Anantharamaiah, K. R., Erickson, W. C, Radhakrishnan, V. 1985, *Nature*, **315**, 647.
Batty, M. J. 1976, *Aust. J. Phys.*, **29**, 419.
Bignell, R. C. 1973, *Astrophys. J.*, **186**, 889.
Brocklehurst, M., Leeman, S. 1971, *Astrophys. Lett.*, **9**, 35.
Brocklehurst, M, Seaton, M. J. 1972, *Mon. Not. R. astr. Soc.*, **157**, 179.
Brown, R. L. 1980, in *Radio Recombination Lines*, Ed. P. A. Shaver, D. Reidel, Dordrecht, p. 127.
Brown, R. L., Lockman, F. J., Knapp, G. R. 1978, *A. Rev. Astr. Astrophys.*, **16**, 445.
Burton, W. B., Gordon, M. A. 1978, *Astr. Astrophys.*, **63**, 7.
Cesarsky, D. A., Cesarsky, C. J. 1973, *Astrophys. J.*, **183**, L143.
Downes, D., Wilson, T. L. 1974, *Astr. Astrophys.*, **34**, 133.
Downes, D., Wilson, T. L, Bieging, J., Wink, J. 1980, *Astr. Astrophys. Suppl. Ser.*, **40**, 379.
Dulk, G. A., Slee, O. B. 1975, *Astrophys. J.*, **199**, 61.
Dupree, A. K. 1974, *Astrophys. J.*, **187**, 25.
Gordon, M. A., Cato, T. 1972, *Astrophys. J.*, **176**, 587.
Gordon, K. J., Gordon, C. P., Lockman, F. J. 1974, *Astrophys. J.*, **192**, 337.
Gordon, M. A., Gottesman, S. T. 1971, *Astrophys. J.*, **168**, 361.
Gottesman, S. T., Gordon, M. A. 1970, *Astrophys. J.*, **162**, L93.

Griem, H. R. 1967, *Astrophys. J.*, **148**, 547.
Hart , L., Pedlar, A. 1976, *Mon. Not. R. astr. Soc.*, **176**, 547.
Jackson, P. D., Kerr, F. J. 1975, *Astrophys. J.*, **196**, 723.
Konovalenko, A. A., Sodin, L. G. 1981, *Nature,* **294**, 135.
Lockman, F. J. 1976, *Astrophys. J.*, **209**, 429.
Lockman, F. J. 1980, in *Radio Recombination Lines,* Ed. P. A. Shaver, D. Reidel, Dordrecht, p. 185.
Matthews, H. E., Pedlar, A., Davies, R. D. 1973, *Mon. Not. R. astr. Soc.*, **165**, 149.
Pankonin, V. 1975, *Astr. Astrophys.*, **38**, 445.
Pankonin, V. 1980 in *Radio Recombination Lines,* Ed. P. A. Shaver, D. Reidel, Dordrecht, p. 111.
Pankonin, V., Parrish, A., Terzian, Y. 1974, *Astr. Astrophys.*, **37**, 411.
Parrish, A., Conklin, E. K., Pankonin, V. 1977, *Astr. Astrophys.*, **58**, 319.
Parrish, A., Pankonin, V. 1975, *Astrophys. J.*, **198**, 349.
Pedlar, A., Davies, R. D. 1980, in *Radio Recombination Lines,* Ed. P. A. Shaver, D. Reidel, Dordrecht, p. 171.
Pedlar, A., Davies, R. D., Hart, L., Shaver, P. A. 1978, *Mon. Not. R. astr. Soc.*, **182**, 473.
Reifenstein, E. C, Wilson, T. L., Burke, B. F., Mezger, P. G., Altenhoff, W. J. 1970, *Astr. Astrophys.*, **4**, 357.
Rieu, N.-Q. 1969, *Astr. Astrophys.*, **1**, 128.
Sarma , N. V. G., Joshi, M. R, Bagri, D. S., Ananthakrishnan, S. 1975, *J. IETE,* **21**, 110.
Shaver, P. A. 1975, *Pramana,* **5**, 1.
Shaver, P. A., Goss, W. M. 1970a, *Aust. J. Phys. Astrophys. SuppL.,* No. 14, 77.
Shaver, P. A., Goss, W. M. 1970b, *Aust. J. Phys. Astrophys. Suppl.,* No. 14, 133.
Silverglate, P. R., Terzian, Y. 1978, *Astrophys. J.*, **224**, 437.
Swarup , G., Sarma, N. V. G., Joshi, M. N., Kapahi, V. K., Bagri, D. S., Damle, S. H., Ananthakrishnan, S., Balasubramanian, V., Bhave, S. S., Sinha, R. P. 1971, *Nature,* **230**,185.
Terzian, Y., Pankonin, V. 1974, in *IAU Symp.* 60: *Galactic Radio Astronomy,* Ed. F. J. Kerr, & S. C. Simonson, p. 241.
Viner , M. R., Vallee, J. P., Hughes, V. A. 1979, *Astr. J.*, **84**, 1335.
Weinreb, S. 1962, *Technical Rep. No*. 412, Massachusetts Inst. Tech., Boston.
Wilson, T. L. 1980, in *Radio Recombination Lines,* Ed. P. A. Shaver, D. Reidel, Dordrecht, p. 205.

J. Astrophys. Astr. (1985) **6**, 203–226

Low Density Ionized Gas in the Inner Galaxy—Interpretation of Recombination Line Observations at 325 MHz

K. R. Anantharamaiah *Raman Research Institute, Bangalore 560080*

Received 1985 June 21; accepted 1985 August 9

Abstract. The recent survey of H 272α recombination line (324.99 MHz) in the direction of 34 HII regions, 12 SNRs and 6 regions of continuum minimum ('blank' regions) in the galactic plane is used to derive the properties of diffuse ionized gas in the inner Galaxy.

The intensity of radio recombination lines at high frequencies is dominated by spontaneous emission in high-density gas and that at low frequencies (325 MHz) by stimulated emission in low-density gas. We have used this property to obtain the electron density in the gas in the direction of blank regions and SNRs, by combining the H 272α measurements (preceeding paper) with the published data at higher frequencies. Further, we have imposed constraints on the electron temperature and pathlength through this gas using the observed high-frequency continuum emission, average interstellar electron density and geometry of the line-emitting regions. The derived properties of the gas are (i) electron density 0.5-6 cm^{-3}, (ii) electron temperature 3000-8000 K and (iii) emission measures 500-3000 pc cm^{-6} The corresponding pathlengths are 50-200 pc.

As the derived sizes of the low-density regions are small compared to the pathlength through the Galaxy, the low-frequency recombination lines cannot be considered as coming from a widely distributed component of the interstellar medium.

The HII regions studied in the above survey cannot themselves produce the H 272α lines detected towards them because of pressure broadening, optical depth, and beam dilution. However, the agreement in velocity of these lines with those seen at higher frequencies suggests that the low-frequency recombination lines arise in low-density envelopes of the HII regions. Assuming that the temperature of the envelopes are similar to those of the cores and invoking geometrical considerations we find that these envelopes should have electron densities in the range 1–10 cm^{-3} and linear sizes of 30–300 pc in order to produce the observed H 272α lines.

Key words: Galaxy, recombination lines—galactic ridge—interstellar medium, electron densities— Hii regions, low density envelopes

1. Introduction

Recombination lines observed at low frequencies (< 1 GHz) preferentially sample conditions in low-density regions whereas those at higher frequencies originate mainly

in higher-density regions. Several surveys of recombination line emission from the galactic plane have been performed at high frequencies (> 1 GHz) (see Wilson 1980 and references therein), and have been used for deducing the properties of the ionized regions. Until recently, recombination line observations at low frequencies (and therefore from correspondingly lower-density regions) were available towards only a few sources in the galactic plane (see Pedlar & Davies 1980 and references therein). Some of these observations have been used to deduce the properties of low-density regions (e.g. Shaver 1976) and to demonstrate the importance of stimulated emission of recombination lines at low frequencies (Pedlar *et al.* 1978).

Apart from the discrete ionized regions (HII regions) in the galactic plane there is evidence for the presence of more widespread lower-density ionized gas in the inner Galaxy from what are known as 'galactic ridge recombination lines' (Gottesman & Gordon 1970; Jackson & Kerr 1975; Lockman 1976; Hart & Pedlar 1976b, and see Lockman 1980 and references therein). These lines which have been observed mainly at centimetre wavelengths are seen in directions in the galactic plane apparently free of discrete continuum sources. There were no low-frequency observations of the ridge lines

Recently, a survey was made of the recombination line emission at 325 MHz towards 53 directions in the galactic plane consisting of 34 HII regions, 12 SNRs and 6 'blank' regions which are free of discrete continuum sources (Anantharamaiah 1985a, hereafter referred to as Paper I). In Paper I we have presented the observations and the parameters of the H 272α lines detected towards 47 of these directions. A discussion of the broad characteristics of the data was also presented in Paper I and it was shown that most of the observed lines arise due to stimulated emission in the presence of background radiation. In this paper we make use of the observed parameters and derive the physical properties of the ionized regions responsible for these lines. In Section 2 we present some general considerations and a brief summary of the relevant theory of line formation. In Section 3 we obtain the properties of the ionized gas observed towards blank regions and SNRs, and in Section 4 towards HII regions. A discussion of the derived parameters is presented in the final section.

2. General considerations

The detection of a recombination line in a given direction essentially yields three line parameters, the peak line intensity T_L, the full line width at half maximum intensity ΔV and the line centre velocity V_{LSR} In addition, the average continuum beam brightness temperature T_{BC} is also measured in the same direction. V_{LSR} can indicate the distance to the source if a model of galactic rotation is used. As the total continuum temperature T_{BC} is dominated by the nonthermal galactic background, at this frequency, it is not possible to use the ratio of line to continuum temperature to derive the electron temperature of the region as usually done at higher frequencies. Further, even the thermal part of the continuum is dominated by emission from high-density ionized regions whereas the low-frequency recombination lines arise mostly in low-density regions (Brown *et al.* 1978). Therefore, at this frequency only the line intensity T_L and the width ΔV are directly related to the source parameters. However the total continuum temperature T_{BC} is an important quantity since it directly affects the line intensity T_L because of stimulated emission (Paper 1).

To derive or put constraints on the properties of the gas responsible for the observed lines, it is thus necessary to combine the line parameters from Paper I with other observations pertaining to the same gas.

2.1 *Theoretical Line Intensities*

Theoretical intensities of low-frequency recombination lines have been discussed in detail by Shaver (1975). The excess temperature produced at the recombination line frequency v by a homogeneous ionized region located in front of a background continuum source is given by

$$\begin{aligned} T_L = {} & T_0\left[e^{-\tau_C}(e^{-\tau_L}-1)\right] \\ & + T_e\left[\frac{b_m\tau_L^* + \tau_C}{\tau_L+\tau_C}(1-e^{-(\tau_L+\tau_C)}) - (1-e^{-\tau_C})\right] \\ & + T_N\left[\frac{1-e^{-(\tau_L+\tau_C)}}{\tau_L+\tau_C} - \frac{1-e^{-\tau_C}}{\tau_C}\right] \end{aligned} \tag{1}$$

where T_0, is the continuum temperature of the background source, T_e the electron temperature of the ionized region and T_N represents the nonthermal background distributed inside this region. The continuum optical depth is given by (Oster 1961)

$$\tau_C = 0.0314 \times v^{-2}\, T_e^{-3/2} \ln\left(4.955 \times 10^{-2}\frac{T_e^{3/2}}{v}\right) N_e N_i L \tag{2}$$

where N_e and N_i (cm^{-3}) are the electron and ion densities, L (pc) is the pathlength through the region and v (GHz) is the frequency. In local thermodynamic equilibrium (LTE), the optical depth at the line centre (for α-lines) is given by (Shaver 1975)

$$\tau_L^* = \frac{8.796 \times 10^{-5} n^3}{\Delta V\, T_e^{5/2}}\left(1+\frac{1.5}{n}\right)\exp\left(\frac{157890}{n^2 T_e}\right)(1+1.48\gamma)^{-1} N_e N_{H^+} L \tag{3}$$

where n is the principal quantum number, N_{H^+} (cm^{-3}) is the ionized-hydrogen density, ΔV (km s^{-1}) is the full Doppler profile width at half maximum and γ is the ratio of the profile width due to pressure or radiation broadening to that due to pure Doppler broadening. The true optical depth in the line becomes

$$\tau_L = b_n \beta_n \tau_L^* \tag{4}$$

with

$$\beta_n = 1 - \frac{k T_e}{h v}\frac{b_{n+1} - b_n}{b_n} \tag{5}$$

where the departure coefficient b_n relates the true population, N_n of the atomic energy level n to its value in LTE, N_n^*: by the equation

$$N_n = b_n N_n^*. \tag{6}$$

The b_n values are usually calculated using the condition of time-independent statistical equilibrium which requires that there are as many transitions into a level as there are out of it (see for example Salem & Brocklehurst 1979). For calculations in this paper, we

have used the computer code published by Brocklehurst & Salem (1977) to obtain the b_n and β_n values.

2.2 *Upper Limit to the Electron Density from Observed Line Widths*

The width of a recombination line due to pressure broadening is directly proportional to the electron density in the region and is a strong function of the principal quantum number n (Griem 1967). The half-power width of the line due to this was calculated by Brocklehurst & Leeman (1971) under the impact approximation as

$$\Delta\nu_{LP} = 3.74 \times 10^{-11} \frac{N_e}{T_e^{0.1}} n^{4.4} \text{kHz}. \tag{7}$$

This allows us to put an upper limit on the electron density N_e of the regions responsible for the lines from the observed widths alone. The contribution to the line-width from Doppler broadening is given by

$$\Delta\nu_{LD} = 2\sqrt{\ln 2}\,\frac{\nu}{c}\left[\frac{2kT_e}{m_H} + \frac{2}{3}\langle V_t^2\rangle\right]^{1/2} \tag{8}$$

where $\langle V_t^2 \rangle^{1/2}$ is the rms turbulent velocity in the region, T_e is the electron temperature and m_H the mass of the emitter (hydrogen). The effective final width can be approximated by

$$\Delta\nu_L^2 = \Delta\nu_{LD}^2 + \Delta\nu_{LP}^2. \tag{9}$$

In Fig. 1 we have plotted the expected width of the H 272α recombination line as a function of electron density. The width has been calculated using Equations (7), (8) and (9) for two different temperatures and assuming an rms turbulent velocity of 20 km s^{-1} which is typical for HII regions. As can be seen from this figure, the width increases sharply for N_e > 50 cm^{-3} irrespective of the temperature of the region. 85 per cent of

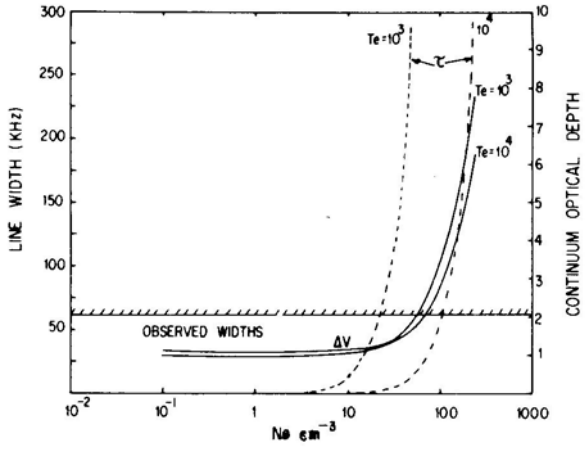

Figure 1. Expected width (FWHM) of the H 272α line (solid line) and continuum optical depth at 325 MHz (dashed line) as a function of electron density at two electron temperatures. Path length through the gas is assumed to be 50 pc. The hatched horizontal line indicates the

the lines observed in the survey reported in Paper I have widths < 60 kHz, which corresponds to an upper limit for the electron density of 60 cm^{-3}. Although the observed widths of the remaining 15 per cent of the lines are indicated as being > 60 kHz in Paper I**,** they may be made up of multiple components and therefore the actual widths of the individual components can be much smaller. Even so, the maximum width of the line, assuming it to be a single component, corresponds to an upper limit for the electron density of 100 cm^{-3}. In Fig. 1 we have also plotted the continuum optical depth at 325 MHz as a function of density assuming a path length of 50 pc. It is interesting that, if these regions have sizes of a few tens of parsecs along the line of sight, then their continuum optical depth at this frequency exceeds unity for densities > 50 cm^{-3}. As the region becomes optically thick the recombination lines merge with the continuum and become undetectable, at least under LTE conditions.

3. Analysis of lines observed toward blank regions and SNRs

Blank regions for our purposes were defined in Paper I as areas in the galactic plane where the continuum emission at 5 GHz is a minimum over the telescope beam of 2° × 6 arcmin used for these observations. The 5-GHz high-resolution map of Altenhoff *et al.* (1978) was used to select 6 such regions. There are no discrete continuum sources within these regions. Fig. 2 shows a typical blank region. The H 272α line has been detected towards all the six such directions.

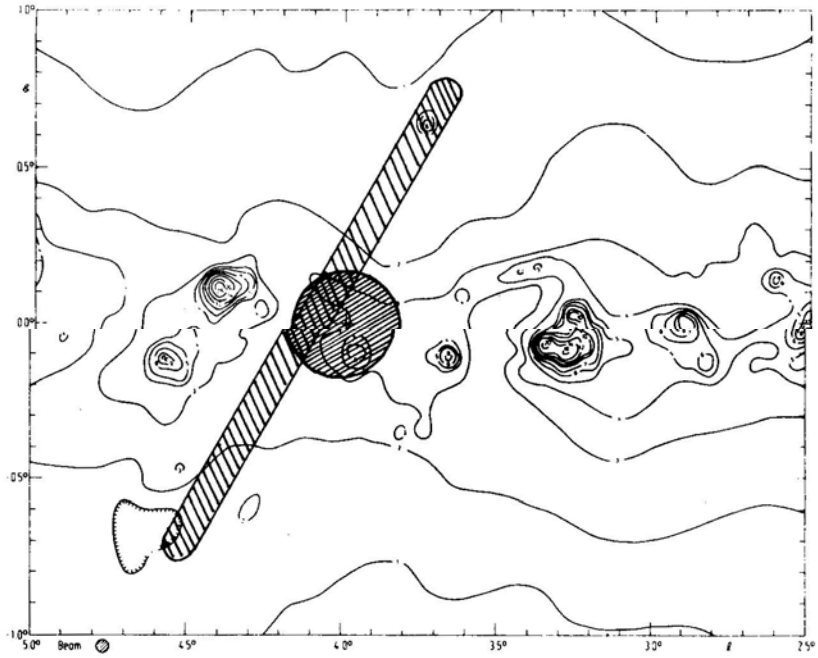

Figure 2. A typical blank region (see text) in the galactic plane for the beam used in the H 272α survey (elongated hatched area). The circular hatched area represents the beam used by Lockman (1976) who observed H 166α line at this position. The 5 GHz continuum map is from Altenhoff *et al.* (1978).

The line emission observed toward blank regions would fall under the category of galactic ridge recombination lines. Such lines were first detected near 18 cm (157α line) by Gottesman & Gordon (1970). Subsequently, similar lines have been reported towards selected positions by Gordon & Gottesman (1971), Jackson & Kerr (1971), Gordon & Cato (1972), Gordon, Brown & Gottesman (1972), Jackson & Kerr (1975) and Mebold *et al.* (1976). Lockman (1976) and Hart & Pedlar (1976b), in another approach, have observed the H 166α line emission (near 21 cm) at a number of positions along the galactic plane (b = 0°) separated by 0°.5 to 1° in galactic longitude from l = 0° to l = 70°. Some of these positions correspond to regions of continuum minimum as in the earlier studies.

In general, recombination lines are not expected from SNRs. Therefore the directions towards them are similar to the blank regions. The only difference is the presence of a strong background source in addition to the galactic nonthermal background.

In Paper I, H 272α line observations have been reported towards 11 directions corresponding to 10 well-known SNRs. Two of the adjacent directions observed (near W 44) corresponds to the same SNR. Recombination lines at higher frequencies have been detected earlier towards at least three of these SNRs (Cesarsky & Cesarsky 1973a, b; Bignell 1973; Downes & Wilson 1974; Pankonin 1975). Dulk & Slee (1972, 1975) have observed a turnover in the continuum spectrum of some of these sources at 80 MHz, which is attributed to free-free absorption by the line-of-sight ionized gas.

In this section we shall make use of the line parameters observed at 325 MHz (Paper I) and higher-frequency measurements to determine or put constraints on the parameters of the line-emitting region. Towards the blank regions and SNRs it is reasonable to assume that the lines observed at the two frequencies originate in the same gas (this may not be true in the direction of HII regions). We can only determine those parameters which have very different functional dependence on the observable quantities like line temperature T_L and width ΔV. Using Equations 1 to 5 and departure coefficients from Salem & Brocklehurst (1979), it can be shown that, for low electron densities, the intensity of recombination lines at a high frequency (e. *g*. H 166α) and of that at a low frequency (e.*g.* H 272α) has very different dependence on the electron density in the line-emitting region. This is a consequence of the dominance of the spontaneous emission at high frequencies and that of stimulated emission due to the background radiation at low frequencies. The line intensity due to spontaneous emission is proportional to the emission measure and therefore to the square of the electron density in the gas. On the other hand, if stimulated emission is dominant, the line intensity is essentially proportional to the electron density itself because of the similar dependence of the non-LTE factor $b_n\beta_n$. on the electron density.

3.1 *A Model for Interpretation of the Observed Line Intensities*

We shall adopt a simple plane-parallel homogeneous cloud model (Fig. 3) in which the electron temperature T_e and the electron density N_e are uniform. The cloud extends over a path length L along the line of sight, resulting in an emission measure $EM = N_e^2 L$. T_0 represents the radiation originating behind the cloud. The cloud cannot be assumed to fill the telescope beam of 2° × 6 arcmin used for the H 272α

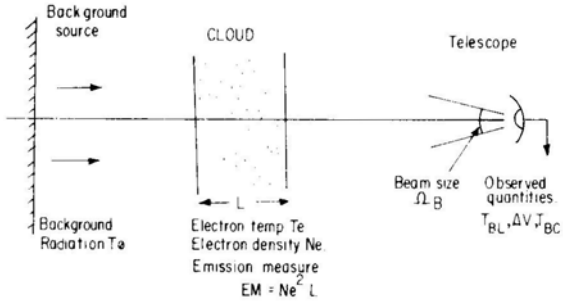

Figure 3. Schematic model used for interpretation of recombination lines in the direction of blank regions and SNRs.

observations. The H 157α and the H 166α emission in the blank regions extend over $b = \pm 0°.5$ perpendicular to the galactic plane (Gordon, Brown & Gottesman 1972; Lockman 1976; Hart & Pedlar 1976b). Assuming the gas to be present uniformly over this range we get a beam dilution factor of 0.6 for the H 272α observations. In all our analysis we have used this value for beam dilution, for the H 272α line.

In this model, the expected line brightness temperature is given by

$$T_{BL} = \frac{\Omega_C}{\Omega_B} T_L \tag{10}$$

where $(\Omega_C./\Omega_B)$ is the beam dilution factor, and T_L is the line temperature calculated using Equation (1). For any specified value of N_e, T_e, EM and line width ΔV, the line and continuum optical depths τ_L, and τ_C can be calculated using equations given in Section 2. b_n. and β_n, can be obtained using the computer code of Broklehurst & Salem (1977). Further, if T_0 and T_N are given, the expected T_L can be calculated using Equation (1).

3.2 *Electron Density of the Gas*

Based on the above model it turns out that the electron density is almost uniquely determined if we use the observed intensities of the H 166α and H 272α lines. From observations of Lockman (1976) the H 166α line measurements are available within 0°.3 in longitude for all the blank regions observed (Paper I) and for two of the positions the H 166α measurements are within the Ooty beam. The observed H 272α line parameters (Paper I), T_{BL}, ΔV and V_{LSR} and the measured total continuum temperature T_{BC}, are given in Table 1 for all the blank regions. The peak H 166*a* line temperature observed by Lockman (1976) at the nearest position is also given in this table. We assume that the two observations pertain to the same gas.

The corresponding parameters for eight of the SNR directions are given in Table 2. The parameters of the high-frequency lines observed towards two of these directions (W 49B and W 44) and the references are also given in Table 2. The source 3 C 391, towards which the H 272α line is narrower than the high-frequency lines will be discussed elsewhere. For the other 6 directions we use the H 166α line parameters

Table 1. Observed parameters for blank regions.

Source	H 272α Parameters				H 166α[1]		5 GHz continuum Temp.[2] K
	Line Temp. K	Width km s^{-1}	Velocity V_{LSR} km s^{-1}	T_{BC} K	T_L K	T_C K	
G 2.1 − 0.0	0.81 (0.13)	47 (4)	5 (2)	740	< 0.016	13.3 (1.2)	0.56
G 4.2 − 0.0	1.28 (0.24)	33 (5)	7 (2)	690	0.045 (15)	10.0 (0.5)	0.40
G 9.4 + 0.1	0.61 (0.13)	42 (7)	10 (3)	730	0.054 (14)	12.1 (0.7)	0.40
G 15.7 − 0.0	0.86 (0.14)	58 (5)	43 (2)	610	0.051 (15)	08.9 (1.0)	0.36
G 17.6 − 0.3	0.67 (0.11)	47 (4)	30 (2)	630	0.027 (14)	08.1 (1.2)	0.34
G 21.2 − 0.0	0.64 (0.11)	26 (3)	98 (2)	580	0.038 (15)	10.4 (0.7)	0.34
	0.46 (0.08)	54 (6)	25 (3)				

1. From Lockman (1976)
2. Estimated from the maps of Altenhoff *et al.* (1978)

Table 2. Observed parameters towards SNRs.

Source		H 272α line parameters						High frequency parameters						
		V_{LSR} km s^{-1}	T_L K	ΔV km s^{-1}	T_{BC} K	T_{BSNR} K	T_0 K	Line	V_{LSR} km s^{-1}	T_L K	ΔV km s^{-1}	T_C K	Ref.	τ_{80}
1		2	3	4	5	6	7	8	9	10	11	12	13	14
G 357.7 − 0.1	...	−7.9 (1.3)	1.3 (2)	40 (3)	930	276	534	166α		0.027 (18)		13.4 (1.4)	1	0.12 (25)
G 6.6 − 0.1	W 28	11 (2)	1.1 (2)	43 (4)	900	284	592	166α		0.052 (19)		16.7(1.2)	1	...
G 11.2 − 0.3	...	37 (2)	0.8 (2)	23 (6)	760	189	475	166α		0.06		15.4	2	0.09 (38)
G 21.8 − 0.6	...	54 (2)	0.7 (12)	44 (5)	790	151	470	166α		0.038 (14)		7.7 (6)	1	...
G 23.0 − 0.3	...	68 (2)	0.84 (14)	55 (4)	770	136	453	166α		0.058 (14)		13.2 (1)	1	...
G 34.6 − 0.6	W 44	48 (1)	0.87 (16)	21 (3)	830	325	576	166α	50	0.036 (09)	21	30	3	...
G 39.2 − 0.3	3 C396	84 (2)	0.66 (13)	21 (5)	570	141	356	166α		0.017 (12)		6.4 (0.6)	1	0.02 (09)
G 43.2 − 0.1	W 49	63 (1)	1.2 (2)	35 (3)	690	315	503	166α	60	0.02	30	...	4	0.44 (09)
								134α	65 (10)	0.019 (03)	45	19	5	

1. Lockman (1976) 2. Hart & Pedlar (1976) 3. Bignell (1973) 4. Cesarsky & Cesarsky (1973b) 5. Downes & Wilson (1974)

observed by Lockman (1976) or Hart & Pedlar (1976b) at the nearest position. These parameters are also listed in the table. For four of these six positions the available H 166α measurement are within the Ooty beam and for the other two positions they are within 0°.4 of the beam centre. The measured value of 80 MHz optical depth, wherever available, is also given in Table 2.

Using Equation (1) and the model described above, it is possible to find those combinations of N_e, T_e and *EM* which produce the observed intensities of both the H 166α and the H 272α lines. The procedure adopted was as follows. For a set of specified N_e and T_e , in the range 0.1–100 cm^{-3} and 100–10000 K respectively, the emission measure required to produce the observed intensity of the H 272α line was calculated using Equations (10) and (1). For the blank regions the background temperature T_0 in Equation (1) was taken to be $T_{BC}/2$ (Table 1). For the SNR directions T_0 was estimated as follows. We first estimated the expected average brightness temperature T_{BSNR} over the 2° × 6 arcmin beam, due to the SNR, using the 408 MHz flux density, spectral index and size given in the catalogue of Clark & Caswell (1976). The contribution to the observed brightness temperature T_{BC} (given in Table 2) from the galactic nonthermal background was then taken to be

$$T_{Bg} = T_{BC} - T_{BSNR}.$$

The effective temperature of the radiation coming from behind the cloud for each of the directions was calculated using

$$T_0 = T_{BSNR} + T_{Bg}/2$$

where it is assumed that half of the observed background originates behind the cloud. The values of T_0 are given in Table 2. As the path lengths involved are not very large, we used $T_N = 0$. A dilution factor (Ω_C/Ω_B) = 0.6 was used in all the calculations.

Similar calculations were performed to obtain the required emission measure to produce the observed high-frequency line intensity. In these calculations, we used a beam dilution factor of unity. For the blank regions we used $T_0 = T_C/2$ and $T_N = 0$. For the SNR directions all of the observed continuum at high frequencies was assumed to originate behind the cloud. The respective widths of the lines at two frequencies, wherever available, was used for the calculation. Otherwise, the observed H 272α line width was used for both low and high-frequency lines.

The results of these calculations are shown in Fig. 4 for the blank region G 4.2–0.0 and for the SNR G 357.7 – 0.1. In these figures we have plotted the required emission measure as a function of electron density N_e to produce the observed intensity of the H 272α and H 166α lines, for four different electron temperatures. The intersection point of the 272α and 166α curves at each of the temperatures gives the electron density N_e (and the corresponding *EM*) which will explain both the observed H 166α and H 272α line intensities. It is remarkable that irrespective of the temperature T_e and emission measure *EM* of the region there is only a very small range of electron densities (bounded by the two vertical dashed lines) that is consistent with the line intensities at both frequencies. This range is less than a factor of 1.5 and for temperatures above 1000 K the required density has practically a unique value.

Using the adopted model, the accuracy of the electron density as determined above depends only on the accuracy of the measurements of the line parameters and the estimate of the beam dilution factor. Based on the errors of the line intensities the derived density is determined to within a factor of two. If the beam dilution changes by

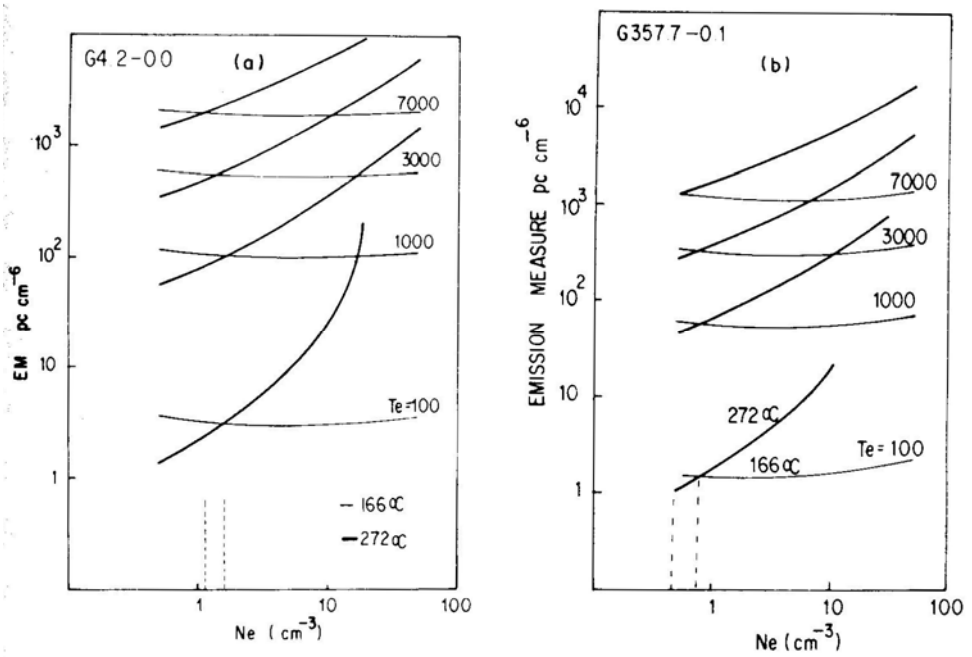

Figure 4. The relation between emission measure and electron density of the gas in order to produce the observed intensity of the H 166α (thin lines) and H 272α (thick lines) lines towards (a) the blank region G 4.2 – 0.0, and (b) for the SNR direction G 357.7 – 0.1. The calculation (see text) is done for different electron temperatures indicated. The intersection point of the thick and thin lines gives the density of the gas. The vertical dashed lines indicate the range of densities allowed for the temperature range of 100 to 7000 K.

a certain factor then the derived density changes by a similar factor. An increase in the beam dilution (i.e. smaller angular-size for the cloud) for the H 272α line results in a decrease in density. An increase in T_0 will increase the derived density.

In the case of W 49, for which two high-frequency measurements are available, we obtained the density in a similar way using both the high-frequency lines. The densities which are derived differ only by a factor of 1.5.

The densities derived from similar calculations for all the blank regions and SNRs are given in column 2 of Tables 3 and 4 respectively. They are in the range of 0.5–7 cm^{-3}. We regard these densities as reliable to within a factor of two. It should be noted here that these densities are the true (or local) electron densities of the line-emitting regions and not the rms electron density as in the case when it is derived (for strong HII regions) from continuum measurements. In the latter case, as also in the case of high-frequency recombination lines, the emission is proportional to the square of the electron density. But at low frequencies, due to the strong dependence of b_n and particularly β_n on the electron density, the strength of the line emission is proportional to the density itself. Therefore, if there is any clumping in the gas, then the clumps themselves should have this derived density and the size of the region should increase to make up for the decreased filling factor. In other words, if the emission measure of this gas is fixed, say by other considerations, then the size of the region (along the line of sight) can be $\geqslant EM/N_e^2$ depending on the filling factor of the ionized gas at density N_e.

Table 3. Derived parameters for blank regions.

		Upper limits from T_C (5 GHz)			Upper limits from PSR *DM*			Lower limits with $L > 50$ pc	
Source	N_e cm^{-3}	*EM* cm^{-6} pc	T_e K	*L* pc	*L* pc	*EM* cm^{-6} pc	T_e K	*EM* cm^{-6} pc	T_e K
G 2.1 – 0.0	0.5	4000	11000	16000	800	200	2100	12.5	500
G 4.2 – 0.0	1.2	3600	10000	3600	400	400	2500	50	800
G 9.4 + 0.1	6.0	3500	8000	97	60	2160	6000	1800	5000
G15.7 – 0.0	2.5	2800	5000	448	160	1000	3100	312	1300
G17.6 – 0.3	2.0	2500	7000	625	200	800	4000	200	1600
G21.2 – 0.0	4.0	2500	8500	156	100	1600	6000	800	4000

Table 4. Properties of ionized gas towards SNRs

		Upper limit from PSR DM			Lower limit with $L > 50$ pc		Values for $T_e = 5000$		
Source	N_e cm^{-3}	*L* pc	T_e K	*EM* cm^{-6} pc	T_e K	*EM* cm^{-6} pc	*EM* cm^{-6} pc	*L* pc	τ_{80}
G 357.7 – 0.1	0.7	570	2500	280	700	25	700	1430	0.11
G 6.6 – 0.1	2.5	160	4000	1000	2000	312	1300	208	0.21
G 11.2 – 0.3	4	100	7000	1600	4500	800	850	53	0.14
G 21.8 – 0.6	3.8	105	6000	1500	4000	722	1050	73	0.17
G 23.0 – 0.2	4	100	5000	1600	3000	800	2000	125	0.33
G 31.9 + 0.0	7	51	8000	2500	7000	2450	1200	25	0.20
G 34.6 – 0.6	1.1	363	6000	440	1800	61	360	297	0.06
G 39.2 – 0.3	0.7	570	5000	280	1500	25	300	612	0.05
G 43.2 – 0.1	1.5	266	3000	600	1100	113	1000	44	0.16

3.3 *Electron Temperature and Emission Measure*

Since in the model we are considering there are only three parameters N_e, T_e and *EM* which characterize the ionized region, and we have used two measured quantities (the intensity of the H 166α and H 272*a* lines) to determine N_e, the other two parameters are related to each other through the observed intensity of the H 166*a* or the H 272*a* line. The method used for determining the electron density N_e ensures that the relation between T_e and *EM* will be very similar irrespective of whether we use the H 166*a* or the H 272*a* line intensity to relate them. A determination of, or putting a constraint on, either T_e or *EM* (or even the path length *L)* will decide or impose a constraint on the other quantity.

Fig. 5 shows the relation between *EM* and T_e . The lines marked 272α and 166α in these figures represent *EM* as a function of T_e required by the intensities of these lines given the electron density N_e which was obtained in the previous section. As expected, the two curves are very similar. On the right-hand ordinate is also marked the effective path length obtained simply from the relation $L = EM/N_e^2$.

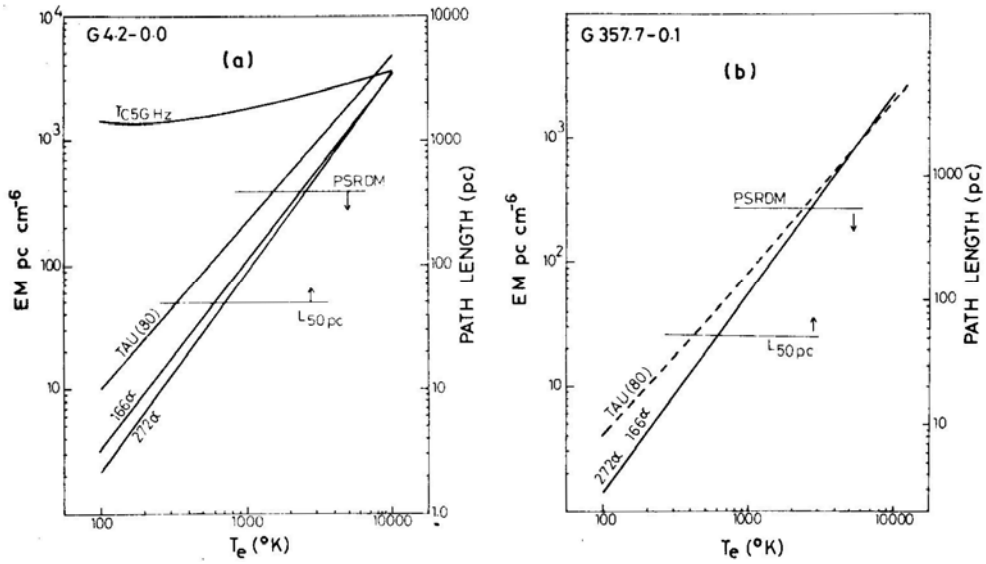

Figure 5. Constraint on the emission measure, electron temperature and path length through the gas towards (a) the blank region G 4.2–0.0 and (b) the SNR direction G 357.7 – 0.1, from considerations of average interstellar electron density (line marked PSRDM), 5 GHz continuum emission (TC5GHz) and geometry of the line emitting region (L 50 pc). See text for arguments. The lines marked 166α and 272α represent the constraint based on the observed recombination lines. An electron density derived from Fig. 4 is used (see Table 2). The combination of T_e and *EM* required to produce an 80 MHz continuum optical depth of 0.25 (T_{AU} 80) is also shown. In the case of G 357.7 – 0.1 no constraint can be imposed using 5 GHz continuum.

Unfortunately, there is no other measured quantity available which can be directly attributed to this gas and which depends on T_e, *EM* or *L* in a different way, to impose a constraint on any of these parameters. However, we can put some limits on these parameters from three considerations.

The first of these is based on the thermal continuum emission from this gas. At a sufficiently high frequency like 5 GHz, the contribution to the galactic background from the nonthermal radiation is very small particularly in the blank areas. Therefore most of the observed continuum at 5 GHz will be thermal. We have estimated the average continuum temperature at 5 GHz at each of the observed blank regions using the high-resolution maps of Altenhoff *et al.* (1978). The values are given in Table 1. We now require that the ionized gas which produces the recombination lines should not produce more than this observed continuum. This will impose an upper limit on the *EM* of the gas which in turn will imply an upper limit on the electron temperature. The nearly horizontal line marked TC5GHz in Fig. 5 represents this constraint. The emission measure cannot be above this line. Combining this limit with the relation between *EM* and T_e we can get an upper limit for T_e. The upper limits for all the blank regions are given in Table 2. The upper limits for *EM* are in the range of 2500–4000 cm^{-6} pc and for T_e in the range of 5000–10000K. We cannot use this argument for the SNR directions since most of observed 5 GHz continuum is emitted by the SNR itself.

Given the density of the gas an upper limit on its path length can be imposed using the pulsar dispersion measure. Vivekanand & Narayan (1982) have analysed the dispersion measure toward 224 pulsars and obtained a model for the galactic electron density of the form

$$N_e(z) = 0.030 + 0.020 \exp\left(\frac{-|z|}{70}\right) \text{cm}^{-3} \tag{11}$$

where z (pc) is the height above the galactic plane. The first term in this expression represents a distributed medium of average density $\langle N_e \rangle$ = 0.03 cm^{-3} having a scale height in excess of 300 pc. The second term describes the contribution from localized higher-density ionized regions (*e.g.* HII regions) which occur in the galactic plane with a scale height of 70 pc. The regions responsible for the recombination lines observed towards blank regions and SNRs can be considered to fall in this category. We can use the second term of Equation (11) together with N_e determined above, to set an upper limit to the effective path length through the gas responsible for the recombination lines.

If N_e is the density of a region lying along a line of sight and L_{gal} is the path length through the entire Galaxy, then the above result imposes a restriction on the effective path length L through the region of the form

$$N_e \frac{L}{L_{gal}} \leqslant 0.02 \text{ cm}^{-3}$$

or

$$L \leqslant \frac{0.02}{N_e} L_{gal}.$$

Using the N_e determined for the blank regions and SNRs and taking L_{gal} = 20 kpc we obtain upper limits of 60–400 pc for the effective path length through the gas responsible for the observed lines. The horizontal lines marked PSRDM in Fig. 5 represents this upper limit. The upper limit on L implies an upper limit on *EM* which in turn implies an upper limit on T_e. These upper limits are given in Tables 3 and 4. In most of the cases these upper limits are lower than those implied by the 5 GHz continuum. The upper limits implied by the pulsar dispersion measure are not as rigorous as the upper limits from the continuum. This is because the contribution to the interstellar electron density from HII regions derived by Vivekanand & Narayan (1982) is an average over the entire Galaxy; in addition, in their analysis there was a scarcity of pulsars in the longitude range of interest here.

It is possible to set a lower limit to the electron temperature and therefore to the emission measure from geometrical considerations. In Fig. 5 it can be seen that a lower electron temperature implies a lower emission measure which in turn implies a smaller effective path length, since the density of the region is fixed. For a temperature of 100 K, (which is typical for HI clouds) the required path lengths are in the range of 0.2–2 pc.

As pointed out by Shaver (1976), with such small path lengths the geometry of these regions would be very peculiar. The scale height of this gas is estimated to be 70–80 pc from a study of the latitude extent of the H 166α emission by Lockman (1976) and Hart & Pedlar (1976b). Therefore this gas would have dimensions of ~ 100 pc in the direction perpendicular to the line of sight. For low electron temperatures, the above small effective path lengths would require these regions to be in the form of thin

extensive sheets or small cloudlets distributed along the line of sight with a very small filling factor. Both these geometries would be inconsistent with the smooth observed line profiles of width 30–50 km s^{-1}.

It is difficult to set any rigorous lower limit to the temperature from these geometrical considerations. However it is reasonable to expect that the path length be comparable to or larger than the lateral extent of the gas, which is of the order of 50–100 pc. This lower limit on the path length requires that the electron temperature be higher than a few thousand degrees. The lower limits to the temperature and *EM* based on a path length of 50 pc through the gas are given in Tables 3 and 4.

It may be possible to set a lower limit to the electron temperature of the ionized region only based on the electron density. This is because ionization always results in heating of the gas. In fact the main source of heating in most of the interstellar regions is through ionization after which the excess energy carried by the liberated electron is converted into kinetic energy of the particles through collisions (Spitzer 1978). The electron density of 1–7 cm^{-3} derived above for the blank regions and SNRs imply high ionization rates for hydrogen. It may not be possible to achieve such electron densities without heating the gas to a considerable degree. We recall that an average of 0.5 eV excess energy of the ionizing photons, over the 13.6 eV ionization potential would result in a kinetic energy of the electrons corresponding to a temperature of > 3000 K.

We conclude that the temperature of the gas responsible for the lines observed towards blank regions and SNRs is greater than a few thousand degrees.

Although there is another measured quantity (τ at 80 MHz) pertaining to the ionized gas, along the line of sight to some of the SNRs (Dulk & Slee 1975), it cannot be used to put an independent constraint on any of the parameters. If one requires that the gas produce all of the observed τ_{80}, the relation between *EM* and T_e is very similar to the corresponding relation for explaining the observed intensity of the H 272α and H 166α lines. In Fig. 5(b) the line marked TAU (80) represents this relation for the observed value of τ_{80} towards the source G 357.7 – 0.1. As can be seen, this line runs almost parallel to the lines marked 272α and 166α and therefore does not give a new constraint. However, we can require that the gas responsible for the recombination lines should not produce more than the observed 80 MHz optical depth. This is easily satisfied for all the SNR directions we have considered. The 80 MHz optical depth of the recombination line emitting regions calculated with $T_e = 5000$ K are given in Table 4. It turns out that the line-emitting regions can account for most of the observed 80 MHz optical depth.

4. Lines observed towards HII regions

4.1 *General Considerations*

These are possibly the best-studied ionized regions of the Galaxy. They appear as prominent sources in the radio continuum surveys of the galactic plane *(e. g.* Altenhoff *et al.* 1970, 1978; Haynes *et al.* 1978) and are more numerous than any other type of galactic radio source.

There are 30 such 'conventional' HII regions towards which the H 272α line has been detected in the observations reported in Paper I. The observed line intensity and width for 21 of these directions are given in Table 5. The intensity of low-frequency recombination lines from these HII regions is expected to be very weak due to the effect

Table 5. Optical depth and sizes of HII regions and upper limits on density.

Source	T_{BL} (272α) K	ΔV km s^{-1}	$N_{e,max}$ cm^{-3}	$N_{e,HII}$ cm^{-3}	T_e K	EM cm^{-6} pc	τ_{325}	size θ arcmin	Beam dilution
1	2	3	4	5	6	7	8	9	10
G 2.3+0.2	0.48 (12)	18 (5)	20		3700	4.2 E+04	0.6	3.6	0.005
G 4.4+0.2	0.39 (09)	66 (13)	90		5700	6.7 E+04	6.5	4.2	0.006
G 6.0−1.2 M 8	1.10(20)	43 (4)	50	370	7700	3.4 E+05	2.0	4.5	0.006
G 7.0−0.3 M 20	0.63 (13)	30 (6)	30	143	7500	7.7 E+04	0.4	5.7	0.008
G 8.1+0.2	0.64 (12)	47 (7)	60		6500	4.7 E+05	3.0	2.9	0.004
G 10.2−0.3 W 31	0.77 (13)	51 (4)	65	356	5700	1.0 E+06	7.0	3.1	0.004
G 12.8−0.2 W 33	0.72 (13)	32 (4)	35	1774	7900	4.8 E+06	23.0	0.8	0.001
G 14.0−0.1	1.00(20)	38 (3)	45		5800	8.4 E+04	0.6	3.3	0.005
G 15.1−0.7 M 17	0.67 (12)	41 (5)	50	581	9100	1.8 E+06	7.0	9.1	0.076
G 16.9+0.7 M 16	0.73 (11)	53 (3)	70		6100	6.9 E+04	0.5	8.1	0.067
G 20.7−0.1	0.45 (11)	19 (6)	15	96	5900	7.4 E+04	0.5	4.5	0.006
G 24.8+0.1 W 42	1.00(15)	77 (4)	100	51	5800	2.8 E+04	0.2	5.0	0.007
G 25.4−0.2 3 C385	0.49 (10)	77 (15)	100	224	7100	2.9 E+05	2.0	3.2	0.004
	0.27 (10)	26 (11)	30						
G 27.3+0.2	0.98 (16)	85 (6)	120		7400	8.6 E+04	0.4	2.9	0.004
G 28.8+3.5 W 40	0.27 (05)	35 (4)	40	273	8500	1.2 E+05	0.5	5.8	0.008
	0.36 (06)	44 (4)	55						
G 29.9+0.0	1.00(20)	35 (4)	40	> 111	6100	1.7 E+05	1.0	4.3	0.006
G 30.8+0.0 W 43	1.20(20)	41 (3)	50	205	6000	5.2 E+05	4.0	5.5	0.008
G 35.1−1.6 W 48	0.61 (11)	55 (6)	70	> 20	7250	1.5 E+04	0.08	5.3	0.007
G 37.8−0.2 W 47	0.31 (09)	33 (11)	35	> 130	8400	5.8 E+04	0.3	2.9	0.004
	0.76 (09)	49 (7)	60						
	0.68 (09)	17 (3)	5						
G 49.0−0.3 W 51B	0.86 (11)	23 (4)	10	87	9000	1.2 E+05	0.5	7.0	0.058
G 206.0−2.1 W 16	0.40(20)	28 (5)	20	18	6000	8.6 E+03	0.06	55	0.46

Parameters for the HII regions are taken from the high-frequency measurements of Shaver & Goss (1970b), Silverglate & Terzian (1979), Viner, Vallée & Hughes (1979), and Downes *et al.* (1980)

of pressure broadening and beam dilution. Most of these HII regions have been studied elsewhere using both the continuum and high-frequency recombination lines. The electron density, temperature and emission measure obtained from such studies, if they are available, are given in columns 5, 6 and 7 of Table 5. The upper limit on the electron density of the gas responsible for the H 272α lines obtained from their observed widths are given in column 4. From a comparison of columns 4 and 5 of this table, it is clear that, with the exception of one or two sources, the HII regions themselves cannot be responsible for the observed H 272α lines. Column 8 of the table shows that most of these HII regions are optically thick at 325 MHz and for this reason too they are unlikely to produce the observed recombination lines. Further, for most of these sources the beam dilution factor is 10^{-2}–10^{-3} (column 10) due to the 2° × 6 arcmin antenna beam used in these observations which is much larger than the few arcmin sizes of these sources (column 9). The beam dilution will reduce the intensity of the already weakened lines (due to pressure broadening and optical depth) to practically undetectable levels. Therefore, the observed H 272α lines in these directions *must* arise in some gas other than the HII regions.

We first compare the location of this gas with respect to the HII regions, as implied by the observed velocities. In column 3 of Table 6 we have given the observed velocity of the H 272α line and in column 4, that of a high-frequency line. There is generally a very good agreement between the two velocities, particularly if we take into account the errors in their determination (they are 2–5 km s^{-1} for both). In any case there is always a substantial emission of the H 272α line at the velocity of the high frequency line. This immediately implies that the lower-density gas responsible for the H 272α line is associated with the HII region. The most reasonable picture for this association is that the low-density gas forms the outer envelope of the dense HII region responsible for the observed high-frequency lines and the continuum.

The picture that emerges therefore is that the HII regions which are prominent in the continuum (having densities of 10^2 – 10^4 cm^{-3}), and which produce most of the observed high-frequency recombination lines, have low-density envelopes which can give rise to low-frequency recombination lines. The high-density cores make practically no contribution to the low frequency lines. There is observational support for the above picture. In a classic paper, Brocklehurst & Seaton (1972) showed that in order to explain the observed line-to-continuum ratio as a function of frequency it is necessary to use models of HII regions which contain extensive outer regions of low density. Hart & Pedlar (1976a) have observed H 166α line emission from 13 positions near the HII region W 3 and conclude that there is an extended low-density region associated with this object.

Based on such a model, we shall now derive or put constraints on the parameters of the low density envelopes from the observed intensity of the H 272α line.

4.2 *Electron Temperature of the Low-Density Envelopes*

The temperature of the low-density envelopes of HII regions is unlikely to be very different from that of the cores. The temperature of a fully ionized region is basically governed by the abundance of heavy elements like oxygen, nitrogen, neon *etc.* (Osterbrock 1974). The electron temperature depends only weakly on the effective temperature of the exciting star or stars and the density of the gas. Since the core and the

outer envelope were presumably parts of the same cloud, the abundance of heavy elements in them is unlikely to be very different. If the exciting star for the outer envelope is embedded in the core, then a case can be made for the outer envelope to be at a somewhat higher temperature. This is because there will be a hardening of the radiation emerging after ionization of the core, which will on the average impart a slightly higher kinetic energy to the electrons liberated in the outer regions. On the other hand, the lower density in the outer regions can slightly reduce the collisional de-excitation of the coolant ions (OII, OIII *etc)* thereby increasing the efficiency of the cooling process. The actual temperature will therefore depend on the relative importance of these two processes. If the exciting star is in the outer region itself, then only the second argument applies and the resulting temperature can be somewhat lower than that of the core.

For our purposes, it is reasonable to assume that the electron temperature of the low-density envelope is essentially the same as that of the core. These temperatures for each of the HII regions is given in column 6 of Table 5. Most of these temperatures are derived from the H 110α measurements by Downes *et al.* (1980), on the assumption of LTE.

4.3 *Electron Density and Emission Measure*

We have used an isothermal, uniform density model (Fig. 6) similar to the one used for the case of blank regions and SNR directions. The difference here is that the high-density core of the HII region is embedded inside the low-density region responsible for the H 272α line. This can have two effects. The continuum radiation from the core can cause stimulated emission of there combination line in the lower-density gas in front of it. Secondly, if the core is optically thick at this frequency, then it can block the line emission originating from behind it. However, the angular sizes of these HII regions (5 arcmin) are very small compared to the 2° × 6 arcmin beam used for observations, and therefore their contribution to the continuum temperature is, in most cases, negligible compared to the nonthermal galactic background which is nearly uniform over the beam. We can therefore neglect to first order both the above effects.

The expected H 272α line brightness temperature is given by Equations (10) and (1). For nearby HII regions, the background temperature T_0 was taken to be equal to the

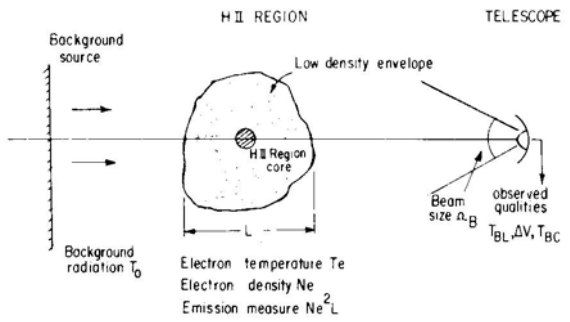

Figure 6. Schematic of the model for interpreting recombination lines observed towards HII regions. High-frequency recombination lines arise mainly from the central core which is also prominent in the radio continuum. The low-frequency line originates in the outer envelope.

observed continuum brightness temperature T_{BC} listed in Table 6. For those HII regions which are known to be at the far kinematic distance, T_0 was calculated using

$$T_0 = (T_{BC} - T_{HII})/2 + T_{HII}$$

where T_{HII} is the beam averaged brightness temperature of the HII region core calculated using its T_e, N_e, EM and its angular size θ derived from high frequency measurements (see Table 5). in the case of the HII region W 16 (the Rosette nebula) we have used $T_0 = 0$ .since it is in the anticentre direction in addition this source is known to be of low density (10–15 cm^{-3}) and large angular size (~ 1^o). Therefore the observed H 272α line can originate from the HII region itself. We have used $T_N = 0$ for all the cases.

We have calculated the emission measure for densities in the range 0.1–100 cm^{-3} necessary to produce the observed intensity of the H 272α recombination line towards each of the 19 HII regions. We have used the electron temperatures derived from high-frequency measurements (Table 5). The calculations were carried out using beam dilution factors of 0.3 and 0.6. The above calculations were not carried out for 11 of the

Table 6. Velocity, background temperature and derived parameters of HII regions.

						Derived parameters		
Source	T_{BC} K	V_{LSR} H 272α km s^{-1}	V_{LSR} H110α km s^{-1}	Distance kpc	T_0 K	N_e cm^{-3}	EM cm^6 pc	L pc
1	2	3	4	5	6	7	8	9
G 2.3 + 0.2	750	9 (2)	5	...	375	...	....	...
G 4.4 + 0.2	700	4 (5)	5.7	17.0	350	1.8	1100	356
G 6.0 − 1.2	660	−4 (1)	3.0	1.4	660	15	7000	29
G 7.0 − 0.3	720	6 (2)	14	1.5	720	7.5	1700	31
G 8.1 + 0.2	770	25 (3)	22	...	770	...	....	...
G 10.2 − 0.3	610	15 (2)	13	9.0	300	3.6	2800	188
G 12.8 − 0.2	730	26 (2)	30	4.4	730	4	1500	92
G 14.0 − 0.1	680	24 (2)	31.5	4	680	4	1600	84
G 15.1 − 0.7	810	9 (2)	11.5	2.4	810	8	3000	50
G 16.9 + 0.7	610	20 (1)	28	2.2	610	7.5	2600	46
G 20.7 − 0.1	590	47 (3)	57	13.8	300	1.1	380	290
G 24.8 + 0.1	660	83 (2)	107	9	330	4	3500	186
G 25.4 − 0.2	650	54 (6) 107 (5)	59	13.2	340	2	1100	276
G 27.3 + 0.2	640	93 (2)	33	15.2	320	4	4800	318
G 28.8 + 3.5	450	72 (2) 19 (2)	0.7	0.7	450	15	3500	15
G 29.9 + 0.0	650	91 (2)	98.5	9	330	3.5	2500	189
G 30.8 + 0.0	830	95 (1)	90	7.1	830	3	1500	149
G 35.1 − 1.6	460	34 (3)	43	3.2	460	7	3500	67
G 37.8 − 0.2	480	0.3 (5) 44 (3) 87 (1)	61	11.5	250	4.8	5500	241
G 49.0 − 0.3	690	61 (2)	60.5	6.6	690	3.1	1400	138
G 206.0 − 2.1	100	5 (2)	7(3)	1.4	0	11	4000	29

Distances are taken from Downes *et al.* (1980) or Radhakrishnan et *al.* (1972)

30 HII regions (towards which H 272α line was detected) either because the velocity did not match that of the high-frequency line, or the distance to the HII region was unknown.

The results of these calculations are shown for two of the HII regions (M 20, M 16) in Fig. 7. The two curves marked 272 (0.3) and 272 (0.6) in the figure shows the required emission measure, as a function of electron density, to produce the observed H 272α line intensity, if the beam dilution factor is 0.3 and 0.6, respectively.

It is reasonable to assume that the extent of the envelope along the line of sight is comparable to its linear size in the perpendicular direction, obtained using a source size of 0°.6 to 1°.2 (*i.e.* a dilution factor of 0.3 to 0.6 in east-west) and known distances. We thus impose the restriction that the emission measure and electron density of the gas be related by

$$EM = N_e^2 L_\perp$$

where $L_\perp$ is the size of the line-emitting region perpendicular to the line of sight given by

$$L_\perp = dD\theta_\alpha$$

where d is the distance to the HII region, θ_α is the east-west beam of the telescope, and D is the beam dilution factor. The region is assumed to fill the beam in the north-south direction *(i.e.,* the angular extent of the gas is > 6 arcmin).

The two inclined straight lines marked L (0.3) and L (0.6) in Fig. 7 shows the above restriction on the density and emission measure of the region for beam dilution factors 0.3 and 0.6 respectively. The intersection of these lines with the corresponding curves marked 272 (0.3) and 272 (0.6) define the emission measure and electron density of the envelope from which the H 272α line is observed. As can be seen from Fig. 7, the derived electron density N_e increases with decreasing beam dilution factor D. The upper limit on N_e obtained from the width of the H 272α line implies a lower limit of 0.2 for the beam dilution factor.

The electron density, emission measure and the path length through the gas obtained assuming the most probable beam dilution factor of 0.6, are given in Table 6. If the

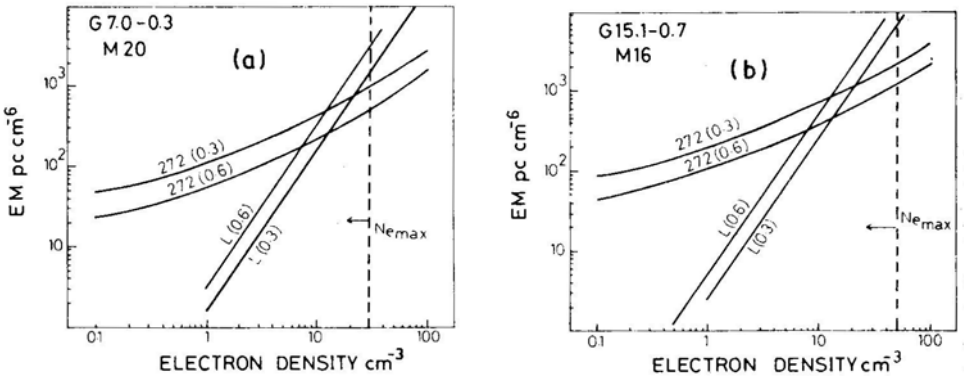

Figure 7. Constraints on the emission measure and electron density of the low-density envelopes of HII regions (a) M 20 and (b) M 16, based on the observed intensity of H 272α lines and geometrical considerations (see text). The vertical dashed line is the upper limit on the electron density implied by the width of the line.

dilution factor D is greater than 0.6 by some factor, then the derived densities will be lower by nearly the same factor. The densities are in the range 1–10 cm^{-3}, emission measures are in the range 1000–4000 pc c m^{-6} and the corresponding path lengths through the regions are 30–300 pc. The temperatures of these are assumed to be the same as those of the cores which are in the range 5000–9000 K.

5. Discussion of the derived parameters

5.1 *Blank Regions and SNRs*

An examination of Tables 2 and 4 reveals that the parameters characterizing the ionized gas towards SNRs and blank areas in the galactic plane are quite similar. The regions responsible for the observed lines have densities in the range of 1–6 cm^{-3}, their temperatures are greater than a few thousand degrees but less than about 8000 K, and they have emission measures of 500 to 3000 cm^{-6} pc. The corresponding path lengths through the gas arc in the range 50–200 pc. The similarity is not surprising since the gas which is observed in these directions (SNRs and blank regions) is the same as that responsible for galactic ridge recombination lines observed at centimetre wavelengths. Any phenomenon that is as widespread and uniform as the galactic ridge recombination lines must have some very general explanation.

The parameters derived here account for the observed strength of the galactic ridge recombination lines, and the high-frequency recombination lines towards SNRs. This is necessarily true since we have made use of these lines to constrain the parameters. They account for most of the 80 MHz continuum optical depth observed by Dulk & Slee (1975). The gas can possibly also account for the background thermal emission seen in the galactic plane.

The parameters characterizing the gas responsible for the galactic ridge recombination lines and the lines towards supernova remnants have been a topic of discussion in the literature since the first observations by Gottesman & Gordon (1970). Shaver (1976) has made the most comprehensive study of the available data on these lines. Combining this data with the few low-frequency (408 and 386 MHz) recombination line measurements then available (Pankonin *et al.* 1974; Pankonin 1975; Gordon *et al.* 1974) he has concluded that the lines arise in HII regions having electron densities 5–10 cm^{-3}, diameters of 20–200 pc and emission measures of 2000–4000 cm^{-6} pc. He favours temperatures of the order of 5000 K. Lockman (1980) has analysed the H 166α data near $l = 36^{o}$ and concludes that the gas responsible for the line emission has a temperature of 1000 K, an emission measure of a few hundred cm^{-6} pc and a density of 1 cm^{-3}.

The parameters derived by us for the line-emitting gas in the direction of SNRs and blank regions are consistent with an interpretation in terms of high-temperature, moderate-density (1–10 cm^{-3}) regions. Our results are very similar to those of Shaver (1976) who also used low-frequency recombination lines for deriving the parameters. In fact the technique adopted by us is similar in many ways to that of Shaver (1976). Although we cannot quantitatively estimate the temperature of the gas, we also favour higher temperatures (a few thousand degrees) based on considerations of pulsar dispersion measure and geometry of the line-emitting region.

Based on these results alone it is not possible to decide the origin of this gas. With the small path lengths of 50–200 pc derived for these regions, they can not be regarded as some component of the general interstellar medium; the average path length through the Galaxy at these longitudes is ~ 20 kpc. This gas could be in the form of a number of small low-density HII regions, low density envelopes of bright HII regions seen in the galactic plane or some other kind of ionized gas produced in localized regions of the interstellar medium. This question will be addressed to in a subsequent paper.

5.2 *H II Regions*

The density and emission measure derived by us for the gas responsible for the observed H 272α recombination lines towards HII regions are about a factor of 10–100 (in most cases more likely 100) less than that of conventional HII regions. There are only a very few low-frequency recombination line observations towards HII regions available in the literature to compare with our results (*e.g.,* Gordon *et al.* 1974; Pankonin *et al.* 1974; Parrish *et al.* 1977; Pedlar *et al.* 1978).

Parrish *et al.* (1977), based on 300 MHz observations towards W 51B, find that this line arises in a region of density < 30 cm^{-3} and has an angular size 25 arcmin. They also argue that this low-density gas is associated with the discrete source W 5I B, due to the observed similar velocities of high and low-frequency lines. This is in fact the argument we have used as a starting point for deriving the parameters. Pedlar *et al.* (1978) interpret their low-frequency observations towards the galactic centre in terms of low-density gas with N_e ~ 10 cm^{-3}. They note that any single component model requires that the electron density be ~ 10 cm^{-3} (irrespective of *EM* and T_e) to account for the low-frequency lines towards the galactic centre. The parameters derived by us are quite consistent with these results.

There is at least one HII region (W 16, the Rosette nebula) in our survey (Paper I) which is known to be large and of low density for which we can directly compare the parameters derived by us with those from high-frequency measurements. We obtain a density of 11 cm^{-3} and *EM* of 4000 pc cm^{-6} which are consistent with the parameters (N_e = 9 cm^{-3}, *EM* = 2600 pc cm^{-6}) derived by Pedlar & Matthews (1973) using the H 166α line, and by Viner, Vallée & Hughes (1979) (N_e = 16 cm^{-3}) using the H 100α recombination line.

A comparison of the parameters for the low-density envelopes of conventional HII regions derived here and those for the regions responsible for the lines observed towards blank regions and SNRs reveals that they are very similar. As the lines observed towards SNRs and blank regions are attributed to the gas responsible for the galactic ridge recombination lines, the above similarity immediately suggests that the latter may also arise in low-density extended envelopes of HII regions seen in the galactic plane. This suggestion will be pursued further in a subsequent paper (Anantharamaiah 1985b) where it will in fact be shown that most of the galactic ridge recombination lines do arise in the extended envelopes of conventional HII regions prominent in the radio continuum surveys. HII regions are so numerous in the inner part of the Galaxy that given the kind of low-density envelopes suggested by the analysis in this paper, they intersect practically every line of sight in the galactic ridge having $l \leqslant 40°$, thereby giving rise to recombination lines in every direction within this range.

Acknowledgements

I thank Rajaram Nityananda, Dipankar Bhattacharya, G. Srinivasan and V. Radhakrishnan for many useful discussions and Peter Shaver for critical comments. I also thank W. M. Goss for useful comments on the manuscript.

This paper is based on a part of the doctoral thesis submitted to the Bangalore University.

References

Altenhoff, W. J., Downes, D., Goad, L., Maxwell, A., Rinehart, R. 1970, *Astr. Astrophys. Suppl.*, **1**, 319.
Altenhoff, W. J., Downes, D., Pauls, T., Schraml, J. 1978, *Astr. Astrophys. Suppl.*, **35**, 23.
Anantharamaiah, K. R. 1985a, *J. Astrophys. Astr.*, **6**, 177, (Paper 1).
Anantharamaiah, K. R. 1985b, In preparation.
Bignell, R. C. 1973, *Astrophys. J.*, **186**, 889.
Brocklehurst, M., Leeman, S. 1971, *Astrophys. Lett.*, **9**, 35.
Brocklehurst, M., Salem, M. 1977, *Computer Phys. Commun.*, **13**, 39.
Brocklehurst, M., Seaton, M. J. 1972, *Mon. Not. R. astr. Soc.*, **157**, 179.
Brown, R. L., Lockman, F. J., Knapp, G. R. 1978, *A. Rev. Astr. Astrophys.*, **16**, 445.
Cesarsky, D. A., Cesarsky, C. J. 1973a, *Astrophys. J.*, **183**, L143.
Cesarsky, D. A., Cesarsky, C. J. 1973b, *Astrophys. J.*, **184**, 83.
Clark, D. H., Caswell, J. L. 1976, *Mon. Not. R. astr. Soc*, **174**, 267.
Downes, D., Wilson, T. L. 1974, *Astr. Astrophys.*, 34, 133.
Downes, D., Wilson, T. L, Bieging, J., Wink, J. 1980, *Astr. Astrophys. Suppl.*, **40**, 379.
Dulk, G. A., Slee, O. B. 1972, *Aust. J. Phys.*, **25**, 429.
Dulk, G. A., Slee, O. B. 1975, *Astrophys. J.*, **199**, 61.
Gordon, K. J., Gordon, C. P., Lockman, F. J. 1974, *Astrophys. J.*, **192**, 337.
Gordon, M. A., Brown, R. L., Gottesman, S. T. 1972, *Astrophys. J.*, **178**, 119.
Gordon, M. A., Cato, T. 1972, *Astrophys. J.*, **176**, 587.
Gordon, M. A., Gottesman, S. T. 1971, *Astrophys. J.*, **168**, 361.
Gottesman, S. T., Gordon, M. A. 1970, *Astrophys. J.*, **162**, L93.
Griem, H. R. 1967, *Astrophys. J.*, **148**, 547.
Hart, L., Pedlar, A. 1976a, *Mon. Not. R. astr. Soc.*, **176**, 135.
Hart, L., Pedlar, A. 1976b, *Mon. Not. R. astr. Soc*, **176**, 547.
Haynes, R. F., Caswell, J. L., Simons, L. W. J. 1978, *Aust. J. Phys. Astrophys. Suppl.*, **45**, 1.
Jackson, P. D., Kerr, F. J. 1971, *Astrophys. J.*, **168**, 29.
Jackson, P. D., Kerr, F. J. 1975, *Astrophys. J.*, **196**, 723.
Lockman, F. J. 1976, *Astrophys. J.*, **209**, 42.
Lockman, F. J. 1980, in *Radio Recombination Lines*, Ed. P. A. Shaver, D. Reidel, Dordrecht, p. 185.
Mebold, U., Altenhoff, W. J., Churchwell, E, Walmsley, C. M. 1976, *Astr. Astrophys.*, **53**, 175.
Oster, L. 1961, *Rev. Mod. Phys.*, **33**, 525.
Osterbrock, D. E. 1974, *Astrophysics of Gaseous Nebulae*, Freeman, San Francisco.
Pankonin, V.1975, *Astr. Astrophys.*, **38**, 445.
Pankonin, V., Parrish, A., Terzian, Y. 1974, *Astr. Astrophys.*, **37**, 411.
Parrish, A., Conklin, E. K., Pankonin, V. 1977, *Astr. Astrophys.*, **58**, 319.
Pedlar, A., Davies, R. D. 1980, in *Radio Recombination Lines*, Ed. P. A. Shaver, D. Reidel, Dordrecht, p. 171.
Pedlar, A., Davies, R. D., Hart, L., Shaver, P. A. 1978, *Mon. Not. R. astr. Soc*, **182**, 473.
Pedlar, A., Matthews, H. E. 1973, *Mon. Not. R. astr. Soc*, **165**, 381.
Radhakrishnan, V., Goss, W. M., Murray, J. D., Brooks, J. W. 1972, *Astrophys. J. Suppl. Ser.*, **24**, 49.
Salem, M., Brocklehurst, M. 1979, *Astrophys. J. Suppl.*, **39**, 633.
Shaver, P. A. 1975, *Pramana*, **5**, 1.

Shaver, P. A. 1976, *Astr. Astrophys.*, **49**, 1.
Shaver, P. A., Goss, W. M. 1970, *Aust. J. Phys. Astrophys. Suppl.*, **14**, 133.
Silvergate, P. R., Terzian, Y. 1979, *Astrophys. J. Supp.*, **39**, 157.
Spitzer, L. 1978, *Physical processes in the Interstellar Medium*, Wiley-Interscience, New York.
Viner, M. R., Vallée, J. P., Hughes, V. A. 1979, *Astr. J.*, **84**, 1335.
Vivekanand, M., Narayan, R. 1982, *J. Astrophys. Astr.*, **3**, 399.
Wilson, T. L. 1980, in *Radio Recombination Lines*, Ed. P. A. Shaver, D. Reidel, Dordrecht, p. 205

J. Astrophys. Astr. (1985) **6**, 227–231

Far Infrared Emission from three New Planetary Nebulae

K. V. K. Iyengar *Tata Institute of Fundamental Research, Homi Bhabha Road, Bombay 400005*

Received 1985 June 11; accepted 1985 August 19

Abstract. As dust emission in the far infrared (FIR) is a characteristic property of planetary nebulae we searched the Infrared Astronomical Satellite (IRAS) point-source catalogue for confirmatory evidence on the two new possible planetary nebulae S 68 and 248 – 5 identified by Fesen, Gull & Heckathorn (1983) and the high-excitation planetary nebula 76 + 36 detected by Sanduleak (1983). We identify the nebulae 248 –5 and 76 + 36 with IRAS sources 07404 – 3240 and 17125 + 4919, respectively and have determined their dust temperature, total FIR emission and optical depth. We also set a lower limit ranging in value from 1.2×10^{-6} to 3.7×10^{-5} for $M_{\rm dust}/M_{\odot}$ of the nebula 248 – 5 depending on whether its grain material is silicate or graphite. S 68 could not be identified with an IRAS source.

Key words: planetary nebulae, dust temperature—planetary nebulae, optical depth—planetary nebulae, far infrared flux

1. Introduction

Most of the galactic planetary nebulae (PNe) with large angular sizes are now believed to be identified through careful searches of Palomar Observatory Sky Survey (POSS). The few that could have been still missed (Weinberger *et al.* 1983) are likely to be due to planetaries of either large angular size with very low surface brightness, or nebulae of very high excitation which appear extremely faint on the POSS prints due to their emitting very strongly in [OIII] $\lambda\lambda$ 4959,5007 lines where the POSS O and E emulsions are relatively insensitive.

Parker, Gull & Kirshner (1979) carried out a deep, wide-field and low-resolution photographic emission-line survey of the galactic plane. Employing a wide-field camera and narrow passband interference filters, they recorded the galactic plane in [OIII] λ 5007, Hα+ [NII] λ 6570, SII λ 6736, H β 4861 and λ 4225 continuum emissions. Fesen, Gull & Heckathorn (1983) searched these plates for objects particularly strong in [OIII] emission which had not been identified till then or had uncertain classifications. Since the survey recorded emission at very faint levels ([OIII] emission measure ~100 pc cm^{-6}), using a relatively small plate scale and low angular resolution Fesen, Gull & Heckathorn (1983) were able to notice only fairly large and bright nebulae. From the very strong [OIII] emission, symmetrical morphology and the presence of faint blue central stars, Fesen, Gull &Heckathorn (1983) suspected S 68 and an anonymous nebula 248 – 5 to be planetary nebulae.

Sanduleak (1983) detected a new, resolved high excitation planetary nebula (1950 coordinates: $\alpha = 17^{\rm h}\ 12^{\rm m}.5$, $\delta = +\ 49°\ 19'$, $1 = 75°.8$, $b = +\ 35°.8$) containing a 14

magnitude O-type central star on objective prism plates taken for the low-dispersion Northern Sky Survey (Pesch & Sanduleak 1983). The nebula was first detected by its strong emission in [OIII] $\lambda\lambda$ 5007, 4959 lines on the spectrum obtained using an objective prism on Kodak IIIa-J plate. A 45 minute exposure, on a Kodak 103a-F plus GG 455 filter combination plate at a dispersion of 1000 Å mm^{-1} at H_α showed that the (OIII) $\lambda\lambda$ 5007, 4959 emission was stronger than the emission of H_α possibly blended with [N II] $\lambda\lambda$ 6548 and 6584. Their objective prism observations thus indicated a high-excitation planetary containing a central star of moderate brightness with a very strong ultraviolet continuum.

The strong [OIII] lines of 4959 and 5007 arise from transitions between the metastable levels of the ground state electron configuration of $O^{+\ +}$ formed in the plasma either around newly formed young stars or around the central stars of planetary nebulae. They thus serve to identify gaseous nebular regions in the sky. In these plasma dust is intimately mixed with ionized gas and is heated by Lyman α radiation (produced as the end product of recombinations in hydrogen) as well as Lyman continuum photons and photons longward of the Lyman α The dust so heated generally has a characteristic temperature of 60–200 K (see Pottasch 1984) and emits in the far infrared. The availability of the IRAS (Infrared Astronomical Satellite) point source catalogue now enables one to seek confirmatory evidence in the far infrared for the presence of such nebulae by identifying them with sources of FIR and to determine their other physical properties such as temperature and mass of dust *etc*. The field of view of the IRAS survey bands at 12, 25, 60 and 100 μm is 0.75 × 4.5, 0.75 × 4.6, 1.5 × 4.7 and 3.0 × 5.0 $arcmin^2$ and happens to be much larger than the sizes of many planetary nebulae (PN). Thus most of the PN appear as point sources to the IRAS photometric survey instrument and should appear listed in the point source catalogue if emitting in far infrared (FIR). We therefore undertook a search of the IRAS point source catalogue (Beichman *et al.* 1985) to identify and to derive information on the dust in these nebulae.

2. Analysis of data, results and discussion

We present in Table 1 data on two of the three nebulae which could be identified with sources in the IRAS catalogue. Listed columnwise in Table 1 are (1) the name of the nebula and its galactic co-ordinates, the IRAS number of the source with which it is identified, (2) its right ascension and declination, (3) the angular size of the source and its distance, (4) the flux densities in the four IRAS photometric survey bands, and (5) the dust temperature, total FIR flux, optical depth at 25 μm and $M_{dust}/M_\odot$ of the nebula determined from this work.

248 – 5 has been detected by IRAS. Definite values are available for its flux density in the 25 and 60 μm bands although the quality of the measurement in the 25 μm band is moderate (flux uncertainty $\gtrsim$ 20 per cent). The data from IRAS catalogue under the heading 'confusion' indicates that this is the only source in the IRAS window at 100 μm. But the cirrus contribution at 100 μm is rather significant. Also 3 small extended sources are detected in the IRAS windows at 25 and 60 μm at this source position. It is well known that planetary nebulae contain density condensations and it is quite likely that the 3 small extended sources detected by IRAS are all density condensations of the same nebula 248 – 5. This nebula has a size 130 × 180 $arcsec^2$, larger than many

Table 1. FIR data on new planetary nebulae.

Name Designation IRAS No.	R. A. (1950)	Dec (1950)	Angular size (arcsec) Distance (kpc)	Flux Density[d] (Jy) 12 μm 25 μm 60 μm 100 μm	Dust Temp (K) Total FIR flux (Wm^{-2}) Optical depth $M_{dust}/M_{\odot}$
248 – 5	$07^h\ 40^m\ 28^s.9$	$-32°\ 40'\ 42''$[a]	130×180[a]	0.26L	85
247.56 – 4.73	07 40 28.8	–32 40 29[c]	1.38	0.26:	9×10^{-14}
07404 – 3240[c]				1.10	2.4×10^{-7}
				2.55L	$(1.2 - 37) \times 10^{-6}$
76 + 36	17 12.5	+49 19[b]	13[b]	0.35L	~ 120[e]
75.8 + 35.8	17 12 30.6	+49 19 20[c]		0.27	$\lesssim 5 \times 10^{-14}$
17125 + 4919[c]				0.64L	$\sim 4 \times 10^{-6}$
				1.00L	

Notes:
a) Data from Fesen *et al.* (1983).
b) Data from Sanduleak (1983); the nebula is circular and the tabulated value is the diametrical size.
c) Data from IRAS point source catalogue.
d) L in column 4 indicates the quoted flux is an upper limit; and: indicates that the quality of measurement is moderate.
e) Estimated assuming the flux density to peak at 25 μm, being the only wavelength band for which we have a definite value for the observed flux density.

planetary nebulae, raising doubts as to its identification (Fesen, Gull & Heckathorn, 1983) as a planetary nebula. However, planetary nebulae with radial sizes > 100 arcsec are not uncommon (see Appendix 1, Pottasch 1984) and cannot by itself be used to question its classification.

From the observed flux densities at 25 and 60 μm we determine a colour temperature of ~ 85 K for the dust radiating in the far infrared and a value of ~ 9×10^{-14} Wm^{-2} for the total flux at earth (in the 4–300 μm interval) and 2.4×10^{-7} for its optical depth at 25 μm.

We use the expression

$$M_{\text{dust}} = \frac{4}{3}\frac{a\rho}{Q_{\nu}(\text{abs})}\frac{\mathrm{d}^2 F_{\nu}}{B_{\nu}(T)}$$

(see formula VIII-5, Pottasch 1984) to estimate the mass of dust (radiating in FIR) in the nebula. We assume Q_v at frequency ν is proportional to a, the radius of dust grains, and use of a value of $a\rho/Q_{30\mu\text{m}}$ (abs) $\simeq 1.5 \times 10^{-3}$ for silicate materials and 5×10^{-2} for small graphite grains (Pottasch 1984) and use values of F_v and B_v (T) at 25μm to evaluate the mass of dust in the nebula. F_v and B_v are the FIR flux density and Planck function in frequency units at frequency v, respectively and T, ρ and Q_v (abs) are the temperature, specific density and absorption efficiency of the grains, respectively d is the distance to the nebula. Using for d the maximum distance of the nebula viz., 1.38 kpc (see Fesen *et al.* 1983) we obtain for $M_{\text{dust}} \simeq 1.2 \times 10^{-6}\ M_{\odot}$ to $3.7 \times 10^{-5}\ M_{\odot}$ depending upon whether the grain materials are silicate or graphite.

A definite value is available only at 25 μm for the flux density of the IRAS source 17125 + 4919 identified with the planetary nebula 76 + 36 discovered by Sanduleak (1983). We have only upper limits to the flux densities at 12, 60 and 100 μm. Assuming the FIR emission from the source to have its peak flux density at 25 μm we assign a temperature of ~ 120 K for the dust. We estimate the total FIR flux from the nebula to be ~ 5×10^{-14} Wm^{-2}, and its optical depth at 25 μm to be ~ 4×10^{-6}.

A search of the IRAS point source catalogue for the FIR counterpart of the nebula S 68 within a radius of 10 arcmin (twice the size of the observing aperture along the direction of its maximum dimension) centred on its optical position did not result in any identification. If this source is an H II region or a planetary nebula it seems to be fainter than the sensitivity limits of detection of the IRAS photometric survey.

Compact H II regions can sometimes be mistaken for planetary nebulae (because of similar sizes). Some of the properties (in the infrared) that can be used to distinguish H II regions from PNe are their, (i) infrared excess, IRE (defined as the ratio of the infrared flux density to the flux density of Lyman-α-radiation produced in the nebula), (ii) dust to ionized gas mass ratio, M_d/M_g and (iii) dust temperature.

The IRE of H II regions is ~ 14 (Panagia 1976) as against an IRE $\lesssim 3$ (see Table 3 of Barlow 1983; Table 2 of Pottasch 1984; and Table 2 of Pottasch *et al.* 1984). M_d/M_g values of H II regions are ~ 10^{-2} as against ~ 5×10^{-4} for PNe (see Table VIII-1; Pottasch 1984, and Pottasch *et al.* 1984). The dust temperature of H II regions covers an extremely wide range (from several hundred degrees to tens of degrees) depending on the wavelength bands of observation, compared to ~ 120 ± 60 K for PNe.

The available infrared data on nebulae (under discussion here) are rather scanty and cannot be decisive in confirming their identification. However, the dust temperatures of the nebulae 248 – 5 and 76 + 36 are consistent with their identification (Fesen, Gull & Heckathorn 1983; Sanduleak 1983) as PNe. Also, the mass of dust in 248 – 5 is typical

of mass of dust in PNe (assuming typical values of $M_d/M_g \sim 5 \times 10^{-4}$ and ionized gas mass $M_g/M_\odot \sim 5 \times 10^{-2}$ for PNe).

3. Conclusions

We identity the new planetary nebulae 248 –5, and 76 + 36 with the IRAS sources 07404 – 3240 and 17125 + 4919, respectively. We determine the dust temperature of the nebula 248 – 5 as ~ 85 K and its total FIR emission and optical depth as $\sim 9 \times 10^{-14}$ Wm^{-2} and 2.4×10^{-7} . We also estimate M_{dust} in the nebula to have a value $(1.2 – 37) \times 10^{-6}$ $M_\odot$. We assign a temperature of ~ 120 K to dust in nebula 76 + 36 emitting in FIR and estimate its total FIR flux and optical depth to be $\lesssim 5 \times 10^{-14}$ and $\sim 4 \times 10^{-6}$ respectively.

The temperature of dust in these two nebulae are similar to those of other planetary nebulae. Also their optical depths are similar to those of other faint planetary nebulae (*viz*., $\lesssim 10^{-5}$). Thus the FIR data from IRAS on these two objects support their identification as planetary nebulae.

Acknowledgements

We thank Professor K. S. Krishna Swamy for useful discussions.

References

Barlow, M. J. 1983, in *IAU Symp.* 103: *Planetary Nebulae*, Ed. D. R. Flower, D. Reidel, Dordrecht, *p*, 105.

Beichman, C, A., Neugebaucr, G., Habing, H. J., Clegg, P. E., Chester, T. G. 1985, *Infrared Astronomical Satellite* (*IRAS*) *Catalogue and Atlases.*

Fesen, R. A., Gull, T. R., Heckathorn, J. N. 1983, *Publ. astr. soc. Pacific*, **95**, 614.

Panagia, N. 1976, in *Infrared and Submillimetre Astronomy*, Ed. G. Fazio, D. Reidel, Dordrecht, p. 43.

Parker, R. A. R., Gull., T. R., Kirshner, R. P. 1979, *An Emission Line Survey of the Milky Way* (NASA-SP 434).

Pesch, P., Sanduleak. N. 1983, *Astrophys. J, Suppl.*, **51**, 171.

Pottasch, S. R. 1984, *Planetary Nebulae*, D. Reidel, Dordrecht.

Pottasch, S. R., Baud, B., Beintema, D., Emerson, J., Habing, H. J., Harris, S., Houck, J., Jennings, R., Marsden, P. 1984, *Astr. Astrophys.*, **138**, 10.

Sanduleak, N. 1983, *Publ. astr. soc. Pacific*, **95**, 619.

Weinberger, R., Dengel, J., Hartl, H.. Sabbadin, F. 1983, *Astrophys. J.*, **265**, 249.

J. Astrophys. Astr. (1985) **6,** 233–237

Has the Crab Pulsar Magnetic Field Grown after its Birth?

D. Bhattacharya *Joint Astronomy Programme, Indian Institute of Science, Bangalore 560012*
C, S. Shukre *Raman Research Institute, Bangalore 560080*

Received 1985 May 1; accepted 1985 August 29

Abstract. We investigate the evolution of rotation period and spindown age of a pulsar whose surface magnetic field undergoes a phase of growth. Application of these results to the Crab pulsar strongly indicates that its parameters cannot be accounted for by the field growth theories.

Key words: pulsars, magnetic field pulsars, evolution —pulsars, individual

1. Introduction

Various authors (Woodward 1978, 1984; Blandford, Applegate & Hernquist 1983 and references therein) have suggested the possibility that the observed magnetic fields of neutron stars were generated after their birth by a thermally driven battery mechanism. In this picture, neutron stars are born with very low magnetic fields $\lesssim 10^8$ G and over a period of about 10^5 yr the fields are built upto $\sim 10^{12}$ G, the typical value inferred for pulsars. It is not clear if the necessary *dipole* fields can be generated in this manner (especially the 'vertical' components in the terminology of Blandford, Applegate & Hernquist 1983). However, assuming it to be possible we shall discuss here the implications for the evolution of rotation period and spindown age of the pulsar.

2. Definitions of relevant timescales

Several different timescales enter the following discussion. They are defined as,

t : the pulsar age

$t_c(t) \equiv$ $P(t)/2\dot{P}(t)$ *is* called the spindown age or the characteristic age of the pulsar Here P and $\dot{P}$ are the pulsar period and its time derivative respectively. The value of t_c for a pulsar at birth is t_c.

τ_m: the characteristic timescale for growth of the pulsar magnetic field.

τ_{sat}: the time taken for the magnetic field to saturate from the start of its growth.

3. Evolution of the pulsar rotation

Assuming a simple 'magnetic dipole radiation' type of slowdown for the pulsar, we have the well-known relation:

$$P(t)\dot{P}(t) = kB^2(t) \simeq 10^{-15} B_{12}^2(t)\ \mathrm{s} \qquad (1)$$

where P is in s, P in s s^{-1} . B_{12} is the magnetic field B in units of 10^{12} G. Integrating Equation (1) one finds,

$$P^2(t) - P_0^2 = 2k \int_0^t B^2(t)\, dt \tag{2}$$

where P_o is the initial period.

In the abovementioned models, the magnetic field of the neutron star grows exponentially with time for ~ 10^5 yr and reaches saturation at B ~ 10^{12} –10^{13} G. It remains at this value till eventual decay sets in at the age of a few million years. In the growth phase, the initial field B_o grows to

$$B(t) = B_0\, e^{t/\tau_m}$$

and thus

$$P^2 - P_0^2 = k\tau_m (B^2 - B_0^2) \tag{3}$$

$$= k\tau_m B^2 (1 - e^{-2t/\tau_m}). \tag{4}$$

The spindown age is now

$$t_c(t) = t_c^0 e^{-2t/\tau_m} + \frac{\tau_m}{2}(1 - e^{-2t/\tau_m}). \tag{5}$$

The variation of t_c with t is as shown in Fig. 1

After saturation has been reached, *i.e.* $t > t_{sat}$, the evolution changes and writing $B(t_{sat}) = B_{sat}$, we have

$$P^2(t) = P^2(t_{sat}) + 2k(t - t_{sat})\, B_{sat}^2 \tag{6}$$

and

$$t_c(t) = t_c(t_{sat}) + (t - t_{sat}) \tag{7}$$

which are the usual constant field evolution formulae.

Although one can discuss the various cases which can be distinguished by different relative magnitudes of the timescales involved, we shall consider only those which are physically reasonable. Obviously, the case when $t_{sat} \lesssim \tau_m$ is not of much interest as it corresponds to a pulsar being born with a magnetic field almost equal to its present

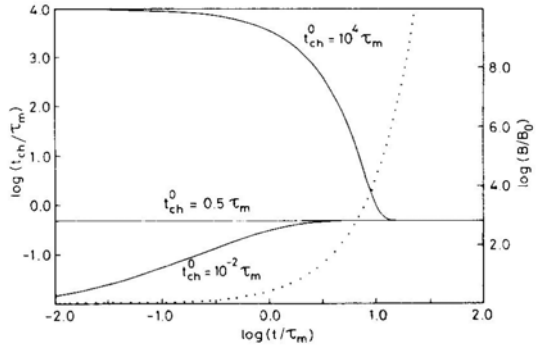

Figure 1. Evolution of spindown age of a pulsar as a function of time during exponential growth of its surface magnetic field. All times are in units of growth timescale τ_m of the magnetic field. Evolution is shown for three different values of initial spindown age t_c, namely, 10^4 τ_m, 0.5 τ_m and 10^{-2} τ_m ,as indicated beside the respective tracks. The spindown age approaches and saturates at the value 0.5 τ_m. The dotted line shows the evolution of surface magnetic field, the corresponding scale being at the right.

value and thus defeating the motivation for the magnetic field growth. In the following we shall therefore assume that $\tau_m \leqslant t_{sat}$. Normally one also expects $t_c^o \geqslant \tau_m$; *e.g.* for $P_o = 10^{-3}$ s and $B_o = 10^8$ G, $t_c \sim 10^9$ yr. Even if $B_o = 10^{10}$ G, t_c would be $\sim 10^5$ yr, Thus we take $t_c > \tau_m / 2$, and find, using Equation 5,

$$\tau_m \leqslant 2t_c. \tag{8}$$

We shall consider two possible histories of the Crab pulsar in relation to the Crab nebula, since it has often been suggested that pulsars may be born in binary systems (see *e.g.*, Gunn & Ostriker 1970). Indeed, on the basis of observed pulsar proper-motions it has been concluded that almost all pulsars are released from binary systems (Radhakrishnan & Shukre 1985). Pulsars born in binary systems would be seen as single pulsars only if the binaries are disrupted. Such binaries are expected to undergo two supernova explosions, a few million years apart (van den Heuvel 1977). Also, due to mass transfer effects in such systems, it will be most likely the second explosion and not the first one which will disrupt them (van den Heuvel 1976). In general, after disruption a binary will thus release two neutron stars —one old and one young. Keeping this in view, we therefore consider in turn the two alternatives, *i.e.*, the Crab pulsar is the one born in either the first or the second explosion in a binary system.

4. The Crab pulsar as a young neutron star

If the Crab pulsar were born in the explosion of AD 1054 which created the nebula, its age is

$$t \simeq 930 \text{ yr}.$$

Also, at present

$$\begin{aligned} P &\simeq 0.033 \text{ s}, \\ t_c &\simeq 1200 \text{ yr}, \end{aligned} \tag{9}$$

and

$$B \simeq 3.7 \times 10^{12} \text{ G}.$$

Using Equation 8 (and also 6 if $t > t_{sat}$), one finds, irrespective of the relative magnitudes of t and t_{sat}, that

$$\tau_m \leqslant 2400 \text{ yr}, \tag{10}$$

clearly at variance with the value of $\sim 10^5$ yr invoked for τ_m in the above-mentioned models.

Thus to reconcile the field growth picture with the present value of the Crab pulsar field one must then consider $\tau_m \leqslant 2400$ yr, as already noted by Blandford, Applegate & Hernquist (1983). In addition, we also impose the modest requirement that the present field is at least one order of magnitude more than the initial field. Now, in the case when $t < t_{sat}$ this implies $\tau_m \lesssim 400$ yr. Also, since

$$P^2 - P_0^2 \leqslant k \tau_m B^2 \qquad \text{(see Equation 4)},$$

substituting observed values for P and B, we get

$$P_0 \geqslant 30.4 \text{ ms}.$$

Such an initial period corresponds to a total energy loss of $\leqslant 3 \times 10^{48}$ erg since the birth of the pulsar and is at least an order of magnitude less than the energy budget of

the Crab nebula. The nebula has $\gtrsim 10^{49}$ erg in the present relativistic-particle and magnetic-field content. We further require $\sim 10^{49}$ erg for post-acceleration and $> 10^{48}$ erg to account for the radiation since its birth (Woltjer 1958; Trimble & Rees 1970; Trimble 1971; Rees & Gunn 1974). As there are compelling reasons to attribute all of this energy to that derived from the rotation of the Crab pulsar, any value of $P_0 \gtrsim 20$ ms is ruled out.

In the other case, when $t_{sat} < t$, using Equation (6) one can show that it is possible to have $P_0 < 20$ ms, but then the requirement $B_{sat} \geqslant 10\ B_0$ implies that $t_{sat}, \lesssim 180$ yr and $\tau_m \lesssim 80$ yr, which essentially amounts to instantaneous field build up.

5. The Crab pulsar as an old neutron star

The other alternative is that the Crab pulsar is older than the nebula and the companion of the star which became a supernova in AD 1054. The pulsar produced in this explosion remains undetected. Equation (9) now changes to

$$t \simeq 4 \times 10^6 \text{ yr.}$$

Since a change in t does not affect the inequality (10), it still holds. In addition, we also find from Equation (7) that $t - t_{sat} \leqslant 1200$ yr. Consequently, the field would have grown by an incredible factor of 10^{700} over 4 x 10^6 yr*, unless the stellar evolution timescale of the companion was $\sim 10^4$ yr, an unacceptably low value. We thus see that it is not possible in the case to explain both B and t_c simultaneously.

It may be argued in this connection that the field might have built up during a short-lived ($\sim 10^4$ yr) accretion phase. But as this accretion must have definitely stopped 930 yr ago, from Equation (7) it follows that the characteristic age at that time was 270 yr. This then is the upper limit on $\tau_m/2$ and we are once more led to an unreasonably fast growth of the field. Also, recent studies of known X-ray binary pulsars do not show any evidence of growing fields during accretion (Ray 1984).

We also investigated a power-law type growth for the magnetic field which may be relevant in the non-linear phase (Blandford, Applegate & Hernquist 1983). The details are not very illuminating but the conclusions are very similar to the above exponential case. For the case when the pulsar is young, it is not possible for both t_c and t to have small values. In the other case when the pulsar is considered to be an old object, again the field must grow in a very short time interval. Similar conclusions can be arrived at also by considering the variation of the braking index with time.

6. Effects of accretion torques

So far we have restricted ourselves to the slowdown of pulsar period due to radiation losses. There is, however, one other factor which affects the rotational history of a pulsar which must be taken into account when applying the field-growth formulae, if the neutron star happens to be in a binary system. During the mass transfer phase the angular momentum of the accreted matter could 'spin up' the neutron star (see, e.g., review by Henrichs (1983) and references therein). Such a decrease in period will reduce

* This corresponds to an initial magnetic momentum of the neutron star less than that of a single neutron (by about 10–645!).

the characteristic age of the pulsar. However, it cannot go on indefinitely and the minimum period the neutron star can attain depends on its surface magnetic field and corresponds to the Eddington accretion rate (Srinivasan & van den Heuvel 1982). As a consequence, the final characteristic age will be ~ 10^7 yr (Radhakrishnan 1984). It is easily seen therefore that such a scenario cannot explain the 1200 yr characteristic age of the Crab pulsar, no matter how the field varies with time.

7. Conclusions

If the Crab pulsar magnetic field has grown significantly in the past 930 years since its birth, the Crab nebula could not have been powered by it unless the field growth occurred in a very short time ($\lesssim$ 200 yr). However, this is then equivalent to the pulsar having its present field essentially at birth. Alternatively, if the pulsar, being a product of the first supernova explosion in a binary system, is older than the nebula, then the field growth picture cannot accommodate the values of the present magnetic field and the characteristic age of the pulsar simultaneously.

Acknowledgements

We would like to thank Rajaram Nityananda for generating our interest in this topic and V. Radhakrishnan for helpful criticism. We are particularly grateful to an anonymous referee for detailed and critical remarks which have helped us to improve the manuscript considerably. DB thanks the National Council of Educational Research and Training for financial support and the Raman Research Institute for extending research facilities.

References

Blandford, R. D., Applegate, J. H., Hernquist, L.1983, *Mon. Not. R. astr. Soc.*, **204**, 1025.

Gunn, J. E., Ostriker, J. P. 1970, *Astrophys. J.*, **160**, 979.

Henrichs, H. F. 1983, in *Accretion Driven Stellar X-ray Sources*, Eds W. H. G. Lewin & E. P. J. van den Heuvel, Cambridge Univ. Press, p. 393.

Radhakrishnan, V.1984, in *Birth and Evolution of Neutron Stars: Issues Raised by Millisecond Pulsars*, Eds S. P. Reynolds & D. R. Stinebring, NRAO, Green Bank, p. 130.

Radhakrishnan, V., Shukre, C. S. 1985, in *Proc. Third Asian Pacific Regional Meeting*, Kyoto, Astrophys. Space Sci. (in press).

Ray, A. 1984, presented at workshop on *Supernovae, their Progenitors and Remnants*, Bangalore, October 1984.

Rees, M. J., Gunn, J. E. 1974, *Mon. Not. R. Astr. Soc.*, **167**, 1.

Srinivasan, G., van den Heuvel, E. P. J. 1982, *Astr. Astrophys.*, **108**, 143.

Trimble, V.1971, in *IAU Symp.* 46: *The Crab Nebula*, Eds R. D. Davies & F. G. Smith, D. Reidel, Dordrecht, p. 12.

Trimble, V, Rees, M. J. 1970, *Astrophys. Lett.*, **5**, 93.

van den Heuvel, E. P. J. 1976, in *IAU Symp.* 73: *Structure and Evolution of Close Binary Systems*, Eds P Eggleton, S. Mitton & J. Whelan, D. Reidel, Dordrecht, p. 73.

van den Heuvel, E. P. J. 1977, *Ann. N.Y. Acad. Sci.*, **302**, 14.

Woltjer, L. 1958, *Bull. astr. Inst Netherl.*, **14**, 39.

Woodward, J. F. 1978, *Astrophys. J.*, **225**, 574.

Woodward, J. F. 1984, *Astrophys. J.*, **279**, 803.

J. Astrophys. Astr. (1985) **6**, 239–246

Quantum Mechanics in the de Sitter Spacetime and Inflationary Scenario

T. Padmanabhan *Tata Institute of Fundamental Research, Homi Bhabha Road, Bombay 400005*

Received 1985 May 23; accepted 1985 September 10

Abstract. We consider the effect of quantizing the homogeneous mode of a scalar field on inflation. It is shown that any semiclassical description of the scalar field is bound to lead to density inhomogeneities which are unacceptably large.

Key words: gravitation, quantum fluctuations—universe, inflationary

1. Inflationary physics

The idea of an inflationary epoch as a cure for various cosmological 'problems' has caught the fancy of the physicists in recent years. As one started looking deeper into these scenarios new problems seem to surface. To begin with, the most (and only!) natural scenario suggested by Guth (1981) led to an extremely inhomogeneous universe (Guth & Weinberg 1983). By adopting a special kind of dynamical symmetry breaking scheme, 'new' inflationary scenario solves this problem (Linde 1982; Albrecht & Steinhardt 1982). However, quantum fluctuations of the scalar field in this model leads to large density inhomogeneities. It is necessary to fine tune the parameters in the potential in a rather arbitrary manner to arrive at 'correct' answers. Since the basic motivation for inflation stems from a desire to avoid fine tuning, it is not entirely clear whether we are any better of in the end.

More fundamental problems have come up recently regarding the 'new' inflation. Doubts have been cast on the validity of the semiclassical analysis which is resorted to, and also on the nature of the initial state of the scalar field prior to slow 'roll over'. (Evans & McCarthy 1985; Mazenko, Unruh & Wald 1985).

To provide complete answer to these questions, it is necessary to go beyond the semiclassical approximation. We must construct a quantum theory for the *interacting* scalar field in a Robertson-Walker background, and, couple suitable expectation value of the energy-momentum tensor of the scalar field to the background geometry as a source term. In this paper, we tackle a much less ambitious project: We treat the homogeneous mode of the scalar field as a quantum variable and describe the self-consistent dynamics of the coupled system. The final result is once again negative: any reasonable description for the initial state of the field leads to too much of inhomogeneities.

We wish to emphasize that the work described here must be considered as a 'toy model'. Taking into account the spatial degrees of freedom may change the nature of the result. Such a possibility is under investigation.

2. Quantum mechanics in de Sitter spacetime

Consider the action for a scalar field φ with a potential $V(\varphi)$:

$$\mathcal{A} = \int \sqrt{-g}\, \mathrm{d}^4 x \{\tfrac{1}{2}\varphi_i \varphi^i - V(\varphi)\}. \tag{1}$$

We shall take the spacetime to be a $k = +1$ universe with the line element:

$$\mathrm{d}s^2 = \mathrm{d}t^2 - S^2(t)\left[\frac{\mathrm{d}r^2}{1-r^2} + r^2(\mathrm{d}\theta^2 + \sin^2\theta\, \mathrm{d}\varphi^2)\right]. \tag{2}$$

By assuming that $\varphi(x, t) = \varphi(t)$ we shall reduce the quantum field theory problem in Equation (1) to a quantum mechanical problem. The action in (1) becomes,

$$\mathcal{A} = 2\pi^2 \int \mathrm{d}t\, S^3(t) \{\tfrac{1}{2}\dot{\varphi}^2 - V(\varphi)\} \tag{3}$$

$$= 2\pi^2 \int \mathrm{d}T \left\{\frac{1}{2}\left(\frac{\mathrm{d}\varphi}{\mathrm{d}T}\right)^2 - S^6(T) V(\varphi)\right\}, \tag{4}$$

where,

$$T = \int \frac{\mathrm{d}t}{S^3(t)}. \tag{5}$$

Corresponding to the action in Equation (4) we have the Schrödinger equation:

$$i\frac{\partial \psi}{\partial T} = -\frac{1}{4\pi^2}\frac{\partial^2 \psi}{\partial \varphi^2} + 2\pi^2 V(\varphi) S^6 \psi. \tag{6}$$

(We are using units with $c = h = 1$ such that, φ^{-1}, S, t, $T^{-1/2}$ and $|\psi|^2$ have the dimensions of length). In a given background geometry, Equation (6) determines the probability functional $\psi[\varphi, t]$. To complete the dynamics, we should use the expectation values of T^i_k as the source of Einstein's equations. From Equations (l) and (3) it follows that,

$$T^0_0 = \tfrac{1}{2}\dot{\varphi}^2 + V(\varphi) = \frac{\hat{p}^2}{8\pi^4 S^6} + V = -\frac{1}{8\pi^4 S^6}\frac{\partial^2}{\partial \varphi^2} + V \tag{7}$$

$$T^1_1 = -\tfrac{1}{2}\dot{\varphi}^2 + V(\varphi) = -\frac{\hat{p}^2}{8\pi^4 S^6} + V = \frac{1}{8\pi^4 S^6}\frac{\partial^2}{\partial \varphi^2} + V. \tag{8}$$

(We have used the fact that the canonical momentum $\hat{p}$ corresponding to φ is $2\pi^2 S^3 \dot{\varphi}$). The expectation values of T^0_0 and T^1_1 in a state $\psi(\varphi)$ are,

$$\langle T^0_0 \rangle \equiv \rho = \frac{a}{S^6} + b; \qquad \langle T^1_1 \rangle \equiv -p = -\frac{a}{S^6} + b \tag{9}$$

with,

$$a = -\frac{1}{8\pi^4}\int_{-\infty}^{+\infty} \psi^*(\varphi)\frac{\partial^2 \psi}{\partial \varphi^2}\mathrm{d}\varphi = a(t) \tag{10}$$

and,

$$b = \int_{-\infty}^{+\infty} |\psi|^2 V(\varphi)\, \mathrm{d}\varphi = b(t). \tag{11}$$

Einstein's equation with T^i as the source are equivalent to a set of two equations:

$$\frac{\dot{S}^2+1}{S^2} = \frac{8\pi G}{3}\langle T_0^0 \rangle = \frac{8\pi G}{3}\left[\frac{a}{S^6}+b\right], \tag{12}$$

$$\frac{da}{dt} = -S^6\frac{db}{dt}. \tag{13}$$

It can be easily verified that Equation (13) is equivalent to the equation of motion for the scalar field in the classical limit. In writing (12) and (13) we have ignored all other source terms except the scalar field. This is justifiable because we shall be mainly concerned with the inflationary phase in which $S(t) \propto \exp(Ht)$; during that epoch, radiation (S^{-4}) and matter (S^{-3}) terms cease to be relevant. Similarly the S^{-6} and S^{-2} terms in Equation (12) can also be ignored.

The complete dynamics is determined by Equations (6), (12) and (13). In order to produce an analytic solution to these equations, we shall approximate the potential $V(\varphi)$ by a constant V_0 for $\varphi < \varphi_f$ and by zero for $\varphi_f < \varphi < \varphi_b$. We assume infinite potential barrier at $\varphi = \varphi_b$. Such an idealization of the Coleman–Weinberg type potential turns out to be adequate for our purposes.

To solve the Schrödinger equation in this potential, it is necessary to know the initial wave function, $\psi[\varphi, 0]$. We shall assume the initial wave function to be a gaussian:

$$\psi[\varphi, 0] = \left(\frac{1}{2\pi\sigma_0^2}\right)^{1/4}\exp\left\{-\frac{(\varphi-\varphi_i)^2}{4\sigma^2}+iL\varphi\right\}. \tag{14}$$

We have chosen Equation (14) such that $\langle\varphi\rangle = \varphi_i$, $(\Delta\varphi) = \sigma^2$ and

$$\left\langle\left(\frac{d\varphi}{dT}\right)\right\rangle = \frac{L}{2\pi^2} \tag{15}$$

represents the 'rolling down' velocity along the flat region.

The addition of a pure phase term in (14) which ensures a non-vanishing $\langle(d\varphi/dT)\rangle$, is absolutely essential. The actual potential has a gentle slope towards larger φ thereby inducing a 'roll over' velocity. Since we have idealized the potential by a constant V_0, it is necessary to put this term by hand.

It should be noted that the choice in Equation (14) is different from the usual choice made in inflationary models. It is usually *assumed* that the wave functional $\psi[\varphi(x), t]$ desribing the state of $\varphi(x)$ is symmetric under $(\varphi \to -\varphi)$. (In other words, φ is as likely to 'roll' towards the positive side as towards the negative side). Such an assumption, however, suffers from the following difficulties:

(i) At a very basic level, one simply does not know whether such an assumption was realized in the early universe or not. Granted this uncertainty, it is worthwhile examining the sensitivity of the results to changes in this particular assumption. Note that the symmetry of the hamiltonian under $(\varphi \to -\varphi)$ does not guarantee the same symmetry for the initial state.

(ii) Once we force the initial state to have the symmetry, $\langle\varphi\rangle$ will vanish. This, in turn, forces us to consider the classical part and the quantum fluctuations in very different manner. Both in quantum mechanics, as well as in the quantum field theory based on Schrödinger (functional) equation, it is conventional to identify $\langle\varphi\rangle$ as the classical limit. Since we can no longer do this, (because $\langle\varphi\rangle$ vanishes, while φ_{class} has to evolve) it is necessary to take φ_{class} as the solution to classical equations and quantize

perturbations of φ *around* φ_{class} by a suitable procedure. Crudely speaking, the φ_{class} 'rolls' down 'carrying' with it the fluctuations $\langle \varphi^2 \rangle^{1/2}$. Such an approach, to say the least, is unusual. It is definitely worthwhile to see whether an initial state can be chosen so that $\langle \varphi \rangle$ represents the classical evolution and $\langle\ [\varphi - \langle \varphi \rangle\ ]^2\ \rangle^{1/2}$ characterizes the fluctuations.

(iii) As was noted repeatedly in the literature, inflation can proceed from any local region of space which satisfies the requisite conditions. If the initial state is thermal or chaotic, there will be a probability distribution for the values taken by φ (x, 0). It is interesting to examine the consequences if inflation proceeds from a region with nonzero value for L, *i.e.* a region where φ has a preference to roll along a specific direction.

These are our reasons to deviate from the usual assumptions and take Equation (14) with $L \neq 0$. We shall interpret $\langle \varphi \rangle$ as the classical limit of the field.

The general solution to the Schrödinger equation (6) for constant V can be easily obtained to be,

$$\psi[\varphi, t] = \int_{-\infty}^{+\infty} \frac{\mathrm{d}l}{\sqrt{2\pi}}\, C(l) \exp il\varphi \exp\left[-\frac{il^2}{2\pi^2} \int \frac{\mathrm{d}t}{S^3} - 2\pi^2 V_0 \int S^3\, \mathrm{d}t \right] \tag{16}$$

where the function $C(l)$ has to be determined from the initial condition (14). Calculating $C(l)$ and substituting in (16) we get the probability distribution to be,

$$P[\varphi, t] = |\psi[\varphi, t]|^2 = \left[\frac{1}{2\pi\sigma^2(t)} \right]^{1/2} \exp \left\{ - \frac{\left(\varphi - \varphi_i - \dfrac{L}{\pi^2} T \right)^2}{4\sigma^2(t)} \right\} \tag{17}$$

with,

$$\sigma^2(t) = \sigma_0^2 \left[1 + \frac{1}{4\pi^4 \sigma_0^4} \left(\int \frac{\mathrm{d}t}{S^3} \right)^2 \right]. \tag{18}$$

Straightforward use of Equations (16) and (17) will also yield the following expectation values:

$$\langle \varphi \rangle = \varphi_i + \frac{L}{\pi^2} \int \frac{\mathrm{d}t}{S^3},$$

$$\langle p \rangle = L. \tag{20}$$

When $V(\varphi)$ is a constant, $\hat{p}^2$ commutes with the Hamiltonian. Therefore, $\langle p^2 \rangle$ is independent of time. Equation (13) is thus identically satisfied. In order to obtain a self-consistent description we only have to solve (12). Obviously, for $(Ht) \gtrsim 1$ the exponential solution

$$S(t) \simeq \frac{1}{H} \exp Ht \tag{21}$$

exists, leading to the usual inflationary scenario. As described before, only the b-term dominates (12) in the limit of $(Ht) \gtrsim 1$. We shall now consider the various constraints on this evolution.

3. Constraints on parameters

We shall take for φ_f and V_0, values similar to that in Coleman-Weinberg

potential:

$$\varphi_f \simeq 1.2 \times 10^{15}\ \text{GeV}; \qquad V_0 \simeq (10^{15}\ \text{GeV})^4 \tag{22}$$

leading to

$$H \simeq 7 \times 10^9\ \text{GeV}. \tag{23}$$

From Equations (19) and (21) it follows that the 'centre' of the wave packet has the trajectory:

$$\langle \varphi \rangle = \varphi_i + \frac{(LH)H}{3\pi^2}(1 - \exp(-3Ht)). \tag{24}$$

In other words the expectation value of the scalar field starts 'rolling over' with constant velocity (*i.e.* for $Ht \ll 1$, $(\langle\varphi\rangle - \varphi_i) \propto t$, but very soon slows down. It approaches the asymptotic value of

$$\langle \varphi \rangle_\infty = \varphi_i + (LH)\frac{H}{3\pi^2}. \tag{25}$$

For successful implementation of reheating we need $\langle\varphi\rangle$ to have 'fallen down' the well as $Ht \to \infty$. In other words,

$$\varphi_i + \frac{LH}{3\pi^2} H \gtrsim \varphi_f. \tag{26}$$

Since $\varphi_f \gg \varphi_i$ we may take this condition to be

$$\left(\frac{LH}{3\pi^2}\right) H \gtrsim \varphi_f. \tag{27}$$

Using Equations (22) and (23) in (27) we get,

$$LH \gtrsim 3 \times 10^6. \tag{28}$$

By taking $\varphi_f \lesssim \langle\varphi\rangle_\infty$, one can easily prolong the roll-ver phase as much as one wants; thus there is no difficulty in achieving sufficient inflation.

The initial state was assumed to be well localized near the origin and definitely far away from φ_f This implies that,

$$\sigma_0 \ll \varphi_f. \tag{28}$$

Equations (28) and (29) constrain the choice of parameters in the initial state.

In order to compute the inhomogeneities produced during the inflation, it is necessary to discuss the spatial degrees of freedom of φ. However, an order of magnitude estimate can be made along the following lines.

It is known that the value of the density contrast $(\delta\rho/\rho)$ is given by (see *e.g* Starobinski 1982; Hawking 1982; Guth & Pi 1982; Bardeen *et al.* 1983)

$$\left(\frac{\delta\rho}{\rho}\right) = \varepsilon \left\langle \frac{H\Delta\varphi}{\dot{\varphi}} \right\rangle_{t=t_1}. \tag{30}$$

Here ε is a number of the order unity, $\Delta\varphi$ is the quantum spread in the scalar field, and $\dot{\varphi}$ is the roll-over velocity. The right-hand side should be evaluated at the time when galactic size perturbations 'freeze out' of the horizon. Physically one may interpret

$$\Delta\tau \equiv \frac{\Delta\varphi}{\dot{\varphi}} \tag{31}$$

as the time lag between the 'leading edge' and 'trailing edge' of the wave packet. Because of this time lag the scalar field 'falls over' the potential at different places at different times, leading to inhomogeneities.

Since we know the evolution of the wave packet the time lag $\Delta\tau$ can be computed directly as,

$$\Delta\tau = t_+ - t_- \tag{32}$$

where $t_\pm$ are the roots of the equation,

$$\langle \varphi \rangle_t \pm \sigma(t) = \varphi_f. \tag{33}$$

Straightforward algebra gives (talking $\varphi_f \gg \varphi_0$; $\sigma_0 \quad \varphi_f$),

$$\Delta\tau \simeq \frac{2\sqrt{2}}{3H}\left(1+\frac{1}{4L^2\sigma_0^2}\right)^{-1}\left(1+\frac{1}{8L^2\sigma_0^2}\right)^{1/2}\exp(3Ht_1) \tag{34}$$

so that,

$$\frac{\delta\rho}{\rho} = \frac{2\sqrt{2}}{3}\varepsilon\left(1+\frac{1}{4L^2\sigma_0^2}\right)^{-1}\left(1+\frac{1}{8L^2\sigma_0^2}\right)^{1/2}\exp(3Ht_1). \tag{35}$$

The disturbing exponential factor is due to the fact that $\langle\varphi\rangle$ is much smaller than the constant velocity assumed in the conventional roll-over, scenario. Note that,

$$\langle\dot{\varphi}\rangle = \left\langle\frac{\mathrm{d}\varphi}{\mathrm{d}t}\right\rangle = \frac{1}{S^3}\left\langle\frac{\mathrm{d}\varphi}{\mathrm{d}T}\right\rangle = \exp(-3Ht)\left(\frac{L}{\pi^2}\right). \tag{36}$$

While $(\mathrm{d}\varphi/\mathrm{d}T)$ remains constant, $(\mathrm{d}\varphi/\mathrm{d}t)$ keeps on decreasing. Clearly, the exponential in Equation (35) makes matters much worse than usual. One way to get out of this trouble will be to assume that the 'freeze-out time t_1' for the relevant length scale is of the order of H^{-1}. (Turner has pointed out that galactic size perturbation crosses the horizon at about $50H^{-1}$ before the end of inflation; *i.e.*, $t_1 \simeq 10H^{-1}$ (Turner 1983). Taking $t_1 \simeq 2H^{-1}$, therefore, can be a drastic approximation.) With this understanding, we write,

$$\frac{\delta\rho}{\rho} \gtrsim \frac{\beta}{\sqrt{2}}\left(1+\frac{1}{4L^2\sigma_0^2}\right)^{-1}\left(1+\frac{1}{8L^2\sigma_0^2}\right)^{1/2} \tag{36}$$

where β is probably a numerical factor of the order of (10–100). On the other hand, we want $(\delta\rho/\rho)$ to be about 10^{-4}. Clearly, it is necessary to have $L^2\sigma_0^2 \ll 1$. In this limit, we get,

$$\frac{\delta\rho}{\rho} = \beta(L\sigma_0) \tag{37}$$

which gives the further constraint,

$$L\sigma_0 \lesssim \beta^{-1}\,10^{-4}. \tag{38}$$

Altogether we have arrived at the following constraints on the parameters (*cf.* Equations (28), (29) and (38))

$$LH \gtrsim 3\times10^6; \qquad \sigma_0 \ll (10^{15}\ \mathrm{GeV}); \qquad L\sigma_0 \lesssim \beta^{-1}\,10^{-4}. \tag{39}$$

If these are the only constraints on the system, then they can be easily satisfied. For

Example, one can choose (with $\beta \simeq 10^2$).

$$L \simeq 5 \times 10^{-4}\,(\mathrm{GeV})^{-1}; \qquad \sigma_0 \simeq 2 \times 10^{-3}\,(\mathrm{GeV}). \tag{40}$$

Unfortunately, these are not the only accepted constraints. It is usually assumed that a scalar field in a de Sitter spacetime has fluctuations which are at least of the order of $(H/2\pi)$. This result corresponds to the usual 'temperature' $(H/2\pi)$ associated with the de Sitter spacetime. If we assume this result to be valid in an inflationary scenario, then it is necessary to satisfy the additonal constraint,

$$\sigma_0 \gtrsim \frac{H}{2\pi} \simeq 10^9\ \mathrm{GeV}. \tag{41}$$

From the first constraint in (39), it follows that,

$$L \gtrsim 3 \times 10^6\, H^{-1} \tag{42}$$

Combining (42) and (41),

$$L\sigma_0 \gtrsim 5 \times 10^5, \tag{43}$$

which is grossly inconsistent with (38). In other words, the simplest version of quantum mechanical inflation leads to density inhomogeneities which are large by a huge factor.

4. Discussion

Treating the scalar field as a quantum mechanical object does not offer any relief from the disturbing conclusions already known in literature. The analysis however brings out two features: (i) The cause of the problems in new inflation is *not* the semiclassical approximation made in the usual analysis, (ii) The condition (41) plays a crucial role in producing too much of inhomogeneities. But for this constraint, one can arrive at acceptable values of density inhomogeneities.

It is possible that Equation (41) is not really as sacred as it is taken to be. It has been argued in literature that thermal effects due to event horizons do not restore a spontaneously broken symmetry (Hill 1985). Possibly, thermal effects do not contribute to the dynamics of de Sitter space either. In this connection it should be remembered that the spacetime is never truly de Sitter; it only approaches the de Sitter spacetime asymptotically.

The discussion presented in the paper needs to be generalized in three different aspects: (i) inclusion of spatial dependence, (ii) examination of other initial conditions, (iii) amore realistic description of the potential $V(\varphi)$. We hope to present such a detailed analysis in a future paper.

References

Albrecht, A., Steinhardt, P. J. 1982, *Phys. Rev. Lett.*, **48**, 1220.
Bardeen, J., Steinhardt, P. J., Turner, M. S. 1983, *Phys. Rev.*, **D28**, 679.
Evans, M., McCarthy, J. G. 1985, *Phys. Rev.*, **D31**, 1799.
Guth, A. H. 1981, *Phys. Rev.*, **D23**, 347.
Guth, A. H., Pi, S.-Y. 1982, *Phys. Rev. Lett.*, **49**, 1110.
Guth, A. H., Weinberg, E. 1983, *Nucl. Phys.*, **B212**, 321.

Hawking, S. 1982, *Phys. Lett.*, 115**B**, 295.
Hill, C. T. 1985, Fermilab Preprint 85/28-T.
Linde, A. D. 1982, *Phys. Lett.*, 1**08B**, 389.
Mazenko, M. G., Unruh, W., Wald, R. 1985, *Phys. Rev.*, **D31**, 273.
Starobinsky, A. A. 1982, *Phys. Lett.*, **117B**, 175.
Turner, M. S. 1983, in *Proc. fourth Workshop on Grand Unification*, Eds H. A. Weldon, P. Langacker & P. J. Steinhardt, Birkhäuser, Basel, p. 228.

J. Astrophys. Astr. (1985) **6,** 247–260

Gravitational Pertubation of Homogeneous Collisionless Dark Matter

T. Padmanabhan & M. M. Vasanthi *Tata Institute of Fundamental Research, Homi Bhabha Road, Bombay 400005*

Received 1985 March 15; accepted 1985 August 12

Abstract. The effect of a perturbing mass on a homogeneous collisionless cloud of dark matter is considered in the linear approximation. It is shown that gravitational potential can have turning points, in sharp contrast with gravitating systems of finite extent. The model offers a reasonable explanation for the observed secondary maxima in the density distribution of rich clusters. The relevance of the model to the flatness of the rotation curves of galaxies is also discussed.

Key words: dark matter, collisionless—cluster of galaxies, dark matter—galaxies, rotation curves

1. Introduction

One of the most intriguing problems in present day astrophysics is related to the fact that estimates of visible matter (at various length scales) fall systematically short of the amount of gravitating matter at the same scale (Rood 1981; Bahcall 1977; Peebles 1979; Faber & Gallager 1979). This problem, usually christened 'Missing mass problem', has attracted considerable attention of late in the form of wide variety of explanations. (For a study of the systematics at various length scales, see Cowsik & Vasanthi 1986.) The explanations range from using the relics of the big bang to modifying Newton's law of gravity (see for *e.g.* Cowsik & McClelland 1973; Pagels & Primack 1982; Olive & Turner 1982; Cabibbo, Farrar & Maiani 1981; Peebles 1982; Sikivie 1982; Milgrom 1983).

Among these explanations there is a sense of naturalness in suggesting that the relics of big bang provide the dark matter. For example, considerable amount of work has been done in recent years to understand the dynamics of the universe dominated by massive neutrinos (Davis *et al.* 1981; Chubb 1983; Doroshkevich *et al.* 1981; Bond, Efstathiou & Silk 1980; Wasserman 1981; Peebles 1982; Melott 1983; Cowsik 1983; Cowsik 1986; Sato & Takahara 1981; Schramm & Steigman 1981; Klinkhamer & Norman 1981).

In the standard big bang scenario, stable massive neutrinos (with mass of the order of ~ 20 eV) would decouple from the rest of the matter at a very early epoch (~ 1 MeV). After this epoch, these neutrinos free-stream in space time as collisionless particles, interacting only through gravity. Such a collisionless species can condense in any potential well and provide the missing mass.

In this paper we shall consider certain mathematical features of such collisionless dark matter which permeates throughout the universe. We shall see that the

gravitational effects in such an infinite medium can have certain peculiarities not exhibited by finite bound gravitating systems. Though we shall call the constituents of dark matter as neutrinos, our analysis will be applicable to any other collisionless relic of big bang.

The mathematical formalism is presented in Section 2 wherein we solve the collisionless Boltzmann equation self-consistently in the linear approximation. We show that gravitational potential in an infinite medium can have maxima and minima.

It is possible that these non-trivial turning points in the gravitational potential are responsible for the phenomena of secondary maxima observed in a number of clusters of galaxies (Baier 1983). We show in Section 3 that the observed features are reasonably well described by our model. In addition, the present model may also provide (at least a partial) explanation to the flat rotation curves of spiral galaxies (Rubin 1979; Rubin *et al.* 1980, 1982; Bosma 1978).

2. Mathematical formalism

2.1 *Collisionless Gas in Linear Approximation*

Consider a system of collisionless neutrinos of mass m_v, in a gravitational potential ϕ (x, *t*). Let f_{total} (x, *v*, *t*) denote the number of neutrinos in the phase space interval $x+d^3x$, $v+d^3v$) at a time *t*. (The subscript 'total' is added for future notational convenience.) Conservation of phase-space density leads to the collisionless Boltzmann equation

$$\left[\frac{\partial}{\partial t}+\mathbf{v}\cdot\nabla-\nabla\phi\cdot\frac{\partial}{\partial\mathbf{v}}\right]f_{\text{total}}(\mathbf{x},\mathbf{v},t)=0. \tag{1}$$

The gravitational potential ϕ (x, *t*) satisfies Poisson's equation

$$\nabla^2\phi(x,t)=4\pi G m_v\int f(x,v,t)d^3v+4\pi G\rho_{\text{ext}}(x,t). \tag{2}$$

Here ρ_{ext} (x, *t*) denotes the mass density of gravitating matter other than the neutrinos. (We shall call them, somewhat loosely, as 'galaxies'!) As already emphasized, we expect the gravitational field of a cluster of galaxies to be dominated by the neutrinos rather than by the $\rho_{\text{ext}}(x,t)$.

In writing down Equations (1) and (2), we have already neglected the expansion of the universe and other general relativistic effects. Such an approximation is definitely valid during recent epochs. The introduction of the expansion of the universe is necessary to discuss the evolution of perturbation in a collisionless gas and will be taken up in a subsequent paper.

The general solution to Equations (1) and (2) is unknown. To make any progress we have to make reasonable approximations. To be specific, let us consider a cluster of galaxies with a neutrino halo, and treat galaxies as a perturbation in the neutrino background. In the (trivial) zeroth order approximation, we shall entirely neglect the galaxies and assume neutrinos to be distributed homogeneously all over the universe. Such a homogeneous distribution of matter does not produce any gravitational potential. Thus, in the zeroth order, we can take

$$f_{\text{total}}(x,v,t)=f_0(v);\quad \rho_{\text{ext}}(x,t)=0 \tag{3}$$

$$\phi(x,t)=0. \tag{4}$$

Let us now 'switch on' the galaxies in the form of ρ_{ext} (x, t). These galactic perturbations will induce clustering in the neutrino background and will make the distribution function space-dependent. Such a space-dependent distribution function will in turn produce a gravitational potential of its own. Thus, in the first order, the potential ϕ (x, t) arises from two sources: (a) A part ϕ_{ext} (x, t) which comes from ρ_{ext}(x, t) and satisfies the equation,

$$\nabla^2\phi_{ext}(x, t) = 4\pi G\rho_{ext}(x, t) \tag{5}$$

and (b) a part ($\phi - \phi_{ext}$) which is due to perturbed neutrino distribution, which we shall call f (x, v,t). That is,

$$f_{total}(x, v, t) = f_0(v) + f(x, v, t), \tag{6}$$

$$\nabla^2[\phi(x, t) - \phi_{ext}(x, t)] = 4\pi G m_v \int f(x, v\, t)\, d^3v. \tag{7}$$

We shall assume that $f \ll f_0$ and linearize (1) in f. This gives,

$$\left[\frac{\partial}{\partial t} + \mathbf{v}\cdot\frac{\partial}{\partial \mathbf{x}}\right] f(\mathbf{x}, \mathbf{v}, t) = \frac{\partial\phi}{\partial \mathbf{x}}\cdot\frac{\partial f_0}{\partial \mathbf{v}}. \tag{8}$$

Once the form of the perturbation, ρ_{ext} (or ϕ_{ext}(x, t)) is specified, Equations (7) and (8) determine the perturbed distribution of dark matter in a cluster.

These equations can be solved in a straightforward manner using Fourier transforms. It is convenient to define the 'one-sided' Fourier transform (Lifshitz & Pitaevskii 1981) of f (x, v, t) (and similarly for ϕ (x ,t)) by,

$$f_{\omega\mathbf{k}}(\mathbf{v}) = \int_0^\infty dt \int d^3\mathbf{x}\, f(\mathbf{x}, \mathbf{v}, t)\, e^{-i\mathbf{k}\cdot\mathbf{x}}\, e^{i\omega t}. \tag{9}$$

The inverse transform is given by

$$f(\mathbf{x}, \mathbf{v}, t) = \int_{-\infty+i\sigma}^{+\infty+i\sigma} \frac{d\omega}{2\pi}\frac{d^3\mathbf{k}}{(2\pi)^3} f_{\mathbf{k}\omega}(\mathbf{v})\, e^{i(\mathbf{k}\cdot\mathbf{x} - \omega t)}. \tag{10}$$

Here the ω integral is taken along a straight line in the complex ω-plane parallel to and above the real axis passing above all the singularities of $f_{k\omega}$. We multiply both sides of (8)by $e^{i\omega t}$ and integrate with respect to t. Defining f_k(v, t) and g_k(v) by,

$$f_k(v, t) = \int d^3x\, f(x, v, t) e^{-ik\ x}, \tag{11}$$

$$g_k(v) = f_k(v, t)|_{t=0} = f_k(v, 0). \tag{12}$$

We can write (8) in Fourier space as,

$$i(\mathbf{k}\cdot\mathbf{v} - \omega) f_{\mathbf{k}\omega}(\mathbf{v}) - g_{\mathbf{k}} = i\mathbf{k}\cdot\frac{\partial f_0}{\partial \mathbf{v}}\phi_{\mathbf{k}\omega}. \tag{13}$$

Equation (7) in the Fourier space reads as

$$-k^2(\phi_{k\omega} - \phi_{k\omega}(ext)) = 4\pi G m_v \int f_{k\omega}(v) d^3v. \tag{14}$$

Equation (13) can be solved to give,

$$f_{\mathbf{k}\omega}(\mathbf{v}) = \frac{i\mathbf{k}\cdot\dfrac{df_0}{d\mathbf{v}}\phi_{\mathbf{k}\omega} + g_{\mathbf{k}\omega}}{i(\mathbf{k}\cdot\mathbf{v} - \omega)} \tag{15}$$

Using (14) and (15) we can determine $\phi_{k\omega}$ to be,

$$\phi_{\mathbf{k}\omega} = \frac{1}{\varepsilon(\mathbf{k}, \omega)} \phi^{\text{ext}}_{\mathbf{k}\omega} - \frac{4\pi G m_v}{\mathbf{k}^2} \int \frac{g_{\mathbf{k}}(\mathbf{v})\, \mathrm{d}^3\mathbf{v}}{i(\mathbf{k}\cdot\mathbf{v} - \omega)} \tag{16}$$

where

$$\varepsilon_{(\mathbf{k}, \omega)} = 1 + \frac{4\pi G m_v}{\mathbf{k}^2} \int \frac{\left(\mathbf{k} \cdot \dfrac{\mathrm{d}f_0}{\mathrm{d}\mathbf{u}}\right)}{(\mathbf{k}\cdot\mathbf{u} - \omega)} \mathrm{d}^3\mathbf{u}. \tag{17}$$

Given the ϕ^{ext} and the initial condition g_k (v), Equation (16) determines $\phi_{k\omega}$ Using $\phi_{k\omega}$ in (15) gives us the perturbed distribution of dark matter. Thus (15) and (16) solve the problem completely in the linear approximation. The potential ϕ(x, t) and the distribution function f(x, v, t) can be obtained by the inverse transformations (10) of Equations (15) and (16).

From Equation (16), it is clear that $\phi_{k\omega}$ arises from two different sources. Initial inhomogenities in the medium, characterized by $g_{k,}$ propagate in time and contribute as the second term in (16). As we are more interested in the effect of external galactic perturbations, we shall take the initial condition,

$$g_k = 0 \tag{18}$$

leading to,

$$\phi_{\mathbf{k}\omega} = \frac{1}{\varepsilon(\mathbf{k}, \omega)} \phi^{\text{ext}}_{\mathbf{k}}. \tag{19}$$

This equation shows that the neutrino background acts as a polarizable medium. The potential in the medium is scaled by a factor ε (**k**, ω) which may be called the 'gravitational permittivity' of the medium. As one can see from (17), ε(**k**, ω) is completely determined by the background distribution function f_0 (v).

There is a minor mathematical point which is worth taking note of at this stage. Expressions like (16), (17) *etc.* contain integrals with integrands that have poles in the real axis (for example, the integral in (17) has a pole at ω = **k·u**). Thus, one has to specify the contour of integration for these expressions. This is a well-known feature in the theory of collisionless plasmas (Lifshitz & Pitaevskii 1981). We assume that the potential was zero at $t = -\infty$ and was switched on adiabatically:

$$(t) \sim \phi_\omega e^{-i\omega t} e^{Pt} \qquad (P \geqslant 0) \tag{20}$$

The exp (pt) factor makes ϕ vanish in the past infinity. The limit of ($p \to 0$) is taken at the end of the calculations. (As it stands (20) diverges at the future infinity; however, because of causality, the behaviour of $\phi(t)$ at future infinity cannot affect physics at any finite time.) Clearly this operation is equivalent to replacing ω by ($\omega + ip$) and taking ($p \to 0$) limit in the end. Such a procedure makes the integral in (16), (17) *etc.* well-defined. Whenever a pole in the real axis is encountered we shall assume that ω has an infinitesimal positive imaginary part.

To understand the effects of ε(**k**, ω) and the polarization of the medium, we have to consider suitable 'test perturbations' in the form of ρ^{ext}(x, t). Let us assume that ρ^{ext}(x, t) arises due to a set of N galaxies. We shall denote the trajectory of the nth galaxy (n =1, 2, . . . , N) by $R_n(t)$. Then if the mass of the nth galaxy is $M_{n\ ,}$ we have,

$$\rho^{\text{ext}}(\mathbf{x}, t) = \sum_{n=1}^{N} M_n \delta(\mathbf{x} - \mathbf{R}_n(t)). \tag{21}$$

Since

$$\nabla^2 \phi^{\text{ext}}(\mathrm{x}, t) = 4\pi G\, \rho^{\text{ext}}(\mathrm{x}, \mathrm{t}), \tag{22}$$

we get,

$$\phi_{\mathbf{k}}^{\text{ext}} = -\frac{4\pi G}{\mathbf{k}^2} \sum_n M_n \int_0^\infty \mathrm{d}t \exp i[\omega t - \mathbf{k} \cdot \mathbf{R}_n(t)]. \tag{23}$$

Two simple cases are of physical importance: (i) The galaxy is at rest; $R(t)$ = R = constant, and (ii) The galaxy is moving with a uniform velocity; $\mathbf{R}(t)$ =$\mathbf{ut}$. The effect of N galaxies in similar state of motion can be found by superposing individual galaxies. In these two cases $\phi_{\mathrm{k}}^{\text{ext}}$ are given by

$$\phi_{\mathbf{k}}^{\text{ext}} = -\frac{4\pi G M}{\mathbf{k}^2} i\mathbf{k} \mathrm{e}^{-i\mathbf{k}\cdot\mathbf{R}}, \qquad \mathbf{R}(t) = \mathbf{R}, \quad \text{case i;} \tag{24}$$

$$\phi_{\mathbf{k}}^{\text{ext}} = \frac{4\pi G\, M i}{\mathbf{k}^2(\mathbf{k}\cdot\mathbf{u} - \omega)}, \qquad \mathbf{R}(t) = \mathbf{u}t, \quad \text{case ii.} \tag{25}$$

Case (i) leads to an interesting steady-state distribution of dark matter which we shall discuss in the remaining sections of this paper. The situation described in case (ii) is of relevance in the discussion of dynamical friction and galactic segregation. This will be discussed in a future publication.

2.2 *The Steady-State Distribution*

Rigorously speaking, galaxies in a cluster cannot be considered to be stationary. However, once the cluster has reached a steady-state configuration, one can meaningfully discuss a time-independent distribution function. This time-independent distribution of galactic matter will induce clustering in the neutrino gas. We are interested in the form of this distribution function.

It is obvious that the time independent solution is determined by the static part of the permittivity *viz.* $\varepsilon(\mathrm{k}, 0)$. (To see this, note that when the inverse transform of ϕ_{kw} is taken, using (20) and (25) it is the pole at ω = 0 that produces the static part of the potential.) Considering the importance of the result, we shall derive it more directly. When f, ϕ and ρ^{ext} are independent of time, it is easy to show that

$$\phi_{\mathbf{k}} = -\frac{4\pi G}{\mathbf{k}^2} \frac{\rho_{\mathbf{k}}^{\text{ext}}}{\varepsilon(\mathbf{k}, 0)} \tag{26}$$

with

$$\varepsilon(\mathbf{k}, 0) = 1 + \frac{4\pi G m_\nu}{\mathbf{k}^2} \int \frac{\mathbf{k} \cdot \dfrac{\mathrm{d}f_0}{\mathrm{d}\mathbf{v}}}{\mathbf{k}\cdot\mathbf{v}} \mathrm{d}^3\mathbf{v}. \tag{27}$$

Assuming f_0 (v) depends only on |v| (which is a reasonable assumption because there are no preferred directions in the velocity space), we get

$$\varepsilon(\mathbf{k}, 0) = 1 + \frac{8\pi G m_\nu}{k^2} \int_0^\infty \left(\frac{\mathrm{d}f_0}{\mathrm{d}v}\right) 2\pi v\, \mathrm{d}v \tag{28}$$

$$= (1 - k_j^2/k^2)$$

where,

$$\frac{1}{\sigma^2} = \frac{4\pi}{n}\int_0^\infty f_0\,\mathrm{d}v, \quad k_J^2 = \frac{4\pi G n m_v}{\sigma^2}.$$

Thus the static part of the permittivity is essentially determined by the Jean's length k_J^{-1} of the background medium. In this case it is instructive to compare (28) with the static part of the permittivity of an electromagnetically active medium. In the electromagnetic case, (28) is replaced by,

$$\varepsilon(\mathbf{k}, 0) = 1 + \frac{k_D^2}{k^2}; \quad k_D^2 = \frac{4\pi\rho_0}{\sigma^2}\left(\frac{e}{m}\right)^2 \tag{29}$$

where k_D^{-1} is the Debye length for the medium. Note that the sign of k^2 is different in (28) and (29).

Substituting (28) into (26), we get the potential to be,

$$\phi_{\mathbf{k}} = -\frac{4\pi G\rho_{\mathbf{k}}^{\mathrm{ext}}}{(k^2 - k_J^2)}. \tag{30}$$

Let us calculate the potential at any point x, due to a galaxy of mass M kept at the origin. Taking $\rho^{\mathrm{ext}}(x) = M\delta(x)$ and using the inverse transformations we get,

$$\phi = -4\pi GM\int\frac{\mathrm{d}^3k}{(2\pi)^3}\frac{\mathrm{e}^{i\mathbf{k}\cdot\mathbf{x}}}{(k^2 - k_J^2)}. \tag{31}$$

In this section we have not bothered to show the $i\varepsilon$ explicitly. It is easy to see (using reasonings similar to that of Equation 20) that k_J should be treated as having an infinitesimal positive part. With this prescription, (31) gives

$$\phi = -\frac{GM}{|\mathbf{x}|}\cos k_J|\mathbf{x}|. \tag{32}$$

Thus the polarization of the medium introduces an extra sinusoidal dependence in $\phi(x)$. This is to be contrasted with the electromagnetic case in which one would have used (29) rather than (28). The change in the sign of k^2 term has the effect of replacing (32) by,

$$\phi = -\frac{Q}{|\mathbf{x}|}\exp(-k_D|\mathbf{x}|) \tag{33}$$

leading to the well-known Debye shielding. Equation (32) emphasizes the fact that gravitational effects cannot be shielded. This oscillatory behaviour of the gravitational field of a test mass in a collisionless gas was derived earlier by Marochnik (1968) in the context of a star in a star cluster.

Let us look at the physics described by Equation (32). In the absence of neutrino background, a galaxy of mass M kept at the origin will produce the Newtonian $|x|^{-1}$ potential. Any test particle, say, a galaxy, will feel this force and will be attracted towards the origin. When the neutrino cloud is present, the situation can be very different. The galaxy at the origin perturbs the background and leads to inhomogenities. Any test particle (at a point x) will now feel the combined effects of the perturbed medium as well as the galaxy at the origin. Depending on the relative distribution of inhomogenities, the test particle may feel a force either towards the origin or away from the origin. Thus—as is clear from (32)—the sign and slope of $\phi(x)$ can be positive or negative, implying either attraction or repulsion.

This peculiar feature, which has no analogue in finite, bound, gravitating systems, can also be understood from another angle. The gravitational potential produced by any spherically symmetric distribution of matter with density $\rho(r)$ satisfies the equation,

$$\frac{1}{r^2}\frac{\partial}{\partial r}\left(r^2\frac{\partial \phi}{\partial r}\right) = 4\pi G\rho(r). \tag{34}$$

Therefore,

$$\frac{\partial \phi}{\partial r} = \frac{G}{r^2}\int_0^r \rho(x)4\pi x^2\,\mathrm{d}x. \tag{35}$$

A turning point for ϕ at, say, $r = R$ would imply the vanishing of the $\partial\phi/\partial r$ at $r = R$, and hence the vanishing of the integral in (35). In normal circumstances $\rho(r)$ is always greater than zero and thus the integral cannot vanish. This argument however assumes that $\rho(r)$ has only finite extent in space and falls faster than r^{-3} at large r. In an infinite homogeneous medium, for example, the integrals like the one in (35) do not exist. We have to do a more careful job. Suppose that the gravitating matter consists of two components ρ_1 (r) and ρ_2 (r). Let ρ_1 (r) fall faster than r^{-3} at large distances. However, suppose ρ_2 (r) is equal to $\bar{\rho}_2 + f$ (r) where $\bar{\rho}_2$ is a constant homogeneous distribution throughout space and f (r) is the deviation from the homogeneity which may be *positive* or *negative* (*i.e.* ρ_2 (r) may be enhanced or depreciated from the mean value $\bar{\rho}_2$). Of course f (r) $<|\bar{\rho}_2(r)|$ so that ρ_2 is always greater than zero. The gravitational potential ϕ due to this distribution satisfies the equation

$$\nabla^2\phi = 4\pi G(\rho_1+\rho_2+f). \tag{36}$$

Because of linearity, we can write $\phi = \psi+n$ where ψ and η satisfy the equations

$$\nabla^2\psi = 4\pi G(\rho_2, \tag{37}$$

$$\nabla^2\eta = 4\pi G(\rho_1+\mathrm{f}). \tag{38}$$

We realise that the potential ψ produced by a distribution $\bar{\rho}_2$ (constant throughout the universe) is formally infinite. But this is of no concern because such a homogeneous distribution of matter does not provide any gravitational force. In other words, the dynamics is completely determined by $\eta(r)$. This $\eta(r)$ can have nontrivial maxima and minima because the source for $\eta(r)$ (which is $\rho_1(r) + f(r)$) need not be positive definite. This is precisely what happens when a homogeneous background of neutrinos is present in the universe. Deviations from homogeneity, which are responsible for gravitational force may be positive or negative. Since such an homogeneous background distribution is of relevance in many a cosmological context (see for example: Peebles 1980 and Weinberg 1972), the above mentioned feature should be kept in mind.

Using (26) and (28) one can immediately obtain the distribution of dark matter:

$$\rho_{\mathbf{k}}^{\nu} = m_\nu \int f_k(\mathbf{v})\,\mathrm{d}^3\mathbf{v} \tag{39}$$

$$= \rho_{\mathbf{k}}^{\mathrm{ext}}\frac{k_J^2}{(k^2-k_J^2)} = -\frac{k_J^2}{4\pi G}\phi_{\mathbf{k}}. \tag{40}$$

In other words,

$$\rho^{\nu}(\mathbf{x}) = -\frac{k_J^2}{4\pi G}\phi(\mathbf{x}). \tag{41}$$

This equation relates the spatial distribution of dark matter to the overall gravitational

potential. Clearly, when $\phi(x)$ is negative [regions of attraction] ρ_v (x) is positive (density enhancement) and vice versa. In the case of a test galaxy at origin, we can use (32) in (41) to obtain,

$$\rho_v(\mathbf{x}) = \frac{Mk_J^3}{(4\pi)} \cdot \frac{\cos k_J|\mathbf{x}|}{k_J|\mathbf{x}|}. \tag{42}$$

The validity of linear perturbation theory requires the condition

$$|\rho_v(\mathbf{x})| \ll \rho_0 \tag{43}$$

which must be kept in mind in using expressions like (42).

The potential due to a distribution of galaxies can be found by superposing potentials of the form (32). For a distribution of galaxies represented by ρ^{ext} (x), this is given by the integral,

$$\phi(\mathbf{x}) = -G \int \frac{\rho^{\text{ext}}(\mathbf{r})}{|\mathbf{r}-\mathbf{x}|} \cos k_J|\mathbf{r}-\mathbf{x}|\, \mathrm{d}^3\mathbf{r}. \tag{44}$$

If $\rho^{\text{ext}}(r)$ is assumed to be spherically symmetric (which is a reasonable assumption for most large clusters of galaxies), then the angular integrations can be performed to give,

$$\phi(\mathbf{x}) = -4\pi G\left[\frac{\sin k_J x}{k_J x}\int_x^\infty \mathrm{d}r\, r\rho(r)\cos k_J r + \frac{\cos k_J x}{k_J x}\int_0^x \mathrm{d}r\, r\rho(r)\sin k_J r\right]. \tag{45}$$

Even though (45) will lead to a much more complicated form than (32) the qualitative features will be the same. In particular one does expect the sinusoidal behaviour of the potential, at least at large x. As a prototype, consider two simple forms for $\rho(r)$: (i) exponential fall with

$$\rho(r) = \bar{\rho}\,\frac{\mathrm{e}^{-r/R}}{(r/R)}, \tag{46}$$

and (ii) a box type fall off with

$$\rho(r) = \begin{cases} \bar{\rho} & \text{for } r \leqslant R, \\ 0 & \text{for } r > R. \end{cases} \tag{47}$$

For these two cases (45) can be evaluated analytically. With (46) we get, with $M_c = \frac{4\pi}{3}\bar{\rho}\,R^3$,

$$\phi(x) = -\frac{3GM_c}{|\mathbf{x}|} - \frac{1}{(1+k_J^2R^2)}\left[\cos k_J x - \mathrm{e}^{-x/R}\right] \tag{48}$$

and for (47) we get

$$\phi(x) = \frac{3GM_c}{R}\,\frac{1}{(k_JR)^2}\left[1 - \frac{\sin k_J x}{k_J x}\,(k_JR\sin k_JR + \cos k_JR)\right], \quad x < R \tag{49}$$

$$= \frac{3GM_c}{R}\,\frac{1}{(k_JR)^2}\,\frac{\cos k_J x}{k_J x}\,[k_JR\cos k_JR - \sin k_JR], \qquad x > R. \tag{50}$$

Both (49) and (50) exhibit the 'cosine' dependence at large distances. It is also clear from (45) that for large x, it is the second integral in the right-hand side that contributes most, leading to the cosine dependence.

In the above analysis we have specified $\rho^{ext}(x)$ in an *ad hoc* manner. In reality, $\rho^{ext}(x)$ will be determined in a self-consistent manner by the response of the galaxies to the gravitational potential. This leads to some interesting tests of the above model which we shall indicate in the next section.

3. Comparison with observation

The discussion in the previous sections has been purely kinematic. In order to apply these results to any realistic astrophysical system, one has to consider the dynamics of the model as well. In particular, is it possible for a homogeneous distribution of collisionless relic to arise in standard big bang model? In the conventional picture of *v*-dominated universe with adiabatic fluctuations the first structures to form and collapse are the super clusters (Bond, Efstathiou & Silk 1980; Bond & Sazlay 1983). In such a picture, it will be very difficult to obtain a homogeneous distribution. On the contrary, there are other scenarios in which such a situation can arise. One simple possibility would be isothermal *v*-fluctuations. A more interesting situation, however can arise if there existed an unstable heavy neutrino which decays to the stable light neutrino (Simpson 1985; Fukugita & Yanagida 1984; Padmanabhan & Vasanthi 1985). The decay products would be relativistic at the time of decay and can provide a homogeneous background at reasonably low redshifts. While the dynamics of such a model is yet to be investigated fully, it is quite likely to be very different from the standard scenario. In general, dark matter observations can be explained with relative ease, if there are two components to dark matter: one of which is distributed reasonably homogeneously and the other clustered at smaller scales.

The above comments as well as the discussion in the following sections are somewhat tentative, and are intended only to point out certain possibilities. Whether these possibilities can be implemented realistically in a consistent astrophysical scenario is a question of dynamics and is beyond the scope of the present paper.

3.1 *Secondary Maxima in Clusters of Galaxies*

Given a reliable functional form of visible matter density in a cluster, one may attempt a self-consistent model-building based on the above discussion. However, as discussed in the last section, the theory predicts a sinusoidal dependence of the potential on the radial distance, as shown in Fig. 1. Qualitatively, we expect test galaxies to cluster around the minima of the potential. In other words, at least in some clusters, one expects a secondary maximum in the density distribution of visible matter. (Of course, such a maximum is observable only when it occurs well within the size of the cluster.)

From Equation (32) it can be seen that the second minimum of the potential occurs around $k_J\, x_m \simeq 2\pi$. Solving the equation for the turning points,

$$\cos k_J x + k_J x \sin k_J x = 0 \tag{51}$$

one finds the value to be,

$$x_m \simeq 6.1\, k_J^{-1}. \tag{52}$$

Using the definition of k_J we estimate

$$x_m = 0.6 \left(\frac{\rho_0}{1.5 \times 10^{-25}\ \mathrm{g\,cm^{-3}}} \right)^{-1/2} \left(\frac{\sigma}{10^3\ \mathrm{km\,s^{-1}}} \right) \mathrm{Mpc}. \tag{53}$$

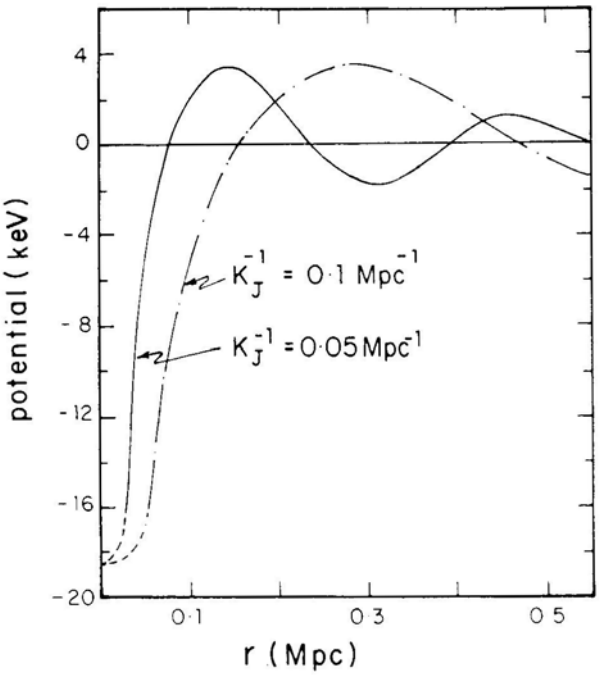

Figure 1. The perturbations of the cluster potential by the galaxies in the core.

We have scaled the expression with the value of ρ_0 usually quoted for the Coma cluster of galaxies. It is believed that ρ_0 for other clusters are somewhat lower. We have scaled the neutrino velocity dispersion σ by a typical galactic velocity dispersion in Coma cluster (900–1200 km s^{-1}). There is *no* deep theoretical reason to expect σ to have the same value, though some models suggest this possibility. Of course, Pauli principle sets the lower-limit

$$\sigma > v_F \simeq (30\ \mathrm{km\,s^{-1}})\left(\frac{\rho}{10^{-25}\ \mathrm{g\,cm^{-3}}}\right)^{1/3}\left(\frac{m_\nu}{50\ \mathrm{eV}}\right)^{-4/3}. \tag{54}$$

Because of these uncertainties the value of x_m will definitely vary from cluster to cluster. We may naively expect a secondary maximum within one order of (53) (*i.e.* in the range of 0.3 to 3 Mpc).

In the Coma cluster of galaxies, the velocity dispersion curves suggest a secondary maximum at about 20 arcmin from the centre which corresponds to a distance scale of about 0.7 Mpc.

A host of other clusters show evidence for a secondary maximum in the density distribution. It is worth noting that no other simple explanation exists for this feature (Baier 1983). We give in Table 1 a list of clusters (which exhibit the secondary maximum), using the values of the redshift to these clusters (Hoessel, Gunn & Thuan 1980).

We have estimated the distances x_m. It may be noted that all these values fall between 0.49 Mpc and 1.44 Mpc, giving excellent qualitative agreement with the value in (53). Assuming that the missing mass density in all these clusters is of the order of

Table 1. List of clusters exhibiting secondary maximum ($H = 50\ h$ km s^{-1} Mpc^{-1}.)

Serial No.	Cluster name	Redshift Z	Position of secondary max arcmin	Position of secondary max h^{-1} Mpc	k_J^{-1} Mpc
1	A147	0.044	7.4	0.57	0.09
2	A576	0.0392	7.3	0.50	0.08
3	A671	0.0497	8.0	0.69	0.11
4	A1225	0.1033	8.0	1.44	0.24
5	A1227	0.0339	8.0	0.47	0.08
6	A1383	0.0598	13.5	1.41	0.23
7	A1775	0.0718	11.5	1.44	0.24
8	A2029	0.0777	7.5	1.02	0.17
9	A2666	0.0273	8.0	0.38	0.06
10	A1656 (Coma)	0.0224	20.0	0.78	0.13

10^{-25} g cm^{-3} (which actually is somewhat large), one may conclude that the dark matter has a velocity dispersion of a few thousands of kilometres per second.

3.2 *Rotation Curves of Galaxies*

Let us consider a galaxy situated somewhere near the first minimum of the potential (as we saw in Section 3.1, this occurs at $r = R$ with $R = 6.1\ k_J^{-1}$). We assume that the centre of the galaxy is located at R and the linear extent of the galaxy is small compared to cluster scale. A star moving in the galaxy at a distance ξ from the centre of galaxy will be subject to the combined gravitational force of the galaxy and the cluster. The potential due to the galaxy at ξ is of the order of

$$\phi_G \simeq -\frac{GM_G}{\xi} \tag{55}$$

where M_G is the mass of the galaxy. The cluster potential at a point r is of the order of

$$\phi_c \simeq -\frac{GM_c}{r}\cos k_J r \tag{56}$$

where M_c is the core mass of the cluster. In our case $r = R + \xi$ with $\xi \ll R$. Expanding in a Taylor series and noticing that $\phi'_c(r)$ is zero, we get

$$\phi_c(\xi) = \left[\frac{GM_c k_J^2}{2R}\cos k_J R\right]\xi^2 + \text{constant} \tag{57}$$

$$\simeq \frac{GM_c k_J^2}{2R}\xi^2, \tag{58}$$

where we have approximated $\cos k_J r$ by unity and dropped an unimportant constant. Thus the total potential felt by the star at ξ is given by

$$\phi_{\text{total}} = \frac{GM_c k_J^2}{2R}\xi^2 - \frac{GM_G}{\xi}. \tag{59}$$

The rotational velocity of a star at ξ is given by

$$v^2(\xi) = \xi \frac{\partial \phi_{\text{total}}}{\partial \xi} = \frac{GM_c k^2}{2R} \xi^2 + \frac{GM_G}{\xi} . \tag{60}$$

Using $kR = 6.1$, v^2 can be written as

$$\left(\frac{v}{v_m}\right)^2 = 5.89 \left(\frac{M_c}{M_G}\right)^{2/3} \left[x^2 + 0.03 \frac{M_G}{M_c} \frac{1}{x} \right] \tag{61}$$

where

$$v_m^2 = 6.3 \frac{GM_c}{R} \left(\frac{M_G}{M_c}\right)^{2/3}$$

and

$$x = (\xi/R).$$

Since $v^2(\xi)$ contains two terms, one increasing with and the other decreasing with ξ, it is easy to see that v^2 can be flat for a range of ξ.

We show in Fig. 2 the result of a numerical computation of v; for a set of fiducial values of parameters (M_c = 1.5 × 1014 $M_\odot$, M_G = 4 ×1011 $M_\odot$). The density distribution of galaxies was smoothened out near $\xi = 0$ to avoid the singularity at the origin. As can be seen from Fig. 2, the rotation curve is reasonably flat for a large range in ξ. The flatness of rotation curves is probably the most convincing evidence for the dark matter. However, one should *not* consider rotation curves as a "crucial" test for dark matter modelling. It is fairly straightforward to explain flat rotation curves once some form of dark matter distribution is invoked. All these models require some special

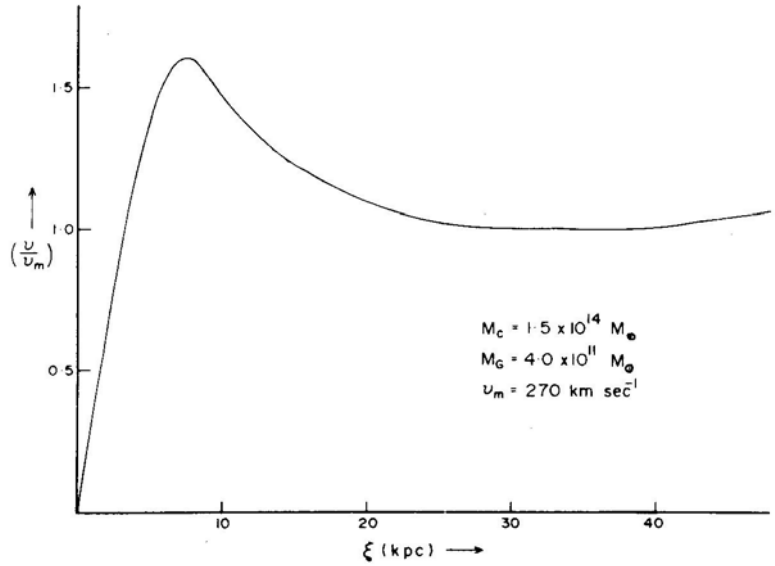

Figure 2. Rotation curve of a fiducial galaxy. The rotational velocity v, is plotted (in units of the flat value v_m) against the distance ξ from the centre of the galaxy. Note that the curve is reasonably flat from $\simeq$ 20 kpc to 50 kpc. M_c is the cluster core mass, and M_G is the galaxy mass. The flatness of the curve does not depend sensitively on the value of these parameters.

alignment of the galaxy with respect to the dark matter distribution (they are usually taken to be concentric). In our case we have assumed that the galaxy is near the mininum of the potential. Thus we do not feel that explanation of rotation curve is a sufficiently critical test of the dark matter distribution. The picture presented here is not complete to every detail (Explanation for flat rotation curves using a neutrino background is also attempted in Cowsik & Ghosh (1986) & Basdevant (1984)). In particular, the present model is incapable of explaining the rotation curves of field galaxies.

4. Conclusions

It is interesting to observe that grativational perturbations in an infinite medium may actually lead to some observable consequences. Various aspects of this work requires further study. It is necessary to develop a model for dark matter distribution by evolving the collisionless Boltzmann equation from the past taking the expansion of the universe into consideration. Such an investigation is especially important in deciding whether dark matter condensates are truly isolated finite gravitating systems (like, say, galaxies or clusters of galaxies) or whether they extend throughout the universe with an increased density contrast near gravitating objects (Padmanabhan & Vasanthi 1985). It would be also interesting to see how sensitively our results depend on various approximations made in this paper (for example, homogeneity of background, linearization of equations *etc.*). Even at this stage the idea that neutrinos or some other 'inos' of finite mass play an essential role in the dynamics of the universe and are responsible for a wide variety of phenomena otherwise not understandable seems to be quite attractive.

Acknowledgement

We are thankful to Professor R. Cowsik who has made significant contribution to the evolution of ideas presented in this paper.

References

Bahcall, N. A. 1977, *A. Rev. Astr. Astrophys.*, **15,** 505.
Baier, F.W.1983, *Astr. Nachr.*, **304,** 211.
Basdevant, J. L.1984, *Astr. Astrophys.*, (Submitted).
Bond, J. R., Efstathiou, G, Silk, J. 1980, *Phys. Rev. Lett.*, **45,** 1980.
Bond, J. R., Szalay, A. S. 1983, *Astrophys. J.*, **274**, 443.
Bosma, A. 1978, *Ph.D. Thesis*, Gröningen University.
Cabbibo, N., Farrar, G R., Maiani, L. 1981, *Phys. Letts.*, **105B,** 155.
Chubb, T. A. 1983, Preprint (E.O. Hulburt center for space research).
Cowsik, R.1983, *Current Sci.*, **52,** 1104.
Cowsik, R. 1985, *J. Astrophys. Astr.*, 7, (inpress).
Cowsik, R., Ghosh, P. 1985, J. *Astrophys. Astr.*, **7**, (in press).
Cowsik, R., McClelland, J.1973, *Astrophys. J.*,**180,** 7.
Cowsik, R.,Vasanthi, M.M.1985, *J. Astrophys. Astr.*, **7**, (in press).
Davis, M., Lecar, M., Pryor, C, Witten, E. 1981, *Astrophys. J.*, **250,** 423.

Doroshkevich, A. G., Khlopov, M. Yu., Sunyaev, R. A., Szalay, A. S., Zeldovich, Ya. B. 1981, *Ann. N.Y. Acad. Sci.*, **375,** 32.
Faber, S. M., Gallagher, J. S. 1979, *A. Rev. Astr. Astrophys.*, **17,** 135.
Fukugita, M., Yanagida, 1984, *Phys. Letts.*, **144B,** 386.
Hoessel, J. G., Gunn, J. E., Thuan, T. X. 1980, *Astrophys. J.*, **241,** 486.
Klinkhamer, F. R., Norman, C. A. 1981, *Astrophys. J.*, **243,** L1.
Lifshitz, E. M., Pitaevskii, L. P. 1981, *Physical Kinetics—Landau and Lifshitz course of Theoretical Physics*, Vol. 10 (Pergamon Press).
Marochnik, L. S. 1968, *Sov. Astr.*, **11,** 873.
Melott, A. L. 1983, *Astrophys. J.*, **264,** 59.
Milgrom, M. 1983, *Astrophys. J.*, **270,** 365.
Olive, K. A., Turner, M. S. 1982, *Phys. Rev.*, **D25**, 213.
Padmanabhan, T., Vasanthi, M. M. 1985, *J. Astrophys. Astr.* (Submitted).
Padmanabhan, T., Vasanthi, M. M. 1985, *Nature*, **317,** 335.
Pagels, H., Primack, J. R. 1982, *Phys. Rev. Lett*, **48,** 223.
Peebles, P. J. E. 1979, *Les Houches Summer School Lecture Notes.*
Peebles, P. J. E., 1980, *Large Scale Structure of the Universe*, Princeton Univ. Press, New Jersey.
Peebles, P. J. E. 1982, *Astrophys. J.*, **258,** 415.
Rood, J. H. 1981, *Rep. Prog. Phys.*, **44,** 1077.
Rubin, V. C. 1979, *Comm. Astrophys.*, **8,** 79.
Rubin, V. C, Ford, W. K. J., Thonnard, N., Burstein, D. 1982; *Astrophys. J.*, **261,** 439.
Rubin, V. C, Thonnard, N., Ford, W. K. J. 1982, *Astr. J.*, **87,** 477.
Rubin, V. C, Ford, W. K., Thonnard, N. 1980, *Astrophys. J.*, **238,** 471.
Sato, H., Takahara, F. 1981, *Progress Theor. Phys.*, **66,** 508.
Schramm, D. N., Steigman, G. 1981, *Astrophys. J.*, **243,** 1.
Sikivie, P. 1982, *Phys. Rev. Lett.*, **48,** 1156.
Simpson, J. J. 1985, *Phys. Rev. Lett.*, **54,** 1891.
Wasserman, J. 1981, *Astrophys. J.*, **248,** 1.
Weinberg, S. 1972, *Gravitation and Cosmology*, Wiley, New York.

J. Astrophys. Astr. (1985) **6**, 261–277

Nature and Distribution of Dark Matter: 1. Dwarf Spheroidals and Milky Way

T Padmanabhan & M.M. Vasanthi *Tata Institute of Fundamental Research, Homi Bhabha Road, Bombay 400005*

Received 1985 June 14; accepted 1985 September 20

Abstract. We argue that observations on Milky Way and dwarf spheroidals imply existence of individual haloes around dwarf spheroidals. If neutrinos (or any other 'hot' particle) provide the dark matter then we show that: (i) Embedding of visible matter inside large (~ few Mpc) dark matter islands is observationally untenable. (ii) Dwarf spheroidals possess dark matter haloes of about 10 kpc radius around them, and have an (M/L) ratio of about 10^4. (iii) The haloes of spiral galaxies (*e.g.* Milky Way) extend to about 100 kpc in radius. If 'cold' dark matter makes up the haloes, then no significant constraints are obtained. We discuss briefly the effect of these constraints on larger scales.

Key words: dark matter—dwarf spheroidals—neutrinos—Milky Way

1. Introduction and summary: Is dark matter hot or cold?

It is likely that most of the matter in the universe is invisible; that is, it emits little or no electromagnetic radiation. The dark matter makes its presence known through gravitational effects. The flat rotation curves of spiral galaxies (Rubin 1979; Rubin *et al.* 1982; Rubin, Thonnard & Ford 1982) and the mass to light ratios of large virialized clusters (see *e.g.* Rood 1981; Faber & Gallagher 1979), are most easily interpreted in terms of dark matter haloes. (Alternative interpretations, involving modification of dynamical laws will not be considered in this paper; (see Milgrom 1983; Bekenstein & Milgrom 1984).

What does the invisible halo consist of? Since most of the visible matter is made of baryons, one may attempt to build the haloes from baryonic matter. However, a variety of observational constraints make baryonic dark matter an unattractive alternative, if not an impossibility, (Hegyi 1984).

Leptonic dark matter could consist of any of the host of particles postulated to exist by the particle physicists. Among leptons, massive neutrinos were one of the earliest candidates (Gerhstein & Zeldovich 1966; Cowsik & McClelland 1972; Marx & Szalay 1972). An experimental claim (as yet unconfirmed by other teams) that electron neutrinos are massive gave impetus to this idea (Lubimov *et al.* 1980). Considerable amount of work was done in recent years regarding the kinematics and dynamics of neutrino dominated universe (Sato & Takahara 1980; Bond, Efstathiou & Silk 1980; Doroshkevich *et al.* 1981; Klinkhamer & Norman 1981; Wasserman 1981; Peebles

1982). Two disturbing features emerged from this analysis: (i) If massive neutrino haloes exist around dwarf spheroidals, with scale lengths comparable to that of visible matter, then the neutrino mass should be greater than about 530 eV which is completely ruled out (Aaronson 1983; Lin & Faber 1983). (ii) The numerical experiments suggest that galaxy formation in a neutrino dominated universe would have taken place at redshifts $z < 2$, which is in contradiction with the existence of high redshift objects conventionally interpreted as the nuclei of galaxies (Frenk, White & Davies 1983; Dekel & Aarseth 1984; Hut & White 1984; Kaiser 1983; Mellot 1983; Faber 1984). These two features make neutrinos rather unattractive. (For attempts to reconcile these features with the hypothesis of neutrino dominance, see Cowsik & Ghosh 1986; Mellot 1985.)

Motivated by these considerations, many people have attempted to model the dark matter by supersymmetric fermions ('sparticles') and axions. Since these particles are heavier than neutrinos, their 'thermal' velocities will be lower, earning them the name 'cold dark matter'. (Neutrino, on the other hand, is an example of 'hot dark matter'.) Cold dark matter can be made to avoid the two difficulties mentioned in the previous paragraph with relative ease (Blumenthal *et al.* 1984; Primack 1984). On the other hand they seem to face some trouble in explaining the largest scale structures *viz.* superclusters and voids (Primack & Blumenthal 1984). Besides, the experimental evidence for the existence of many of the cold dark matter candidates is weaker than that for the nonzero mass of the neutrino. (Theoretical ideas have to be hastily reshaped if the mass of any species of neutrinos is proved to be definitely non-zero!).

Taking an unprejudiced viewpoint, one may ask: Do observations give a clear cut 'yes' or 'no' answer to the existence of 'hot' or 'cold' dark matter?

We attempt to discuss this question in a series of three papers. In the present paper we analyse the constraints on dark matter distribution which arise from observations on our Galaxy and the dwarf satellites. The second paper will discuss groups and clusters of galaxies; the third paper will consider various dynamical aspects of clustering.

Within the scope of existing observations, we have *not* been able to provide a clear cut 'yes-no' answer to the question we have raised. However, rather stringent constraints can be imposed on the scale length, shape and densities of dark matter haloes. We find that neutrino ('hot' dark matter) distribution is much more severely constrained than any cold dark matter scenario. If neutrinos constitute the dark matter, then, we show:

(i) Scenarios in which galaxies are embedded in large (~ Mpc) neutrino 'islands' are ruled out by observations.
(ii) The halo around our Galaxy cannot extend significantly beyond ~ 60 kpc.
(iii) Dwarf spheroidals must have, a halo which extends upto about 10 kpc from their centre. This will give dwarf spheroidals a mass to light ratio of 10^4(!) making them very peculiar objects.

Cold dark matter, on the other hand does not lead to such stringent conditions. We leave the reader to judge for himself whether these constraints effectively rule out neutrino dominance.

The paper is organized as follows: In Section 2, we review and analyse the existing observational data about Milky Way and dwarf spheroidals. Section 3 compares standard theoretical modelling with the observations and determines the constraints. Section 4 discusses various offshoots, arguments and counterarguments based on the previous sections.

2. Dark matter observations

2.1 *Milky Way*

The visible matter in our Galaxy does not extend significantly beyond l0 kpc. Presumably the effects of dark matter haloes would be most pronounced at distances > 10 kpc. The rotation curve derived from 21 cm observations is reasonably flat right from about 8 kpc. Using CO observations of molecular complexes related to H II regions, the flat rotation curve can be extended out to 16 kpc. At larger distances, globular clusters can be used as tracers of dark matter. The data from globular clusters (as well as 21 cm and CO observations) are summarized in Fig. 1. (The data are taken from the conclusions of Innanen, Harris & Webbink 1983; Faber & Gallagher 1979; Hartwick & Sargent 1978; Peebles 1979; Mihalas & Binney 1981; Gunn, Knapp & Tremaine 1979; Similar data are also presented in Lynden-Bell 1983.)

Within the limits of observational error, the data are very well fit by the mass radius curve,

$$M(r) = (1.4 \pm 0.2) \times 10^{10}\, M_{\odot}\, (r/1\ \mathrm{kpc}). \tag{1}$$

The error-bar in the coefficient arises from the spread in the data points. The mean curve (solid line) and the spread (broken lines) are shown in Fig. 1.

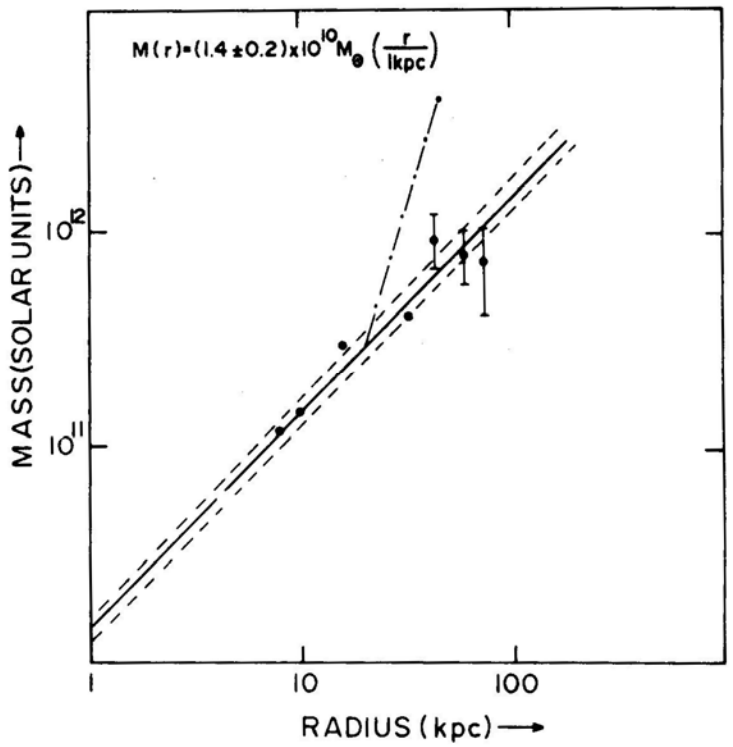

Figure 1. Total mass M within a radius r plotted against the radius r of the Milky Way galaxy. The solid line is the best fit curve for $M(r)$ equation. The broken lines are the best fit lines with upper and lower limits on error bar. The dot-dash line represents the $M - r$ curve corresponding to Equation (13) in the text.

For judging the goodness of fit, the data were tested with a power law $M \propto r^n$. The best fit value for n turns out to be 0.9 with a σ^2 (mean square deviation) of 0.0095. On the other hand, the theoretical curve $M \propto r$, shown in the figure has a σ^2 of 0.01 which is comparable to 0.0095, indicating a good fit. For future reference, we may note that $M \propto r^3$ curve leads to a σ^2 of 0.58, nearly sixty times higher.

We note that, in the range 8 kpc < r < 75 kpc, the mass distribution (1) is equivalent to the density fall off

$$\rho(\mathrm{r}) = 8.1 \times 10^{-23} \mathrm{g\ cm^{-3}}\ (r/1\ \mathrm{kpc})^{-2} \tag{2}$$

2.2 *Dwarf Spheroidals*

The seven dwarf spheroidals Fornax, Sculptor, Leo I, Leo II, Draco, Ursa Minor and Carina are usually considered to be the satellite galaxies of Milky Way. The gravitational mass of these objects were determined recently (Faber & Lin 1983; Aaronson 1983). In Fig. 2, we have plotted the gravitational mass of the dwarf spheroidals against their radii, in a log-log plot. The 'best fitting' curve is,

$$M\,(r) = 3.6 \times 10^6\, M_\odot\ (r/1\ \mathrm{kpc})^{2.4} \tag{3}$$

However, the σ^2 for this fit is about 0.24. For comparison we tried $M \propto R$ curve and $M \propto R^3$ curve which give σ^2 values of 0.31 and 0.26 respectively. Clearly the data are too scattered for being fitted into any single power law curve with significantly small σ^2.

For Draco and Ursa Minor mass estimates are available from velocity dispersion (Aaronson 1983) while for others the masses are estimated from tidal non-disruption. One may plot the mean density of dwarf spheroidals against their distance from Milky Way. (The distances are heliocentric distances.) This plot is shown in Fig. 3. The solid line in the figure corresponds to the relation,

$$\rho_{\mathrm{DS}}(r) = 9.2 \times 10^{-22}\ \mathrm{g\ cm^{-3}} (r/1\ \mathrm{kpc})^{-2} \tag{4}$$

The σ^2 for this fit is 0.009; for comparison, the best fit curve for $\log \rho - \log r$ has a slope of (– 2.2) and σ^2 of 0.006. Thus the mean densities of dwarf spheroidals falloff as the inverse square of the distance from Milky Way. This is to be expected because tidally limited mass estimates are used for most dwarfs. A comparison of (4) and (2) shows that ρ_{DS} exceeds the expected dark matter halo density of Milky Way at the same location by about a factor of 10. We shall discuss this point more fully in the next section.

2.3 *Spirals*

The flat rotation curve of Milky Way signals the relation $M \propto r$. It is well known that this feature is exhibited by a large number of spiral galaxies. If we denote the mass-radius relation of n^{th} spiral galaxy in a sample by

$$M\,(r) = c_n r \tag{5}$$

then we may ask the question: How different are the numbers in the set $\{c_n\}$? If the dark matter halo around the galaxies are more fundamental units than the visible galaxies, then we would expect the $\{c_n\}$ to be 'reasonably' close to each other. One main source of

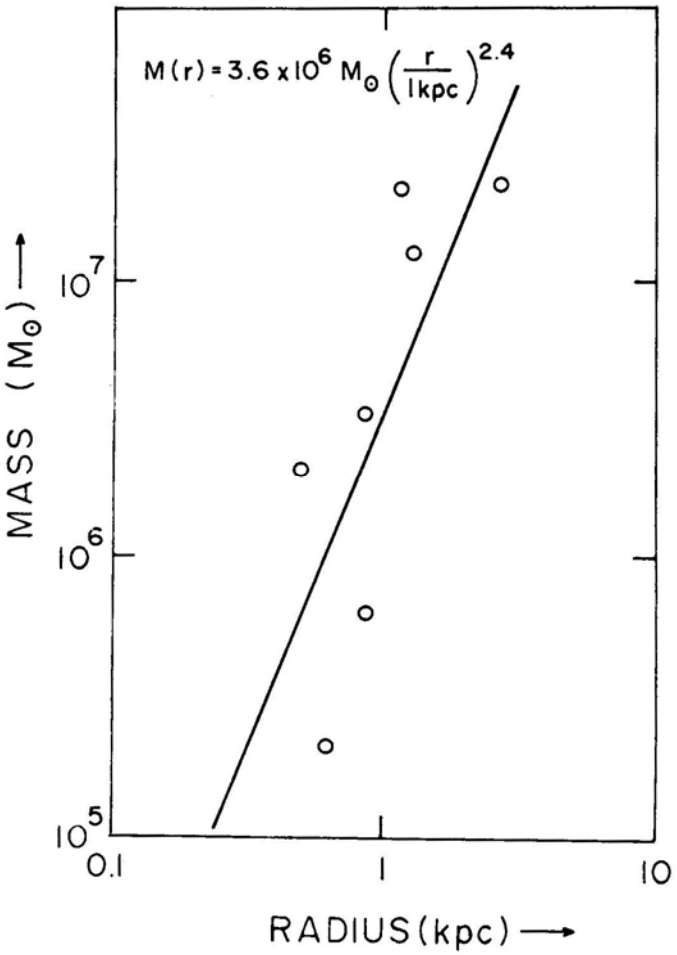

Figure 2. The mass M of the dwarf spheroidals plotted against the radius r of the dwarf spheroidals. The solid line is the best fitting curve,

$$M(r) = 3.6 \times 10^6\, M_\odot\, (r/1\ \text{kpc})^{2.4}.$$

scatter in the $\{c_n\}$ is the mass variation in the visible part of the galaxies themselves. (Since M in (5) is the total mass, the variation in visible part will affect c_n). This scatter can be minimized by studying the relation (5) for various types of spirals individually.

In Figs 4(a, b) we have plotted the mass–radius relation for SAB and SA types spirals. The data are taken from the table given by Faber & Gallagher (1979). The gravitational mass estimated from rotation velocity at the Holmberg radius is plotted against the corresponding Holmberg radius. In a further attempt to minimize the effect of visible part of the galaxy we have used only those spirals with (Holmberg) radius greater than 15 kpc.

In the case of SAB galaxies all the points lie within a strip indicated by dotted lines in Fig. 4(a) corresponding to (with solid line showing the best fit),

$$M(r) = (3\text{–}9) \times 10^{10}\, M_\odot\, (r/1\ \text{kpc}). \tag{6}$$

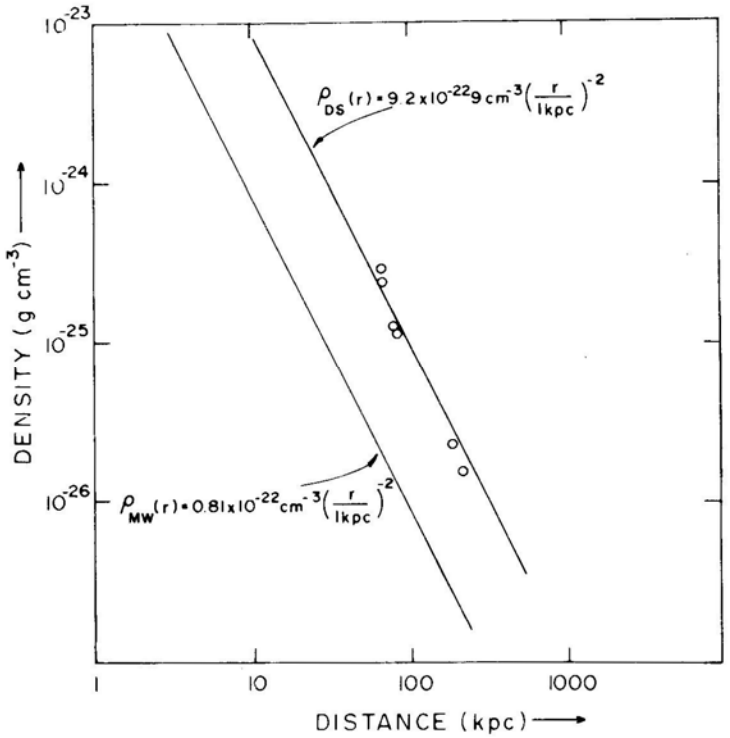

Figure 3. The solid line shows mean density of dwarf spheroidals plotted against the distance of dwarf spheroidals from the centre of the Milky Way. The thin line shows the density falloff of MW as a function of its distance from the centre of MW.

On the other hand all SA galaxies are bound within the mass–radius curves

$$M(r) = (0.5\text{–}2.5) \times 10^{11}\, M_{\odot}\, (r/1\ \mathrm{kpc}). \tag{7}$$

Considering the scales and uncertainties involved one may reasonably assume that c_n's do not differ from each other drastically.

In other words, all spirals are embedded in individual dark matter haloes with r^{-2} density profile. We shall attempt later (in Section 4 as well as in subsequent papers) to treat galaxies with dark haloes as basic units. Spiral galaxy observations add credibility to this assumption.

We shall now consider the constraints on the theoretical models which arise from the above observations.

3. Theoretical models

The constraints on theoretical models naturally depend on some basic assumptions as well as on the nature of the dark matter: (a) neutrino (hot) or (b) cold dark matter. We shall discuss (a) and (b) separately below.

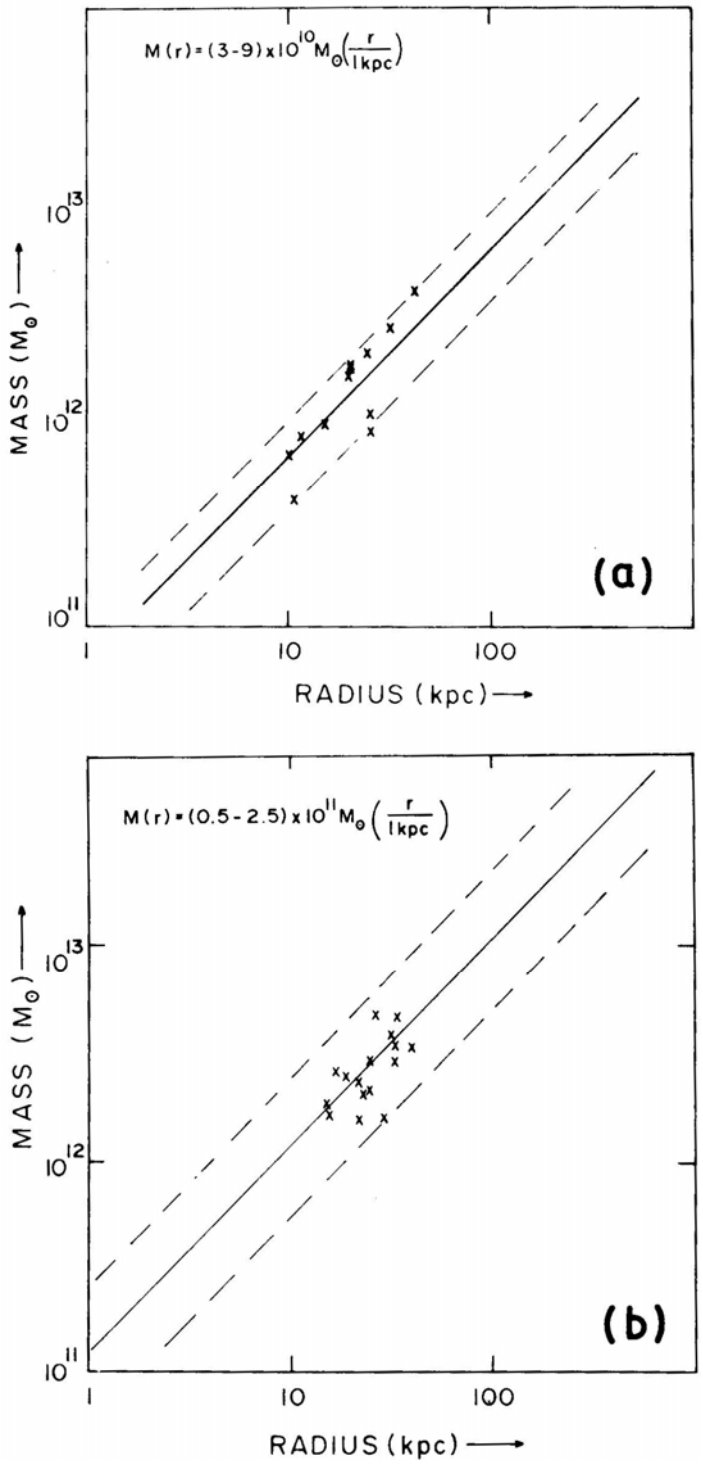

Figure 4. Mass-radius relationship for a) SAB spirals b) SA spirals. The solid line shows the best fit curve.

3.1 *Neutrino* (*Hot*) *Dark Matter*

Assuming neutrinos constitute the dark matter in the universe, we have the well-known constraint from cosmology (Gerhstein & Zeldovich 1966; Cowsik & McClelland 1972)

$$\sum_i m_i \leqslant 100\ \mathrm{eV} \cdot \Omega h^2. \tag{8}$$

Here the sum is over all species of neutrinos, h is the Hubble constant in units of 100 km s^{-1} Mpc^{-1} and Ω is the ratio between mass density of the universe and critical density. Assuming a single species of neutrino and that $\Omega h^2 \sim 1/2$, we shall take m_ν to be less than 50 eV. The only existing experimental support for massive neutrinos suggests a bound 14 eV < m_ν < 40 eV. Thus $m_\nu \sim 30$ eV will be used for scaling the expressions in what follows.

Tremaine & Gunn (1979) have shown that m_ν must satisfy the constraint,

$$m_\nu^4 > \frac{9\,h^3}{4(2\pi)^{5/2} g_\nu G \sigma_\nu r_{cv}^2} \tag{9}$$

where σ_ν is the velocity dispersion of neutrinos bound in a gravitational potential well of core radius r_{cv}. The constraint (9) arises from the theorem (see for example, Lynden-Bell 1967), which states that maximum coarse grained phase space density can only decrease with time. Equation (9) can be rewritten as (note a crucial printing error in the original paper of Tremaine & Gunn 1979).

$$m_\nu > (101\ \mathrm{eV})\ (\sigma_\nu/100\ \mathrm{km\ s^{-1}})^{-1/4} (r_{cv}/1\ \mathrm{kpc})^{-1/2}\ g_\nu^{-1/4}. \tag{10}$$

If we make the following two crucial assumptions: (i) the σ_ν for neutrinos in dwarf spheroidals is the same as that of baryonic matter ~ 10 km s^{-1} (Aaronson 1983) and (ii) the r_{cv} for neutrinos in dwarf spheroidals are of the same order as that of tidal radii of baryonic matter ~ 1 kpc, then we get $m_\nu > 170$ eV, in violent contradiction with (8). Clearly hot dark matter picture is in trouble.

The only way to escape this situation is to relax the assumptions (i) and (ii) in the above paragraph. If one assumes that the velocity dispersion of neutrinos is much higher than that of baryonic matter, making the r_{cv} much larger than $r_{c\ \mathrm{baryons}}$ (= r_{cb}). Clearly this will bring down the right hand side of (10) allowing one to escape the constraint. The question that faces us is the following: How much can one push up r_{cv} and σ_ν?

There are three essentially different approaches which one may consider at this stage: (i) Neutrinos form large (few Mpc) dark matter islands in which our local group and dwarf spheroidals are embedded (Cowsik & Ghosh 1986). There is no dark matter bound to dwarf spheroidals individually, (ii) Dwarf spheroidals are imbedded in the haloes of our Galaxy. The neutrino halo extends for ~ 250 kpc around Milky Way. No significant amount of dark matter is attached to dwarf spheroidals. (iii) Dwarf spheroidals do have a neutrino halo around them, but this halo has $r_c \gg r_{cb}$.

We shall now show that approaches (i) and (ii) are theoretically and observationally unsound; it is essential to assume that there exists dark matter bound individually to dwarf spheroidals.

To see this consider the mass and density profiles of Milky Way shown in Figs 1 and 3. Milky Way dark matter, right up to 75 kpc, is definitely not a constant density profile.

The density enhancement between 10 kpc and 100 kpc is by a factor 100 and cannot be treated at all as a small perturbation on a constant density background. The best analysed dwarf spheroidals Draco and Ursa Minor are at about 67 kpc which is in the region of $M \propto r$ behaviour. (This conclusion is independently supported by the standard Milky Way modelling by Lin & Lynden-Bell (1982) based on Magellanic Stream and by Frenk & White (1982) based on globular cluster orbits.) Dark matter halo around our Galaxy is best represented by an isothermal sphere.

Is it possible to assume that the visible matter in dwarf spheroidals only sample the neutrinos which are actually bound to the halo around Milky Way, but just happen to be streaming in the vicinity of dwarfs? This is impossible because of two reasons.

Firstly observations show that the density of gravitating matter in dwarf spheroidals is more than ten times higher than that of Milky Way halo density at that point. (See Equations 2 and 4.) This ten-fold local enhancement of density indicates the existence of about $10^6\ M_\odot$ of dark matter *bound* to the dwarf spheroidals. Secondly, considerations of tidal stability imply the existence of dark matter *bound* to dwarf spheroidals. Consider embedding a dwarf spheroidal in the isothermal halo of our Galaxy. The condition for the tidal stability of the dwarf spheroidals can be derived from Chandrasekhar (1942); (Section 5.5; Equations 5.601 to 5.613.) We get

$$(\bar{\rho}_\nu + \bar{\rho}_B)_{\text{bound}} > 6\ \rho_{bg}. \tag{11}$$

Here $\bar{\rho}_\nu$ and $\bar{\rho}_B$ on the left denote average density of neutrinos and baryons (stars) *bound* to the dwarf spheroidal, while ρ_{bg} is the density of background dark matter (*not* bound to dwarf spheroidal; part of Milky Way halo or still larger structure), at the vicinity of the dwarf spheroidal. Since ρ_{bg} in the vicinity of Draco or Ursa Minor (~ 67 kpc) is about 2 times 10^{-26} g cm^{-3} , the density of matter bound to Draco should satisfy the condition,

$$(\bar{\rho}_\nu+\bar{\rho}_B)_{\text{bound}} > 1.2\times10^{-25}\ \text{g cm}^{-3} \tag{12}$$

In a size of 1 kpc, this implies a gravitationally bound mass of ~ 8 ×10 $M_\odot$, which is more than one order of magnitude higher than the visible matter (both Draco and Ursa Minor have visible mass of ~ $2\times10^5\ M_\odot$; see Faber & Lin 1983). In other words the amount of dark matter *bound* to these dwarf spheroidals must be quite high (~7.8 $\times10^6\ M_\odot$) to ensure tidal stability. Thus, both observationally and theoretically, there must exist dark matter *bound* to dwarf spheroidals.

Before we proceed further we would like to emphasize three important points relevant to this discussion, (i) Equation (11) was derived assuming the satellite galaxy to be orbiting Milky Way in a low eccentricity orbit. Eccentricity of the orbit will change the numerical coefficient 6 in Equation (11) to a higher value making matters worse (King 1962). (ii) The background density $\rho_{bg}(r)$ may vary very little over the *visible* extent (~1 kpc) of the dwarf spheroidal. We shall show later that even $(\rho_\nu)_{\text{bound}}$ does not vary significantly over the visible extent of the dwarf spheroidals. This does not affect the tidal stability argument, (iii) On the other hand, the fact that ρ_{bg} is; not globally constant is crucial for the tidal stability argument. This is because a globally constant density distribution tidally *compresses* matter rather than *disrupts.*

The last point mentioned above shows that we may be able to make the tidal constraint less severe by flattening the $r_{bg}\,(r)$ to a constant value beyond some radius r_f. Since Draco is at ~ 67 kpc, r_f < 67 kpc (at least). Further Draco and Ursa Minor have ρ_ν of the order of ~2×10^{-25} gcm^{-3}. To provide this much of background density the

Milky Way halo must flatten from about $r_f \sim 20$ kpc. (From (2) we see that $\rho_{bg} \simeq 2 \times 10^{-25}$ gem^{-3} when $r \sim 20$ kpc.) In other words, one requires a density profile like,

$$\rho_{bg} = 8 \times 10^{-23} \text{ g cm}^{-3} (r/1 \text{ kpc})^{-2} \qquad r \leqslant 20 \text{ kpc}$$

$$= 2 \times 10\text{–}25 \text{ g cm–}3 \qquad r \geqslant 20 \text{ kpc} \qquad (13)$$

Such a drastic assumption leads to many more problems: First of these is the direct contradiction with accepted mass-radius relation for Milky Way halo. (We have indicated modified mass profile based on (13) by a dash dot line in Fig. 1 which goes outside the error bars of known observations.) Secondly it is impossible to ensure the dynamical stability of an artificial configuration like the one in (13) where density falls by *two orders* of magnitude and then remains constant. Lastly a configuration like (13) will over-estimate the mass of local group (Milky Way–Andromeda systems) by a large factor. For example, if we assume (13) to be valid up to ~ 300 kpc (tidally limited radius of Milky Way by Andromeda) the mass contribution of Milky Way to our local group is greater than $3 \times 10^{14} M_\odot$! This is nearly two orders higher than the *upper bound* ($8.6 \times 10^{12} M_\odot$) obtained by studying the infall of local group towards Virgo cluster (Lynden-Bell 1983). In short, there is no escape from assuming the existence of dark matter bound to dwarf spheroidals.

Granted that neutrinos are bound around dwarf spheroidals what kind of constraints can we obtain regarding their distribution?

From (10) it is clear that one has to increase the velocity dispersion σ_v and the core radius r_v of the neutrino distribution. We shall now see how much latitude exists in these parameters. Suppose that the baryons are described by a truncated isothermal sphere with core radius $r_{b,}$ velocity dispersion σ_b and cutoff radius r_t. (The sharp cutoff at an outer radius could be tidal truncation or because of the Gaussian falloff arising from neutrino core.) Observationally, for the four dwarfs Sculptor, Draco, Ursa Minor and Carina (which Faber & Lin 1983 cite as having $M/L > 1$), the tidal cutoff radius r_t varies between 0.5 kpc to 1.28 kpc with a mean value of 0.94 kpc. One may take the core radius r_b to be about one-tenth of cutoff radius; *i.e.* $r_b \sim 100$ pc. The σ_b for dwarfs are quite uncertain. Estimating from the visible mass, as

$$\sigma_b \sim (GM_b/r_t)^{1/2} \qquad (14)$$

it varies between 0.59 km s^{-1} and 2.63 km s^{-1} with an average of 1.4 km s^{-1} . (This value is consistent with Aaronson's (1983) measurements, though he uses a χ^2 bound of 6.4 km s^{-1} for this discussion.) As for neutrino halo we shall assume it to be a concentric isothermal sphere with core radius r_v and velocity dispersion σ_v. When concentric isothermal spheres form out of violent relaxation (or virialization) their core densities will be comparable (see *e.g.* Sato 1981). Since central densities of isothermal spheres are related to core radius and velocity dispersion as,

$$\rho_c = 9\sigma^2/(4\pi G r^2) \qquad (15)$$

the equality $\rho_{vc} \simeq \rho_{bc}$ implies, (for a discussion of this assumption, see Appendix 2),

$$\sigma_v/\sigma_v = \sigma_b/r_b. \qquad (16)$$

Using Equation (16), after some simple algebra Equation (10) can be rewritten as,

$$m_v > (1010\text{eV})(1 \text{ km s}^{-1}/\sigma_b)^{1/4}(100 \text{ pc}/r_b)^{1/2}(r_b/r_v)^{3/4} \qquad (17)$$

or equivalently,

$$(r_v/r_b) > 109(m_v/30\ \text{eV})^{-4/3}(1\ \text{km s}^{-1}/\sigma_b)^{1/3}(100\ \text{pc}/r_b)^{2/3}. \quad (18)$$

The right-hand side is scaled to 'physically reasonable' parameters. (For comparison we note that with σ_b = 10km s^{-1}, r_b = 200 pc the coefficient 109 becomes 32.) We see from (18) that the neutrino core radius must be nearly 100 times the baryonic core radius; with r_b ~ 100 pc, r_v ~ 10 kpc. (By resorting to the extreme limits of σ_b ~ 10 km s^{-1}, r_b ~ 200 pc, we will get r_v ~ 6.4 kpc.)The baryonic matter with cutoff at r_t ~ 1 kpc is situated well within the neutrino core.

Such a large neutrino core will give an *M/L* value *at the tidal radius* r_t to be about,

$$M/L = 3(r_t/r_b)^2 \sim 300. \quad (19)$$

However the true *M/L* associated with the dwarf spheroidal is much higher than 300, because the halo extends much further than r_t. One may estimate the tidally limited halo radius by setting,

$$(M_v/x^3) > [M_{bg}/(R-x)^3] \quad (20)$$

where $M_v(x)$ is the halo mass around dwarf within a distance x from its centre and M_{bg} is the mass in the halo of Milky Way within a distance $R - x$ from Milky Way. (R is the centre to centre distance between the spheroidal and Milky Way.) Simple calculation based on our model will give,

$$x/R < [1+ (225\ \text{km s}^{-1}/\sigma_v)]^{-1} \quad (21)$$

For Draco, with R ~ 70 kpc, σ_v ~ 100 km s^{-1}, x is about 20 kpc. Within 20 kpc, Draco will have a halo mass of 5 × 10^{10} $M_\odot$ and *M/L* ratio of about 10^4! If neutrinos constitute the dark matter, then dwarf spheroidals are the most peculiar objects in this universe.

In this picture, dwarf spheroidals of mass ~ 5 ×10^{10} $M_\odot$ is moving in the halo of Milky Way galaxy. Dynamical friction will lead to an orbital relaxation timescale of the order of, (Chandrasekhar 1942)

$$t_d \sim v^3/G.^2 M\rho = 6 \times 10^{10}\ y\ (M/5 \times 10^{10}\ M_\odot)^{-1}(v/200\ \text{km s}^{-1})^3\ (\rho/10^{-26}\ \text{g cm}^{-3})^{-1}. \quad (22)$$

This estimate of t_d can easily change by a factor of 10 when finite size of haloes are taken into account. Chandrasekhar's original formula, for example has a coefficient, of the order of $(8\pi)^{-1}$ on the right-hand side making matters worse. To save the situation it is necessary to assume that Milky Way halo density is considerably depleted at the vicinity of dwarf spheroidals.

If all the above assumptions are granted, then 30 eV neutrinos may still be used to model Milky Way and dwarf spheroidals, as far as *kinematic* features are concerned. We hope to discuss the dynamical features in a subsequent paper.

3.2 *Cold Dark Matter*

The fact that cold dark matter candidates can easily account for dark matter in dwarf spheroidals has been emphasized in literature repeatedly (Blumenthal *et al*. 1984; Primack & Blumenthal 1983; Primack 1984). Since cold dark matter has significantly lower velocity dispersion than neutrinos, they can cluster easily at 10^7 $M_\odot$ scales. As the

mass of cold dark matter candidates are expected to be about > 1 keV, the phase space constraint is easily satisfied. If the existence of stringent constraints is treated as a negative aspect, then cold dark matter does better than neutrinos.

4. Discussion and conclusions

Contrary to claims often made in literature, the existence of dark matter in dwarfs does not rule out the possibility of neutrino dominance. On the other hand, it does impose stringent conditions on the distributional properties of dark matter. It is important to see whether these constraints can be respected at the scales of groups and clusters of galaxies. We intend to discuss this matter in detail in a subsequent paper; we shall merely present an outline here.

To begin with, we expect the kinematic modelling of dark matter in the universe to satisfy the following two criteria:

(i) There is only one kind of dark matter in the universe

This is probably most drastic of the simplifying assumptions we are making. Unfortunately this assumption is required to obtain any reasonable constraint whatsover. (With just two components for dark matter, it turns out that dark matter parameters get completely out-of-hand.) Within the context of this paper, this assumption implies that dark matter in dwarf spheroidals is of the same kind as dark matter in our Galaxy. When larger structures are considered, this assumption works as a powerful Occam's razor.

(ii) Dark matter clustering pattern is similar all over the universe.

As stated above, this assumption is (admittedly) vague. If the dark matter dominates the dynamics at all scales, we expect baryons to be secondary perturbations in the sea of dark matter. Thus we expect dark matter to be distributed in a similar pattern all throughout the universe. For example, the clustering scale of dark matter is expected to be of the same order everywhere in the universe.

These two assumptions imply that dark matter is predominantly distributed around the galaxies (and smaller dwarfs) as an extensive halo (~ 80 – 100 kpc). We take this pattern to be the basic unit; even though halo of individual galaxies might overlap in rich clusters if intergalactic spacing is less than about ~ 150 kpc. Consider a system of N (gravitationally bound) galaxies, each with a visible matter radius r_v (~ 10 kpc) and dark matter halo extension of r_h(~ 100 kpc), confined to a region of size R ('cluster size'). (The average intergalactic separation $D(\sim N^{-1/3} R)$ decides whether the haloes overlap or not.) We can easily estimate the $(M/L)_c$ for the cluster from the $(M/L)_g$ for individual galaxies evaluated at $r = r_v$. The total mass in the cluster is,

$$\begin{aligned} M_{\text{total}} &= N\, M_{\text{galaxy}}(r < r_h) \\ &= N\, M_{\text{gal}}(r < r_v)\cdot(r_h/r_v) \\ &= N\,(M/L)_{\text{gal},\,r=r_v}\cdot M_{\text{lum, gal}}\cdot(r_h/r_v) \end{aligned} \tag{23}$$

so that,

$$\frac{M_{\text{total}}}{N\,M_{\text{lum, gal}}} = (M/L)_{\text{cluster}} = (M/L)_{\text{galaxy},\,r=r_v}(r_h/r_v). \tag{24}$$

In other words cluster (M/L) ratios will be (r_h/r_v) times the galactic (M/L) ratios measured around the visible edges of galaxies. Since we expect (r_h/r_v) to be > 10, and $(M/L)_{gal}$ ~ 10 – 20 (taking ellipticals also into account) we get $(M/L)_{clusters}$ ~ 100 – 200 which is not widely off the mark.

The intergalactic separation D in such a system will be of the order of ($N^{-1/3}$ R). If $D > 2r_h$ there is no significant merging of haloes and the dark matter resides around each individual galaxy. On the other hand, if $D < 2\ r_h$ (as it often happens), the halo material in the overlap region $1 = 2\ r_h - D$ will form a common background, of nearly uniform density. The mass in this background halo will be,

$$M_{bg} \simeq N\ M_{gal,(r<r_v)} \cdot [(2r_h - D)/r_v] \tag{25}$$

so that,

$$M_{bg}/M_{total} \simeq (2r_h - D)/r_h. \tag{26}$$

In the dense regions of the cluster, M_{bg} can be significant part of M_{total}. Such a common halo, in our picture is dynamically generated. Galaxies are primary carriers of dark matter.

The above discussion is intended to show that one may be able to describe (M/L) observations at all scales without resorting to specific clustering at various scales.

Appendix 1

Criterion for Tidal Stability

We indicate below the derivation of Equation (11) in the text, based on Chandrasekhar (1942).

Consider a coordinate system $S(x, y, z)$ with origin at the centre of Milky Way galaxy (MW). Let a dwarf spheroidal (DS) be going around MW in a circular orbit. Let the distance to the centre of DS be R. We assume both MW and DS to be spherically symmetric with relation to their respective centres, and that the linear extent of visible matter in DS (~ 1 kpc) is much smaller than the distance R (~ 70 kpc).

The gravitational potential felt by a star bound within the DS, is the sum of two terms $V(r)$ and $U(r)$: $V(r)$ is the potential due to all the matter bound to MW and is distributed in a spherically symmetric fashion about the origin (centre of MW). The background halo *attached* to MW, through which DS is moving, contributes to $V(r)$. The $U(r)$ denotes the potential due to all matter bound to DS and is spherically symmetric about the *centre of DS*. Since the DS is moving, $U(r)$ has a complicated functional dependence on the inertial coordinates. All the stars bound to the DS as well as any dark matter *bound* to DS will contribute to $U(r)$. In the rest frame of the DS, we shall take the shape of DS to be a constant density sphere, with mean density, $\bar{\rho}_{bound} = (\bar{\rho}_v + \bar{\rho}_B)_{bound}$.

Under these assumptions the tidal stability condition (Equation 5.613 of Chandrasekhar 1942) becomes,

$$[(d^2V/dr^2) - (1/r)(dV/dr)]_{r=R} + (4\pi/3)G\bar{\rho}_{bound} > 0 \tag{A1.1}$$

using,

$$(1/r^2)d/dr(r^2 dV/dr) = 4\pi G\rho_{bg}(r) \tag{A1.2}$$

where $\rho_{bg}(r)$ is the density of MW halo at r, and defining a 'mean density' by,

$$\bar{\rho}_{bg}(r) \equiv \left(\frac{4\pi}{3} r^3\right)^{-1} \int_0^r 4\pi x^2 \, \rho_{bg}(x) \, dx \tag{A.13}$$

we can transform (A1.1) into a more useful expression. Simple algebra gives,

$$d^2V/dr^2 - (1/r)(dV/dr) = 4\pi G \, \rho_{bg}(r) - (3/r)(dV/dr)$$

$$= 4\pi G[\rho_{bg}(r) - \bar{\rho}_{bg}(r)] \tag{A1.4}$$

so that (A1.l) becomes,

$$\bar{\rho}_{bound} > 3[\bar{\rho}_{bg}(R) - \rho_{bg}(R)]. \tag{A1.5}$$

This relation shows that: (i) a non-trivial criterion is esbalished only when $\bar{\rho}_{bg}(R) > \rho_{bg}(R)$. In particular, if MW halo was globally constant then $\bar{\rho}_{bg} = \rho_{bg}$ and (A1.5) is identically satisfied, (ii) the existence of MW halo matter in the vicinity of DS *does* help tidal stability (note the $(-\rho_{bg}(R))$ term on the right hand side) but not completely.

We shall assume that density of matter bound to MW, $\rho_{bg}(r)$, has the following form:

$$\rho_{bg}(r) = \rho_0 \qquad r \leqslant r_c$$

$$= \rho_0 (r_c/r)^2 \qquad r \geqslant r_c \tag{A1.6}$$

where r_c is the core radius of MW with $r_c \lesssim 8$ kpc. Using (A1.6) in (A1.3) and (A1.5), we get,

$$\bar{\rho}_{bound} > 6\rho_{bg}(R)[1 - r_c/R]. \tag{A1.7}$$

Neglecting r_c($\lesssim 8$ kpc) compared to R ($\gtrsim 70$ kpc) we get Equation (11) of the text,

$$\bar{\rho}_{bound} > 6\rho_{bg}(R) \tag{A1.8}$$

ensuring tidal stability.

If (A1.8) is not satisfied, any normal astronomical system will get tidally disrupted. Mathematically speaking, violation of (A1.8) will make all stellar orbits, except those which satisfy very special initial conditions, to grow exponentially in time (see Chandrasekhar 1942, op. cit. Equation 5.621).

Appendix 2

Dependence of the Results on the Ratio (ρ_{vc}/ρ_{bc}) of Dwarf Spheroidals

In the text, we have assumed that the core densities of neutrinos and baryons are equal in the dwarf spheroidals (see Equations 15 and 16). We shall here examine the sensitivity of our results to this assumption. To do this, let us put, (in the text, we took $\alpha = 1$)

$$\rho_{vc} = \alpha^2 \cdot \rho_{bc} \tag{A2.1}$$

so that (16) is replaced by,

$$(\sigma_v/r_v) = \alpha(\sigma_b/r_b). \tag{A2.2}$$

It is straightforward to work out the α-dependence in various constraints. Equations

(17), (18) and (19) are replaced by Equations (A2.3–5):

$$m_v > (1010\ \mathrm{eV}/\alpha^{1/4})(\sigma_b/1\ \mathrm{km\,s^{-1}})^{-1/4}(r_b/100\ \mathrm{pc})^{-1/2}(r_b/r_v)^{3/4} \quad \text{(A.2.3)}$$

$$r_v/r_b > (109/\alpha^{1/3})(m_v/30\ \mathrm{eV})^{-4/3}(\sigma_b/1\ \mathrm{km\,s^{-1}})^{-1/3}(r_b/100\ \mathrm{pc})^{-2/3} \quad \text{(A.2.4)}$$

$$M/L > 3(r_t/r_b)^2\alpha^2. \quad \text{(A.2.5)}$$

The maximum distance up to which the DS-halo extends (due to tidal effect of our Galaxy) is determined by Equations (20), (21) in the text. This equation (21) is modified to, (v_{MW} = 225 km s^{-1})

$$x/R \leqslant [1 + (v_{MW}/\sigma_b)(r_b/r_v)(1/\alpha)]^{-1}. \quad \text{(A2.6)}$$

Given some specific model for the formation of the DS and the haloes, α can be estimated dynamically. Once α is estimated, the above equations present the constraints. In the absence of such a clearcut model, we have two possible routes open to us: (i) Use kinematic constraints to limit the range of α, and investigate results for this particular range, (ii) Use qualitative, 'guesstimates' for α based on simplified dynamics. We shall pursue both these routes here.

We know that $\rho_b > \rho_v$ (at the core) for most astronomical systems. Thus we expect α to be less than one. Observations on our Galaxy, for example, clearly indicate an increase in (*M/L*) with radial distance. Dark matter is distributed smoothly and over a larger scale, compared to visible matter, giving $\rho_b > \rho_v$ at the core. Dynamically, we expect $\rho_b > \rho_v$ because of the following reason: In the standard big bang scenario, baryons 'fall into' the potential well of neutrinos and quickly attain the same density contrast as neutrinos (Sato 1981). Thus, just after formation,

$$\delta_b = \frac{\rho_b - \bar{\rho}_b}{\bar{\rho}_b} = \frac{\rho_b}{\bar{\rho}_b} - 1 = \delta_v = \frac{\rho_v}{\bar{\rho}_v} - 1. \quad \text{(A2.7)}$$

So that in the beginning, (taking $\Omega_b \sim 0.01$ and $\Omega_v \sim 1$ where $\Omega = \bar{\rho}/\rho_c$)

$$\frac{\rho_v}{\rho_b} \approx \frac{\bar{\rho}_v}{\bar{\rho}_b} = \frac{\Omega_v}{\Omega_b} \approx 10^2. \quad \text{(A2.8)}$$

Neutrinos, being dissipationless maintain their configuration (core radius, density *etc.*) through violent relaxation and virialization. Baryons undergo dissipation and sink to the centre increasing ρ_b. Since we see baryons to be lumped at scales ten times (or more) smaller than the neutrino haloes, baryonic density would have enhanced by a factor of about 10^3. In that case (ρ_v/ρ_b) today would be $\sim 10^2 \times 10^{-3} \cdot \sim 10^{-1}$, or $\alpha \sim 0.3$. Note that a contraction of baryonic matter by a factor $\sim 10^{2/3} \sim 5$ is enough to produce an $\alpha < 1$, starting from (A2.8).

These conclusions are reinforced by consideration of the maximum value allowed for *x* in (A2.6). Demanding that $x_m < 20$ kpc (*i.e.* DS halo does not extend for more than 20 kpc) with,

$$x_m/R = [1 + (v_{MW}/\sigma_b)(r_b/r_v)(1/\alpha)]^{-1} \quad \text{(A2.9)}$$

it can be seen that $\alpha \lesssim 1$. On the other hand, too low a value of α will reduce the (*M/L*) value of DS *via* (A2.5). References cited in the text suggests an (*M/L*) value for DS galaxies to be greater than about 10.

With all these considerations in mind one may estimate the value of α to be in the range of (0.01, 1.00). (It is known from (A2.8) that $\alpha = (\rho_v/\rho_b)^{1/2}$ is definitely less

than 10). For this range which varies by a factor of 100, $\alpha^{1/4}$ and $\alpha^{1/3}$ produce factors of the order of 3–5. Since only these low powers of α appear in (A2.3)and (A2.4) our results are not very sensitive to α. Note that as α varies from 10^{-2} to 1, the ratios of core densities change from 10^{-4} to 1, which is sufficiently realistic range.

These arguments (partially at least) justify not including α in our discussion in the text.

Acknowledgement

We thank an anonymous referee for drawing our attention to the above point.

References

Aaronson, M. 1983, *Astrophys. J.*, **266**, L11.
Bekenstein, J., Milgrom, M. 1984, *Astrophys. J.*, **286**, 7.
Blumenthal, G. R., Faber, S. M, Primack, J. R., Rees, M. J. 1984, *Nature*, **311**, 517.
Bond, J. R., Efstathiou, G., Silk, J. 1980, *Phys. Rev. Lett*, **45**, 1980.
Bosma, A. 1978, *PhD Thesis*, Groningen Univ.
Chandrasekhar, S. 1942, in *Principles of Stellar Dynamics*, Dover, New York.
Cowsik, R., Ghosh, P. 1986, *J. Astrophys. Astr.*, **7**, (in press).
Cowsik, R., McClelland, J. 1972, *Phys. Rev. Letts.*, **29**, 669.
Dekel, A., Aarseth, S. J. 1984, *Astrophys. J.*, **283**, 1.
Doroshkevich, A. G., Khlopov, M. Yu., Sunyaev, R. A., Szalay, A. S., Zeldovich, Ya. B. 1981, *N. Y. Acad. Sci*.,**375**, 32.
Faber, S. M. 1984, in *Proc.* 1*st ESO-CERN Symp., Large-Scale Structure of the Universe, Cosmology and Fundamental Physics*, Eds G. Sethi & L. Van Hove, ESO, Germany, p. 187.
Faber, S. M, Gallagher, J. S. 1979, *A. Rev. Astr. Astrophys.*, **17**, 135.
Faber, S. M., Lin, D. N. C. 1983, *Astrophys. J.*, **266**, L17.
Frenk, C. S., White, S. D. M. 1982, *Mon. Not. R. astr. Soc*, **198**, 173.
Frenk, C. S., White, S. D. M., Davies, M. 1983, *Astrophys. J.*, **271**, 417.
Gerhstein, S. S., Zeldovich, Ya. B. 1966, *JETP Lett.*, **4**, 174.
Gunn, J. E., Knapp, G. R., Tremaine, S. D. 1979, *Astr. J.*, **84**, 1181.
Hartwick, F. D. A., Sargent, W. L. W. 1978, *Astrophys. J.*, **221**, 512.
Hegyi, D. J. 1984, in *Formation and Evolution of Galaxies and Large Structures in the Universe*, Eds J. Audouze & J. Tran Thanh Van, D. Reidel, Dordrecht, p. 149.
Hut, P., White, S. D. M. 1984, *Nature*, **310**, 637.
Innanen, K. A., Harris, W. E., Webbink, R. F. 1983, *Astr. J.*, **88**, 338.
Kaiser, N. 1983, *Astrophys. J.*, **273**, L17.
Klinkhamer, F. R., Norman, C. A. 1981, *Astrophys. J.*, **243**, L1.
King, I. 1962, *Astr. J.*, **67**, 471.
Lin, D. N. C, Faber, S. M. 1983, *Astrophys. J.*, **266**, L21.
Lin, D. N. C, Lynden-Bell, D. 1982, *Mon. Not. R. astr. Soc*, **198**, 707.
Lubimov, V. A., Novikov, E. G., Nozik, V. E, Tatyakov, E. F., Kosik, V. S. 1980, *Phys. Lett.*, **94B**, 266.
Lynden-Bell, D. 1967, *Mon. Not. R. astr. Soc*, **136**, 101.
Lynden-Bell, D. 1983, in *Kinematics, Dynamics, and Structure of Milky Way*, (Ed. W. C. H. Shutter, D. Reidel, Dordrecht), p. 349.
Marx, G., Szalay, A. S. 1972, in *Proc. Neutrino* 72, Technoinform, Hungary, p. 123.
Mellot, A. 1983, *Mon. Not. R. astr. Soc*, **202**, 595.
Mellot, A., 1985, *Astrophys. J.*, **289**, 2.
Mihalas, D., Binney, J., (Eds) 1981, *Galactic Astronomy*, Freeman, San Francisco.
Milgrom, M. 1983, *Astrophys. J.*, **270**, 365, 371, 384.
Peebles, P. J. E. 1979, in *Proc. Physical Cosmology, Les H ouches, Session XXXII*, North-Holland, New York, p. 213.

Peebles, P. J. E. 1982, *Astrophys. J.*, **258**, 415.
Primack, J. R., 1984, preprint SLAC-PUB-3387.
Primack, J. R., Blumenthal, G. R., 1984, in *Formation and Evolution of Galaxies and Large Structures in the Universe*, Eds J. Audouze & J. Tran. Thanh Van, D. Reidel, Dordrecht, p. 163.
Rood, H. J.,1981, Rep. *Prog. Phys.*, **44,** 1076.
Rubin, V. C. 1979, *Commun. Astrophys.*, **8**, 79.
Rubin, V. C, Ford, W. K. J., Thonnard, N., Berstein, D. 1982, *Astrophys. J.*, **261,** 349.
Rubin, V. C, Thonnard, N., Ford, W. K. J. 1982, *Astr. J.*, **87**, 477.
Sato, H. 1981, *N. Y. Acad. Sci.*, **375**, 43.
Sato, H., Takahara, P. 1980, *Prog. Theo. Phys.*, **64**, 2029.
Tremaine, S. D., Gunn, J. E. 1979, *Phys. Rev. Lett.*, **42,** 407.
Wasserman, I. 1981, *Astrophys. J.*, **248,** 1.